

3-24-2016

Image-Based Bidirectional Reflectance Distribution Function of Human Skin in the Visible and Near Infrared

Jeffrey R. Bintz

Follow this and additional works at: <https://scholar.afit.edu/etd>

Part of the [Optics Commons](#)

Recommended Citation

Bintz, Jeffrey R., "Image-Based Bidirectional Reflectance Distribution Function of Human Skin in the Visible and Near Infrared" (2016). *Theses and Dissertations*. 288.
<https://scholar.afit.edu/etd/288>

This Thesis is brought to you for free and open access by the Student Graduate Works at AFIT Scholar. It has been accepted for inclusion in Theses and Dissertations by an authorized administrator of AFIT Scholar. For more information, please contact richard.mansfield@afit.edu.



**IMAGE-BASED BIDIRECTIONAL
REFLECTANCE DISTRIBUTION FUNCTION
OF HUMAN SKIN IN THE VISIBLE AND
NEAR INFRARED**

THESIS

Jeffrey R. Bintz, Second Lieutenant, USAF
AFIT-ENG-MS-16-M-004

**DEPARTMENT OF THE AIR FORCE
AIR UNIVERSITY**

AIR FORCE INSTITUTE OF TECHNOLOGY

Wright-Patterson Air Force Base, Ohio

DISTRIBUTION STATEMENT A
APPROVED FOR PUBLIC RELEASE; DISTRIBUTION UNLIMITED.

The views expressed in this document are those of the author and do not reflect the official policy or position of the United States Air Force, the United States Department of Defense or the United States Government. This material is declared a work of the U.S. Government and is not subject to copyright protection in the United States.

AFIT-ENG-MS-16-M-004

IMAGE-BASED BIDIRECTIONAL REFLECTANCE
DISTRIBUTION FUNCTION OF HUMAN SKIN
IN THE VISIBLE AND NEAR INFRARED

THESIS

Presented to the Faculty
Department of Electrical and Computer Engineering
Graduate School of Engineering and Management
Air Force Institute of Technology
Air University
Air Education and Training Command
in Partial Fulfillment of the Requirements for the
Degree of Master of Science in Electrical Engineering

Jeffrey R. Bintz, B.S.E.E.

Second Lieutenant, USAF

March 2016

DISTRIBUTION STATEMENT A
APPROVED FOR PUBLIC RELEASE; DISTRIBUTION UNLIMITED.

IMAGE-BASED BIDIRECTIONAL REFLECTANCE
DISTRIBUTION FUNCTION OF HUMAN SKIN
IN THE VISIBLE AND NEAR INFRARED

THESIS

Jeffrey R. Bintz, B.S.E.E.
Second Lieutenant, USAF

Committee Membership:

Dr. Michael J. Mendenhall
Chair

Dr. Michael A. Marciniak
Member

Maj. Samuel D. Butler, PhD
Member

Dr. James "Tommy" Lloyd
Member

Abstract

Human detection is an important first step in locating and tracking people in many missions including search and rescue (SAR) and intelligence, surveillance, and reconnaissance (ISR) operations. Remotely identifying a human target that blends into the environment is a difficult task. Systems that acquire color imagery provide limited detection capabilities in large cluttered areas. As an alternative, recent detection systems utilize hyperspectral and multispectral technology to increase the acquired spectral content in imagery and subsequently better identify targets. At wavelengths in the visible and near infrared region of the electromagnetic spectrum, an individual can be identified by their unique skin parameters. Skin tissue has a spectral response to incident radiation and isolating the percent of incident flux reflected will give an overall reflectance signature. Current detection methods base the skin pixel selection criteria on a diffuse skin reflectance model. However, it can be observed that human skin exhibits a combination of specular and diffuse reflectance. The objective of this effort is to better characterize human skin reflectance by collecting image-based bidirectional reflectance distribution function (BRDF) skin measurements for future model incorporation into the skin pixel selection criteria used in the existing multispectral skin detection system. Skin measurements obtained by this image-based instrumentation could be used to distinguish separable specular and diffuse skin reflectance components or simply provide a vast collection of data defining a variety of angular and wavelength dependent imaging scenarios. Integrating multispectral BRDF data should reduce misdetections and better describe skin reflectance as a function of illumination source, target, and detector orientation.

Table of Contents

	Page
Abstract	iv
List of Figures	vii
List of Tables	xxiii
I. Introduction	1
1.1 Problem Statement	1
1.2 Research Goals	2
1.3 Thesis Overview	5
II. Background	7
2.1 Hyperspectral Imaging	7
2.2 Human Skin Spectra	9
2.3 Reflection Estimation	11
2.4 Skin Detection	12
2.4.1 Normalized Difference Equations	12
2.4.2 Skin Detection and False Alarm Suppression Algorithms	13
2.5 Scene Geometry Impact on Feature Space	16
2.5.1 Diffuse Assumption	18
2.5.2 Angular Dependent Model	19
2.6 Bidirectional Reflectance Distribution Function (BRDF)	21
2.6.1 Radiometry	21
2.6.2 BRDF Background	23
2.6.3 Image-Based BRDF Measurement Approach	26
2.6.4 Related Skin Reflection Work	28
2.7 Geometric Optics	29
2.8 Summary	31
III. Methodology	32
3.1 Image-Based BRDF Measurement System	32
3.1.1 Monocular Multispectral Camera System	32
3.1.2 BRDF Measurement Setup	38
3.2 Extracting Angular BRDF Coordinates	43
3.2.1 Grid-Patterned Laser Projection	43
3.2.2 Image Preprocessing and Grid Extraction	43
3.2.3 Surface Normal Extraction	46
3.2.4 BRDF Coordinate Mapping	51
3.3 Measuring Human Skin BRDF	56

	Page
3.3.1 Image Acquisition	56
3.3.2 Data Analysis Method	57
3.4 Summary	59
IV. Experiment and Results	60
4.1 Experiment	60
4.2 Displaying BRDF Data	64
4.3 Measurement Results	65
4.4 Effects on Skin Detection	90
4.4.1 Effect on Skin Detection Features	90
4.4.2 Evaluating BRDF effects in Typical Imaging Scenarios	114
4.5 Summary	118
V. Conclusion	119
5.1 Concluding Remarks	119
5.2 Future Work	120
5.2.1 Model Incorporation	120
5.2.2 Image-Based BRDF Measurement System	121
Appendix A. Measurement Results	123
Appendix B. IRB Approval	169
Bibliography	173

List of Figures

Figure		Page
1.	Typical imaging scenarios depicting potential locations of the sun, facial geometry, and skin detection camera system. The blue arrows represent incident light from the sun. The green arrows represent reflected light off the surface of the human target. The red distributions are BRDF cross-sections with specular reflectance peaks marked by red arrows.	3
2.	Laboratory image displaying the image-based BRDF bench-top measurement setup. The modules of the Image-based BRDF measurement system shown include the multispectral camera system, light source, forearm resting location, projection laser, swing arm, and detent tracking device.	4
3.	Example angular measurement scenario. Each image location captures several angular-dependent samples.	6
4.	Hyperspectral measurements of from Type I/II skin, Type III/IV skin, a plastic doll, and brown cardboard [28] (included here with permission from author). Each object’s response is slightly different, allowing it to be distinguishable based on its spectra. Skin categories will be discussed in Section 2.2.	8
5.	Spectra of Type I/II skin, Type III/IV skin, and Type V/VI skin with corresponding melanosome percentages generated with data from [28].	10
6.	(NDGRI, NDSI) feature space from an urban image test set scene in [25]. Values were acquired by the authors in [25] using the SpecTIR HuperSpecTIR Version 3 (HST3) Hyperspectral Imager [13]. Blue dots are skin features and red dots are background features. Contours represent Gaussian mixture models for skin and background pixels.	14
7.	Gaussian mixture models for skin and background samples.	15

Figure	Page
8. ROC curves generated for each of the K=5 models from cross validation. Curves are from the urban image test set in [25].	16
9. Typical imaging scenarios depicting potential locations of the sun, facial geometry, and camera system. The blue arrows represent incident light from the sun. The green arrows represent reflected light off the surface of the human target. The red distributions are BRDF cross-sections with specular peaks marked by red arrows.	17
10. 2D Feature space from urban test set example ([25]) illustrating broad skin pixel grouping due to the features' angular, melanin content, and wavelength dependency. Values were acquired using the HST3 Hyperspectral Imager. Red dots are skin features and green dots are background features.	18
11. 2D Feature space of living and cadaver measured skin (green) and diffuse modeled skin (black) for Type I/II, Type II/IV, and Type V/VI skin from [28] (included here with permission from author). The red circles represent spectral confusers and background pixels.	20
12. Three categories of reflectance: perfectly specular, perfectly diffuse, and the combination of diffuse and specular reflectance.	24
13. Hemispherical geometry of the BRDF, defining the elevation and azimuth angles for both the source and observer.	25
14. Image recreation of setup found in [20] depicting the image-based BRDF measurement system applicable to curved surfaces.	26
15. In [14], the proposed image-based BRDF measurement system (included here by permission from author and publisher). In this system the camera is fixed and the light source rotates.	27

Figure	Page
16. Skin BRDF measurement setup in [20] (included here with permission from author). Radiometric information is acquired with a RGB camera and geometric information is acquired with a 3D range scanner. Reference materials are placed on the subjects head for automation purposes.	28
17. Existing monocular multispectral camera layout.	33
18. Block diagram for the existing monocular multispectral camera layout developed in [30]. Included in the image are the four cameras, fore optic, three dichroic mirrors, two iris diaphragms, two magnification lenses, and two filters.	36
19. CAD drawing showing existing monocular multispectral camera layout at scale. (A, B) Two Goodrich SWIR cameras, (C) one ThorLabs Monochrome camera, and (D) one ThorLabs RGB camera.	37
20. Bench-top CAD drawing featuring the 3' × 6' optical bench top with mounted swing arm and pivot hardware. The camera layout is assembled on a 12" × 18" × 0.25" breadboard mounted on top of the swing arm.	39
21. The ASD Pro Lamp is used as the light source in the image-based BRDF measurement system. The lamp has a 50 W quartz-tungsten-halogen bulb and is designed for indoor lab reflectance measurements over the region 350-2500nm.	40
22. The Brightline Pro Red Complex-Pattern-Generating Alignment Laser used in the image-based BRDF measurement system. The output power is adjusted from 5 to 40 mW and is used to project a highly visible focus-adjusting laser grid on the target for extracting surface normals.	41

Figure	Page
23.	A CAD drawing of the image-based BRDF bench-top measurement system. The existing monocular multispectral camera system is elevated on a rotating arm. A grid-pattern projection laser is mounted mid-way down the swing-arm, while the light source is stationary on the table, level with the camera system's fore-optic, and marking the x -axis for the system's coordinate system (discussed in Section 3.2). The human subject's forearm rests on top of the central cylinder. 42
24.	A typical grid projection onto the human subject's forearm using the red Laserglow, class 2, grid pattern generating laser. The grid pattern becomes distorted as it wraps around the curved surface. 44
25.	An example of pre-processing from subject 3, position 2 of the measurement test. (Left) Image shows the red channel. (Middle) This image displays the results from sharpening, contrast, and the binary conversion processes. (Right) This image shows the results after median filtering. 45
26.	An example of pre-processing from subject 3, position 2 of the measurement test. (Left) Image shows the skeletonized grid. (Middle) This image displays the results from the edge detection function with each color representing a separate segment. (Right) This image shows the linearized segments. 46
27.	On the left is an example of a final grid reconstruction from subject 3, position 2 of the measurement test. The image shows the grid segments in varying color and the forearm edge in purple. On the right is the corresponding mask. 47
28.	A CAD drawing showing the orientation of all modules relative to the x , y , and z axes. The light sources marks the x -axis and the camera system rotates within the xy -plane. 48

Figure	Page
29.	Illustration of the geometry used in calculating θ_R in the surface normal extraction method. d_{grid} is the length of one side of a projected grid square at the object distance of a perpendicular flat target, while d_{meas} is the length of d_{grid} projected onto the surface of the forearm as imaged by the camera system. 49
30.	A top-view cross-sectional illustration of the forearm depicting the angles and vectors used to calculate the horizontal component of the surface normal. This component is calculated from the horizontal laser grid lines. θ_R is the equivalent angle from Figure 29, while θ_I is the horizontal component being solved for. 50
31.	A side-view cross-sectional illustration of the forearm depicting the angles and vectors used to calculate the vertical component of the surface normal. This component is calculated from the vertical laser grid lines. θ_R is the equivalent angle from Figure 29, while θ_I is the vertical component being solved for. 50
32.	A detailed vector and angle illustration showing relations used in the BRDF measurement system. Elements are labeled and described in Table 5 53
33.	This diagram illustrates the transformation of the surface normal vector to the z -axis along with the projections on to the xy -plane (blue circle) of the same transformation of the light source and camera vectors. The transformation is used to extract the azimuthal angle, ϕ_r , relative to the surface normal. Elements are titled and described in Table 5. 55
34.	Example masked matrices in image forms of θ_i , ϕ_r , and θ_r (left, middle, right). Each image is from subject 3, position 2 of the image-based BRDF measurement system. 57
35.	Example masked matrices in image forms of estimated reflectance values from the 660nm band at camera positions (from left to right, top to bottom) 6, 36, 66, 96, 126, 156 degrees from the light source. 58

Figure	Page
36. Spectral reflectance measurements acquired from the ASD Field Spectrometer for each human test subject. Prior to BRDF data collection, these measurements were acquired from the test subject's left forearm. The legend shows the subject control number and their corresponding estimated Fitzpatrick Skin Type.	62
37. BRDF skin measurements obtained from Subject 4 in the 540nm, 660nm, 850nm, 1080nm, and 1580nm bands. Estimated Fitzpatrick Skin Type: V, Hair Coverage: Low.	68
38. BRDF skin measurements obtained from Subject 5 in the 540nm, 660nm, 850nm, 1080nm, and 1580nm bands. Estimated Fitzpatrick Skin Type: I/II, Hair Coverage: Low.	70
39. BRDF skin measurements obtained from Subject 6 in the 540nm, 660nm, 850nm, 1080nm, and 1580nm bands. Estimated Fitzpatrick Skin Type: I, Hair Coverage: High.	73
40. Subject 1 - BRDF values are plotted versus θ_i , for all $\theta_i = \theta_r$ forward-scattering combinations.	75
41. Subject 2 - BRDF values are plotted versus θ_i , for all $\theta_i = \theta_r$ forward-scattering combinations.	76
42. Subject 3 - BRDF values are plotted versus θ_i , for all $\theta_i = \theta_r$ forward-scattering combinations.	77
43. Subject 4 - BRDF values are plotted versus θ_i , for all $\theta_i = \theta_r$ forward-scattering combinations.	78
44. Subject 5 - BRDF values are plotted versus θ_i , for all $\theta_i = \theta_r$ forward-scattering combinations.	79
45. Subject 6 - BRDF values are plotted versus θ_i , for all $\theta_i = \theta_r$ forward-scattering combinations.	80
46. Three ranges for θ_i values are evaluated at ϕ_r close to 180 degrees and plotted in BRDF vs θ_r space for Subject 5 (Type I/II, Low hair coverage) with data from the 540nm band.	81

Figure	Page
47. Three ranges for θ_i values are evaluated at ϕ_r close to 180 degrees and plotted in BRDF vs θ_r space for Subject 5 (Type I/II, Low hair coverage) with data from the 660nm band.	82
48. Three ranges for θ_i values are evaluated at ϕ_r close to 180 degrees and plotted in BRDF vs θ_r space for Subject 5 (Type I/II, Low hair coverage) with data from the 850nm band.	83
49. Three ranges for θ_i values are evaluated at ϕ_r close to 180 degrees and plotted in BRDF vs θ_r space for Subject 5 (Type I/II, Low hair coverage) with data from the 1080nm band.	84
50. Three ranges for θ_i values are evaluated at ϕ_r close to 180 degrees and plotted in BRDF vs θ_r space for Subject 5 (Type I/II, Low hair coverage) with data from the 1580nm band.	85
51. Three ranges for θ_i values are evaluated at ϕ_r close to 180 degrees and plotted in BRDF vs θ_r space for Subject 5 (Type I/II, Low hair coverage) with data from the 540nm band.	86
52. Three ranges for θ_i values are evaluated at ϕ_r close to 180 degrees and plotted in BRDF vs θ_r space for Subject 5 (Type I/II, Low hair coverage) with data from the 660nm band.	87
53. Three ranges for θ_i values are evaluated at ϕ_r close to 180 degrees and plotted in BRDF vs θ_r space for Subject 5 (Type I/II, Low hair coverage) with data from the 850nm band.	87
54. Three ranges for θ_i values are evaluated at ϕ_r close to 180 degrees and plotted in BRDF vs θ_r space for Subject 5 (Type I/II, Low hair coverage) with data from the 1080nm band.	88
55. Three ranges for θ_i values are evaluated at ϕ_r close to 180 degrees and plotted in BRDF vs θ_r space for Subject 5 (Type I/II, Low hair coverage) with data from the 1580nm band. Specular data is cropped for $\theta_i=75-80$ degrees for a better display of the other two ranges of θ_i	88

Figure	Page
56. NDSI and NDGRI calculations from Subject 4 data.....	91
57. NDSI and NDGRI calculations from Subject 5 data.....	92
58. NDSI and NDGRI calculations from Subject 6 data.....	93
59. Subject 4 - NDSI and NDGRI values for all $\theta_i = \theta_r$ forward-scattering combinations.....	95
60. Subject 5 - NDSI and NDGRI values for all $\theta_i = \theta_r$ forward-scattering combinations.....	96
61. Subject 6 - NDSI and NDGRI values for all $\theta_i = \theta_r$ forward-scattering combinations.....	97
62. Three ranges for θ_i values are evaluated at ϕ_r close to 180 degrees and plotted in NDSI vs θ_r space for Subject 4.	99
63. Three ranges for θ_i values are evaluated at ϕ_r close to 180 degrees and plotted in NDSI vs θ_r space for Subject 5.	100
64. Three ranges for θ_i values are evaluated at ϕ_r close to 180 degrees and plotted in NDSI vs θ_r space for Subject 6.	101
65. Three ranges for θ_i values are evaluated at ϕ_r close to 180 degrees and plotted in NDGRI vs θ_r space for Subject 4.	103
66. Three ranges for θ_i values are evaluated at ϕ_r close to 180 degrees and plotted in NDGRI vs θ_r space for Subject 5.	104
67. Three ranges for θ_i values are evaluated at ϕ_r close to 180 degrees and plotted in NDGRI vs θ_r space for Subject 6.	105
68. Spectrometer measurements from [28] (red) overlaid on data obtained in this study. Both sets of data are from the identical imaging scenario, where $\theta_i \approx 12$ degrees, $\theta_r \approx 35$ degrees, and $\phi_r \approx 0$ degrees.	107

Figure	Page
69. Subject 1 - (NDSI, NDGRI) feature space plots where three ranges for θ_i values are evaluated at ϕ_r close to 180 degrees for nine groupings of θ_r	108
70. Subject 2 - (NDSI, NDGRI) feature space plots where three ranges for θ_i values are evaluated at ϕ_r close to 180 degrees for nine groupings of θ_r	109
71. Subject 3 - (NDSI, NDGRI) feature space plots where three ranges for θ_i values are evaluated at ϕ_r close to 180 degrees for nine groupings of θ_r	110
72. Subject 4 - (NDSI, NDGRI) feature space plots where three ranges for θ_i values are evaluated at ϕ_r close to 180 degrees for nine groupings of θ_r	111
73. Subject 5 - (NDSI, NDGRI) feature space plots where three ranges for θ_i values are evaluated at ϕ_r close to 180 degrees for nine groupings of θ_r	112
74. Subject 6 - (NDSI, NDGRI) feature space plots where three ranges for θ_i values are evaluated at ϕ_r close to 180 degrees for nine groupings of θ_r	113
75. Three possible imaging scenarios: A) Overhead imaging configuration of a standing human target with the sun directly above target, B) Ground imaging configuration of a standing human target with the sun directly above target, C) Overhead imaging configuration of a lying human target with the sun directly above target.....	115
76. Incident light (blue) and reflected light (green) scenarios that may lead to misdetections. As the ray combinations get darker, the farther away the resulting pixel cluster in (NDSI, NDGRI) space will deviate from other data, e.g., the diffuse data obtained with a spectrometer.	117
77. BRDF skin measurements obtained from Subject 1 in the 540nm, 660nm, 850nm, 1080nm, and 1580nm bands. Estimated Fitzpatrick Skin Type: III, Hair Coverage: Low.	125

Figure	Page
78. BRDF skin measurements obtained from Subject 2 in the 540nm, 660nm, 850nm, 1080nm, and 1580nm bands. Estimated Fitzpatrick Skin Type: II/III, Hair Coverage: Low.	128
79. BRDF skin measurements obtained from Subject 3 in the 540nm, 660nm, 850nm, 1080nm, and 1580nm bands. Estimated Fitzpatrick Skin Type: II/III, Hair Coverage: Medium.	131
80. Three ranges for θ_i values are evaluated at ϕ_r close to 180 degrees and plotted in BRDF vs θ_r space for Subject 1 (Type III, Low hair coverage) with data from the 540nm band.	132
81. Three ranges for θ_i values are evaluated at ϕ_r close to 180 degrees and plotted in BRDF vs θ_r space for Subject 1 (Type III, Low hair coverage) with data from the 660nm band.	132
82. Three ranges for θ_i values are evaluated at ϕ_r close to 180 degrees and plotted in BRDF vs θ_r space for Subject 1 (Type III, Low hair coverage) with data from the 850nm band.	133
83. Three ranges for θ_i values are evaluated at ϕ_r close to 180 degrees and plotted in BRDF vs θ_r space for Subject 1 (Type III, Low hair coverage) with data from the 1080nm band.	133
84. Three ranges for θ_i values are evaluated at ϕ_r close to 180 degrees and plotted in BRDF vs θ_r space for Subject 1 (Type III, Low hair coverage) with data from the 1580nm band.	134
85. Three ranges for θ_i values are evaluated at ϕ_r close to 180 degrees and plotted in BRDF vs θ_r space for Subject 2 (Type II/III, Low hair coverage) with data from the 540nm band.	134
86. Three ranges for θ_i values are evaluated at ϕ_r close to 180 degrees and plotted in BRDF vs θ_r space for Subject 2 (Type II/III, Low hair coverage) with data from the 660nm band.	135

Figure	Page
87. Three ranges for θ_i values are evaluated at ϕ_r close to 180 degrees and plotted in BRDF vs θ_r space for Subject 2 (Type II/III, Low hair coverage) with data from the 850nm band.	135
88. Three ranges for θ_i values are evaluated at ϕ_r close to 180 degrees and plotted in BRDF vs θ_r space for Subject 2 (Type II/III, Low hair coverage) with data from the 1080nm band.	136
89. Three ranges for θ_i values are evaluated at ϕ_r close to 180 degrees and plotted in BRDF vs θ_r space for Subject 2 (Type III, Low hair coverage) with data from the 1580nm band.	136
90. Three ranges for θ_i values are evaluated at ϕ_r close to 180 degrees and plotted in BRDF vs θ_r space for Subject 3 (Type II/III, Medium hair coverage) with data from the 540nm band.	137
91. Three ranges for θ_i values are evaluated at ϕ_r close to 180 degrees and plotted in BRDF vs θ_r space for Subject 3 (Type II/III, Medium hair coverage) with data from the 660nm band.	137
92. Three ranges for θ_i values are evaluated at ϕ_r close to 180 degrees and plotted in BRDF vs θ_r space for Subject 3 (Type II/III, Medium hair coverage) with data from the 850nm band.	138
93. Three ranges for θ_i values are evaluated at ϕ_r close to 180 degrees and plotted in BRDF vs θ_r space for Subject 3 (Type II/III, Medium hair coverage) with data from the 1080nm band.	138
94. Three ranges for θ_i values are evaluated at ϕ_r close to 180 degrees and plotted in BRDF vs θ_r space for Subject 3 (Type II/III, Medium hair coverage) with data from the 1580nm band.	139
95. Three ranges for θ_i values are evaluated at ϕ_r close to 180 degrees and plotted in BRDF vs θ_r space for Subject 4 (Type V, Low hair coverage) with data from the 540nm band.	139

Figure	Page
96. Three ranges for θ_i values are evaluated at ϕ_r close to 180 degrees and plotted in BRDF vs θ_r space for Subject 4 (Type V, Low hair coverage) with data from the 660nm band.	140
97. Three ranges for θ_i values are evaluated at ϕ_r close to 180 degrees and plotted in BRDF vs θ_r space for Subject 4 (Type V, Low hair coverage) with data from the 850nm band.	140
98. Three ranges for θ_i values are evaluated at ϕ_r close to 180 degrees and plotted in BRDF vs θ_r space for Subject 4 (Type V, Low hair coverage) with data from the 1080nm band.	141
99. Three ranges for θ_i values are evaluated at ϕ_r close to 180 degrees and plotted in BRDF vs θ_r space for Subject 4 (Type V, Low hair coverage) with data from the 1580nm band.	141
100. Three ranges for θ_i values are evaluated at ϕ_r close to 180 degrees and plotted in BRDF vs θ_r space for Subject 6 (Type I, High hair coverage) with data from the 540nm band.	142
101. Three ranges for θ_i values are evaluated at ϕ_r close to 180 degrees and plotted in BRDF vs θ_r space for Subject 6 (Type I, High hair coverage) with data from the 660nm band.	142
102. Three ranges for θ_i values are evaluated at ϕ_r close to 180 degrees and plotted in BRDF vs θ_r space for Subject 6 (Type I, High hair coverage) with data from the 850nm band.	143
103. Three ranges for θ_i values are evaluated at ϕ_r close to 180 degrees and plotted in BRDF vs θ_r space for Subject 6 (Type I, High hair coverage) with data from the 1080nm band.	143
104. Three ranges for θ_i values are evaluated at ϕ_r close to 180 degrees and plotted in BRDF vs θ_r space for Subject 6 (Type I, High hair coverage) with data from the 1580nm band.	144

Figure	Page
105. Three ranges for θ_i values are evaluated at ϕ_r close to 180 degrees and plotted in BRDF vs θ_r space for Subject 1 (Type III, Low hair coverage) with data from the 540nm band.	144
106. Three ranges for θ_i values are evaluated at ϕ_r close to 180 degrees and plotted in BRDF vs θ_r space for Subject 1 (Type III, Low hair coverage) with data from the 660nm band.	145
107. Three ranges for θ_i values are evaluated at ϕ_r close to 180 degrees and plotted in BRDF vs θ_r space for Subject 1 (Type III, Low hair coverage) with data from the 850nm band.	145
108. Three ranges for θ_i values are evaluated at ϕ_r close to 180 degrees and plotted in BRDF vs θ_r space for Subject 1 (Type III, Low hair coverage) with data from the 1080nm band.	146
109. Three ranges for θ_i values are evaluated at ϕ_r close to 180 degrees and plotted in BRDF vs θ_r space for Subject 1 (Type III, Low hair coverage) with data from the 1580nm band. Specular data is cropped for $\theta_i=75-80$ degrees for a better display of the other two ranges of θ_i	146
110. Three ranges for θ_i values are evaluated at ϕ_r close to 180 degrees and plotted in BRDF vs θ_r space for Subject 2 (Type II/III, Low hair coverage) with data from the 540nm band.	147
111. Three ranges for θ_i values are evaluated at ϕ_r close to 180 degrees and plotted in BRDF vs θ_r space for Subject 2 (Type II/III, Low hair coverage) with data from the 660nm band.	147
112. Three ranges for θ_i values are evaluated at ϕ_r close to 180 degrees and plotted in BRDF vs θ_r space for Subject 2 (Type II/III, Low hair coverage) with data from the 850nm band.	148
113. Three ranges for θ_i values are evaluated at ϕ_r close to 180 degrees and plotted in BRDF vs θ_r space for Subject 2 (Type II/III, Low hair coverage) with data from the 1080nm band.	148

Figure	Page
114. Three ranges for θ_i values are evaluated at ϕ_r close to 180 degrees and plotted in BRDF vs θ_r space for Subject 2 (Type III, Low hair coverage) with data from the 1580nm band. Specular data is cropped for $\theta_i=75-80$ degrees for a better display of the other two ranges of θ_i	149
115. Three ranges for θ_i values are evaluated at ϕ_r close to 180 degrees and plotted in BRDF vs θ_r space for Subject 3 (Type II/III, Medium hair coverage) with data from the 540nm band.	150
116. Three ranges for θ_i values are evaluated at ϕ_r close to 180 degrees and plotted in BRDF vs θ_r space for Subject 3 (Type II/III, Medium hair coverage) with data from the 660nm band.	150
117. Three ranges for θ_i values are evaluated at ϕ_r close to 180 degrees and plotted in BRDF vs θ_r space for Subject 3 (Type II/III, Medium hair coverage) with data from the 850nm band.	151
118. Three ranges for θ_i values are evaluated at ϕ_r close to 180 degrees and plotted in BRDF vs θ_r space for Subject 3 (Type II/III, Medium hair coverage) with data from the 1080nm band.	151
119. Three ranges for θ_i values are evaluated at ϕ_r close to 180 degrees and plotted in BRDF vs θ_r space for Subject 3 (Type II/III, Medium hair coverage) with data from the 1580nm band. Specular data is cropped for $\theta_i=75-80$ degrees for a better display of the other two ranges of θ_i	152
120. Three ranges for θ_i values are evaluated at ϕ_r close to 180 degrees and plotted in BRDF vs θ_r space for Subject 4 (Type V, Low hair coverage) with data from the 540nm band.	153
121. Three ranges for θ_i values are evaluated at ϕ_r close to 180 degrees and plotted in BRDF vs θ_r space for Subject 4 (Type V, Low hair coverage) with data from the 660nm band.	153

Figure	Page
122. Three ranges for θ_i values are evaluated at ϕ_r close to 180 degrees and plotted in BRDF vs θ_r space for Subject 4 (Type V, Low hair coverage) with data from the 850nm band.	154
123. Three ranges for θ_i values are evaluated at ϕ_r close to 180 degrees and plotted in BRDF vs θ_r space for Subject 4 (Type V, Low hair coverage) with data from the 1080nm band.	154
124. Three ranges for θ_i values are evaluated at ϕ_r close to 180 degrees and plotted in BRDF vs θ_r space for Subject 4 (Type V, Low hair coverage) with data from the 1580nm band. Specular data is cropped for $\theta_i=75-80$ degrees for a better display of the other two ranges of θ_i	155
125. Three ranges for θ_i values are evaluated at ϕ_r close to 180 degrees and plotted in BRDF vs θ_r space for Subject 6 (Type I, High hair coverage) with data from the 540nm band.	156
126. Three ranges for θ_i values are evaluated at ϕ_r close to 180 degrees and plotted in BRDF vs θ_r space for Subject 6 (Type I, High hair coverage) with data from the 660nm band.	156
127. Three ranges for θ_i values are evaluated at ϕ_r close to 180 degrees and plotted in BRDF vs θ_r space for Subject 6 (Type I, High hair coverage) with data from the 850nm band.	157
128. Three ranges for θ_i values are evaluated at ϕ_r close to 180 degrees and plotted in BRDF vs θ_r space for Subject 6 (Type I, High hair coverage) with data from the 1080nm band.	157
129. Three ranges for θ_i values are evaluated at ϕ_r close to 180 degrees and plotted in BRDF vs θ_r space for Subject 6 (Type I, High hair coverage) with data from the 1580nm band. Specular data is cropped for $\theta_i=75-80$ degrees for a better display of the other two ranges of θ_i	158
130. NDSI and NDGRI calculations from Subject 1 data.	159
131. NDSI and NDGRI calculations from Subject 2 data.	160

Figure	Page
132. NDSI and NDGRI calculations from Subject 3 data.....	161
133. Subject 1 - NDSI and NDGRI values for all $\theta_i = \theta_r$ forward-scattering combinations.....	162
134. Subject 2 - NDSI and NDGRI values for all $\theta_i = \theta_r$ forward-scattering combinations.....	163
135. Subject 3 - NDSI and NDGRI values for all $\theta_i = \theta_r$ forward-scattering combinations.....	164
136. Three ranges for θ_i values are evaluated at ϕ_r close to 180 degrees and plotted in NDSI vs θ_r space for Subject 1.	165
137. Three ranges for θ_i values are evaluated at ϕ_r close to 180 degrees and plotted in NDSI vs θ_r space for Subject 2.	165
138. Three ranges for θ_i values are evaluated at ϕ_r close to 180 degrees and plotted in NDSI vs θ_r space for Subject 3.	166
139. Three ranges for θ_i values are evaluated at ϕ_r close to 180 degrees and plotted in NDGRI vs θ_r space for Subject 1.	167
140. Three ranges for θ_i values are evaluated at ϕ_r close to 180 degrees and plotted in NDGRI vs θ_r space for Subject 2.	167
141. Three ranges for θ_i values are evaluated at ϕ_r close to 180 degrees and plotted in NDGRI vs θ_r space for Subject 3.	168

List of Tables

Table	Page
1. The Fitzpatrick scale used to define skin color and its sun response [22].	9
2. Specifications for the Goodrich SU640KTSX-1.7RT [30].	34
3. Specifications of the ThorLabs DCC1645C Color Camera [30].	35
4. Specifications of the ThorLabs DCC1545M Monochrome Camera [30].	35
5. The element titles and descriptions of the BRDF coordinate system used in the image-based BRDF measurement system. Color coded angular and vector elements match those presented in Figure 32.	52
6. Tabular listing of the reflectance values for each panel and camera combination [30]. Camera numbers are in reference to Figure 18.	56
7. Table shows each subject with control number, along with their corresponding estimated Fitzpatrick Skin Type (discussed in Section 2.2) and their estimate hair coverage on their forearm (Low, Medium, or High).	61

IMAGE-BASED BIDIRECTIONAL REFLECTANCE
DISTRIBUTION FUNCTION OF HUMAN SKIN
IN THE VISIBLE AND NEAR INFRARED

I. Introduction

1.1 Problem Statement

Detecting a small or partially exposed object in a large field of view is a difficult task, especially if the object is camouflaged or amongst a significant amount of background clutter. This is the task of many Air Force missions. In fact, search and rescue (SAR) and intelligence, surveillance, and reconnaissance (ISR) missions do exactly this, where remote sensing techniques are used to locate and track people of interest. Recently, hyperspectral and multispectral imaging are used in a wide variety of remote sensing systems. For example, the Civil Air Patrol deployed the Airborne Real-Time Cueing Hyperspectral Enhanced Reconnaissance (ARCHER) sensor system, which collects high resolution spectral content in the range of 500-1100 nm to aid in airborne SAR and ISR signature matching [36]. The additional spectral content increases the distinguishability of objects that are typically undetectable with the human eye.

Previous work demonstrated the concept of hyperspectral imaging for skin detection [25, 28, 29]. The hyperspectral image-based skin detection methodology was developed enough that the research group from [25, 28, 29] designed a compact monocular multispectral detection system to exploit the reflectance of human skin in the visible (VIS) and three near-infrared (NIR) bands [30]. The monocular multispectral

system utilizes four cameras to acquire content in the RGB, 800 nm, 1080 nm, and 1580 nm bands. Through image processing, indices for skin detection and false alarm suppression are computed. Current methods base their skin pixel selection criteria on a diffuse skin reflectance model. In this research, the work expands upon preceding skin characterization by collecting image-based bidirectional reflectance distribution function (BRDF) measurements for the future incorporation of a more accurate model, which accounts for both the diffuse and specular components of human skin reflectance. Integrating key attributes attained from the BRDF measurements will reduce misdetections and better characterize skin reflectance as a function of illumination source, target, and detector location.

1.2 Research Goals

In order to better detect people in remote sensing applications, we must improve the accuracy of skin detection. Lighting conditions, human orientation, and camera location all play a factor in how reflectance is recorded by the detector and is portrayed in Figure 1. In previous work, a diffuse model was used, assuming skin reflectance was invariant to different incident and reflected light scenarios. Different scene configurations limited the accuracy of the results obtained in [28, 30]. That being said, the range of possible source, target, and detector orientations lead to a requirement to better characterize the angular dependence of skin reflectance in changing scenarios.

When the flow of light is interrupted by a surface, the energy is partially absorbed by the material and partially scattered back into the environment [19]. The amount of light scattered and its directional distribution depend on the composition and structure of the material. Human skin, for example, has a unique directional distribution the light reflected from it. The bidirectional reflectance distribution function

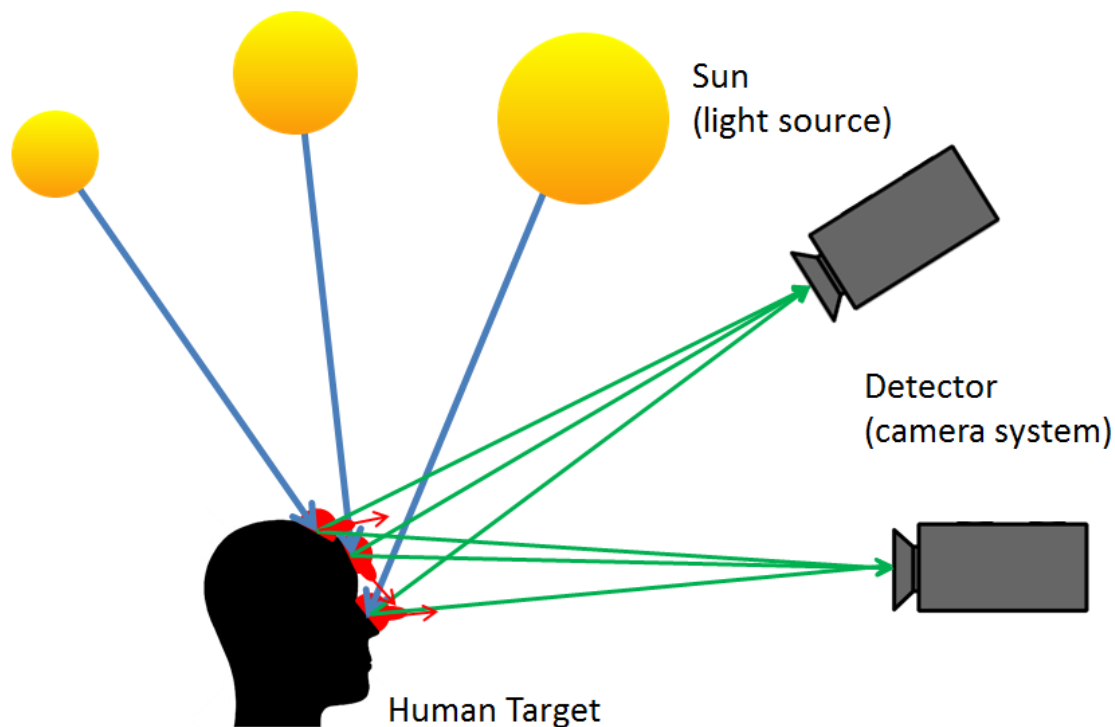


Figure 1. Typical imaging scenarios depicting potential locations of the sun, facial geometry, and skin detection camera system. The blue arrows represent incident light from the sun. The green arrows represent reflected light off the surface of the human target. The red distributions are BRDF cross-sections with specular reflectance peaks marked by red arrows.

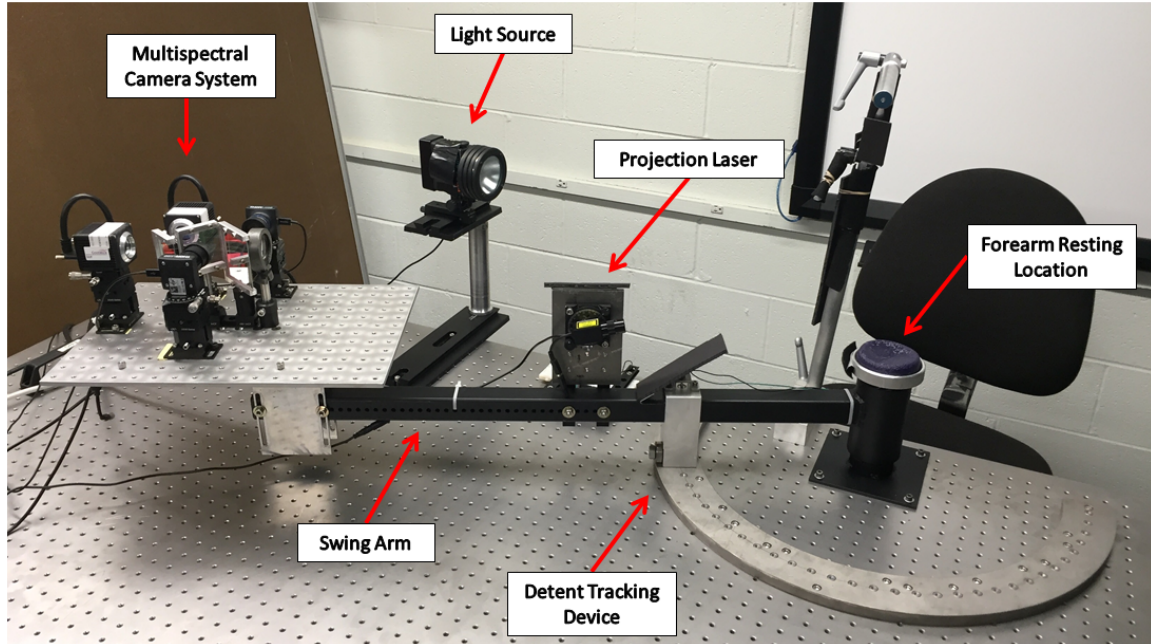


Figure 2. Laboratory image displaying the image-based BRDF bench-top measurement setup. The modules of the Image-based BRDF measurement system shown include the multispectral camera system, light source, forearm resting location, projection laser, swing arm, and detent tracking device.

(BRDF) fully describes directional reflectance for a given material. In this research, an image-based BRDF measurement system is constructed, allowing the collection of skin reflectance values from a large domain of source, target, and detector locations as seen in Figure 2 and Figure 3. The targets consist of human subject forearms of varying skin type. By collecting data across five spectral channels, sixteen detector locations, and a range of surface normals, these measurements (over 30 million samples per subject) will span the diffuse and specular components of skin reflectance, leading to a high fidelity BRDF model usable in the existing detection algorithms to improve skin detection performance.

1.3 Thesis Overview

As an overview, Chapter II is a review of the fundamental material needed in understanding the methods used in the current human skin detection algorithms. This includes hyperspectral imaging, the composition of human skin, the image processing used in skin detection, the impact of scene geometry, a review of radiometry, BRDF, and foundational knowledge of the optics used in the construction of the camera system. It further describes, in detail, the concept of the BRDF and draws from the existing literature in order to give the reader a better understanding of image-based BRDF measurements and related skin measurement work. Chapter III details the methodology used to extract the BRDF measurements. The chapter describes the design of the image-based measurement system while giving specifications of the system components and the physical layout of the modules. Additionally, the chapter describes the technique used to extract the angular BRDF coordinates, image acquisition approach, and methods of analysis. In Chapter IV, the experimental procedure, data interpretation, and measurement results are presented. A comparison is made across the angular scenarios, each wavelength, and each subject. More significantly, the impact of BRDF on the indices used for skin detection and false alarm suppression is demonstrated. Lastly, Chapter V summarizes the contributions of this research, its contribution to the overall BRDF integration effort, and provides insights into future research.

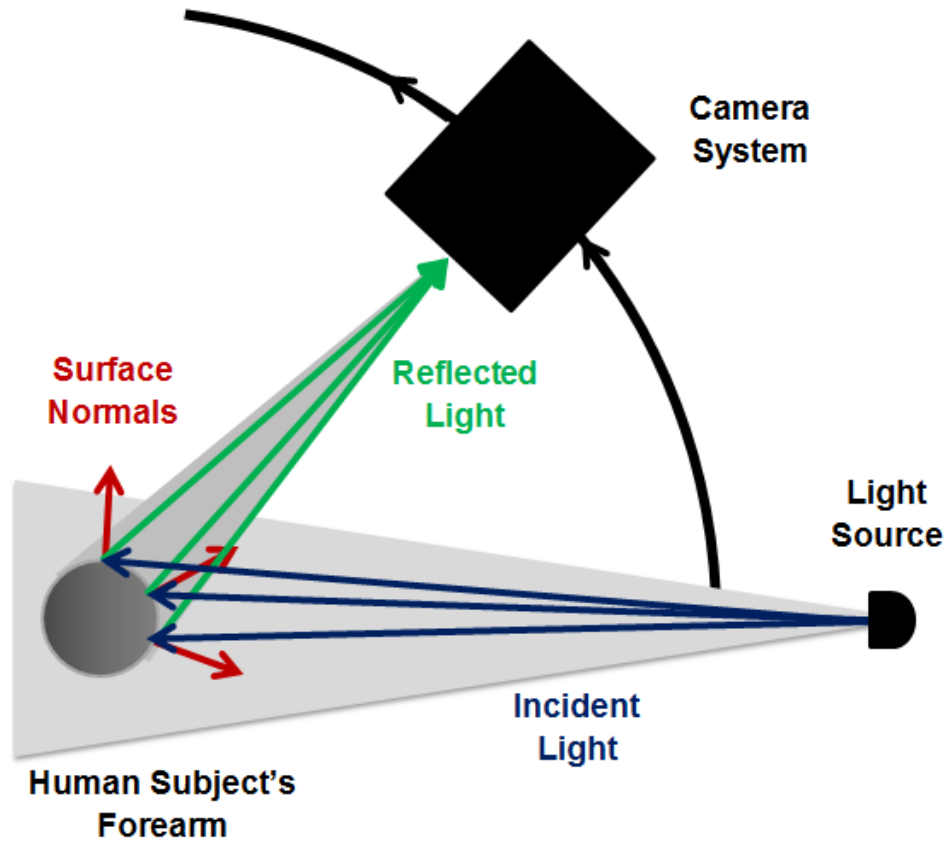


Figure 3. Example angular measurement scenario. Each image location captures several angular-dependent samples.

II. Background

Chapter II covers the fundamental background necessary in understanding the skin detection system and Bidirectional Reflectance Distribution Function (BRDF) measurement techniques used in this research. Hyperspectral imaging is discussed to give the reader an understanding of the origins and impact of the technology. Next, the human skin spectrum is reviewed to show the unique spectral features exploited in the detection of human skin. The detection algorithms and reflectance estimation methods are discussed to show how the images are processed. In Section 2.5, the results and corresponding issues with the current diffuse assumption are discussed to show the reader what is being addressed in this research effort. Next, an overview of BRDF is presented and the necessary background in radiometry, image-based measurement techniques, and related work. Lastly, geometric optics is presented to give an overview of these concepts used to reconstruct the monocular multispectral camera system to meet the needs of the image-based BRDF application.

2.1 Hyperspectral Imaging

Hyperspectral imaging is a commonly used remote sensing technology that is now used in a wide range of detection applications due to its effectiveness and versatility. Hyperspectral imagers are able to acquire hundreds of spectral channels in the visible, near infrared, and short wave infrared regions. By collecting such a large number of wavelengths over such a broad spectrum, similar materials can be distinguished based on the object's spectral response (see Figure 4 as an example). Characterizing natural materials, e.g., minerals, rock, and vegetation, is a long standing field of study utilizing hyperspectral technology [11, 31, 32]. Spectral and spatial resolution continues to improve in hyperspectral imagers allowing a single pixel to acquire increasingly more

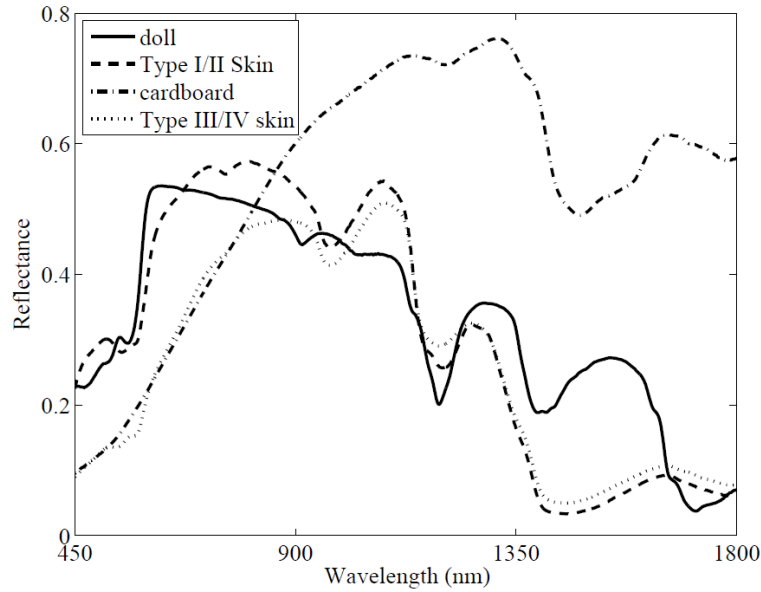


Figure 4. Hyperspectral measurements of from Type I/II skin, Type III/IV skin, a plastic doll, and brown cardboard [28] (included here with permission from author). Each object’s response is slightly different, allowing it to be distiguishable based on its spectra. Skin categories will be discussed in Section 2.2.

data. Hyperspectral technology is frequently sought for use in military operations for its ability to provide combat search and rescue (CSAR) services and advanced intelligence, surveillance, and reconnaissance (ISR). Over a large geographic area, objects of interest and anomalous materials such as aircraft debris and human targets in CSAR operations can be detected [34, 37, 38]. A hyperspectral system developed for CSAR or ISR applications must be simple enough to operate by a potentially fatigued or non-hyperspectral expert. Furthermore, the system must discriminate small objects among a vast and complex scene in a variety of overhead scenarios at a real-time rate [18, 35, 36]. In this research, an existing multispectral skin detection system is utilized for reflectance measurements targeting improvements in the skin detection algorithms [30].

2.2 Human Skin Spectra

Human skin is a complex material made up of different layers, each holding different physical properties that affect their response to radiation. Skin can be described as six layers of dermal tissue with varying amounts of water and melanosomes followed by a underlying layer of subcutaneous fat. With knowledge of layer depths and parameters such as water, blood, collagen, and melanosomes, a reflectance model can be defined. Work in [28] details the organization of tissue layers in human skin, the reflection at each skin tissue layer, and the reflectance model generated using the Kubelka-Munk transport equations. In this study, it is important to have a good understanding of the characteristics of human skin reflectance signatures.

Table 1. The Fitzpatrick scale used to define skin color and its sun response [22].

Type	Color	Sun Response
I	Very Fair	Always Burns
II	Fair	Usually Burns
III	White to Olive	Sometimes Burns
IV	Brown	Rarely Burns
V	Dark Brown	Very Rarely Burns
VI	Black	Never Burns

Table 1 defines Fitzpatrick's skin characterization for Type I-Type VI skin, and is a function of the skins melanin content and its likelihood of burning due to exposure to ultraviolet radiation [22]. Light-skinned adults on the very fair-color end of the spectrum contain melanosome percentages near 1.6%, while darkly pigmented adults on the other end of the spectrum contain melanosome percentages near 43% [28]. An estimated Fitzpatrick skin type can be qualitatively categorized based on the skins reflectance reading at 685 nm [28], which is the leading indicator for melanosome percentage.

In Figure 5, skin reflectance measurements are plotted for Fitzpatrick Skin Type

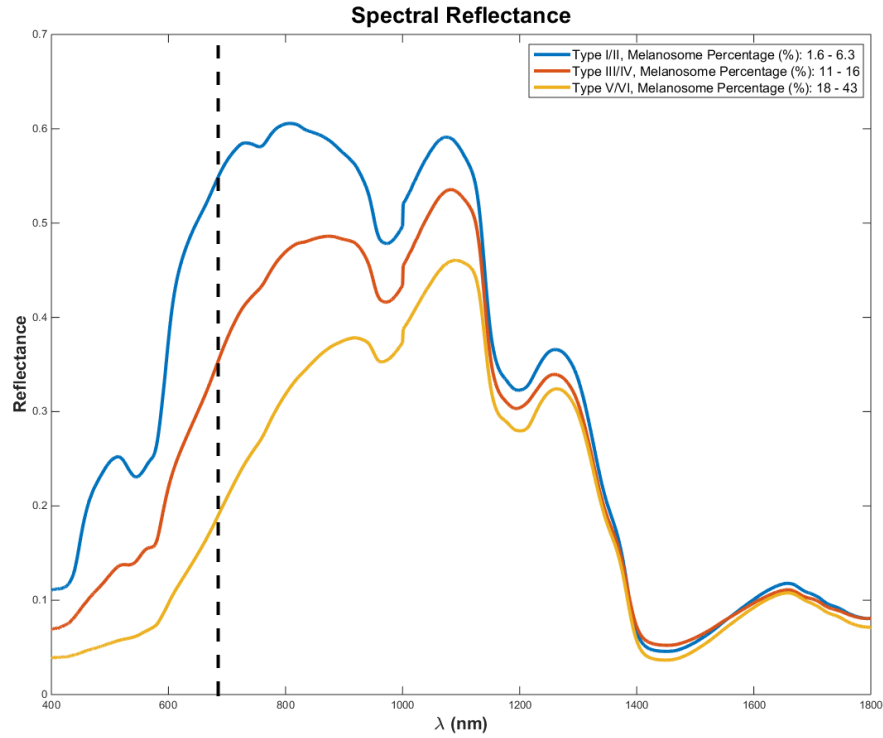


Figure 5. Spectra of Type I/II skin, Type III/IV skin, and Type V/VI skin with corresponding melanosome percentages generated with data from [28].

I/II, Type III/IV, and Type V/VI. There are several unique features apparent in the spectra. The first defining feature of skin reflectance is its dependence on melanin. As melanin content increases, reflectance decreases due to melanin absorption in the VIS and NIR regions. As wavelength increases, melanin absorption is less prevalent beyond 1100 nm [12]. Second, in VIS region the *w*-shaped feature is due to hemoglobin absorption. Lastly, water absorption becomes significant beyond 1150 nm accounting for the decrease in reflectance at longer wavelengths and causes the skin reflectance to merge. These key features are exploited in the skin detection algorithms [28] described in the Section 2.4.

2.3 Reflection Estimation

In many hyperspectral imaging applications, the illumination and path characteristics of a scene are changing or unknown due to atmospheric effects, weather, time of day, etc. Therefore, many hyperspectral remote sensing systems convert radiance values to reflectance values. Reflectance is used because, unlike radiance, reflectance is a property of the material and independent of illumination and path characteristics [30]. Passive sensors gather radiation that is emitted or reflected by the target and background, which is dependent on illumination and path characteristics. There are several techniques used to transform an image from radiance to estimated reflectance. The technique used in [25] is the Empirical Line Method (ELM) [6]. To perform ELM, the reflectance and radiance measurement for at least two materials must be known for each sensor in the system. The material's known reflectance spectra can be acquired using a field spectrometer and the radiance measurements are taken from the image pixel values. The unknown spectral reflectance values can be estimated by the radiative affine transform as follows:

$$\hat{\rho}(\lambda) = \frac{L(\lambda) - \hat{b}(\lambda)}{\hat{a}(\lambda)}, \quad (1)$$

where

$$\hat{a}(\lambda) = \frac{L_2(\lambda) - L_1(\lambda)}{\rho_2(\lambda) - \rho_1(\lambda)}, \text{ and} \quad (2)$$

$$\hat{b}(\lambda) = \frac{L_1(\lambda)\rho_2(\lambda) - L_2(\lambda)\rho_1(\lambda)}{\rho_2(\lambda) - \rho_1(\lambda)}. \quad (3)$$

L_1 and L_2 are the measured radiance values corresponding to the reflectance values ρ_1 and ρ_2 of the two known media. Using Equation (2), the unknown reflectance is found using the radiance value, L , from the pixel being converted. ELM is a

linear approximation used in remote sensing to incorporate the source, detector, and transmission effects. In order to use ELM, there are two criteria that need be met. First, the field of view is uniformly illuminated. Second, no portion of the image is saturated or undersaturated. Disrupting these assumptions will produce a non-linear relationship.

In Section 2.6, the concept of bidirectional reflectance is introduced. It is important to note that estimated reflectance is converted from radiance values measured as a result of the target's BRDF. The amount of light reaching the sensor depends on the illuminated source, target, and detector angular locations. That being said, BRDF values may more commonly exceed one or dip below zero.

2.4 Skin Detection

2.4.1 Normalized Difference Equations.

A normalized difference equation is used when comparing two values of interest and is defined as:

$$d(A, B) = \frac{A - B}{A + B} \quad (4)$$

Normalized difference calculations are used to make detections more selective and can reduce false-alarms. In addition, the calculation compresses the data by a factor of two by combining two values into a single new field for further computations. As an example, if reflectance values $\{0.95, 0.65\}$ are compared against $\{0.65, 0.35\}$, a difference calculation would show both equal to 0.3 and a detection would be considered based on a threshold value. However, a normalized difference calculation would result in 0.1875 and 0.3, respectively, showing how a normalized difference calculation is more selective by considering constant gain factors [30].

2.4.2 Skin Detection and False Alarm Suppression Algorithms.

A two-dimensional (2D) feature space is used to separate skin pixels from background pixels [29]. The two features are defined as the Normalized Difference Skin Index (NDSI) and the Normalized Difference Green Red Index (NDGRI), both are based on Equation (4). A likelihood ratio test (LRT) with varying detection thresholds is used to construct Receiver Operating Characteristic (ROC) curves, where equal error rates (EER), detection probability, and false alarm probability are obtained.

The NDSI is one of many normalized difference indices used in the exploitation of a target's known absorption characteristics. The NDSI, motivated by the Normalized Difference Vegetation Index [31], is an effective method used in detecting human skin. As a function of reflectance at 1080 nm and 1580 nm, the NDSI exploits the melanin absorption and a stable low-valued point beyond the water vapor absorption band, respectively. The NDSI is defined as

$$\gamma_i = \frac{\hat{\rho}_i(1080nm) - \hat{\rho}_i(1580nm)}{\hat{\rho}_i(1080nm) + \hat{\rho}_i(1580nm)}, \quad (5)$$

where $\hat{\rho}_i(\lambda)$ is the reflectance value at a given wavelength, λ , for the i^{th} pixel.

The NDGRI is a secondary index used for false alarm suppression. In a typical scene, there can be several other water-bearing objects that have similar reflectance due to water absorption (*e.g.*, vegetation, snow, or cloudy water). In-scene objects that also contain a significant amount of water must be addressed because the primary detection feature relies heavily on the water absorption characteristics of skin. Exploiting the observation that skin is more red than green (see Figure 5), the NDGRI aids in reducing false alarm rates. The NDGRI is defined as:

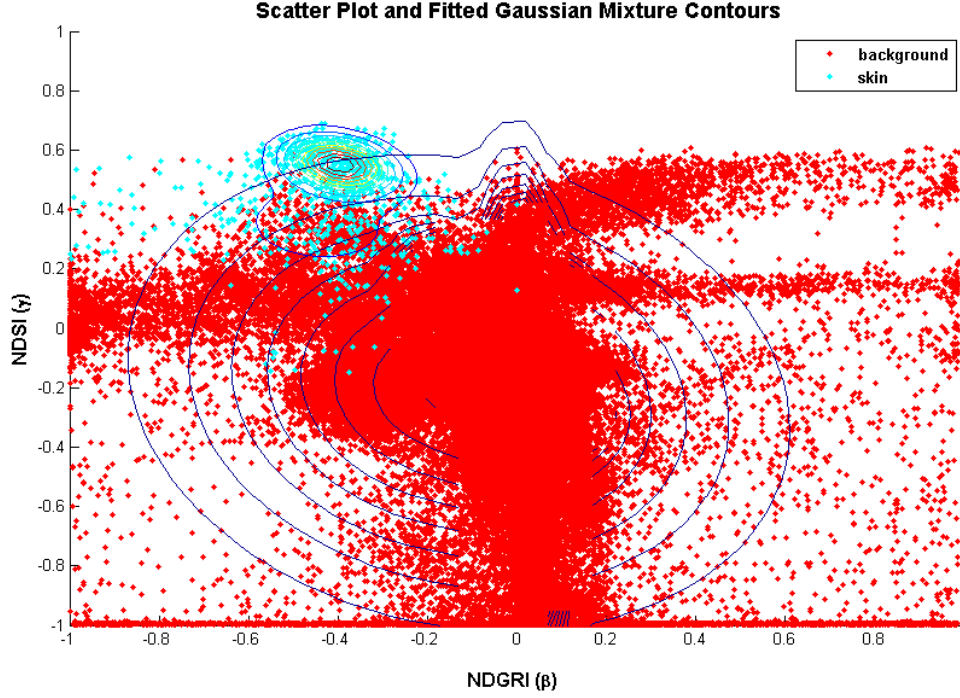


Figure 6. (NDGRI, NDSI) feature space from an urban image test set scene in [25]. Values were acquired by the authors in [25] using the SpecTIR HuperSpecTIR Version 3 (HST3) Hyperspectral Imager [13]. Blue dots are skin features and red dots are background features. Contours represent Gaussian mixture models for skin and background pixels.

$$\beta_i = \frac{\hat{\rho}_i(540nm) - \hat{\rho}_i(660nm)}{\hat{\rho}_i(540nm) + \hat{\rho}_i(660nm)} \quad (6)$$

where $\hat{\rho}_i(\lambda)$ is the reflectance value at a given wavelength, λ , for the i^{th} pixel. Figure 6 shows the 2D (NDGRI, NDSI) feature space resulting from the application of Equation (5) and Equation (6). The data used for Figure 6 was collected from an image acquired from an urban hyperspectral image test set. The skin pixels, marked in blue, form a cluster in the upper left quadrant, while the background pixels, marked in red, form a wider spread across the feature space (background distribution is similar for non-urban environments). Both the skin pixels and background pixels are fit to functional forms with Gaussian mixture models, parameterized using expectation

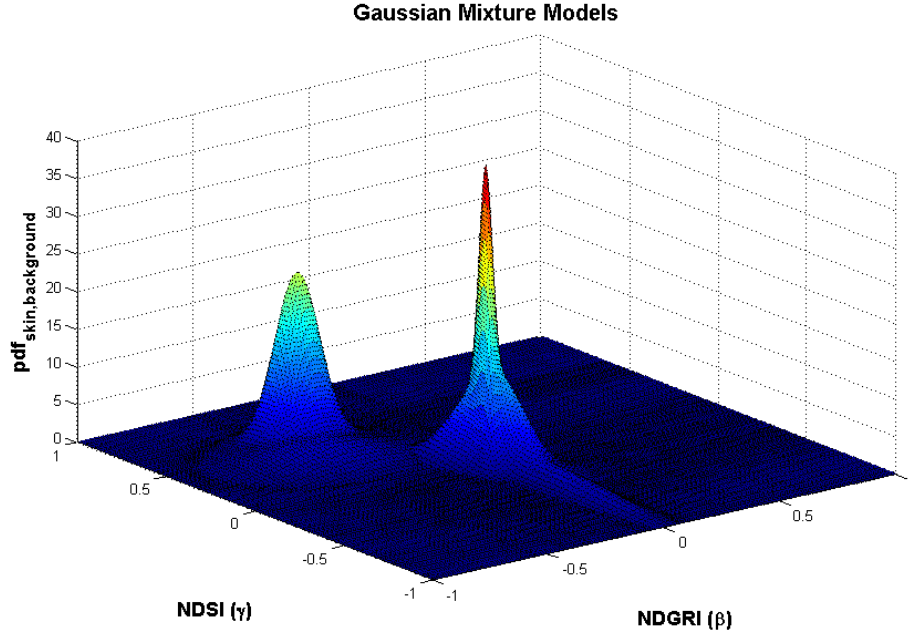


Figure 7. Gaussian mixture models for skin and background samples.

maximization, and shown in Figure 7 [26]. Given the two probability distribution functions (*pdf*), a LRT is used. The LRT minimizes the Bayes Risk and provides flexibility in choosing a threshold (η) that meets a desired EER or specific true detection and false alarm rates. The likelihood ratio test is defined as:

$$\Lambda_{\Theta}(\theta) = \frac{f_s(\theta)}{f_b(\theta)} \underset{H_b}{\overset{H_s}{\gtrless}} \eta, \quad (7)$$

where $f_s(\theta)$ is the *pdf* of the human skin pixels, $f_b(\theta)$ is the *pdf* of background pixels, H_s is the hypothesis that the sample is skin, and H_b is the hypothesis that the sample is background. Lastly, results are obtained through K-fold cross validation (for K=5 [9]). An equal number of samples is assigned to each of the K-bins using stratified random sampling and the LRT threshold iterates from $\left[\min \left(\frac{f_s(\theta)}{f_b(\theta)} \right) \max \left(\frac{f_s(\theta)}{f_b(\theta)} \right) \right]$. Results are evaluated with EERs, true detection probabilities, and false alarm probabilities extracted from the generated ROC curves, such as those ROC curves shown

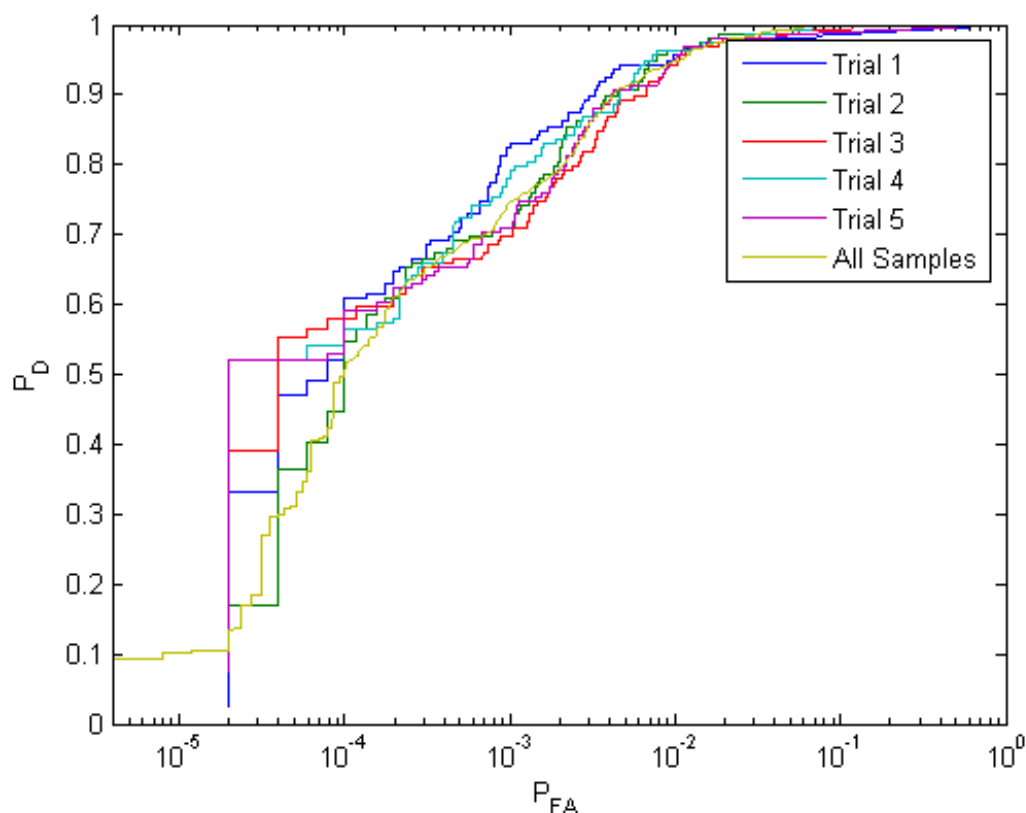


Figure 8. ROC curves generated for each of the K=5 models from cross validation. Curves are from the urban image test set in [25].

in Figure 8.

2.5 Scene Geometry Impact on Feature Space

Scene geometry in hyperspectral imaging applications can have a tremendous impact on detection results. A robust skin detection system needs to acquire accurate results in any remote sensing scenario. The current detector theory is based on a diffuse reflectance model [1, 28]. Incorporating the results of a BRDF study on human skin will be beneficial in modeling the amount of energy that is incident on a sensor at any given source, target and detector angular scenario. Understanding both the specular and diffuse reflectance components of human skin will lead to a better

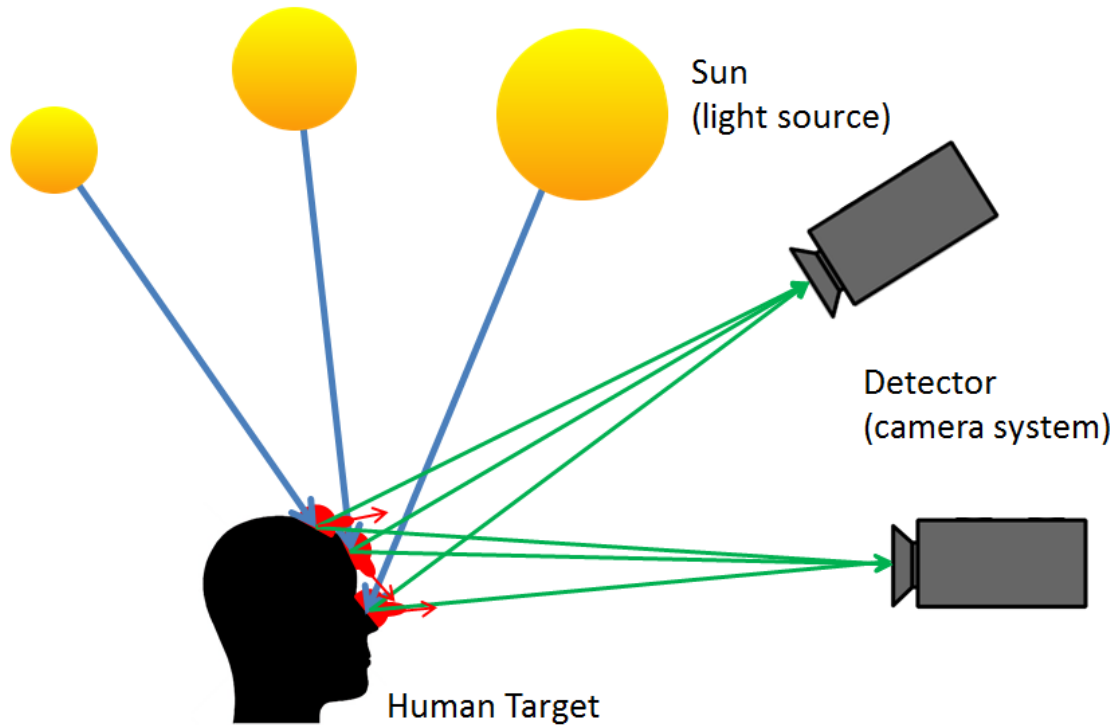


Figure 9. Typical imaging scenarios depicting potential locations of the sun, facial geometry, and camera system. The blue arrows represent incident light from the sun. The green arrows represent reflected light off the surface of the human target. The red distributions are BRDF cross-sections with specular peaks marked by red arrows.

understanding of what needs to be accounted for in the skin detection algorithms. Figure 1, repeats here as Figure 9 for convenience, illustrates a typical scenario depicting three incident light locations from the sun striking three geometrically different locations of the human head. In the illustration, the blue arrows represent incident light, the green arrows represent reflected light, and the red distribution represents a cross-section of the BRDF with the peak specular component marked with a red arrow. As seen in the figure, the reflected light (green arrows) may capture a diffuse reflectance, a specular peak reflectance, or a slightly off-specular peak reflectance. The variation of reflectance component also corresponds to a variation in magnitude. This variation can be accounted for with BRDF skin measurements.

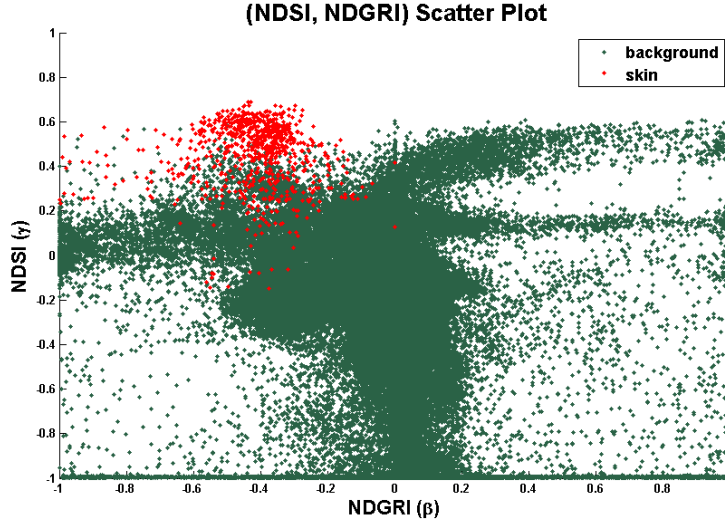


Figure 10. 2D Feature space from urban test set example ([25]) illustrating broad skin pixel grouping due to the features' angular, melanin content, and wavelength dependency. Values were acquired using the HST3 Hyperspectral Imager. Red dots are skin features and green dots are background features.

2.5.1 Diffuse Assumption.

Current detector theory ignores the wavelength and angular dependent specularly of human skin reflectance by approximating the indices of refraction as constant across the VIS and NIR regions for all angular scenarios. However, there is a known 4% specular reflectance between the air and stratum corneum at normal incidence [28]), with specularly varying with angle, melanin content, and wavelength. The current reflectance approximation imagines the reflectance distribution as a simple uniform hemispherical dome where reflectance values are equal in all directions for all incident angles. Figure 10, shows data collected from an HST3 Hyperspectral Imager and plotted using the indices backed by a diffuse assumption, with detection theory also lacking the specularly dependence on melanin content and wavelength. This pixel set in [25] was collected from an urban test set where human skin was oriented in different directions relative to the sun and imager.

As seen in Figure 10, the skin pixels in the upper left quadrant form a rela-

tively wide distribution when compared to those taken with a field spectrometer in Figure 11. The wide spread across the feature space is due to the range of skin reflectance values acquired from the imager. The skin, sun, and imager angular locations affect the amount of energy incident on the sensor's FPA. When observation angles are near the specular peak, reflectance values are greater than those of the diffuse component. Specularity can depend on wavelength, angular scenario, and an individual's melanosome percentage. In Figure 11, data is collected with an Analytical Spectral Devices (ASD) FieldSpec[®] 3 portable spectrometer which acquires data through the use of a hand-held contact probe containing a fiber optic cable and light source. When taking contact probe measurements, the light source is 12 degrees off-normal and the fiber optic is 35 degrees off-normal, both along the same azimuthal angle relative to the surface normal. In this fixed angle scenario, the collected data captures the magnitude of the diffuse reflectance component. Therefore, utilizing a diffuse assumption in the algorithms is appropriate and results in the tight cluster shown in the plot. By capturing full BRDF measurement sets, a model can be applied to the current skin detection algorithms, which should result in a tighter skin pixel cluster like what is seen from the field spectrometer and portrayed in Figure 11.

2.5.2 Angular Dependent Model.

As stated in Section 2.4.2, the skin pixel selection criteria are based on two indices, the NDSI and the NDGRI. With the BRDF measurements, one can incorporate a BRDF model into the indices in order to account for the angular-dependency. A more accurate NDSI and NDGRI, constructed with the BRDF, are redefined as:

$$\gamma_i(\theta_i, \theta_r, \phi_r) = \frac{(f_{BRDF_i}(1080nm, \theta_i, \theta_r, \phi_r)) - (f_{BRDF_i}(1580nm, \theta_i, \theta_r, \phi_r))}{(f_{BRDF_i}(1080nm, \theta_i, \theta_r, \phi_r)) + (f_{BRDF_i}(1580nm, \theta_i, \theta_r, \phi_r))} \quad (8)$$

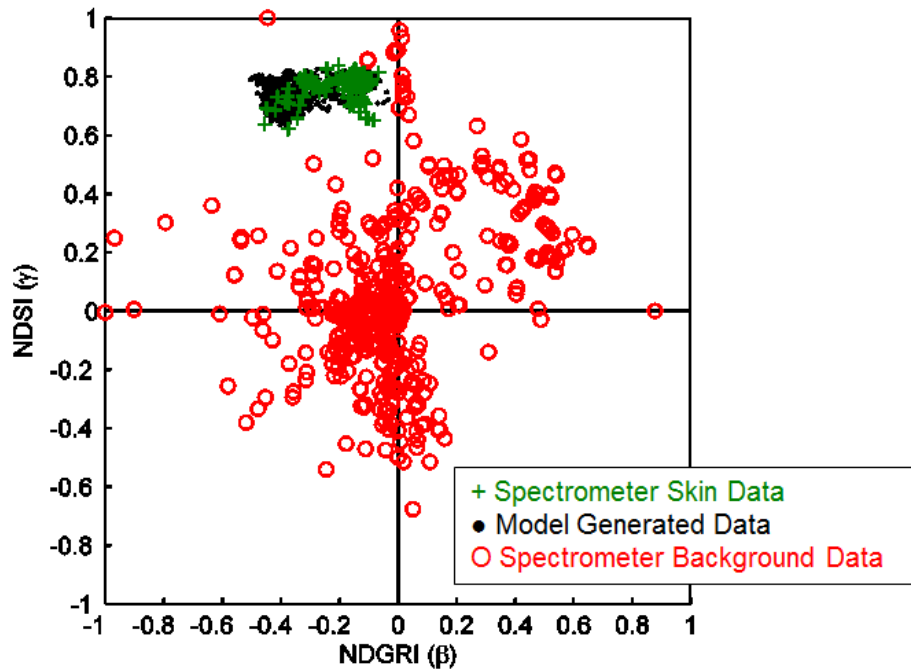


Figure 11. 2D Feature space of living and cadaver measured skin (green) and diffuse modeled skin (black) for Type I/II, Type II/IV, and Type V/VI skin from [28] (included here with permission from author). The red circles represent spectral confusers and background pixels.

$$\beta_i(\theta_i, \theta_r, \phi_r) = \frac{(f_{BRDF_i}(540nm, \theta_i, \theta_r, \phi_r)) - (f_{BRDF_i}(660nm, \theta_i, \theta_r, \phi_r))}{(f_{BRDF_i}(540nm, \theta_i, \theta_r, \phi_r)) + (f_{BRDF_i}(660nm, \theta_i, \theta_r, \phi_r))} \quad (9)$$

where f_{BRDF_i} is the BRDF at a given wavelength and angular scenario for the i^{th} pixel. The BRDF is discussed in detail in Section 2.6.

2.6 Bidirectional Reflectance Distribution Function (BRDF)

2.6.1 Radiometry.

The radiant characterization of human skin requires a system of radiometric quantities based on the distribution of power or flux (Φ_e). Radiometric quantities from [5] describe the flux densities used to characterize sources. Flux is defined in units of watts (W) or, in calculations pertaining to photon detectors, photon units (photon-count/s). The following equation shows the relationship between energy flux (Φ_e) and photon flux (Φ_q)

$$\Phi_q = \Phi_e \frac{\lambda}{hc}, \quad (10)$$

where c is the speed of light, h is Planck's constant, and λ is wavelength. All energy-derived quantities based on the *Joule* unit can be converted to photon derived quantities by utilizing Equation (10).

Now consider the radiometric quantities that define how power is distributed with respect to unit area. Irradiance (E_e) is the amount of power per unit area incident on a surface and characterizes a passive receiver surface. Exitance (M_e) is the amount of power per unit area that leaves a surface and characterizes a self-emission source or reflected radiation. As a function of incident surface area (A_d), irradiance in W/cm² is defined as:

$$E_e = \frac{\partial \Phi_e}{\partial A_d}, \quad (11)$$

while exitance in W/cm^2 is defined as:

$$M_e = \frac{\partial \Phi_e}{\partial A_s}, \quad (12)$$

where A_s is source area.

Next consider radiance, which characterizes an extended source by incorporating the projected source area and unit solid angle. Radiance (L_e) is the amount of power radiated per source area per unit solid angle ($\partial \Omega_d$). In differential form:

$$L_e = \frac{\partial^2 \Phi_e}{\partial A_s \cos \theta_s \partial \Omega_d}. \quad (13)$$

The cosine correction, θ_s , accounts for the unit solid angles that are off normal. Given radiance and configuration parameters, one can arrive at any given radiometric quantity by manipulating Equation (13). Keep in mind that radiometric quantity can vary with wavelength. For example, spectral radiance, $L_e(\lambda)$, is the quantity at a specific wavelength, λ . Integrating spectral radiance over a given band will lead to the total radiance, L_e , over that region.

Self emission is often a leading contributor to spectral radiation signatures, especially in the infrared. Governed by blackbody radiation, an object at a specific temperature, T (in kelvin), will emit radiation as a function of wavelength. Below, Planck's law describes the electromagnetic radiation emitted by a perfect blackbody:

$$L_e(\lambda) = \frac{2hc}{\lambda^5 (e^{\frac{hc}{\lambda kT}} - 1)} \left(\frac{w}{m^2 - Sr - m} \right). \quad (14)$$

where k is Boltzmann's constant. However, actual objects emit just a fraction of the blackbody radiation. Emissivity ($\epsilon(\lambda)$) accounts for this factor in graybodies

and selective radiators. Graybodies have emissivities that are less than one and are spectrally flat ($\epsilon(\lambda) = \epsilon$), while selective radiators have emissivities that are less than one and vary with wavelength ($\epsilon(\lambda)$).

Lastly, consider the influence of media apparent properties, which describe surface behavior towards incident flux. When electromagnetic radiation falls on a surface, it is partly reflected, absorbed, and transmitted. The percentages are defined as reflectance (ρ), absorptance (α), and transmittance (τ). The fractions of incident flux taking on each quantity are defined as:

$$\rho = \frac{\Phi_{reflected}}{\Phi_{incident}}, \quad (15)$$

$$\alpha = \frac{\Phi_{absorbed}}{\Phi_{incident}}, \text{ and} \quad (16)$$

$$\tau = \frac{\Phi_{transmitted}}{\Phi_{incident}}. \quad (17)$$

In all scenarios, the conservation of energy states that:

$$1 = \rho + \alpha + \tau. \quad (18)$$

In thermal equilibrium, Kirchoff's law dictates that $\epsilon = \alpha$, indicating a good absorber must be good emitter.

2.6.2 BRDF Background.

Light reflects off media in different ways due to microscopic imperfections, perhaps described as inherent microfacets, on the surface material. As shown in Figure 12, the variations of reflectance can be categorized as perfectly diffuse, perfectly specular, or a combination of specular and diffuse components. For modeling reasons,

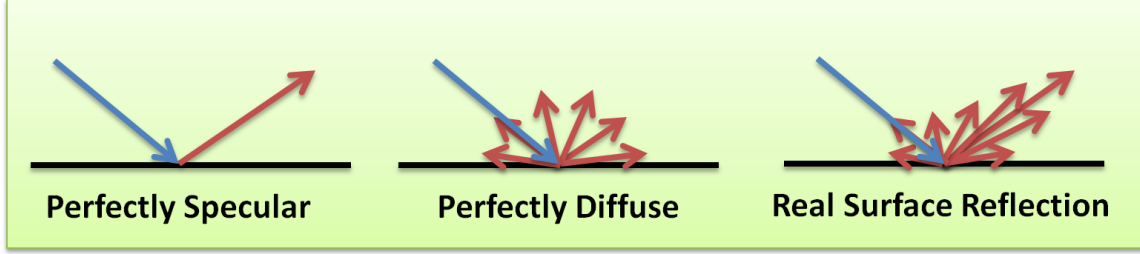


Figure 12. Three categories of reflectance: perfectly specular, perfectly diffuse, and the combination of diffuse and specular reflection.

three categories exist. However, in reality, all materials exhibit some combination of specular and diffuse components. Perfectly diffuse reflectance is depicted by a uniform hemispherical spread of reflecting light off the surface, while perfectly specular reflectance is depicted by a single reflected ray at a location derived by Snell's law. The bidirectional reflectance distribution function (BRDF) fully characterizes the reflectance of a material over all angles and captures both specular and diffuse components. With a model containing both diffuse plus specular components, the diffuse reflectance typically maintains a dome shape, while the specular component forms a lobe shape. BRDF is a simplified version of the bidirectional scatter distribution function, which characterizes reflectance and transmittance of a material. In the skin detection application, transmittance measurements are not needed since the imaged parts of the human body let little to no light through them [15].

In [33], the BRDF (f_{BRDF}) characterizes surface reflectance with the following definition:

$$f_{BRDF}(\theta_i, \theta_r, \phi_i, \phi_r, \lambda) \triangleq \frac{L_r(\theta_r, \phi_r, \lambda)}{E_i(\theta_i, \phi_i, \lambda)}. \quad (19)$$

The associated angles and coordinate system used are shown in Figure 13, where the z -axis marks the direction of the surface normal vector, the y -axis marks the location of $\phi_i = 0$ (direction of fixed light source vector in this study), ϕ_r is the azimuthal reflected angle off the y -axis θ relative to the surface normal, and θ_i and

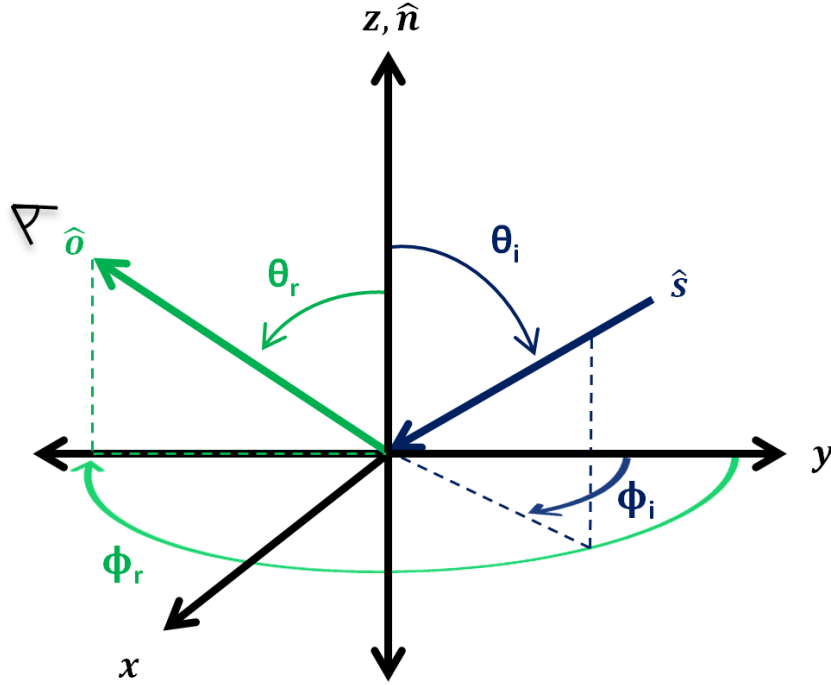


Figure 13. Hemispherical geometry of the BRDF, defining the elevation and azimuth angles for both the source and observer.

θ_r are the angles off surface normal of the incident and reflected light, respectively. More details regarding the measurements system, angles, and coordinate system are described in Chapter III. Similar to Equation (15), f_{BRDF} is a reflectance value per steradian. Since reflectance is a unitless measurement, f_{BRDF} is in units of $1/sr$. For example, a perfectly specular surface would have $f_{BRDF}=0$ except where $\theta_r = \theta_i$ and $\phi_r = \phi_i + \pi$. A perfectly diffuse (Lambertian) surface would have $f_{BRDF} = \frac{\rho(\theta_i, \phi_i)}{\pi}$. Typically, a BRDF model is used to extract the reflected radiance off a surface. With a full BRDF model and a given irradiance, the reflected spectral radiance can be computed as follows:

$$L_r(\theta_r, \phi_r, \lambda) = \int_0^{2\pi} \int_0^{\frac{\pi}{2}} BRDF(\theta_i, \theta_r, \phi_i, \phi_r, \lambda) L_e(\theta_i, \phi_i) \cos(\theta_i) \sin(\theta_i) d\theta_i d\phi_i. \quad (20)$$

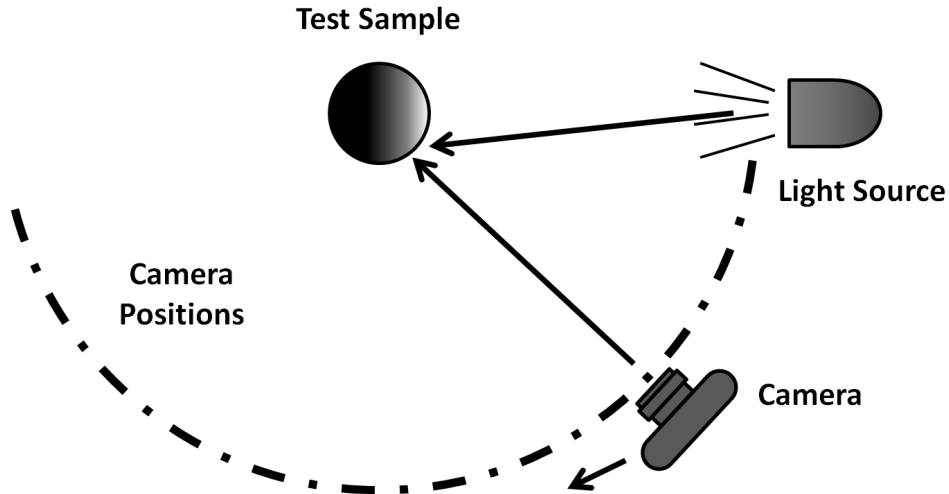


Figure 14. Image recreation of setup found in [20] depicting the image-based BRDF measurement system applicable to curved surfaces.

2.6.3 Image-Based BRDF Measurement Approach.

The objective of a BRDF measurement system is to collect data from several illumination source, target, and detector angular scenarios. In addition, the BRDF can also vary spectrally, therefore, it is important to collect data across all angles and wavelengths of interest. With these described conditions, BRDF measurements can take several hours to multiple days to acquire. Complete BRDF measurements are intensive and time consuming and many measurement systems include expensive robotics, complex optics, and fixed/flat samples [3, 15, 21]. In this study, it is not practical for a living human subject to remain still for an extended period of time. Often times, more efficient methods are chosen to meet the needs of a specific application. Following the work in [4, 14, 20], this research effort utilizes a multispectral image-based technique to capture many data points simultaneously, which reduces data collection time and complexity.

Utilizing image-based approaches like those in [4, 7, 14, 20, 21, 23], a camera will increase BRDF measurement rates due to the method's densely spaced samples. In-

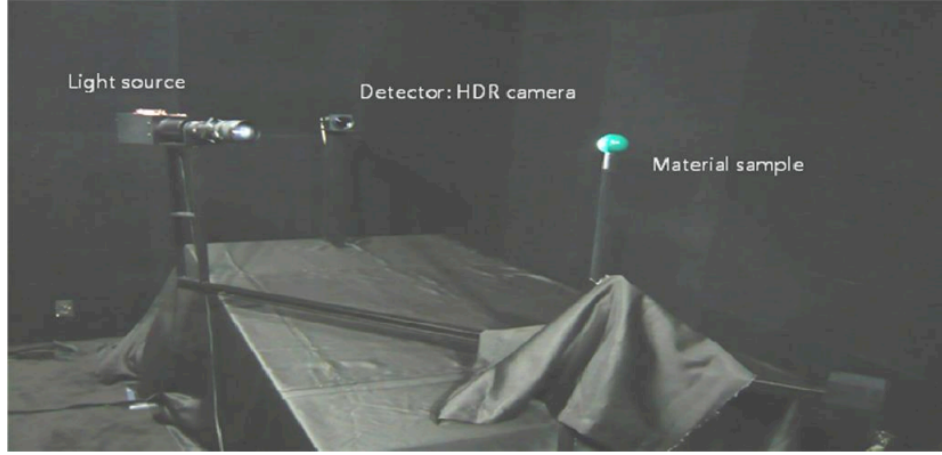


Figure 15. In [14], the proposed image-based BRDF measurement system (included here by permission from author and publisher). In this system the camera is fixed and the light source rotates.

stead of moving a single detector, each pixel in the focal plane array (FPA) collects data from a slightly different angle based on the target's geometry. In [20], they illuminate cylindrical samples and acquire images as they rotate the camera at fixed intervals around the target as shown in Figure 14. Given the geometry of the sample and the camera specifications, they can map pixel values to an area on the sample based on the instantaneous field of view. From there, they calibrate the source and detector to determine estimated reflectance values for a given pixel. With a curved surface, rotating the detector near-150-180 degrees from the fixed illumination source will allow acquisitions from a large domain of illumination and reflection directions; θ_i and θ_r vary on $[0, \pi/2]$ and ϕ_r vary on $[0, \pi]$. Figure 15 shows a fast and accurate image-based system for measuring isotropic reflection from [14], where the high-dynamic-range (HDR) camera is stationary and the light source rotates. Image-based measurements have been verified by comparison against gonireflectometers (approaches used in [3, 24, 39]) and have shown accuracy rivaling expensive, automated, and custom-built BRDF instruments [21]. That being said, an image-based BRDF measurement process is the an effective way of measuring human skin re-

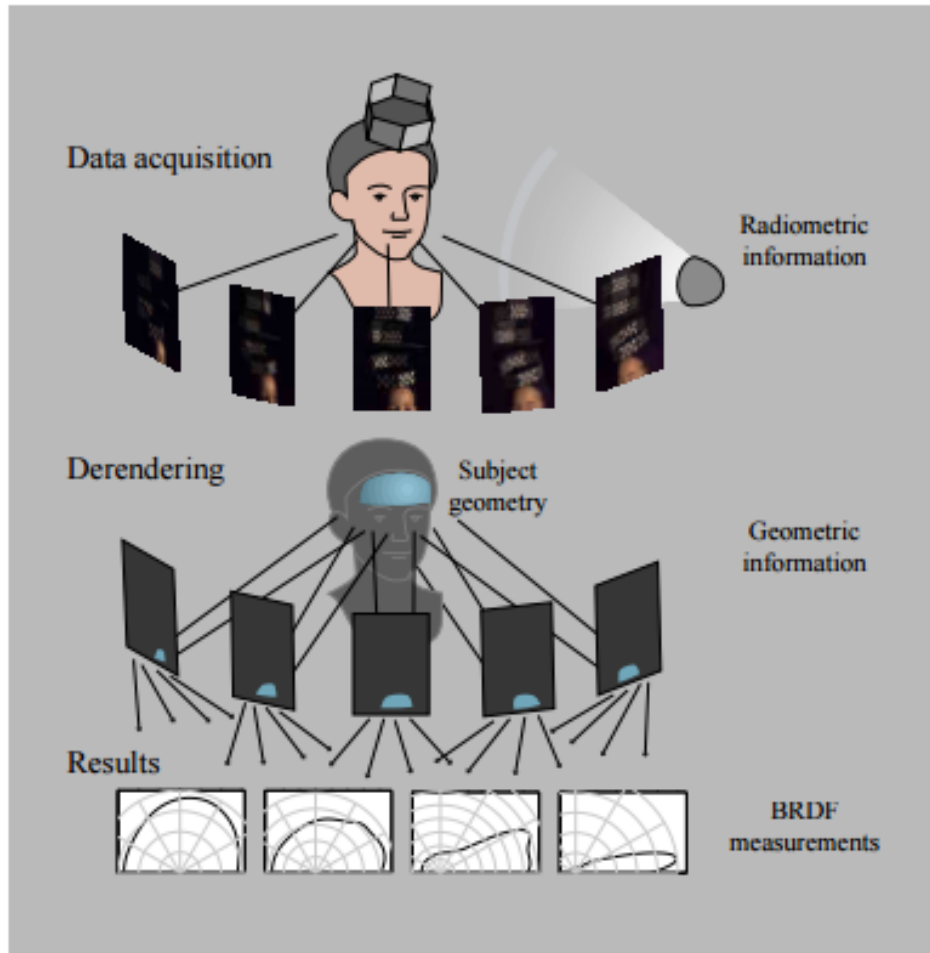


Figure 16. Skin BRDF measurement setup in [20] (included here with permission from author). Radiometric information is acquired with a RGB camera and geometric information is acquired with a 3D range scanner. Reference materials are placed on the subjects head for automation purposes.

flectance distributions fast and accurately in the laboratory [21].

2.6.4 Related Skin Reflection Work.

BRDF measurement approaches are applied in [3, 20, 40, 41] for measuring human skin reflectance. In [3], RGB channel BRDF measurements were acquired of a flat cadaver skin sample (sample 39 of the Columbia-Utrecht Reflectance and Texture Database) at 205 different combinations of viewing and illumination directions using

a set up consisting of a 24-bit RGB camera, a robot arm to orient the flat texture samples, a halogen bulb, a photometer, and a 3-CCD color video camera. In [20], using a commercial-grade Kodak DCS 420 digital camera and electronic flash, the authors collect many samples of various human subject heads and separately measure facial geometry with a Cyberware 3030/PS range scanner. The process is shown in Figure 16. Lastly, [40, 41] use a face-scanning dome to acquire face geometry and skin reflectance. The dome consists of 16 digital RGB cameras and 150 LED light sources evenly distributed on a wire-framed sphere containing a sitting human target. A commercial 3D face-scanning system collects the facial geometry. Since related skin BRDF measurement work is done in the computer graphics and rendering community, only visible wavelengths are of interest and measurements are collected with RGB cameras. Research presented in this thesis utilizes similar preceding measurement approaches in order to collect BRDF data in the VIS and NIR wavelengths used in the skin detection algorithms.

2.7 Geometric Optics

In this research effort, an existing monocular multispectral camera system is used to acquire BRDF measurements. Therefore, it is important to understand the geometric optics utilized to reconstruct the system in this application. The existing camera system contains several lenses and mirrors to affect the propagation of light through the system and subsequently acquire focused images. A lens is a transmissive device used to converge or diverge collected light. A dichroic mirror is a device with a given transition region that reflects certain wavelengths of light while transmitting others, each to a desired location. Collectively, these devices are used to image an object to a distance described by the thin-lens equation [5]:

$$\frac{1}{p} + \frac{1}{q} = \frac{1}{F}, \quad (21)$$

where F is the focal length of the lens, p is the distance from the object to the lens, and q is the distance from the lens to the image. In cases where $p \gg q$ the focal length is approximately equal to the image distance, $F \approx q$. The magnification M of a thin lens is defined as the ratio of the image height to object height. Using the concept of similar triangles, magnification is defined as:

$$M = -\frac{q}{p}. \quad (22)$$

The object area A_{obj} and image area A_{img} can also be related by the magnification factor:

$$\frac{A_{img}}{A_{obj}} = M^2. \quad (23)$$

Now consider aperture stop and its relation to f -number ($F/\#$). The f -number describes the amount of aperture used compared to the focal length distance. In this study, $F/\#$ is defined as:

$$F/\# = \frac{F}{D_{lens}}, \quad (24)$$

where D_{lens} , dictated by aperture stop, is the diameter of the lens or the exposed diameter of the lens.

Lastly, we examine the field of view (FOV) and instantaneous field of view (IFOV) of an optical system. The FOV is the angular coverage of an optical system. Using the half-angle FOV convention in [5]:

$$FOV_{half-angle} = \left| \tan^{-1} \left(\frac{h_{obj}}{p} \right) \right| = \left| \tan^{-1} \left(\frac{h_{img}}{q} \right) \right|, \quad (25)$$

where h_{obj} is the height of the object and h_{img} is the height of the image. IFOV is a term used in imaging systems which originated from scanning systems and describes the moving footprint of the individual detector on the object at any instant. However, the term IFOV can define the angular coverage of a single detector or pixel in any given system. In this study, IFOV is defined as the instantaneous field of view of a single pixel in a FPA.

2.8 Summary

Chapter II provided the foundational material needed in understanding the technology, modeling, measurements, and algorithms used in skin detection. In addition, the chapter covered the material on the bidirectional reflectance distribution function (BRDF) used in this research effort to better characterize skin reflectance. With an understanding of the unique features found in human skin reflectance spectra, detection and estimation algorithms can distinguish skin pixels from background pixels in multispectral imagery. However, the results from the skin detection algorithms can be limited by the assumption that skin exhibits entirely diffuse reflectance characteristics. Taking image-based BRDF measurements in a wide range of angular scenarios will better characterize skin reflectance by incorporating the specular and diffuse attributes.

III. Methodology

Chapter III presents the image-based BRDF measurement system constructed for skin reflectance measurements. The monocular multispectral camera system from [30] is presented. A brief discussion outlines the components and changes made to the original camera layout so it can be used for this research. Next, the hardware and software in the BRDF measurement setup are presented. Here, a detailed description of the setup gives the reader an understanding of where all modules are located and oriented relative to the BRDF concept diagram in Figure 13. Section 3.2 outlines how target geometry information is extracted and how surface normals, camera location, and light source locations are mapped to their respective BRDF angular coordinates. In Section 3.3, the BRDF measurement approach is discussed, including image acquisition and data formatting methods. Lastly, a summary of the methodology prepares the reader for the experiment and results in Chapter IV.

3.1 Image-Based BRDF Measurement System

3.1.1 Monocular Multispectral Camera System.

The monocular multispectral camera system was developed in [30] for skin detection, melanin estimation, and false-alarm suppression. The system was presented and proven as a simplified low-cost substitute for hyperspectral imaging. The existing compact camera layout consists of four cameras, two Goodrich SU640KTSX-1.7RT Short Wave Infrared (SWIR) InGaAs cameras, one ThorLabs DCC1645C CMOS RGB Camera, and one ThorLabs DCC1545M CMOS monochrome camera, all seen in Figure 17. The four cameras collectively acquire spectral content in the RGB, 850 nm, 1080 nm, and 1580 nm bands. Content collected in the 1080 nm and 1580 nm bands is used for skin detection, while content collected in the red and green bands is

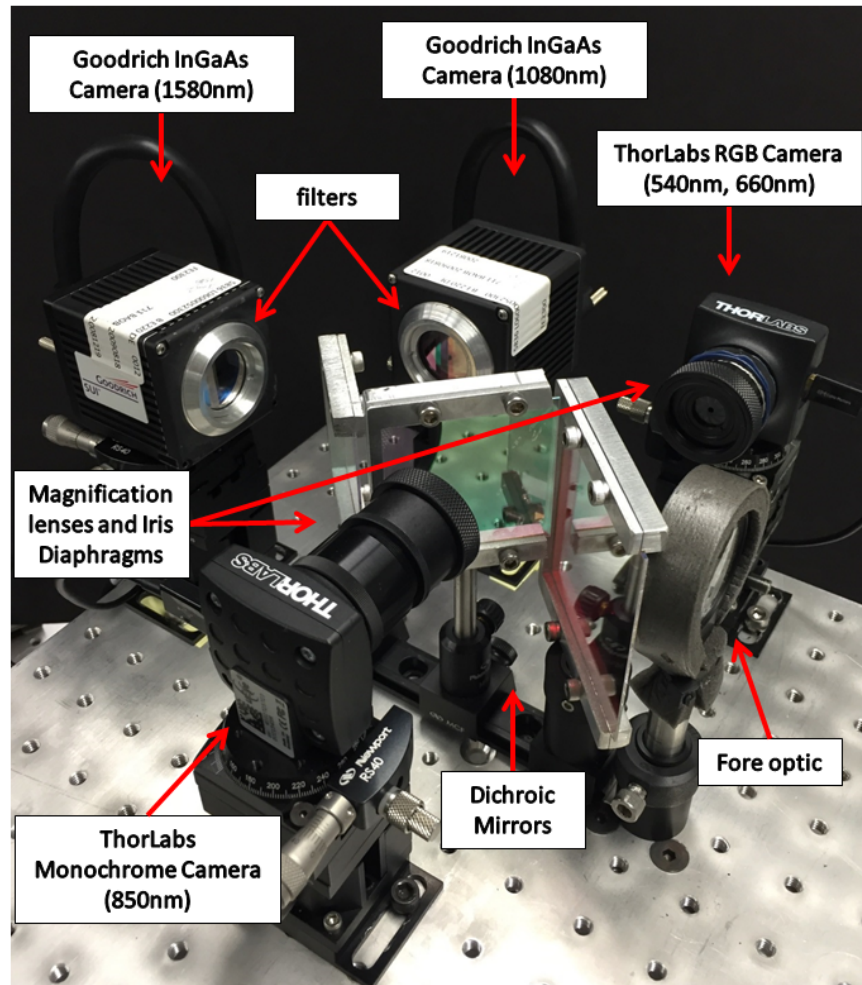


Figure 17. Existing monocular multispectral camera layout.

used for false-alarm suppression. The content from 850 nm and 1080 nm collectively serves in melanin estimation.

The camera selections were made based on their spectral response and FPA format compatibility across the system. The SWIR cameras were the foundation of the layout, while the Thorlabs cameras were chosen afterwards based on their resolution and pixel pitch. The camera specifications are presented in Tables 2, 3, and 4. As demonstrated in the tables, the SWIR cameras have an array format of 640×512 with a $25 \mu\text{m}$ pixel pitch, while the color and monochrome cameras have an array format of 1024×1280 with a $3.6 \mu\text{m}$ and $5.2 \mu\text{m}$ pixel pitch, respectively. The pixel pitch and array format affects the field of view (FOV) size and resolution. In order to maintain a fixed FOV, a magnification lens are applied to each of the Thorlabs cameras. In order to maintain a fixed resolution, the lower resolution SWIR camera content is interpolated in image processing efforts of Section 3.3.

Table 2. Specifications for the Goodrich SU640KTSX-1.7RT [30].

Parameter	Value
Spectral Response	900nm-1700nm
Pixel Pitch	$25\mu\text{m}$
Array Format	640×512
Image Depth	12 bit
Frame Rate	30 fps
Camera Body Size (H \times W \times D)	2.1in \times 2.1in \times 2.55in

Table 3. Specifications of the ThorLabs DCC1645C Color Camera [30].

Parameter	Value
Spectral Response	Visible Light
Format	RGB
Pixel Pitch	3.6 μ m
Array Format	1280 \times 1024
Image Depth	10 bit
Frame Rate	25 fps
Camera Body Size (H \times W \times D)	1.88in \times 1.68in \times 1.00in

Table 4. Specifications of the ThorLabs DCC1545M Monochrome Camera [30].

Parameter	Value
Spectral Response	Visible Light
Format	Monochrome
Pixel Pitch	5.2 μ m
Array Format	1280 \times 1024
Image Depth	10 bit
Frame Rate	25 fps
Camera Body Size (H \times W \times D)	1.88in \times 1.68in \times 1.00in

In addition to the cameras, one fore optic, two secondary magnification lenses, two iris diaphragms, three dichroic mirrors, and two filters complete the construction of the system. A 38.1 mm Newport PAC075 achromatic doublet fore optic with 150 mm focal length was chosen to balance the desired FOV, image distances, and object distance of the system, while correcting for chromatic aberrations in the visible spectrum [30]. The two secondary lenses are chosen based on the magnification need for the Thorlabs camera to match the SWIR cameras. In the BRDF measurement application, changes to the object distance (distance from subjects forearm relative to the camera system's fore optic) affected the image distance and FOV. Therefore, each camera distance relative to the foreoptic is modified and a new magnification lens is chosen for the Thorlabs monochrome camera. The magnification lens for the Thorlabs RGB camera did not need replacement. The new FOV is 57x71 mm at an

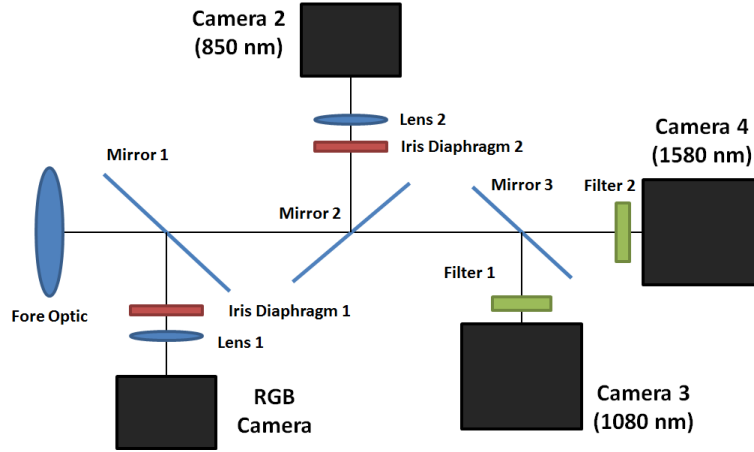


Figure 18. Block diagram for the existing monocular multispectral camera layout developed in [30]. Included in the image are the four cameras, fore optic, three dichroic mirrors, two iris diaphragms, two magnification lenses, and two filters.

object distance of 85 cm. A 25.4 mm LB1811-B Bi-convex lens with a focal length of 35 mm is used for the monochrome camera and a 25.4 mm LB1757-A Bi-convex lens with a focal length of 30 mm is used for the color camera. Shown in Figure 18 and Figure 19, three dichroic mirrors are strategically placed to divide the spectrum among each of the cameras. Each of the mirrors efficiently reflects wavelengths of light that need to reach a specific camera, while efficiently transmitting the wavelengths collected by the cameras in the rear. Lastly, two filters are attached to each of the SWIR cameras to limit their spectral response to the 1080 nm and 1580 nm bands.

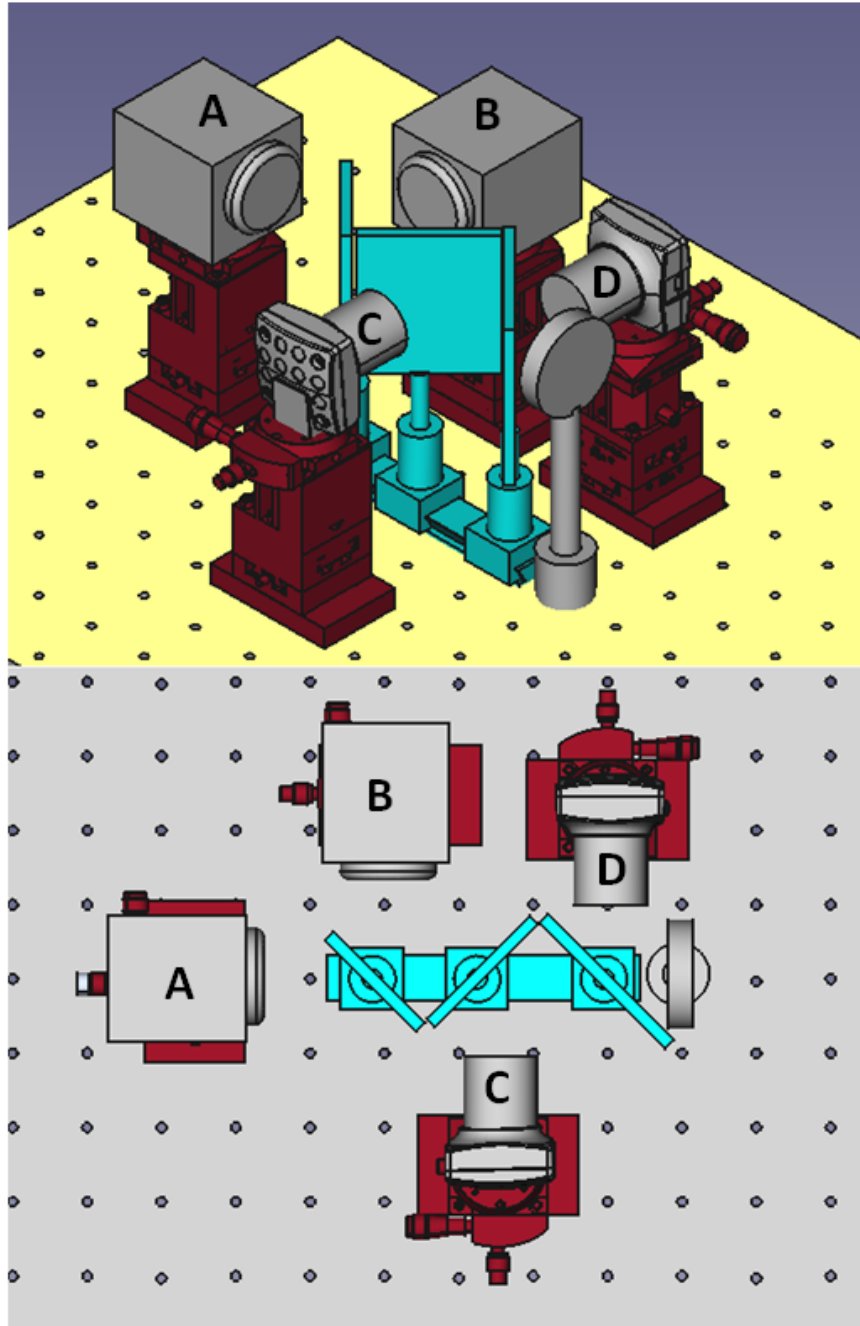


Figure 19. CAD drawing showing existing monocular multispectral camera layout at scale. (A, B) Two Goodrich SWIR cameras, (C) one ThorLabs Monochrome camera, and (D) one ThorLabs RGB camera.

3.1.2 BRDF Measurement Setup.

Following the skin detector work in [30] and image-based measurement work in Section 2.6.3, this research incorporates the existing compact camera layout into a bench-top image-based BRDF measurement system to provide spectral and angular reflectance data of human skin at 540 nm, 660 nm, 850 nm, 1080 nm, and 1580 nm. A bench-top measurement system is developed to acquire the requisite angular-dependent skin reflectance spectra.

A 1-meter long swing-arm, 12" \times 18" \times 0.25" optical bread board, and detent equipped locking device are custom machined components and mounted to a 3' \times 6' optical bench-top shown in Figure 20. The existing monocular multispectral camera system is assembled on the optical bread board making the object distance, from the central point of the swing arm to the fore optic, 85 cm. Cameras, mirrors, and lenses are aligned with translational and rotational stages (shown to scale in Figure 19) using the knowledge discussed in Section 2.7 and a matte black foam board box covers the system to limit noise caused by stray light. The optical bread board is mounted on top the swing-arm, allowing the camera system to rotate 0-180 degrees along a plane approximately 43 cm above the optical bench-top. At this elevation, the fore optic is aligned vertically with the mid-section of a human forearm (target), which sits upright in the center of rotation during data collection. The motion is controlled by a detent equipped semicircle device with radius 30.5 cm (12 inches), capable of locking the swing-arm at 36 angular locations at 5-degree increments.

At 6.09 degrees off the zero degree location of the detent device, a platform secures a fixed ASD Pro Lamp light source to the optical bench-top. The center of the light source is aligned vertically with the center of the camera system's fore optic and points directly at the target, 66 cm away. Shown in Figure 21, the ASD Pro Lamp has a 50-W quartz-tungsten-halogen light source, a color temperature of 2950 Kelvin,

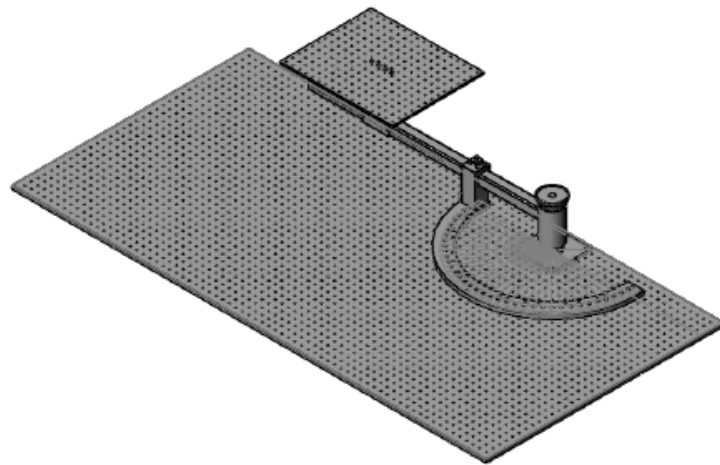
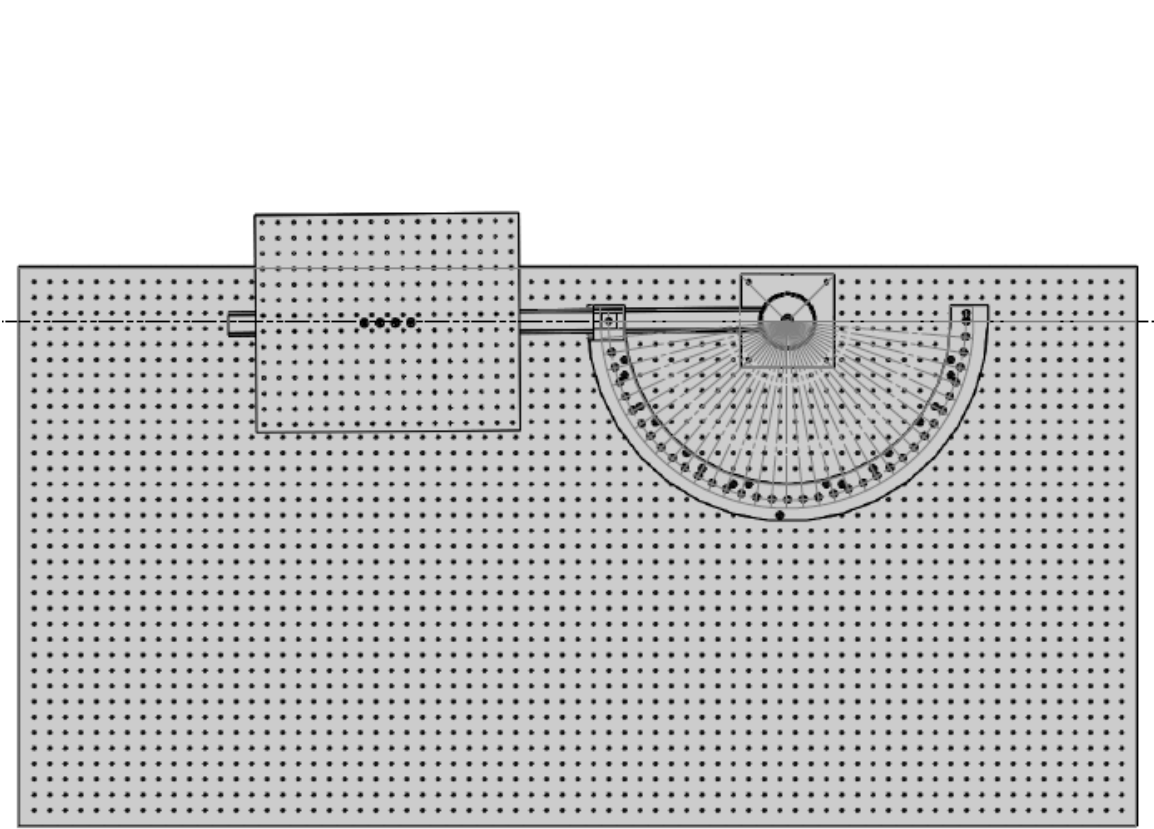


Figure 20. Bench-top CAD drawing featuring the 3' × 6' optical bench top with mounted swing arm and pivot hardware. The camera layout is assembled on a 12" × 18" × 0.25" breadboard mounted on top of the swing arm.

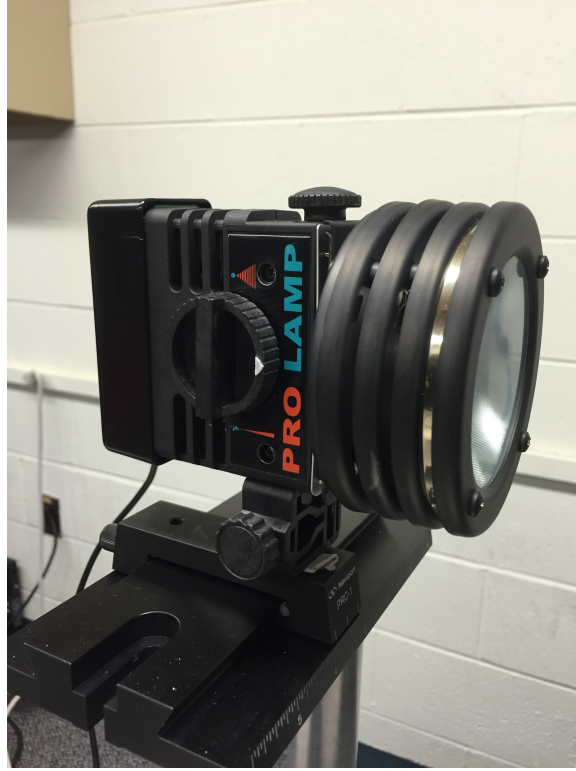


Figure 21. The ASD Pro Lamp is used as the light source in the image-based BRDF measurement system. The lamp has a 50 W quartz-tungsten-halogen bulb and is designed for indoor lab reflectance measurements over the region 350-2500nm.

and produces stable and uniform illumination of the target over the 350-2500 nm range. Midway down the swing-arm, a Laserglow Technology Class 2 grid patterned laser is mounted to the arm at a height of approximately 68.5 cm above the optical bench-top, positioned to project a red grid patterned laser across the target. Shown in Figure 22, the laser is positioned in order to extract the geometry of the arm at each swing-arm location. The integration of all modules is seen in Figure 23.

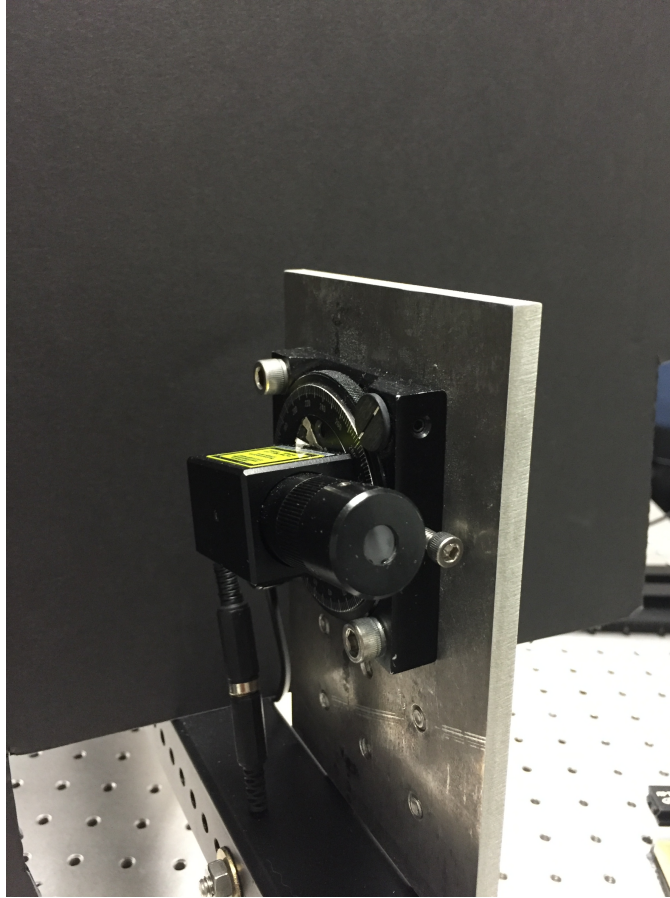


Figure 22. The Brightline Pro Red Complex-Pattern-Generating Alignment Laser used in the image-based BRDF measurement system. The output power is adjusted from 5 to 40 mW and is used to project a highly visible focus-adjusting laser grid on the target for extracting surface normals.

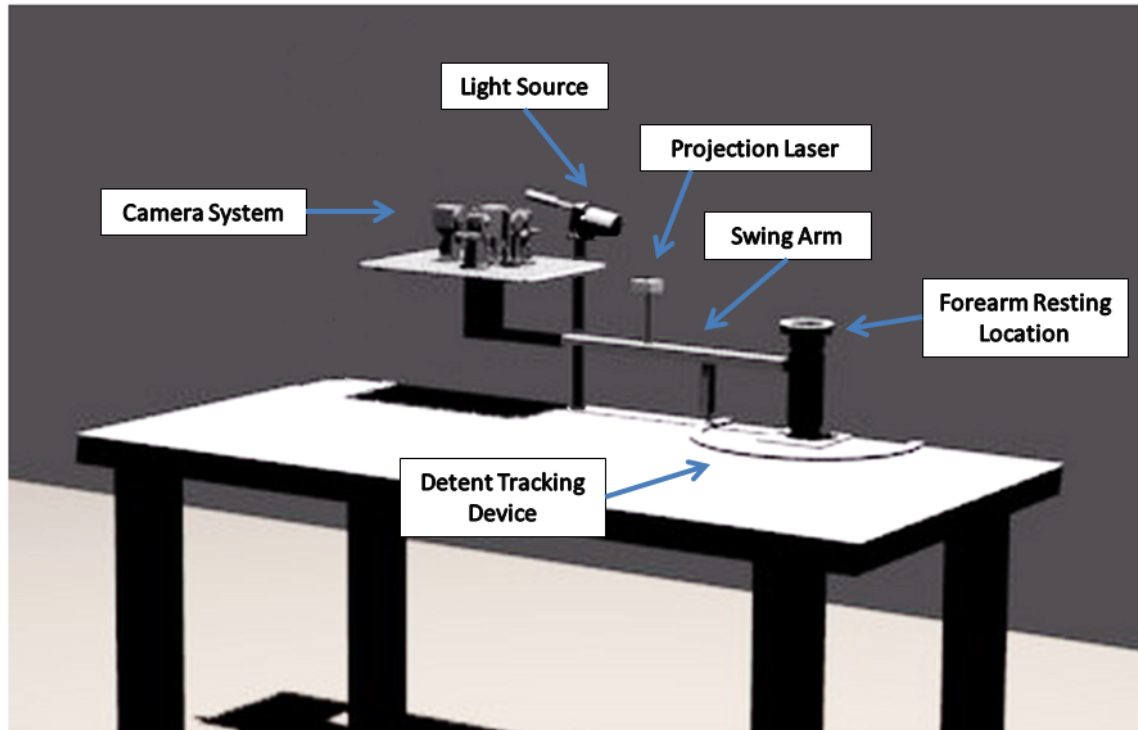


Figure 23. A CAD drawing of the image-based BRDF bench-top measurement system. The existing monocular multispectral camera system is elevated on a rotating arm. A grid-pattern projection laser is mounted mid-way down the swing-arm, while the light source is stationary on the table, level with the camera system's fore-optic, and marking the x -axis for the system's coordinate system (discussed in Section 3.2). The human subject's forearm rests on top of the central cylinder.

3.2 Extracting Angular BRDF Coordinates

3.2.1 Grid-Patterned Laser Projection.

An essential step in acquiring BRDF measurements is extracting the geometry information from the target. The surface normals at every sample need to be acquired in order to solve for the angular coordinates used in the BRDF. In this research, a grid projection laser is used to extract the desired surface geometry of the forearm. The Laserglow Technology's Brightline Pro Red complex-pattern-generating alignment laser was chosen for its output power, ability to project a grid pattern, and focus-adjusting capability for high precision applications. If the grid projection deviates from a flat perpendicular plane, the pattern becomes distorted as it wraps around angled surfaces, as seen on the forearm in Figure 24. By measuring the change of each grid segment, surface normals can be acquired. Segment measurement is done by acquiring an RGB image of the projected grid with the ThorLabs DCC1645C camera described in Section 3.1.1, and then evaluating the red component.

3.2.2 Image Preprocessing and Grid Extraction.

The RGB image of the projected laser grid in Figure 24 is acquired in a dark setting to reduce red channel noise for improved grid-line to background contrast. In addition, only the left half of the forearm (relative to the camera) is imaged. This geometry is used in order to simplify the number of incident light, camera path, and surface normal angular scenarios to one general equation described in Section 3.2.3. The left edge of the FOV is approximately aligned with the center of the forearm where surface normals are parallel with the optical path of both the laser and the camera. The right edge of the FOV extends past the edge of the forearm to ensure the system captures all available surface normals.

Since the grid patterned projection laser is relatively lower powered and the room

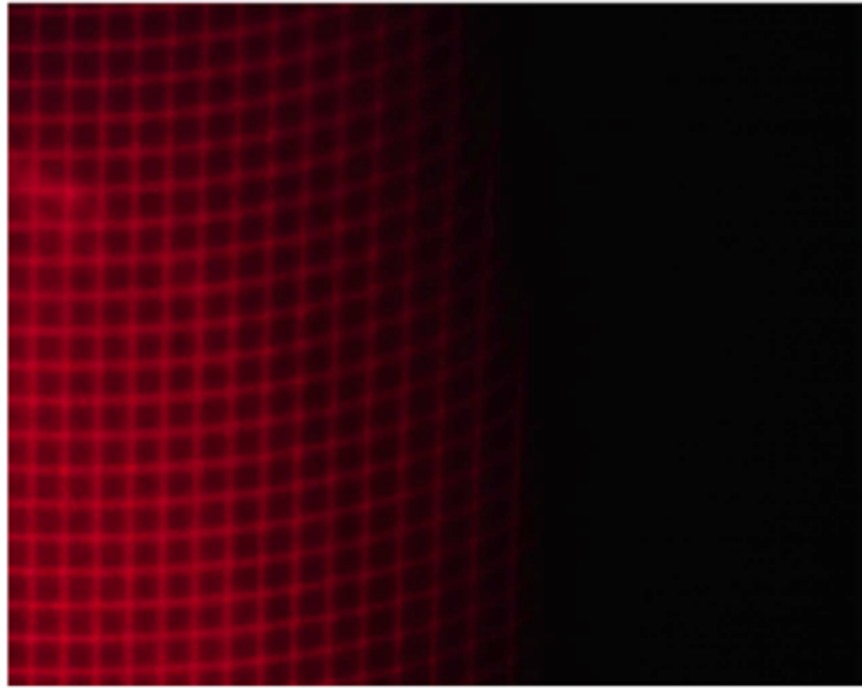


Figure 24. A typical grid projection onto the human subject's forearm using the red Laserglow, class 2, grid pattern generating laser. The grid pattern becomes distorted as it wraps around the curved surface.

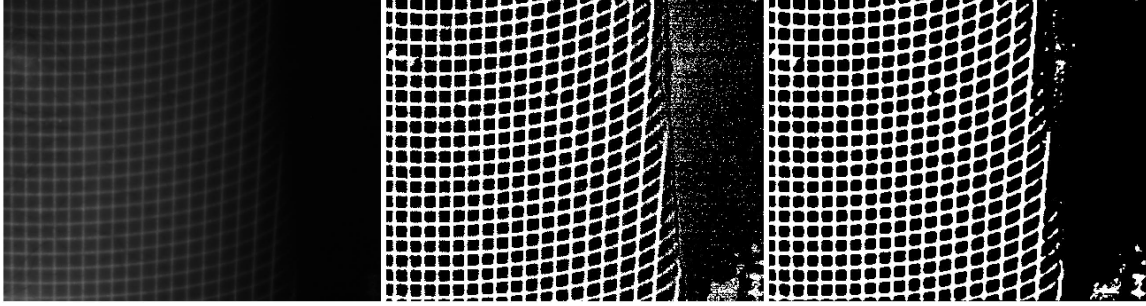


Figure 25. An example of pre-processing from subject 3, position 2 of the measurement test. (Left) Image shows the red channel. (Middle) This image displays the results from sharpening, contrast, and the binary conversion processes. (Right) This image shows the results after median filtering.

setting is dark, it is necessary to perform preprocessing on the grid images in order to extract the line segments for each box and the forearm edge. The red channel is extracted from the RGB image (Figure 25 (Left)) and a higher contrast image is formed through image sharpening techniques and then converted to binary based on an appropriate threshold (Figure 25 (Middle)). A median filter is applied to clean up regions where no grid lines are expected (Figure 25 (Right)). The image is then skeletonized, which results in line segments of one pixel width (Figure 26 (Left)). An edge-linking function is used to form a list of separated segments, which contain each pixel coordinate. Where an edge junction is encountered, the list is terminated and a separate list is generated for each of the branches (Figure 26 (Middle)). The segments are linearized based on their end point locations (vertices) and pixel deviation from the line (edges) between those endpoints. The data structure that contains the vertices is arranged so the vertices closest to the images origin (top left corner) are listed first. Then, the edges are reordered based on their distance from the images origin (Figure 26 (Right)).

The final grid reconstruction consists of many stages which delete anomalies, such as gaps or segments that do not belong. A detection algorithm is developed to mark the edge of the forearm. The final grid reconstruction and forearm edge detection

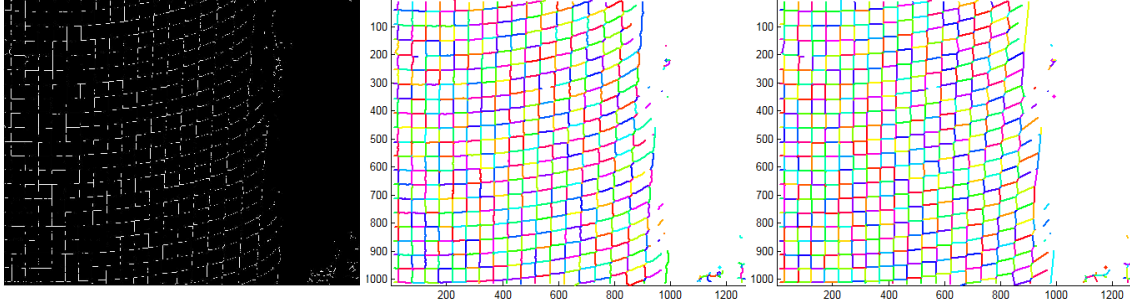


Figure 26. An example of pre-processing from subject 3, position 2 of the measurement test. (Left) Image shows the skeletonized grid. (Middle) This image displays the results from the edge detection function with each color representing a separate segment. (Right) This image shows the linearized segments.

can be seen in Figure 27 (left). Lastly, a mask is made from the forearm grid reconstruction that filters out any values reflectance values recorded by the camera system where the forearm geometry does not exist as shown in Figure 27 (right).

3.2.3 Surface Normal Extraction.

It is important for the reader to understand the orientation of the image-base BRDF measurement modules relative to the x , y , and z axes shown in Figure 28. The light source marks the x -axis and the camera system rotates within the xy -plane elevated above the optical bench top. The x , y , and z axes are in reference to the image-based BRDF measurement system and not BRDF surface coordinates where the surface normal vector marks the z -direction.

The final grid and forearm edge reconstructions are used to generate the surface normals for the forearm. The horizontal grid segment lengths are used to determine the horizontal angular component of the surface normal off the light source vector (x -axis) in the xy -plane, while the vertical grid segment lengths determine the vertical angular component of the surface normal off the xy -plane at the location marked by the rotation of the horizontal angular component. Figure 30 shows the angles used in computing the horizontal angular component in the two potential camera and surface

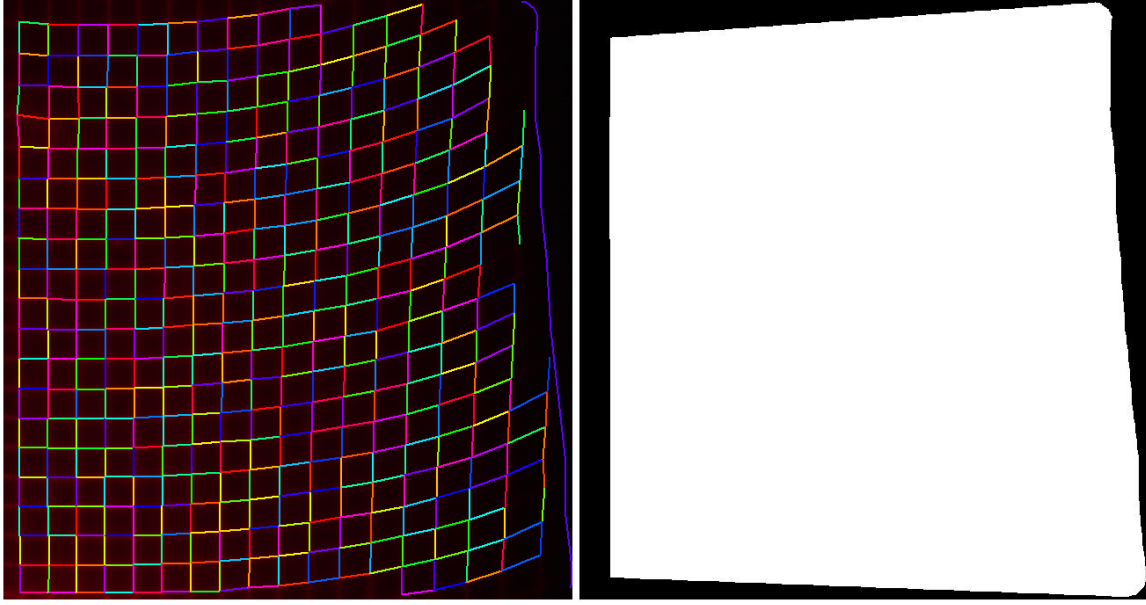


Figure 27. On the left is an example of a final grid reconstruction from subject 3, position 2 of the measurement test. The image shows the grid segments in varying color and the forearm edge in purple. On the right is the corresponding mask.

normal scenarios; in scenario one the surface normal is outside and to the left of the light source, while in scenario two the surface normal is between the light source and the camera. These are the only potential scenarios due to imaging only the right-half of the forearm. Figure 31 shows the angles used in computing the vertical angular component of the surface normal (see Section 3.2.4).

In Figure 30 and Figure 31, the first angle that is solved for is the horizontal angle between the surface normal and the camera location, θ_R , using the following equation derived from the diagram in Figure 29:

$$\theta_R \approx \cos^{-1} \left(\frac{d_{grid}}{d_{meas}} \right), \quad (26)$$

where d_{grid} is the length of one segment of the grid projection on a flat perpendicular object at target distance and d_{meas} is the length of one segment of the grid projection calculated from the image of the forearm.

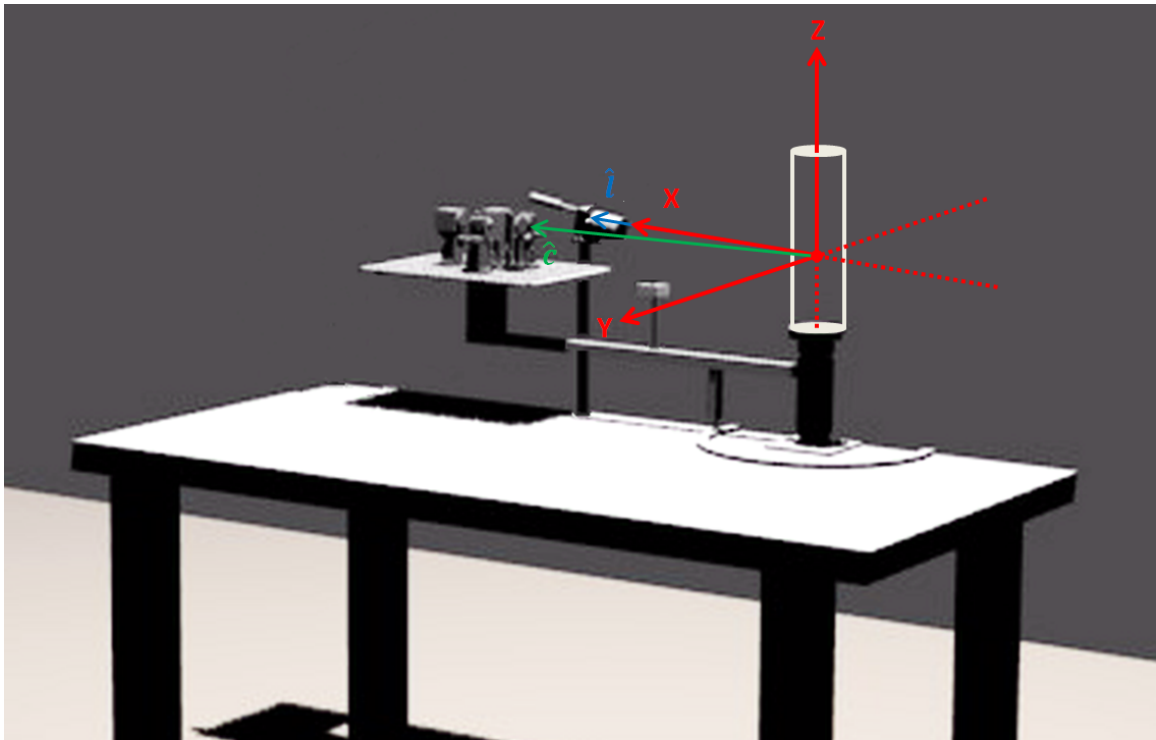


Figure 28. A CAD drawing showing the orientation of all modules relative to the x, y, and z axes. The light sources marks the x-axis and the camera system rotates within the xy-plane.

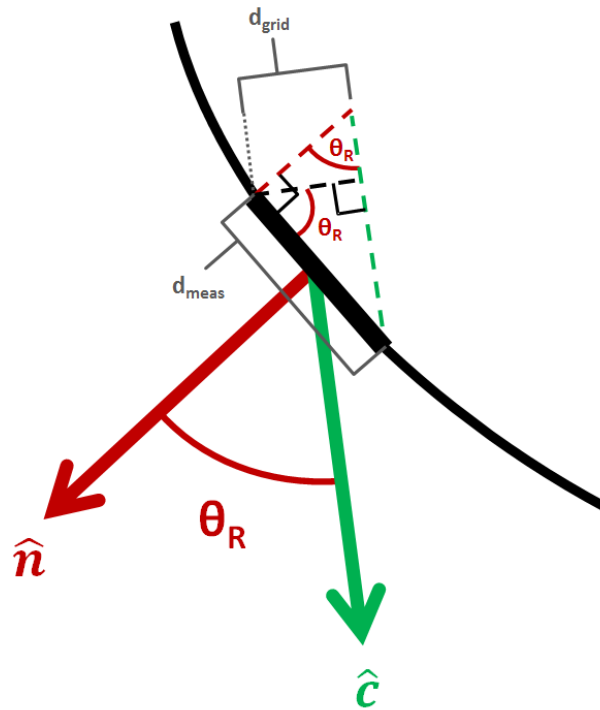


Figure 29. Illustration of the geometry used in calculating θ_R in the surface normal extraction method. d_{grid} is the length of one side of a projected grid square at the object distance of a perpendicular flat target, while d_{meas} is the length of d_{grid} projected onto the surface of the forearm as imaged by the camera system.

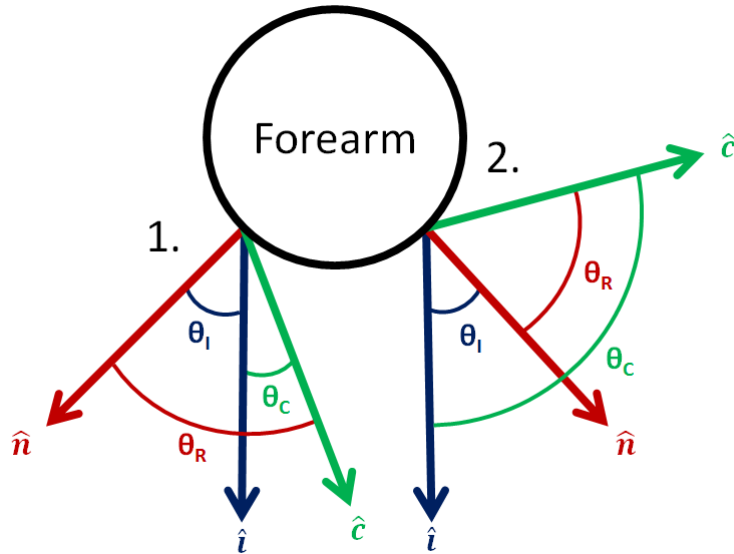


Figure 30. A top-view cross-sectional illustration of the forearm depicting the angles and vectors used to calculate the horizontal component of the surface normal. This component is calculated from the horizontal laser grid lines. θ_R is the equivalent angle from Figure 29, while θ_I is the horizontal component being solved for.

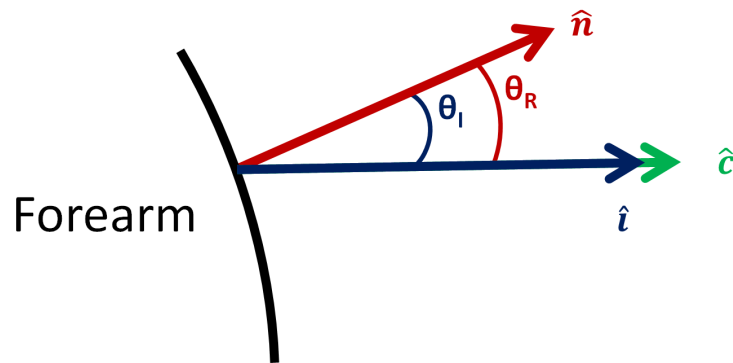


Figure 31. A side-view cross-sectional illustration of the forearm depicting the angles and vectors used to calculate the vertical component of the surface normal. This component is calculated from the vertical laser grid lines. θ_R is the equivalent angle from Figure 29, while θ_I is the vertical component being solved for.

Next, the horizontal and vertical angular components of the surface normals are solved for as

$$\theta_h = \theta_I \approx -(\theta_R - \theta_C) \quad (27)$$

and

$$\theta_v = \theta_I \approx \theta_R, \quad (28)$$

where θ_h is the horizontal angular component, θ_v is the vertical angular component, and θ_C is the rotation angle of the camera system (these angles are better visualized in Figure 32 in the next section). With these angles, unit vectors can be placed at the respective midpoint of the vertical or horizontal segment. At the forearm edge, 87 degrees is computed for the horizontal components of the vectors along the forearm edge (computed based on approximating the forearm as a cylinder of radius 4.49cm; the approximate average radius calculated with 247 male girth forearm circumference measurements from [10])) and the vertical component is assigned from the nearest vertical grid segment. The vectors are interpolated across the entire forearm within the masked region from Section 3.2.2. Through vector addition of the horizontal and vertical components, each with an x , y , and z component, the surface normals are computed.

3.2.4 BRDF Coordinate Mapping.

A surface normal is one of the three reference vector elements in the BRDF coordinate system. The other two are the light source direction (a vector) and the camera system direction (a vector). From these reference vector elements, the three main BRDF angular coordinates, θ_i , θ_r , and ϕ_r , can be solved for (θ_i and θ_r are different from θ_I and θ_R). Sometimes ϕ_i is included, however, in this work ϕ_i is set equal

to zero and corresponds to the direction of the light source. Figure 32 and Table 5 illustrate and outline the vector and angle elements used in the BRDF coordinate system.

Table 5. The element titles and descriptions of the BRDF coordinate system used in the image-based BRDF measurement system. Color coded angular and vector elements match those presented in Figure 32.

Vector Element	Description
$\hat{\mathbf{n}}$	Surface Normal $\langle x, y, z \rangle$
$\hat{\mathbf{n}}_h$	Surface Normal, Horizontal Component $\langle x, y, 0 \rangle$
$\hat{\mathbf{n}}_v$	Surface Normal, Vertical Component $\langle x, y, z \rangle$
$\hat{\mathbf{i}}$	Light Source $\langle x, 0, 0 \rangle$
$\hat{\mathbf{c}}$	Camera/Grid Laser $\langle x, y, 0 \rangle$
Angle Element	Description
θ_r	Angle between $\hat{\mathbf{n}}$ and $\hat{\mathbf{c}}$
θ_h	Angle between $\hat{\mathbf{n}}_h$ and $\langle x, 0, 0 \rangle$
θ_v	Angle between $\hat{\mathbf{n}}_v$ and $\hat{\mathbf{n}}_h$
θ_i	Angle between $\hat{\mathbf{i}}$ and $\hat{\mathbf{n}}$
ϕ_r	Azimuthal angle between $\hat{\mathbf{c}}$ and $\hat{\mathbf{i}}$ (relative to $\hat{\mathbf{n}}$)

The angle between the light source vector and the surface normal vector is θ_i , while θ_r is the angle between the camera vector and the surface normal vector. Therefore, these angles can be solved for with a simple equation of an angle between two vectors:

$$\theta = \cos^{-1} \left(\frac{\hat{v}_1 \hat{v}_2}{|\hat{v}_1| |\hat{v}_2|} \right), \quad (29)$$

where θ is the angle between vectors, \hat{v}_1 and \hat{v}_2 .

The azimuthal angle between the camera vector and the light vector relative to the surface normal is ϕ_r . In order to solve for ϕ_r , the camera vector and light source

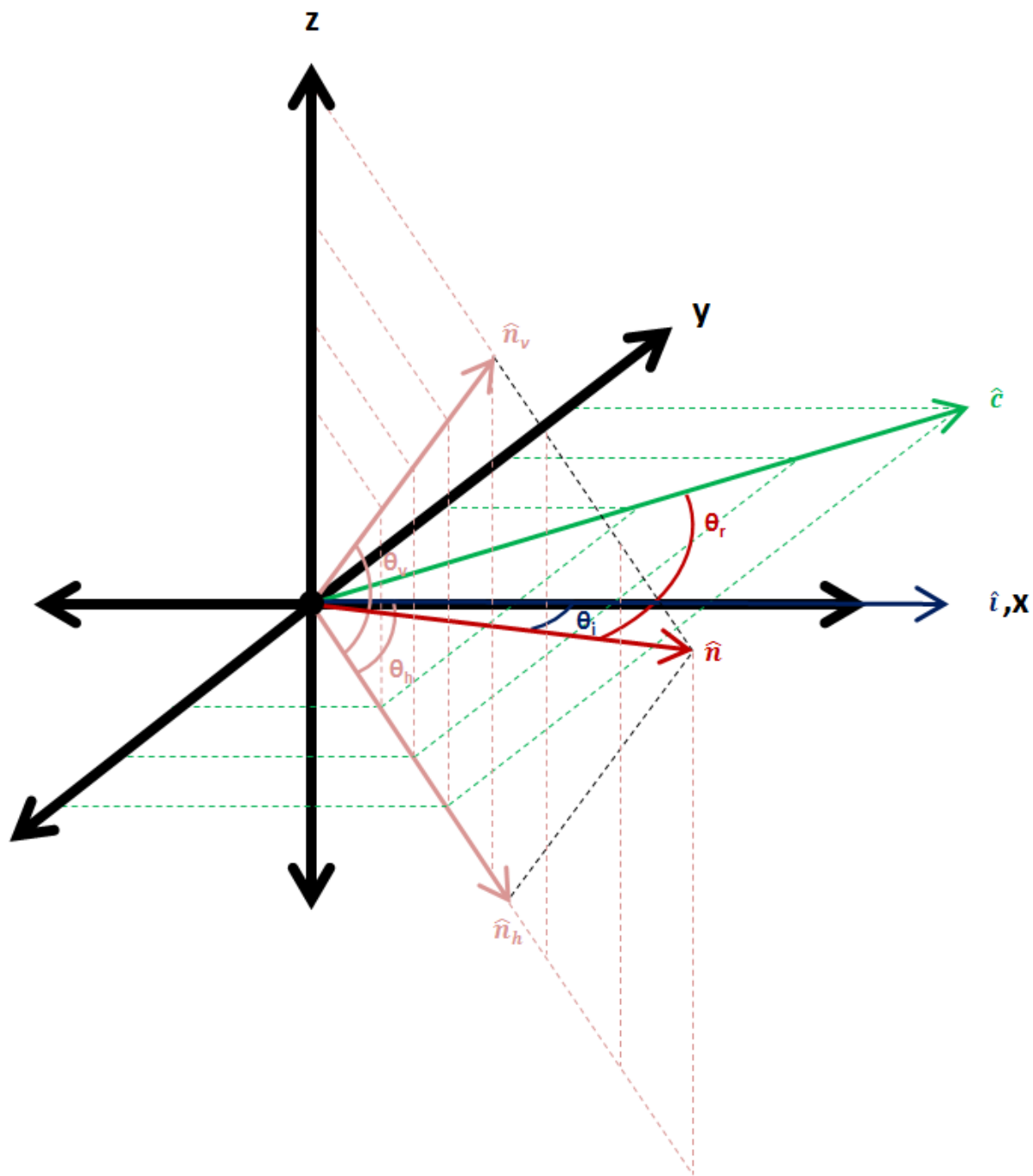


Figure 32. A detailed vector and angle illustration showing relations used in the BRDF measurement system. Elements are labeled and described in Table 5

vector are transformed as follows [2]:

$$\begin{aligned}\hat{c}' &= R_z(\phi_{\hat{n},h})R_y(\theta_{\hat{n},h})\hat{c} \\ \hat{c}'' &= \text{proj}_{xy}\hat{c}'\end{aligned}\tag{30}$$

$$\begin{aligned}\hat{l}' &= R_z(\phi_{\hat{n},h})R_y(\theta_{\hat{n},h})\hat{l} \\ \hat{l}'' &= \text{proj}_{xy}\hat{l}'\end{aligned}\tag{31}$$

where R_z and R_y are rotation matrices, with angles $\phi_{\hat{n},h}$ and $\theta_{\hat{n},h}$, respectively, and are solved from rotating the surface normal to the z -axis; \hat{l}'' and \hat{c}'' are the projections of the transformed vectors onto the xy -plane shown in Figure 33. Now, ϕ_r is the angle between vector \hat{l}'' and vector \hat{c}'' and is solved for using the equation to compute the angle between two vectors presented in Equation (29).

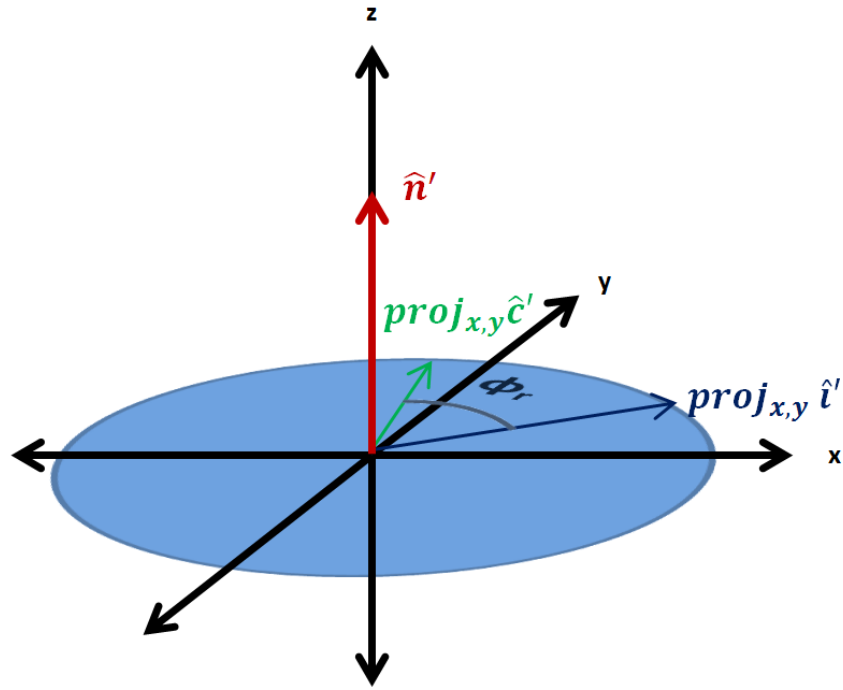


Figure 33. This diagram illustrates the transformation of the surface normal vector to the z -axis along with the projections on to the xy -plane (blue circle) of the same transformation of the light source and camera vectors. The transformation is used to extract the azimuthal angle, ϕ_r , relative to the surface normal. Elements are titled and described in Table 5.

3.3 Measuring Human Skin BRDF

3.3.1 Image Acquisition.

At the start of the image acquisition phase, an image is captured from each camera of both a gray and white Spectralon[®] diffuse-reflectance target. The white Spectralon[®] target has diffuse reflectance values slightly under one, while the gray Spectralon[®] target has diffuse reflectance values just above zero. These images are later used to convert pixel values to estimated reflectance with the Empirical Line Method (ELM) described in Section 2.3. The Spectralon[®] target reflectance values for each camera and panel used in ELM are presented in Table 6 from [30].

Table 6. Tabular listing of the reflectance values for each panel and camera combination [30]. Camera numbers are in reference to Figure 18.

Averaged Reflectance Values		
Configuration	White Panel	Gray Panel
Camera 1 Red Channel (660 nm)	0.9897	0.0772
Camera 1 Green Channel (540 nm)	0.9898	0.0752
Camera 2 (850 nm)	0.9894	0.0911
Camera 3 with Semrock FF01-1060/12-25 (1080 nm)	0.9895	0.1064
Camera 4 with Semrock NIR01-1570/3-25 (1580 nm)	0.9870	0.1317

The remainder of the image acquisition begins with the swing-arm at the first detent location, 6.09 degrees from the light source. At every location, the camera system, laser, and light source go through a specific collection sequence to ensure data is properly acquired. First, with the laser on and the lamp shuttered, the laser projection is captured by the ThorLabs color camera. Then, with the lamp unshuttered and the laser turned off, all four cameras acquire images for their respective spectral content in the 540nm, 660nm, 850nm, 1080nm, and 1580nm bands (540nm and 660nm are extracted from the RGB images). This is accomplished for every swing-arm position from 0-180 degrees at 5 degree increments. Depending on the experiment, the range of positions can be shorter and the increments can be larger

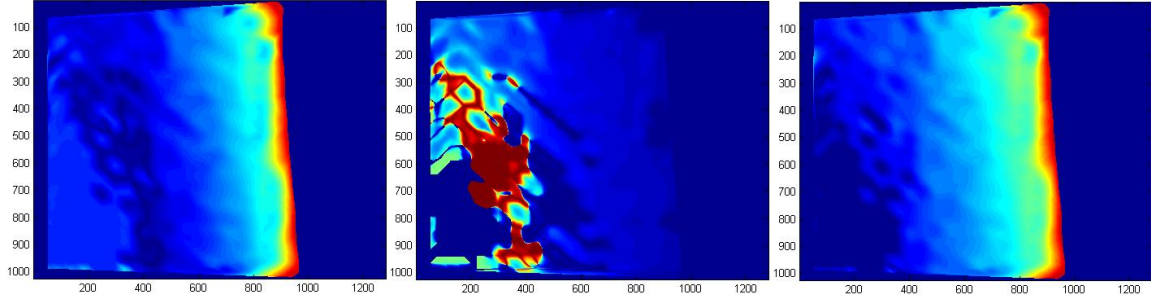


Figure 34. Example masked matrices in image forms of θ_i , ϕ_r , and θ_r (left, middle, right). Each image is from subject 3, position 2 of the image-based BRDF measurement system.

(but restricted to multiples of 5 degrees due to machining limitations).

3.3.2 Data Analysis Method.

After the image acquisition phase, there are N images for the laser grid acquisition and each wavelength, where N is the number of angular locations of the camera. In addition, there are two Spectralon[®] images for each wavelength. The data analysis begins with the BRDF coordinates and masks calculated for each location using the methods described in Section 3.2. Figure 34 shows an example of a masked-matrix in an image form of θ_i , ϕ_r , and θ_r .

Lastly, each image from all wavelengths and locations is converted to estimated reflectance through the use of ELM and framed with its corresponding location mask. Examples of reflectance values in the 660nm band from six locations are shown in Figure 35.

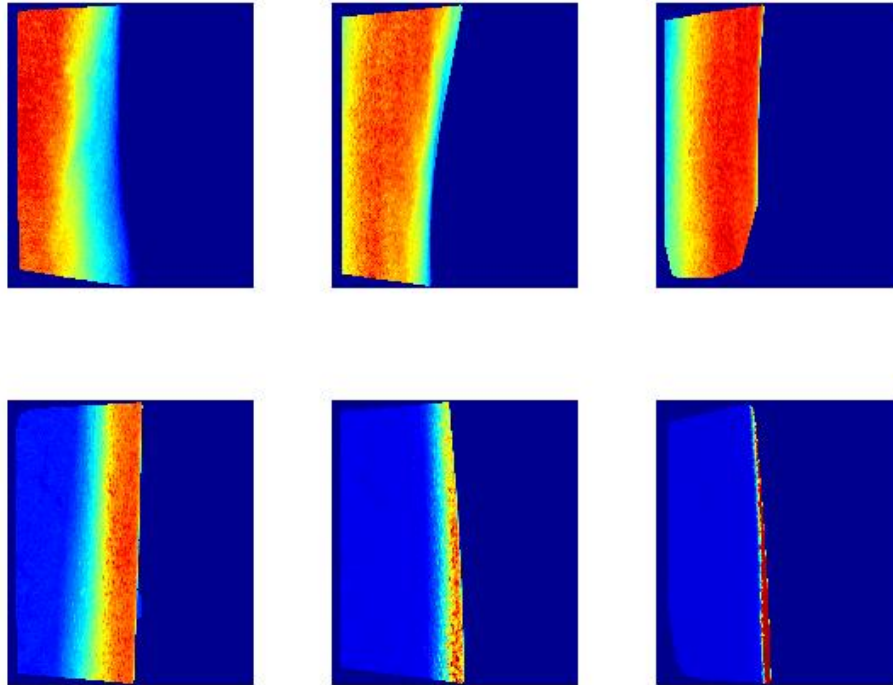


Figure 35. Example masked matrices in image forms of estimated reflectance values from the 660nm band at camera positions (from left to right, top to bottom) 6, 36, 66, 96, 126, 156 degrees from the light source.

3.4 Summary

The entirety of the image-based BRDF measurement system is discussed in Chapter III. The layout and instrumentation of the BRDF measurement set up is presented, including the existing monocular multispectral camera system and the modifications required for this image-based BRDF measurement application. Specifications of each component and its location are described to give the reader an understanding of the importance of each module. The second half of the chapter provides further details regarding the grid-pattern laser use, grid extraction algorithms, surface normal acquisition, and BRDF coordinate calculations. Lastly, the BRDF measurement approach is presented to give the reader an understanding of the steps and methods used in image acquisition and data analysis, which leads to the results in Chapter IV.

IV. Experiment and Results

In the previous chapter, the image-based BRDF measurement system, coordinate extraction, and measurement approach are presented. In Chapter IV, experiment-specific details are presented followed by a brief discussion on the formulation from Modified Beckmann-Kirchhoff (MBK) theory used in plotting the image-based BRDF measurements. Next, the image-based BRDF measurements are presented for all test subjects and all wavelengths of interest. Furthermore, the effects on the skin detection algorithms are examined by transforming the BRDF measurements to NDGRI and NDSI space in order to see the angular dependency of the indices. Lastly, the BRDF measurements are interpreted through physical scenarios encountered in typical remote sensing applications.

4.1 Experiment

Since human skin is the target of all measurements in this application, human test subjects were essential in the execution of this research. That being said, Institutional Review Board (IRB) approval is needed for the use of human volunteers in this effort. The protocol discussed in Chapter III was reviewed and approved by the Air Force Research Laboratory IRB via expedited review procedures due to the minimal risk of the data collection. All requirements, as set by the IRB and its legal counsel, have been fully complied with. In addition, informed consent documents from all individuals were properly filled out. IRB approval for the use of human volunteers in research can be viewed in Appendix B of this thesis.

It is important to collect data from a variety of skin types in order to determine if BRDF measurements depend on melanin content. A total of six human test subjects are included in this work, ranging from an estimated Fitzpatrick Skin Type of Type-I

Table 7. Table shows each subject with control number, along with their corresponding estimated Fitzpatrick Skin Type (discussed in Section 2.2) and their estimate hair coverage on their forearm (Low, Medium, or High).

Human Subject	Estimated Fitzpatrick Skin Type	Hair Coverage
Subject 1	III	Low
Subject 2	II/III	Low
Subject 3	II/III	Medium
Subject 4	V	Low
Subject 5	I/II	Low
Subject 6	I	High

to Type-V. The human subject control numbers, along with their corresponding estimated Fitzpatrick Skin Type and estimated hair coverage, is provided in Table 7. As stated in Section 2.2, estimated Fitzpatrick Skin Type is qualitatively categorized based on the subject’s skin reflectance spectrometer reading at 685 nm (leading indicator for melanosome percentage) when compared to spectrometer readings and their corresponding estimated Fitzpatrick Skin Type in [28]. Hair coverage is qualitatively categorized as low, medium, or high coverage. Prior to using the BRDF image-based measurement system, spectral reflectance measurements are acquired from each test subject using the ASD field spectrometer described in Section 2.5.1 (calibrated against a white Spectralon[®] calibration cap). These spectral measurements, relating closely to the diffuse reflectance component of their skin, can be seen in Figure 36. Within the melanin absorption region of the spectra (below 1100 nm), a range of melanin content across the test subjects is evident.

Before each use of the image-based BRDF measurement system, an image is acquired from each camera of both a gray and white Spectralon[®] diffuse-reflectance panel. These images are later used in post-processing to convert pixel values to estimated reflectance values with the Empirical Line Method (ELM) discussed in Section 2.3 and Section 3.3.1. Not only does ELM account for the different sensors and optical paths across the cameras, the method also helps account for different

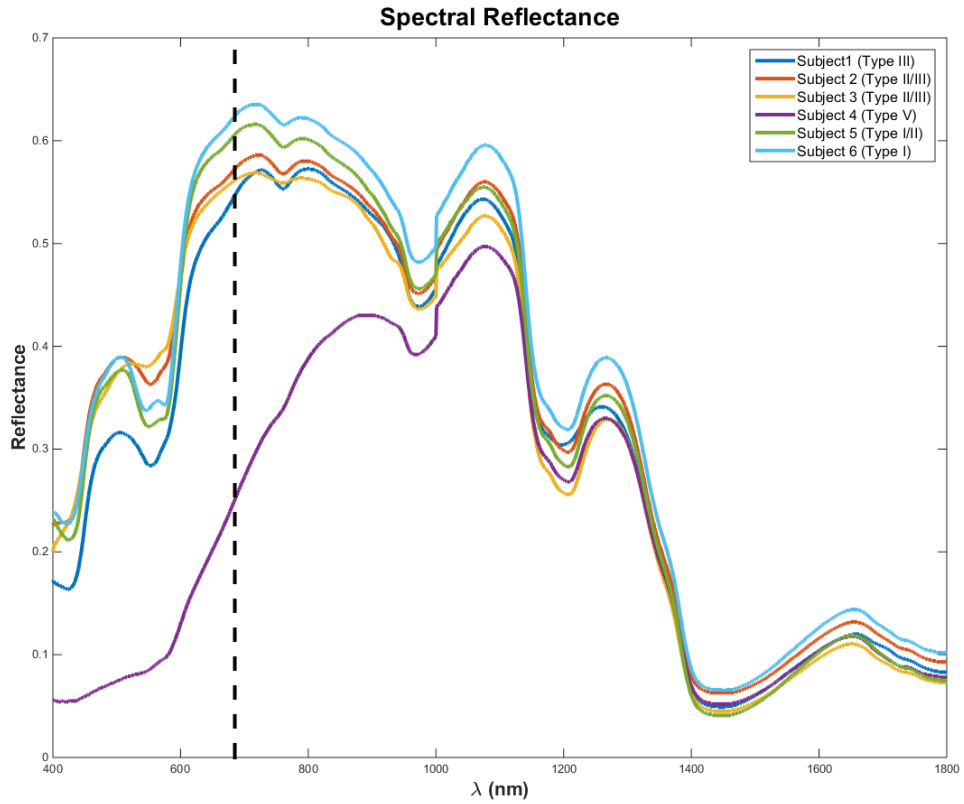


Figure 36. Spectral reflectance measurements acquired from the ASD Field Spectrometer for each human test subject. Prior to BRDF data collection, these measurements were acquired from the test subject’s left forearm. The legend shows the subject control number and their corresponding estimated Fitzpatrick Skin Type.

sources of noise.

Following the ASD Field Spectrometer and Spectralon[®] target measurements, each human subject is seated for image-based BRDF skin measurements using our instrumentation. A number of actions are completed before each collection to maintain minimal background noise during the data collection process. The laboratory test room is dark for collection, with the exception of the light source and grid projection laser. All electronic instrumentation is powered on approximately 30 minutes before data collection to obtain a relatively constant hardware response across collects. In addition, all reflective materials surrounding the target that could provide background noise are covered such that any stray light is reflected away from the camera system.

For each data collection, the multispectral camera system sweeps from 6.09 degrees to 156.09 degrees relative to, and in plane with, the light source (0-150 degrees on the semi-circle detent device). The FOV of the camera system is flooded by the exposed light source at angles beyond 156.09 degrees. The sweep is accomplished in 10-degree increments, totaling 16 locations. An increment of 10 degrees provides sufficient angular diversity; enough data for high sample density and averaging to occur at similar angular scenarios. When compared to 5-degree increments, 10 degrees allows for a shorter data collection time, a duration which is approximately 15 minutes. Since the experiment requires human subjects to sit and remain relatively still, a short data collection was important in this application. Lastly, all device shuttering in the data collection process discussed in Section 3.3.1 is accomplished manually with nontransparent black foam board.

4.2 Displaying BRDF Data

Several different BRDF models have been developed since the formal definition of the BRDF in 1977 [27]. Work in [2] examines two classes of often-used BRDF models: the microfacet class of models and the Modified Beckmann-Kirchhoff (MBK) scalar wave optics model. In this thesis, formulation used in displaying the BRDF measurements follows that from MBK theory which is discussed in further detail in [2, 8, 16, 17]. In MBK theory, the BRDF is calculated in direction cosine space (α, β) instead of spherical space (θ, ϕ) . Direction cosine space is defined in [2] as

$$\Delta\alpha = \alpha_s - \alpha_i = \lambda v_y = \sin(\theta_s)\sin(\phi_s - \pi) \quad (32)$$

$$\Delta\beta = \beta_s - \beta_i = \lambda v_x = \sin(\theta_s)\cos(\phi_s - \pi) - \sin(\theta_i), \quad (33)$$

where $\theta_s = \theta_r$ and $\phi_s = \phi_r$; a result from defining the angle as scatter as opposed to reflection. The π arises from the 180° difference in defining the $\phi = 0$ location defined in Chapter III versus in the linear systems model. Here, in-plane forward scatter is represented by $\phi_s = \pi$ and backscatter, $\phi_s = 0$; however, in some linear systems papers such as [17], forward scatter is defined as $\phi_s = 0$. For isotropic samples, the angular dependence simplifies to

$$\begin{aligned} \eta_r^2 &= (\Delta\alpha)^2 + (\Delta\beta)^2 = \sin^2(\theta_i) + \sin^2(\theta_r) + 2\sin(\theta_i)\sin(\theta_r)\cos(\phi_r) \\ \eta_r &= \sqrt{\sin^2(\theta_i) + \sin^2(\theta_r) + 2\sin(\theta_i)\sin(\theta_r)\cos(\phi_r)}, \end{aligned} \quad (34)$$

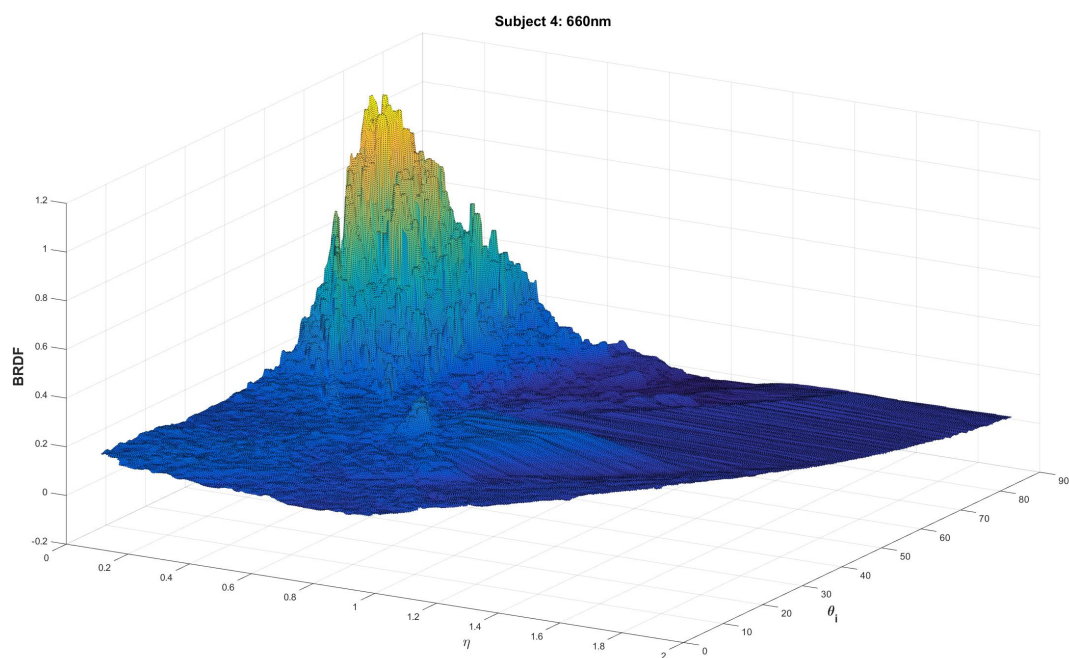
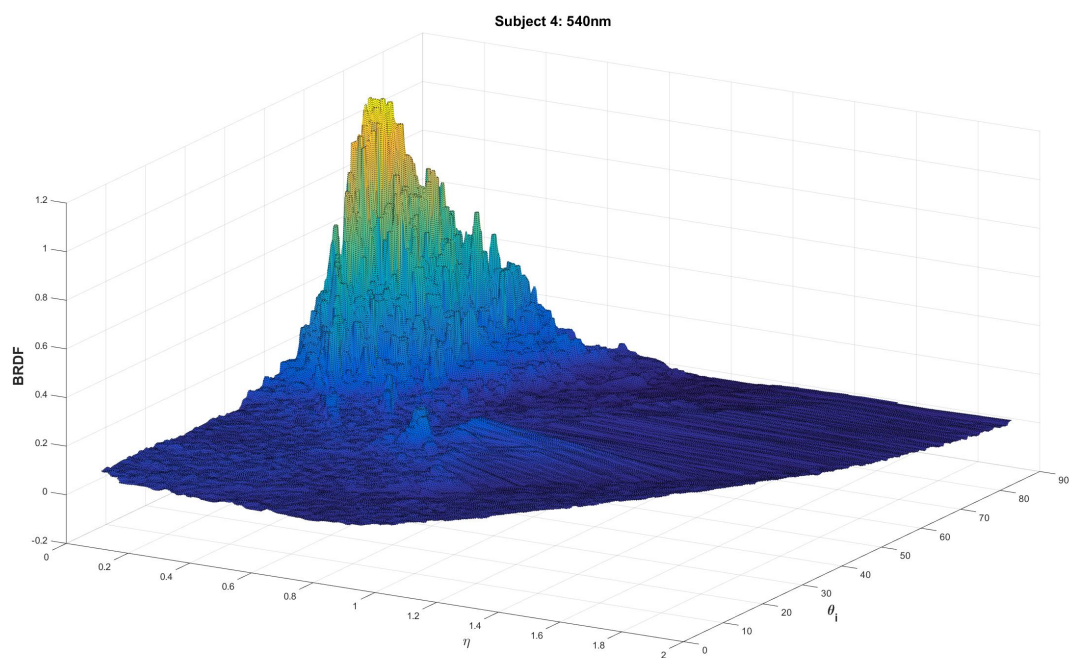
using reflected as opposed to scattered subscripts. Note the dependency on θ_i , θ_r , and ϕ_r limits η_r values between 0 and 2. In Section 4.3 and 4.4, resulting BRDF measurements are displayed as a function of θ_i and η_r , allowing for interpretation

and the study of future model incorporation in skin detection algorithms. Other data display approaches used in this chapter include spherical space plots.

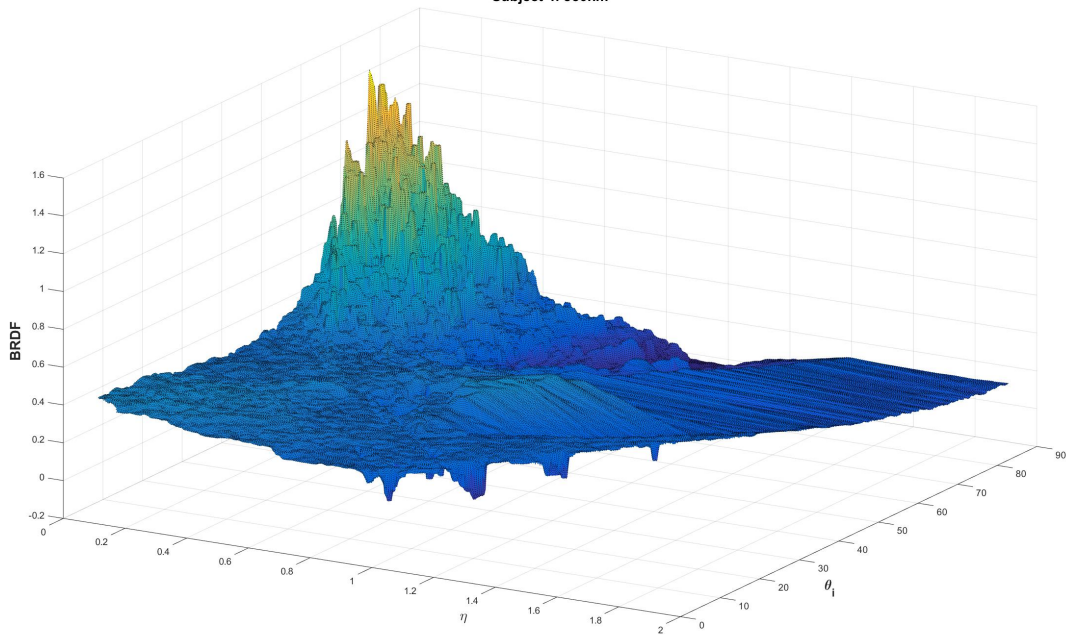
4.3 Measurement Results

In this section, BRDF skin measurements collected from the image-based BRDF measurement system are presented for the human test subjects at wavelengths of 540 nm, 660 nm, 850 nm, 1080 nm, and 1580 nm. All subjects exhibited similar trends, however, a select few are featured in certain interpretations based on the subjects characteristics. Subject plots that are not featured for select interpretations are presented in Appendix A. Three dimensional surface plots are generated from fitted surfaces calculated from the densely scattered data. The surface plots display BRDF values as a function of θ_i and η_r : the x -axis is η_r , the y -axis is θ_i (degrees), and the z -axis is $BRDF(\theta_i, \eta_r)$ (sr^{-1}). Important features and trends are discussed regarding the wavelength, melanin content, hair coverage, and angular dependency.

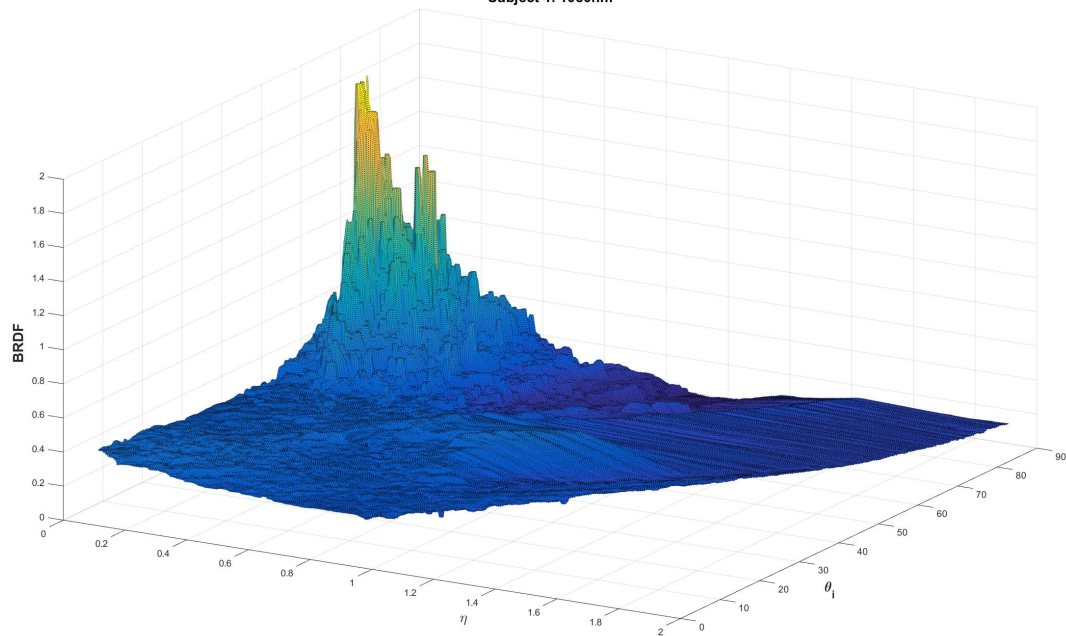
Figures 37-39 show the BRDF skin measurements from Subject 4, Subject 5, and Subject 6 in the 540 nm, 660 nm, 850 nm, 1080 nm, and 1580 nm bands (for plots of remaining subjects, see Figures 77-79 in Appendix A):



Subject 4: 850nm



Subject 4: 1080nm



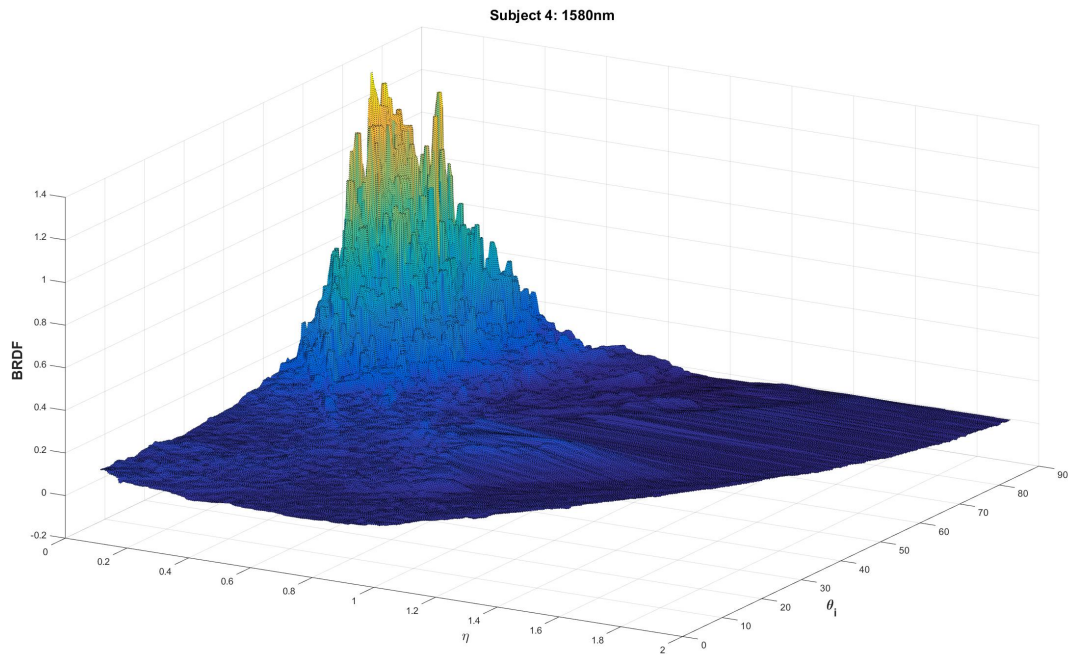
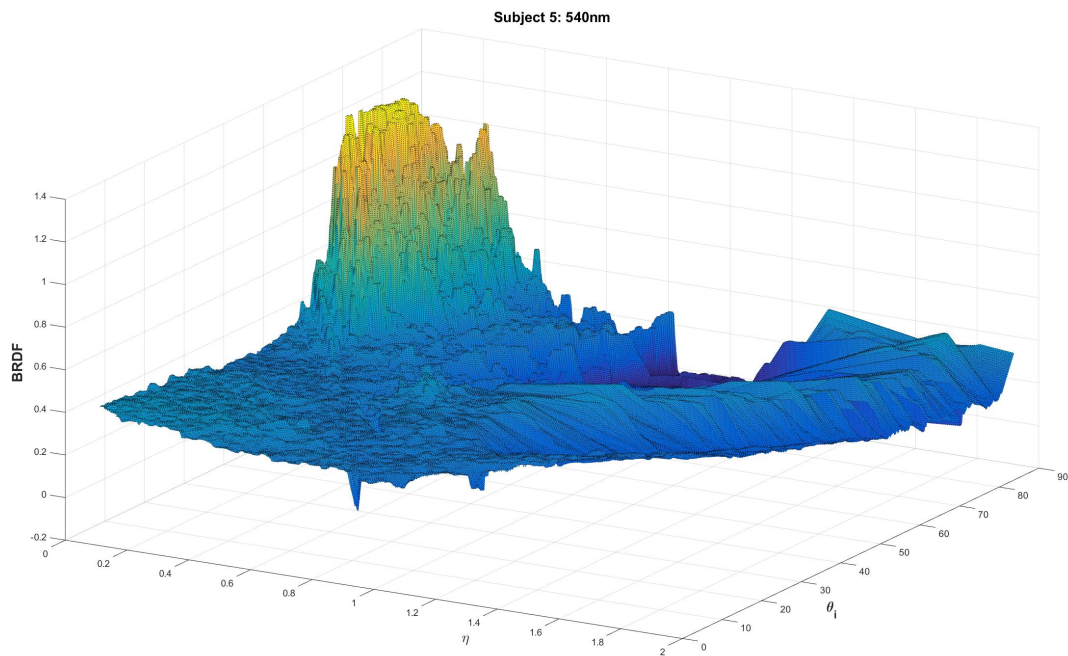
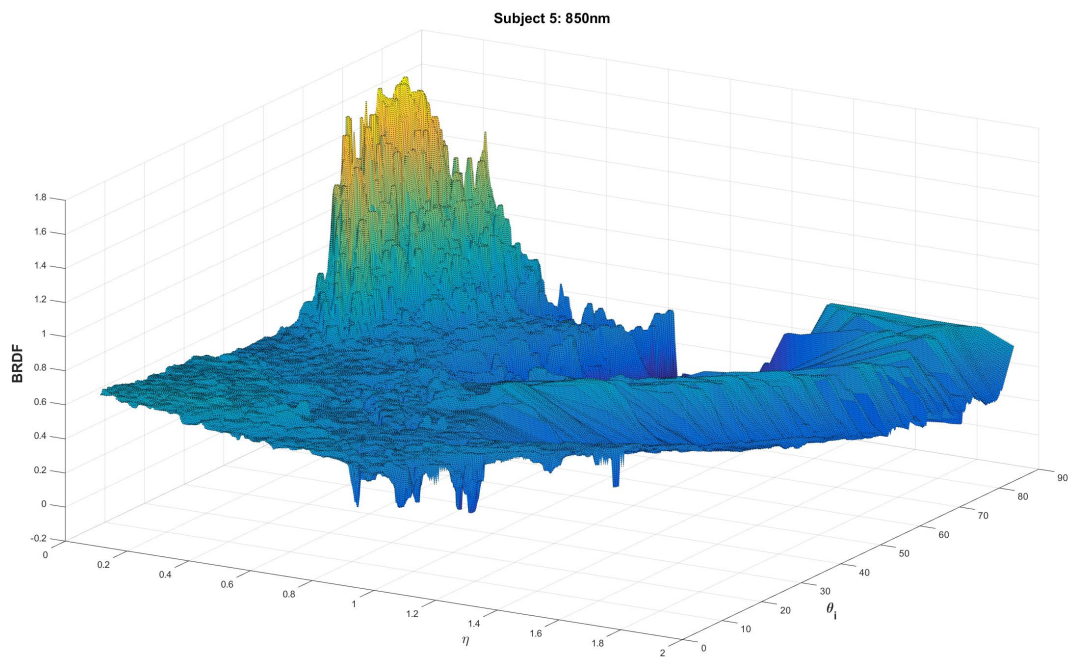
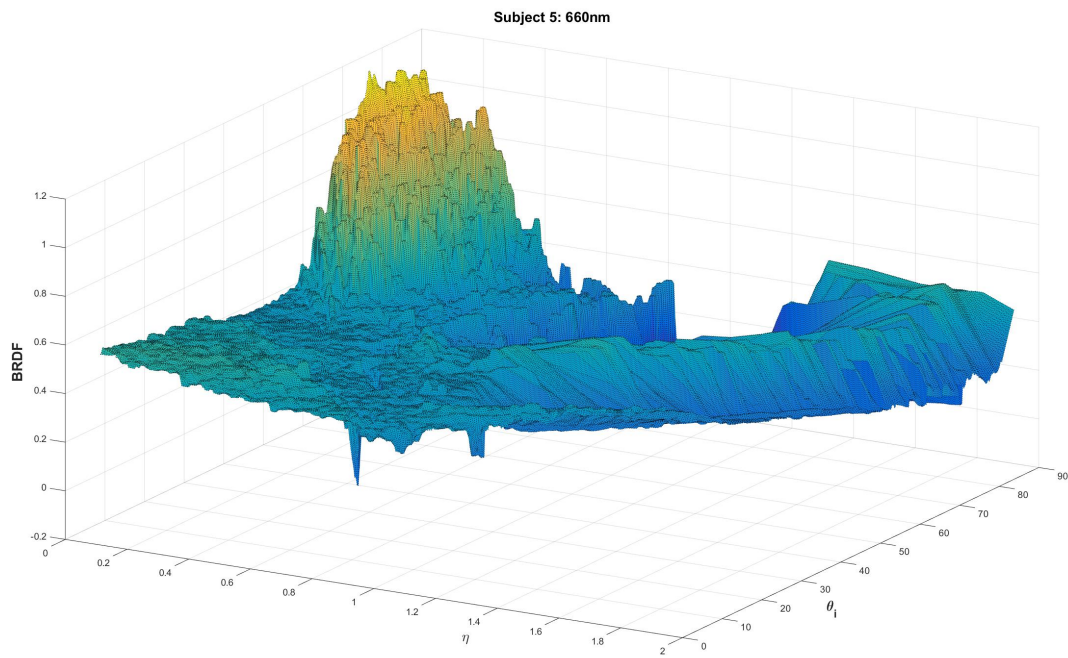


Figure 37. BRDF skin measurements obtained from Subject 4 in the 540nm, 660nm, 850nm, 1080nm, and 1580nm bands. Estimated Fitzpatrick Skin Type: V, Hair Coverage: Low.





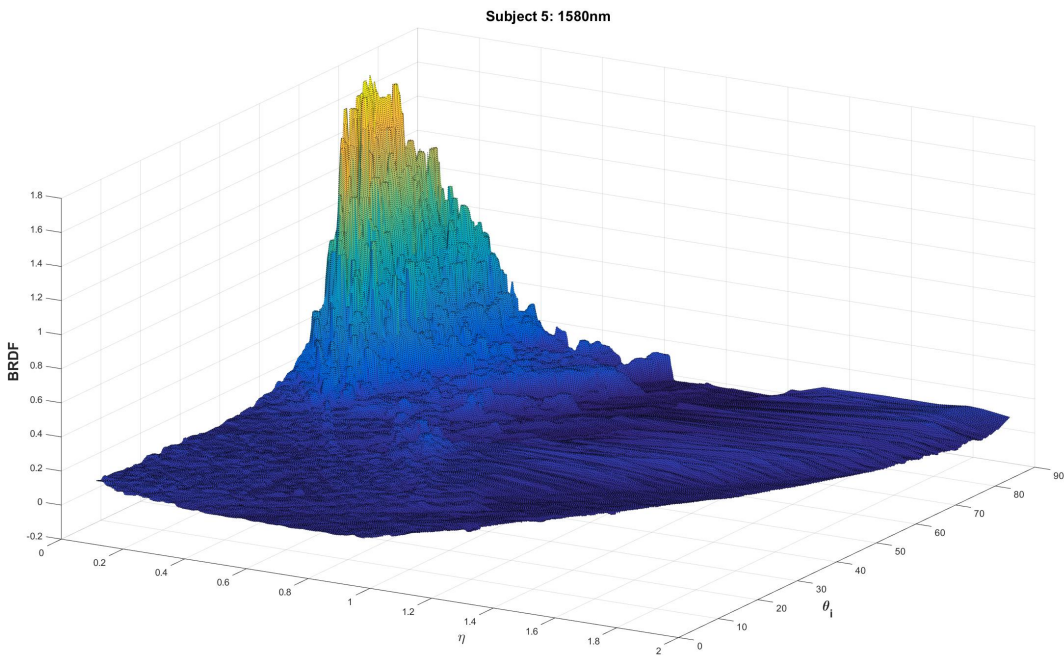
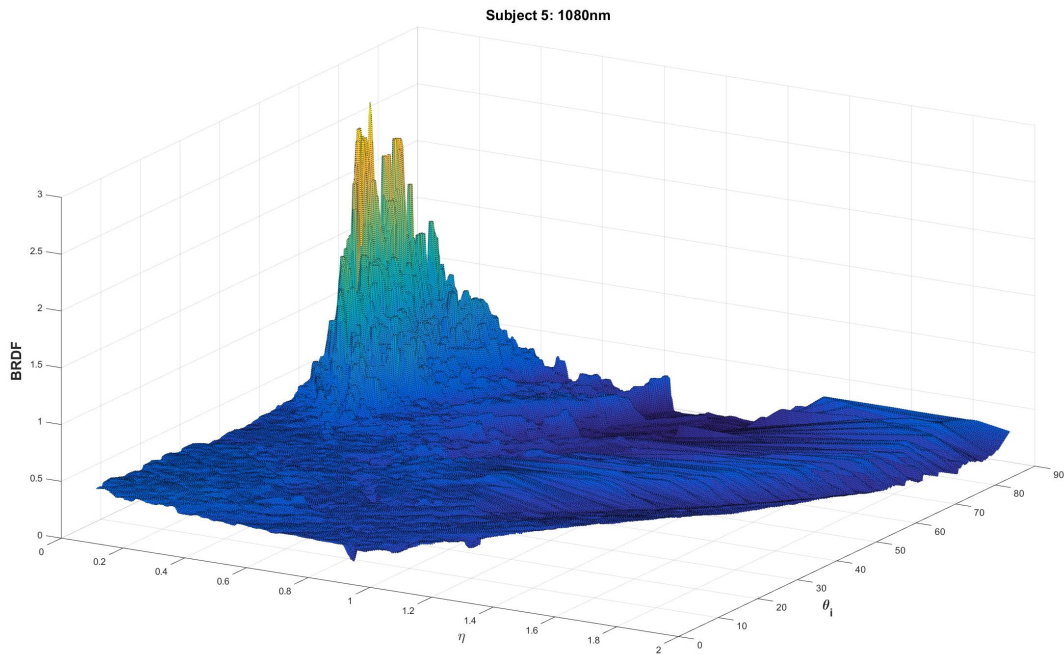
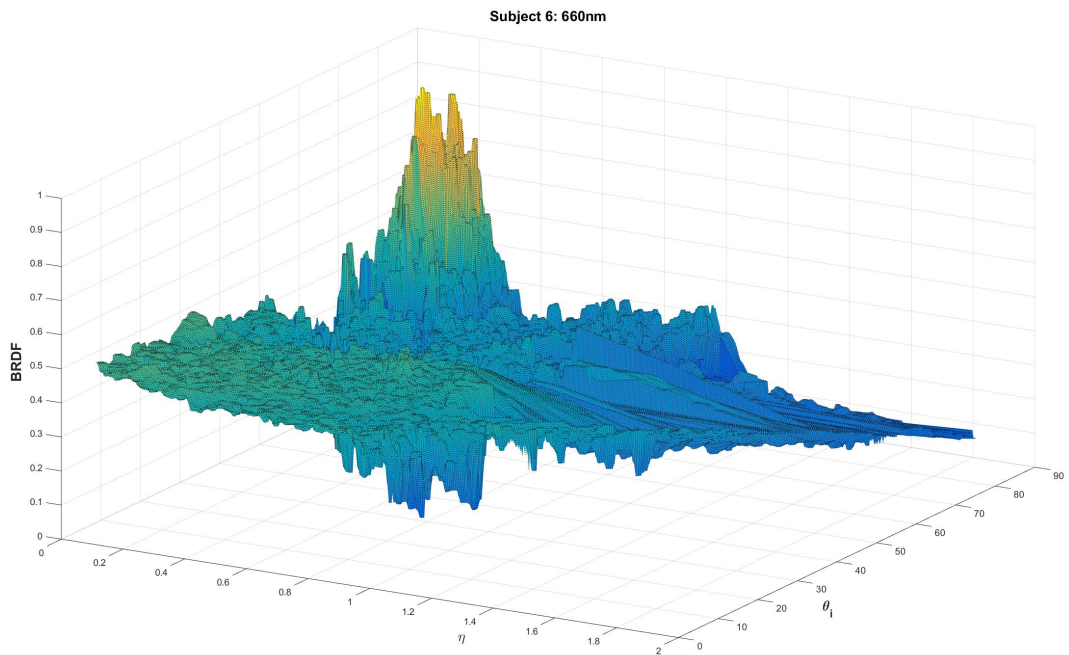
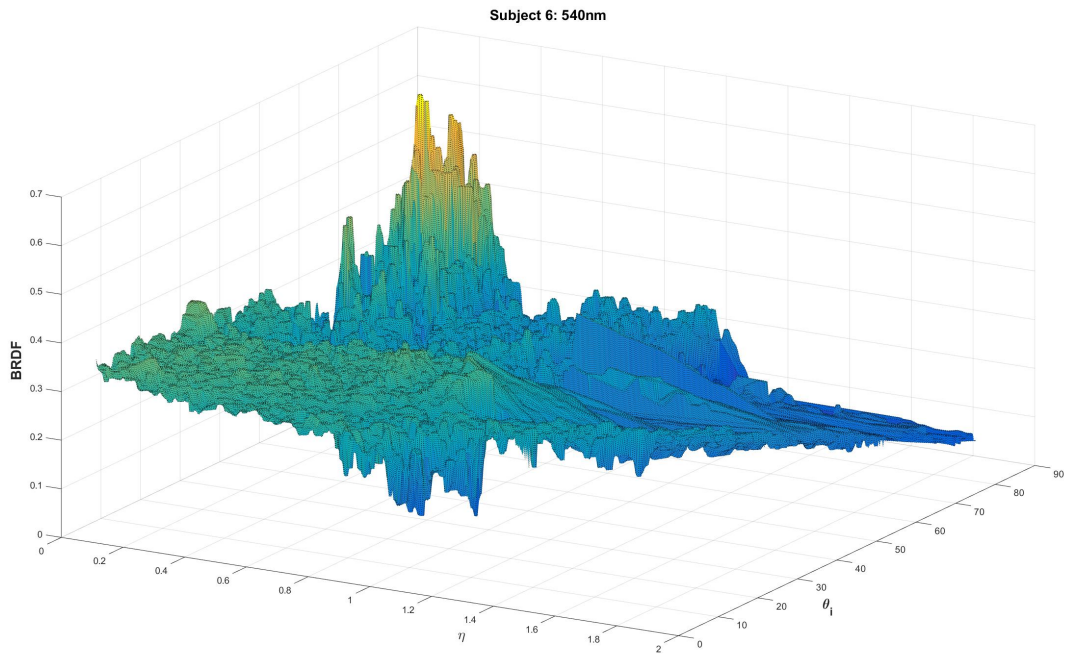
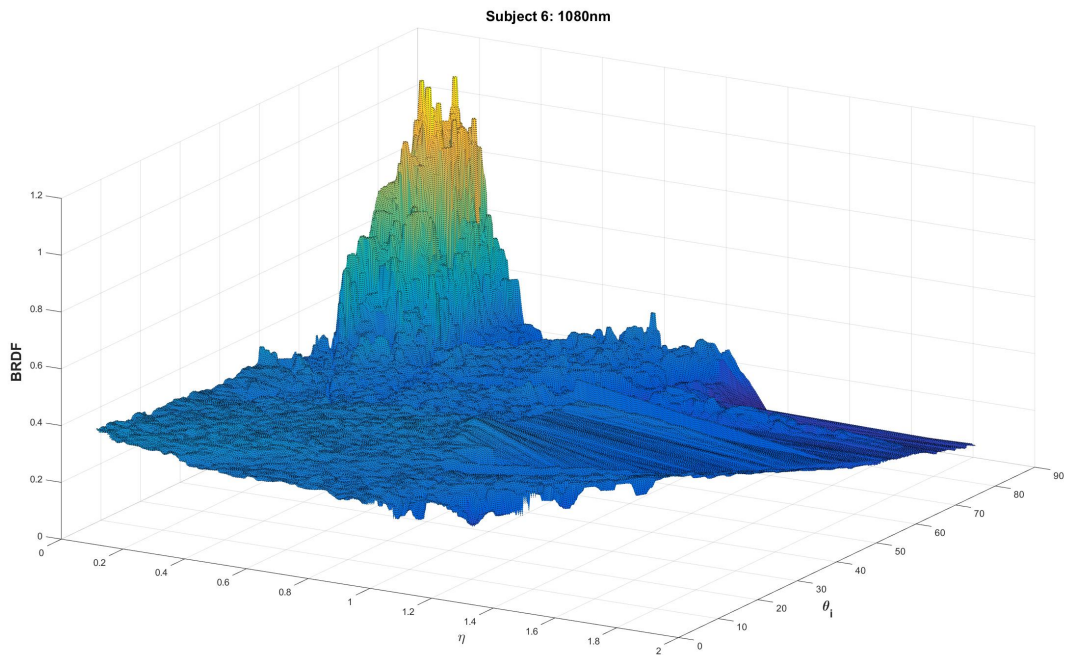
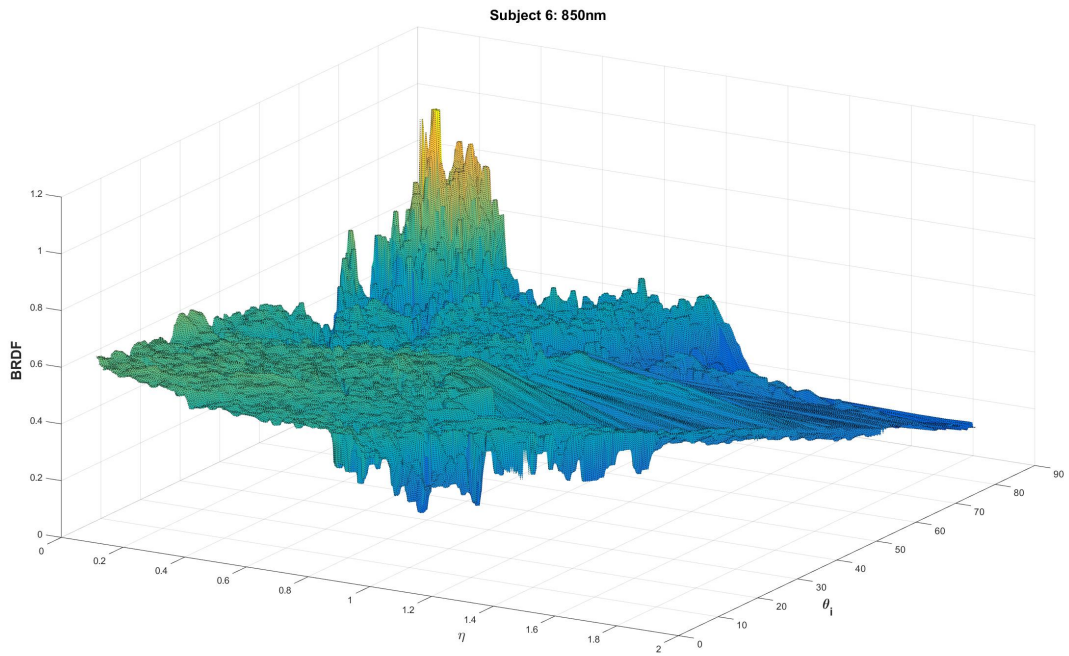


Figure 38. BRDF skin measurements obtained from Subject 5 in the 540nm, 660nm, 850nm, 1080nm, and 1580nm bands. Estimated Fitzpatrick Skin Type: I/II, Hair Coverage: Low.





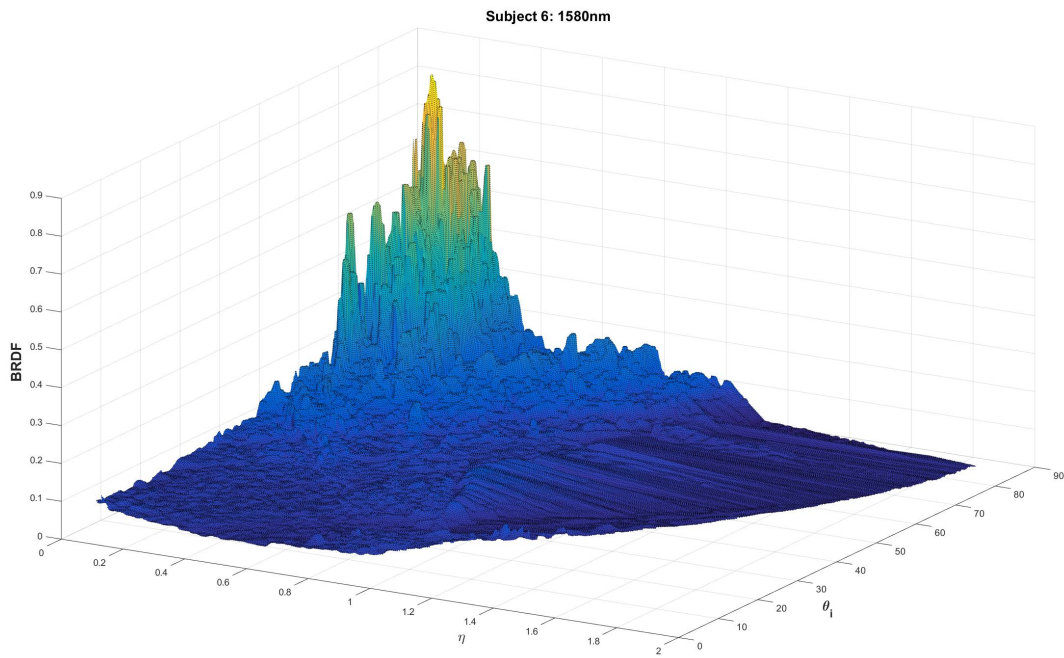


Figure 39. BRDF skin measurements obtained from Subject 6 in the 540nm, 660nm, 850nm, 1080nm, and 1580nm bands. Estimated Fitzpatrick Skin Type: I, Hair Coverage: High.

Examining the plots, it is evident that several trends exist. Some of the most valuable information for skin detection algorithms is located in the $BRDF, \theta_i$ - plane, where $\eta = 0$. Along that cross-section is where the specular measurements are located, ranging from $\theta_i = \theta_r \approx 0$ degrees at $\phi_r \approx 0/180$ degrees (may be referred to as direct backscatter) to $\theta_i = \theta_r \approx 90$ degrees at $\phi_r \approx 180$ degrees (near grazing angles). Note that the direct backscatter specular reflectance component of skin at $\theta_i = \theta_r \approx 0$ degrees, $\phi_r \approx 0/180$ degrees is just a fraction of the BRDF value near grazing angles. In fact, the plots exhibit rapid growth beyond the slight dip in values at $\theta_i = \theta_r \approx 45$ degrees, $\phi_r \approx 180$ degrees. The specular trend can be seen for every subject and wavelength in Figures 40-45, where BRDF values are plotted versus θ_i , for all $\theta_i = \theta_r$ forward-scattering combinations. These specular plots were generated with the mean of the first 50 samples slices from the η -plots where η values are between 0 and 0.2. BRDF values corresponding to θ_i -angles beyond 75 degrees cannot be trusted due to limitations of the imaging scenarios and geometry extraction. Beyond 75 degrees, one would expect the specular component to continue to increase as angles reach grazing.

Subject 1: Specular Component Plots (Mean of first 50 sample slices at η values near 0)

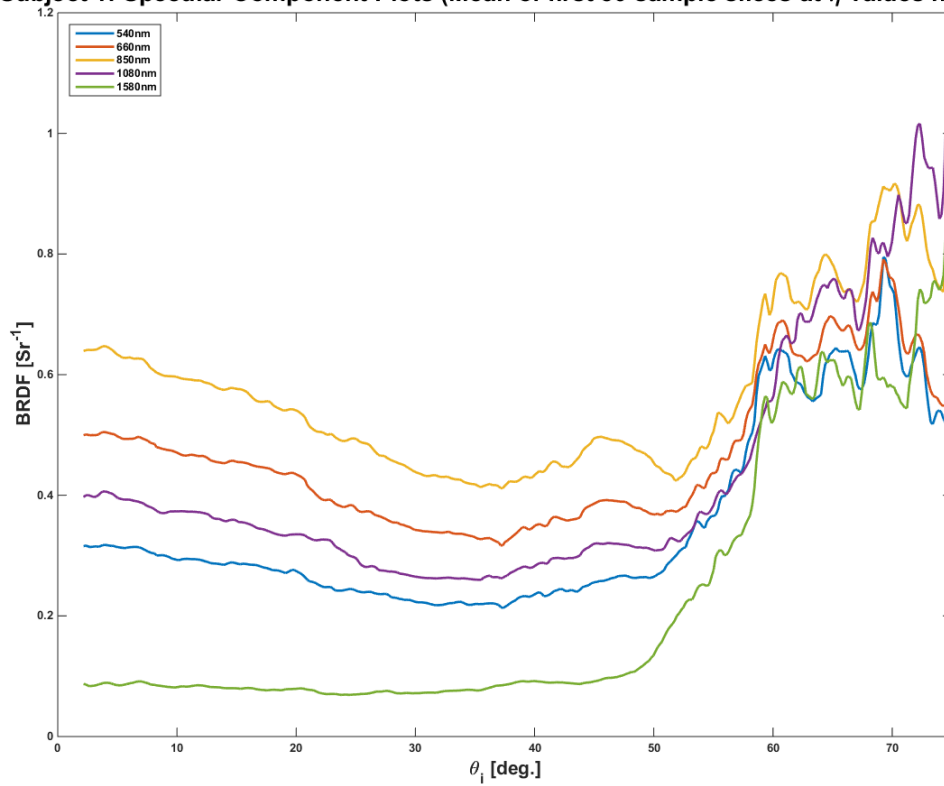


Figure 40. Subject 1 - BRDF values are plotted versus θ_i , for all $\theta_i = \theta_r$ forward-scattering combinations.

Subject 2: Specular Component Plots (Mean of first 50 sample slices at η values near 0)

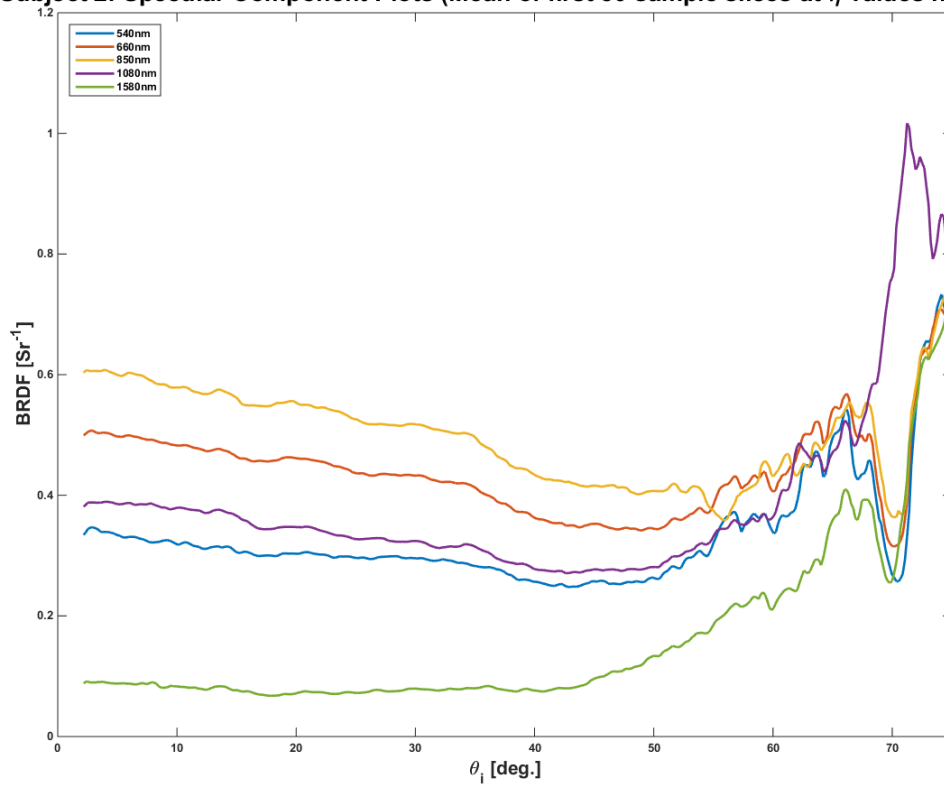


Figure 41. Subject 2 - BRDF values are plotted versus θ_i , for all $\theta_i = \theta_r$ forward-scattering combinations.

Subject 3: Specular Component Plots (Mean of first 50 sample slices at η values near 0)

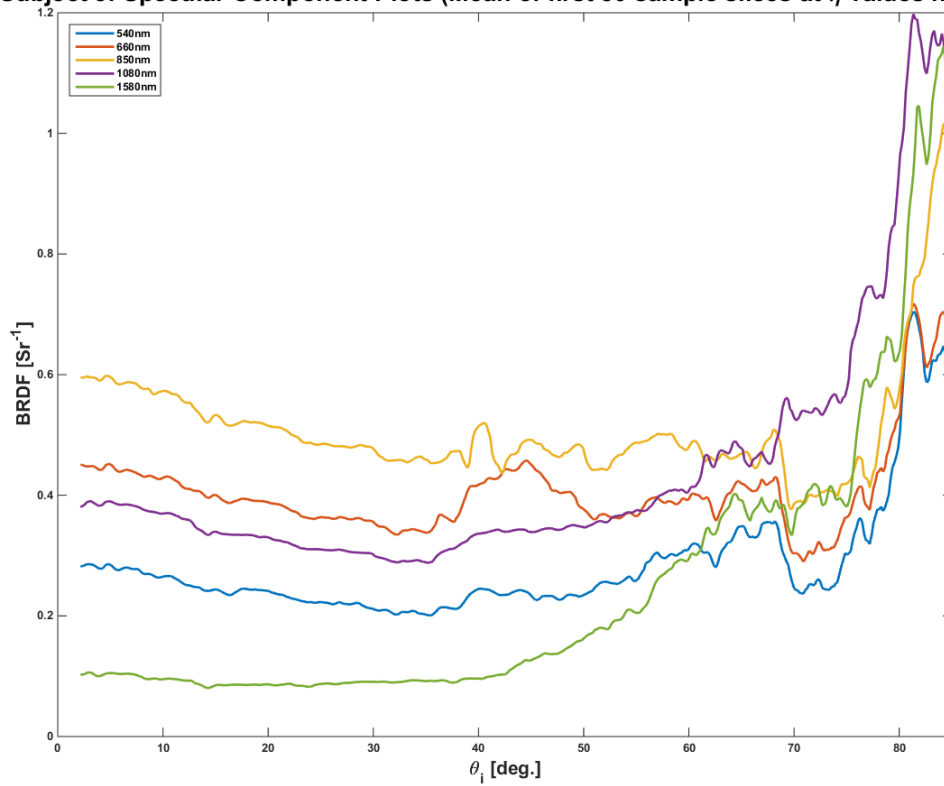


Figure 42. Subject 3 - BRDF values are plotted versus θ_i , for all $\theta_i = \theta_r$ forward-scattering combinations.

Subject 4: Specular Component Plots (Mean of first 50 sample slices at η values near 0)

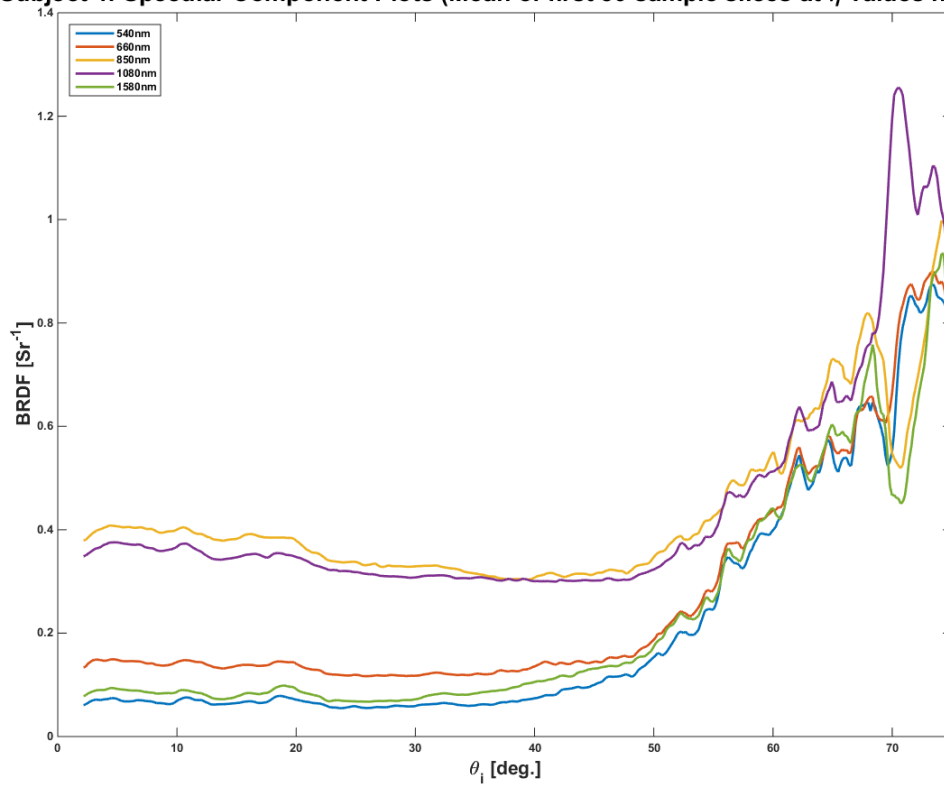


Figure 43. Subject 4 - BRDF values are plotted versus θ_i , for all $\theta_i = \theta_r$ forward-scattering combinations.

Subject 5: Specular Component Plots (Mean of first 50 sample slices at η values near 0)

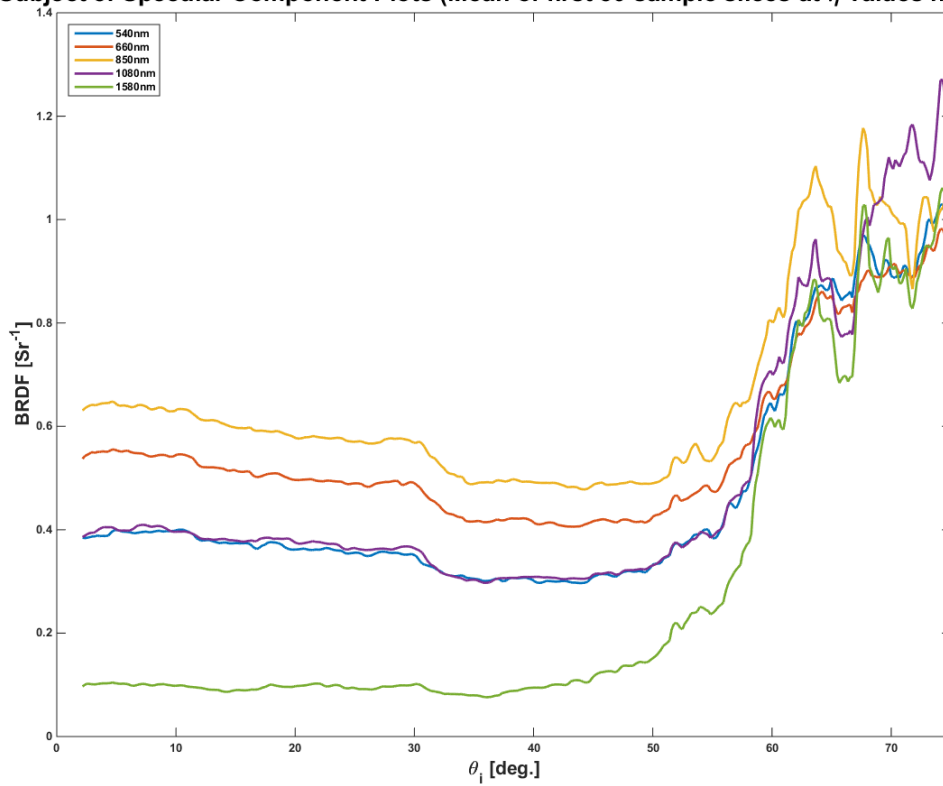


Figure 44. Subject 5 - BRDF values are plotted versus θ_i , for all $\theta_i = \theta_r$ forward-scattering combinations.

Subject 6: Specular Component Plots (Mean of first 50 sample slices at η values near 0)

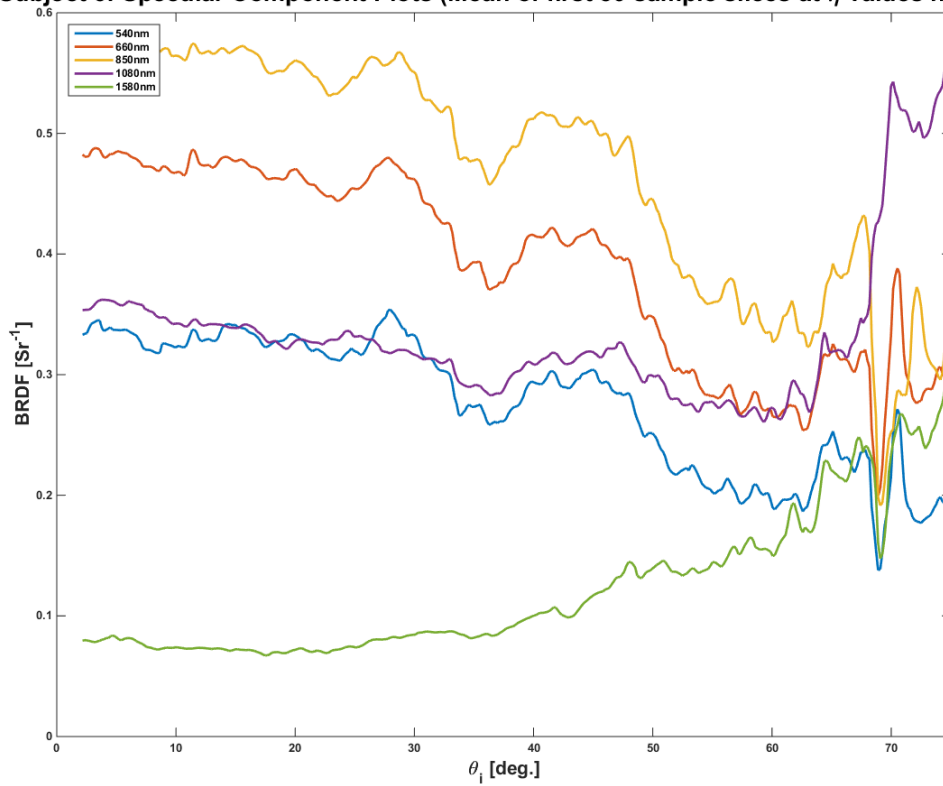


Figure 45. Subject 6 - BRDF values are plotted versus θ_i , for all $\theta_i = \theta_r$ forward-scattering combinations.

As an alternative visual, this phenomena is also seen in Figures 46-50, where three ranges for θ_i values are evaluated at ϕ_r close to 180 degrees and plotted in BRDF vs θ_r space for Subject 5 at each wavelength (for plots of remaining subjects, see Figures 80-104 in Appendix A). Specular peaks should occur at θ_r values equal to θ_i . This is clear for θ_i ranges of 5-10 and 75-80 degrees. These plots gauranty the display of specular measurements while showing diffuse measurements where reflected and incident angle are not equal. The general trends of each sample/pixel pool in Figures 46-50 can be visualized with their corresponding mean and error-bars (symmetric bars that are each two standard deviation units in length).

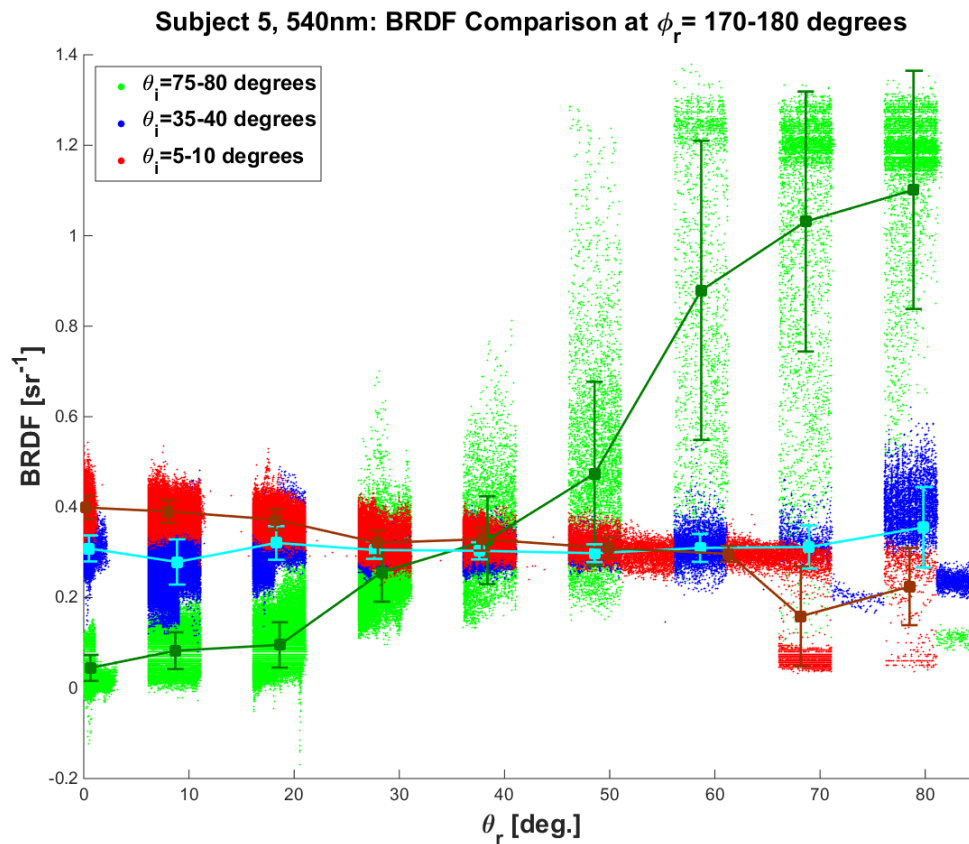


Figure 46. Three ranges for θ_i values are evaluated at ϕ_r close to 180 degrees and plotted in BRDF vs θ_r space for Subject 5 (Type I/II, Low hair coverage) with data from the 540nm band.

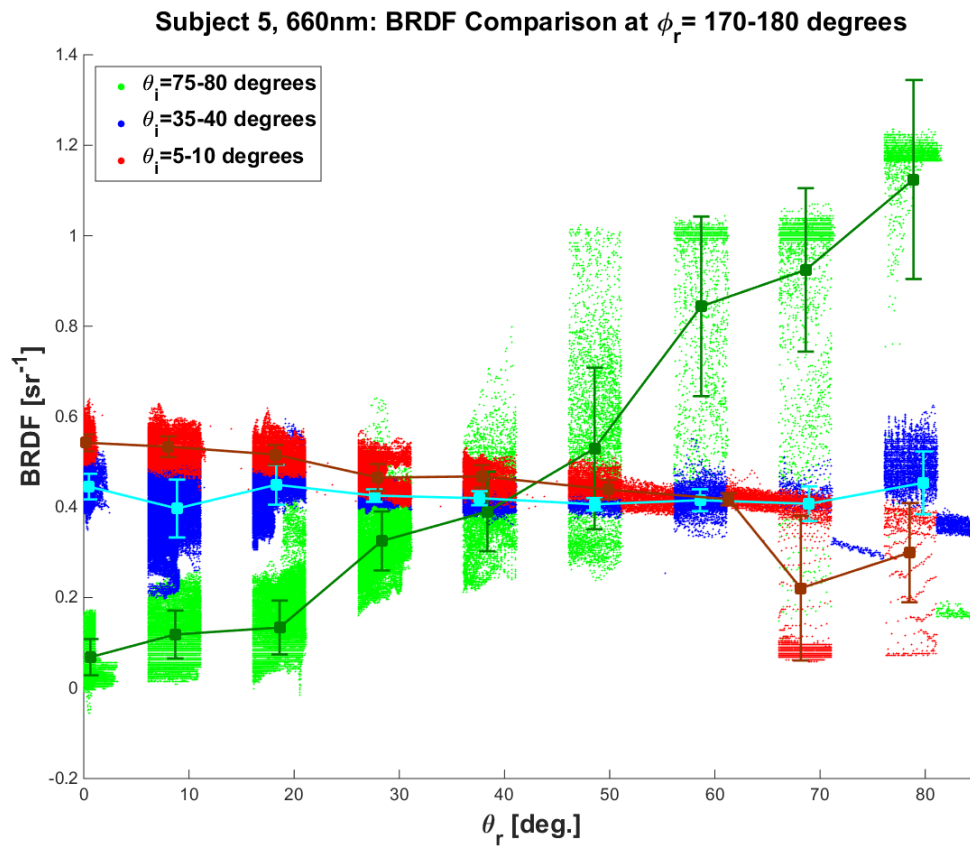


Figure 47. Three ranges for θ_i values are evaluated at ϕ_r close to 180 degrees and plotted in BRDF vs θ_r space for Subject 5 (Type I/II, Low hair coverage) with data from the 660nm band.

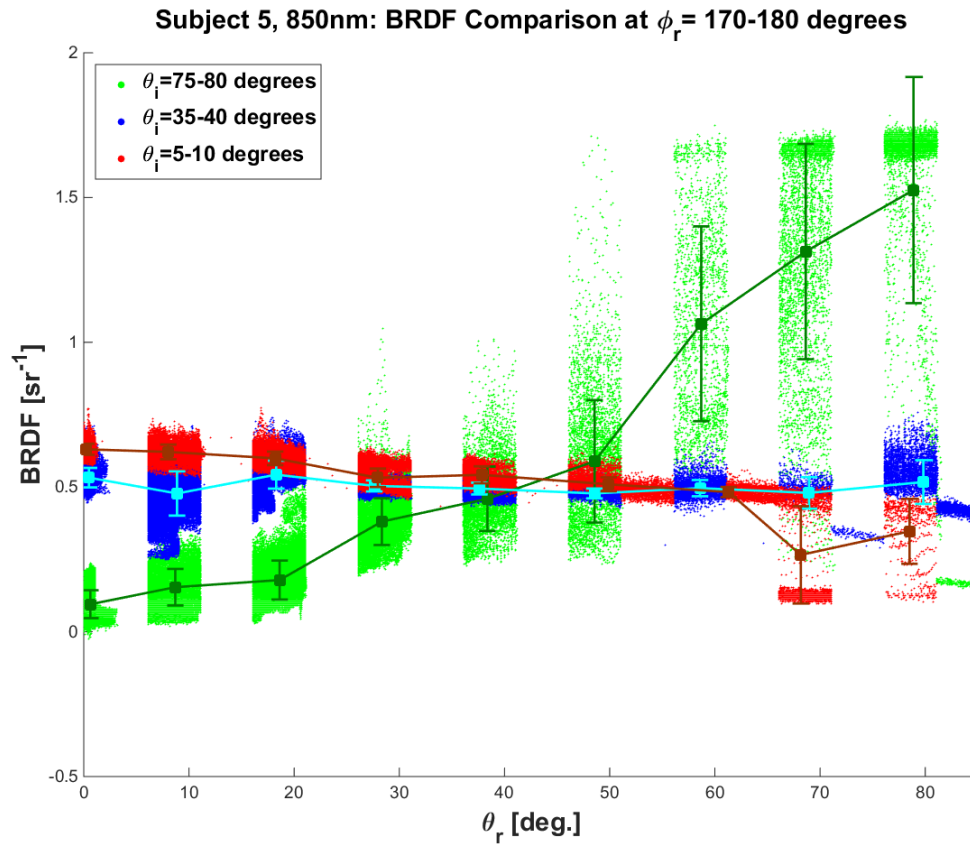


Figure 48. Three ranges for θ_i values are evaluated at ϕ_r close to 180 degrees and plotted in BRDF vs θ_r space for Subject 5 (Type I/II, Low hair coverage) with data from the 850nm band.

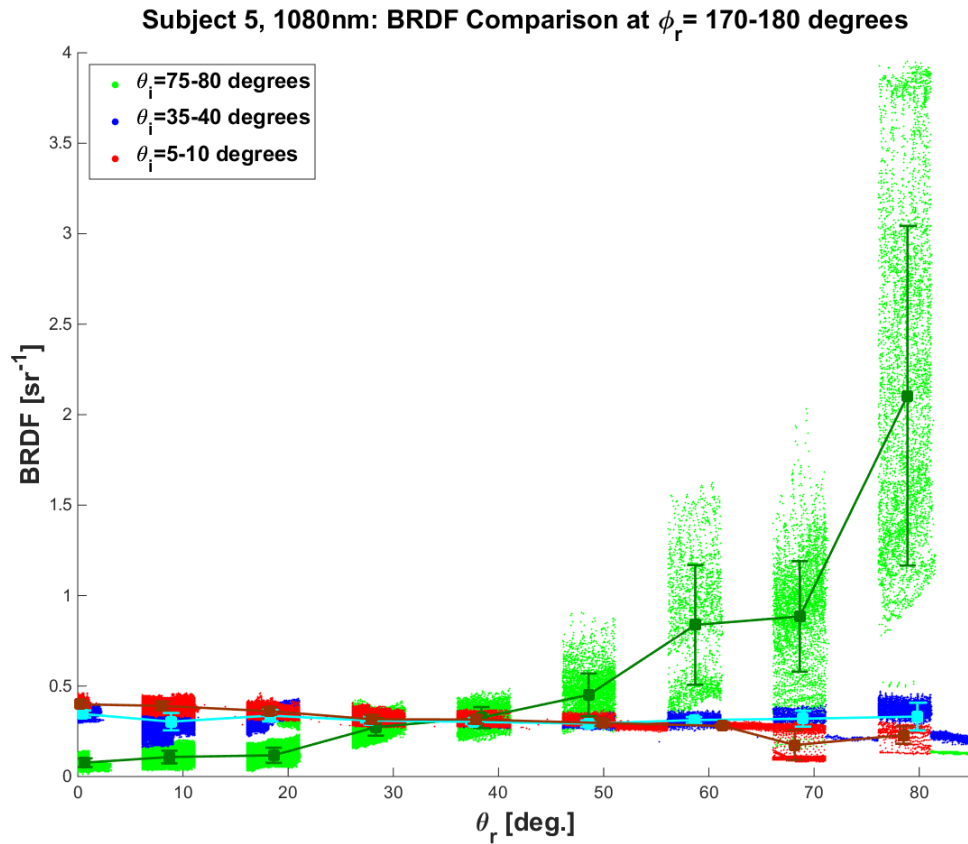


Figure 49. Three ranges for θ_i values are evaluated at ϕ_r close to 180 degrees and plotted in BRDF vs θ_r space for Subject 5 (Type I/II, Low hair coverage) with data from the 1080nm band.

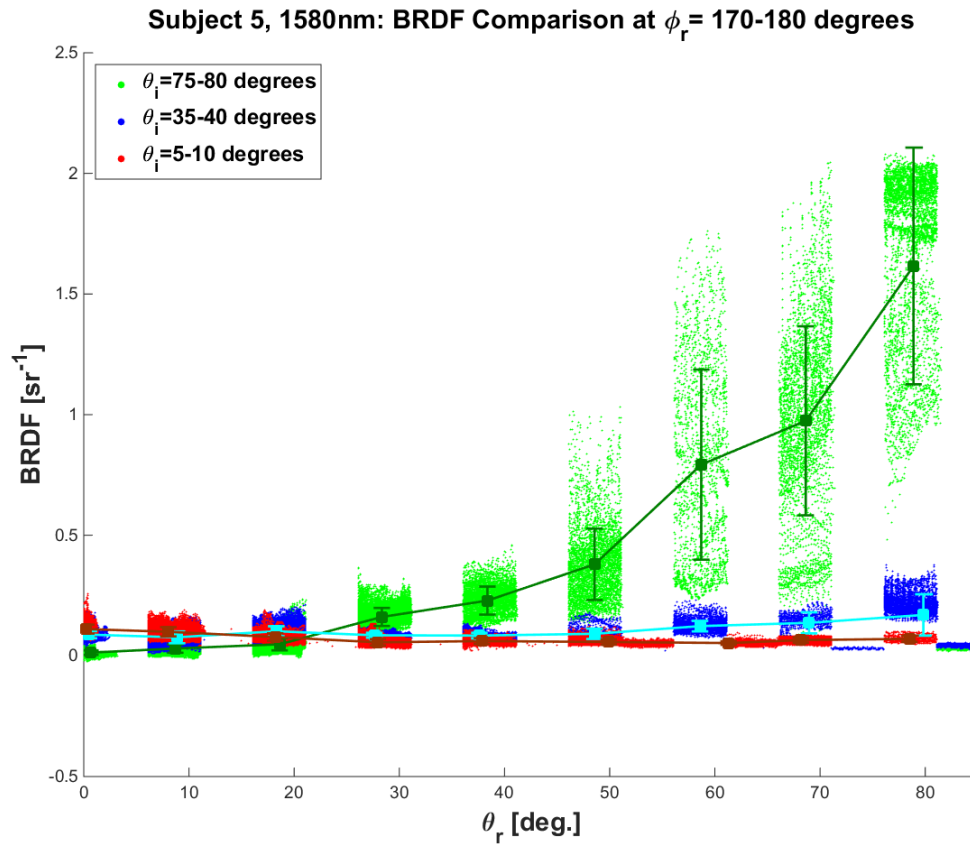


Figure 50. Three ranges for θ_i values are evaluated at ϕ_r close to 180 degrees and plotted in BRDF vs θ_r space for Subject 5 (Type I/II, Low hair coverage) with data from the 1580nm band.

Similar to Figures 46-50, polar plots for Subject 5 are seen in Figures 51-55 including backscatter scenarios where $\phi_r = 0-10$ degrees (for plots of remaining subjects, see Figures 105-129 in Appendix A). The values plotted correspond to the mean and error-bars from the cartesian plots with the addition of backscatter scenarios that are computed with identical methods. The discontinuity in the back scatter region is due to limited back scatter data due to the measurement setup specifically at these points.

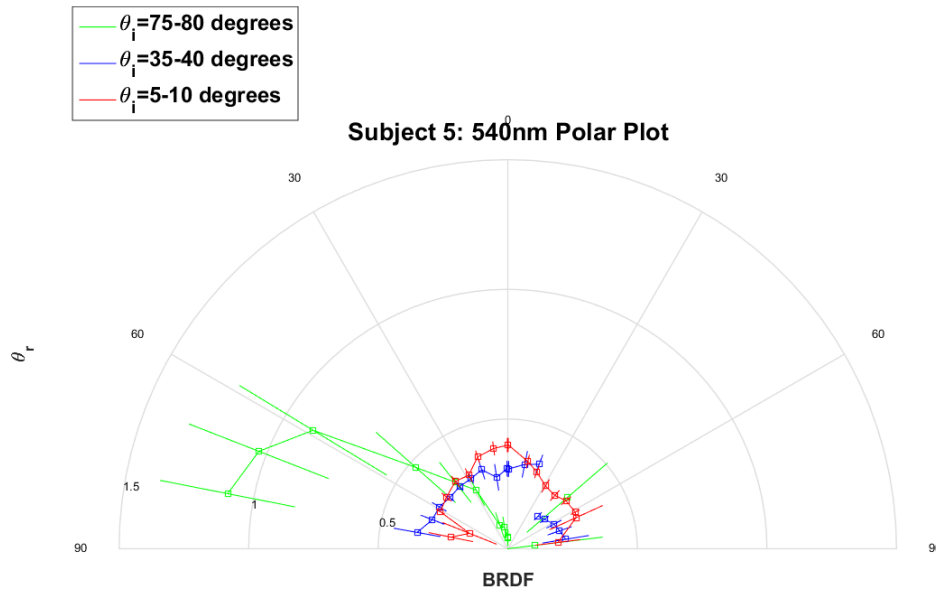


Figure 51. Three ranges for θ_i values are evaluated at ϕ_r close to 180 degrees and plotted in BRDF vs θ_r space for Subject 5 (Type I/II, Low hair coverage) with data from the 540nm band.

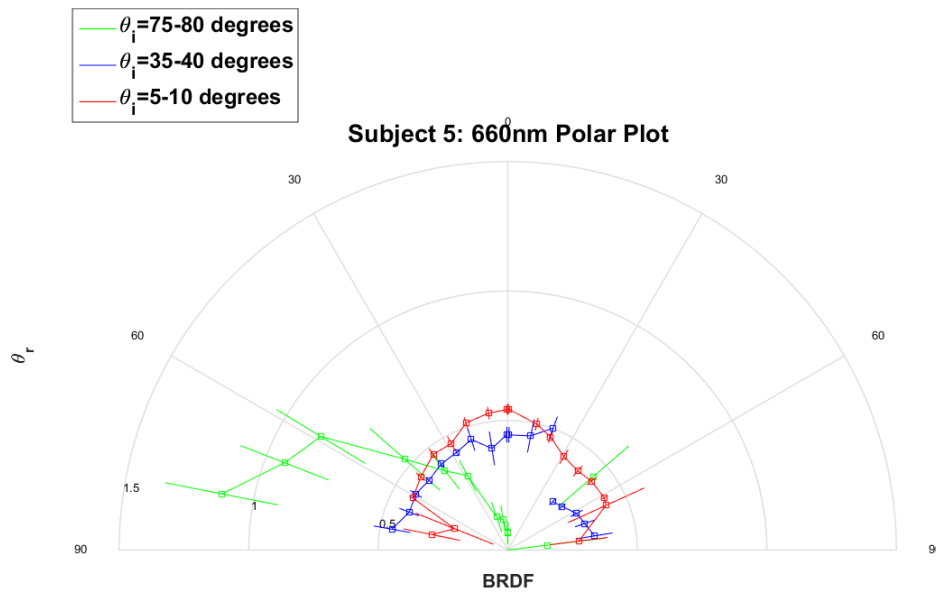


Figure 52. Three ranges for θ_i values are evaluated at ϕ_r close to 180 degrees and plotted in BRDF vs θ_r space for Subject 5 (Type I/II, Low hair coverage) with data from the 660nm band.

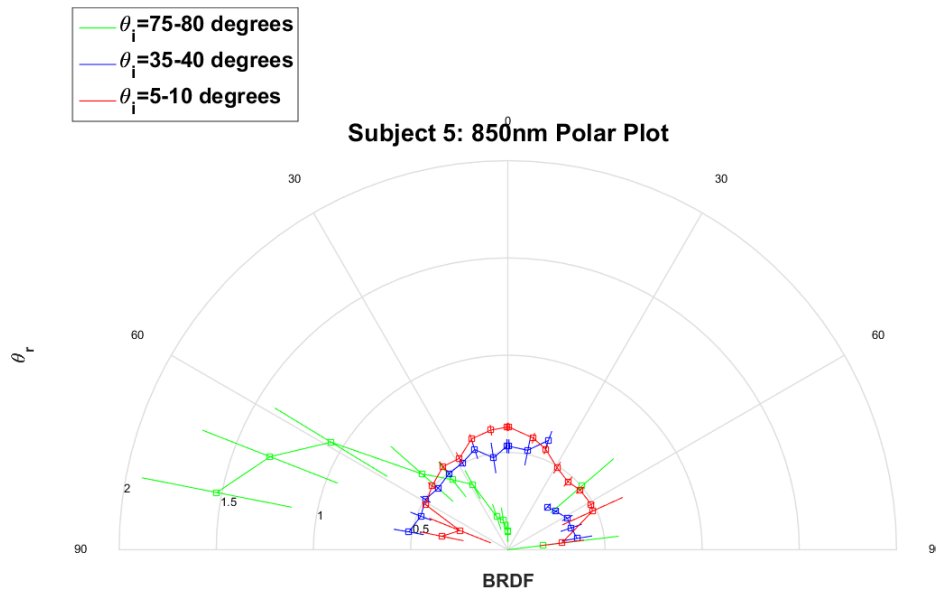


Figure 53. Three ranges for θ_i values are evaluated at ϕ_r close to 180 degrees and plotted in BRDF vs θ_r space for Subject 5 (Type I/II, Low hair coverage) with data from the 850nm band.

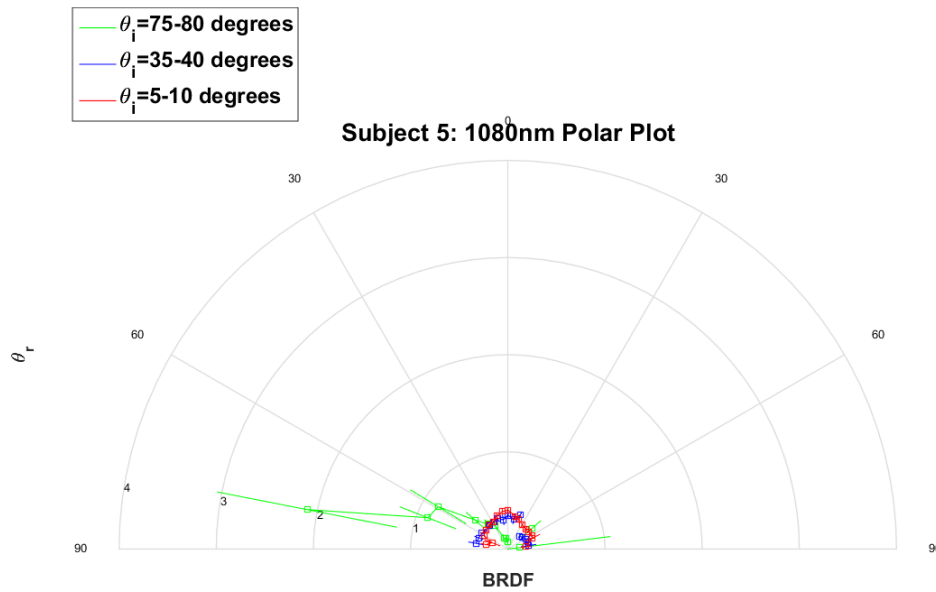


Figure 54. Three ranges for θ_i values are evaluated at ϕ_r close to 180 degrees and plotted in BRDF vs θ_r space for Subject 5 (Type I/II, Low hair coverage) with data from the 1080nm band.

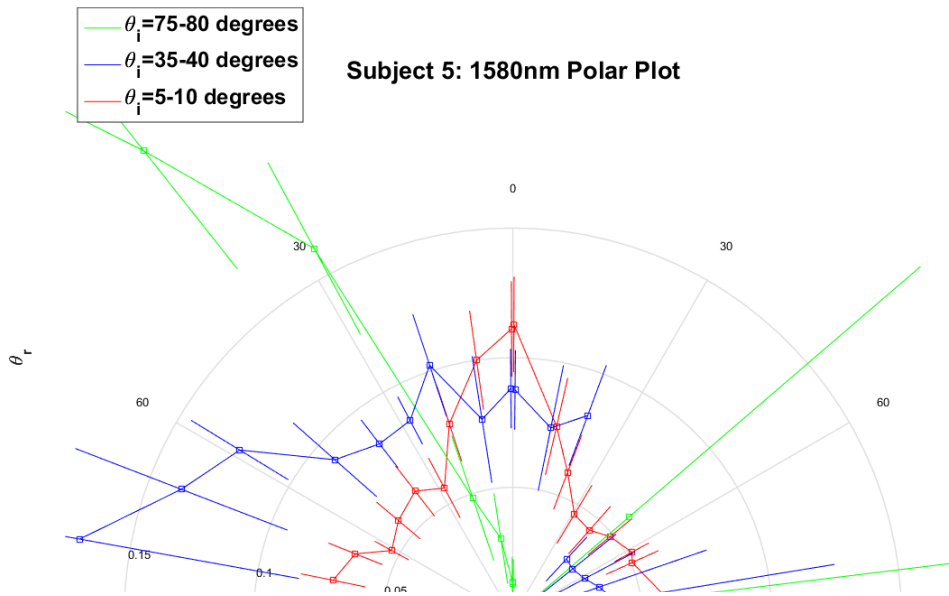


Figure 55. Three ranges for θ_i values are evaluated at ϕ_r close to 180 degrees and plotted in BRDF vs θ_r space for Subject 5 (Type I/II, Low hair coverage) with data from the 1580nm band. Specular data is cropped for $\theta_i = 75-80$ degrees for a better display of the other two ranges of θ_i .

As for the diffuse reflectance component in Figures 37-39, this component can be examined for different angular combinations as η values increase. Another common feature that is interesting among the VIS plots is the low point in values around $\eta \approx 0.8$, beyond $\theta_i \approx 45$ degrees. This common low point shows as incident angles approach grazing, the specular component grows rapidly and the diffuse component decreases with slightly smaller values at $\theta_r \approx 0$ degrees and slightly larger values recorded in the $\phi_r \approx 0$ degree, $\theta_i \approx 45+$ degree backscatter region. This trend can be seen for Subject 5 in Figures 51-55 for the range of incident angles near grazing.

Figures 37-39 and Figures 40-45 show a BRDF dependency on wavelength, as well. Plots in the 540 nm, 660 nm, and 850 nm bands all display similar reflectance characteristics with slightly varying magnitudes, while the 1080 nm band shows more specularly near grazing (perhaps because 1080 nm is before the water absorption band and water exhibits high specularly). The 1580 nm band shows more diffuse attributes at $\theta_i = \theta_r \approx 0$ (perhaps because of water absorption). It can be seen that the diffuse reflectance component is commonly the smallest for 1580 nm and the largest for 850 nm.

Lastly, the melanin content and hair coverage of the human skin being measured influences the BRDF values. In Figures 40-45, wavelength trends correspond to estimated skin type. Subject 1, Subject 2, and Subject 3 (Type II-III Skin Type), Subject 5 and 6 (Type I-II Skin Type), and Subject 4 (Type V Skin Type) each respectively share a similar wavelength dependence, with similar magnitude order and grouping of BRDF values. More specifically for melanin dependency, comparing a Type-I/II - low hair coverage subject (Subject 5) to a Type-V - low hair coverage subject (Subject 4), the diffuse and off-grazing BRDF measurements are much larger for a lighter skinned individual. Additionally, it should be noted that there is less of a wavelength dependence for the diffuse and off-grazing BRDF measurements for darker skinned

individuals, especially among 540 nm, 660 nm, and 1580 nm. As for hair coverage, when comparing Subject 5 and Subject 6, both exhibiting low amounts of melanin, it is apparent that the high hair coverage in Subject 6 significantly decreases BRDF measurements in the near grazing scenarios (perhaps because there is more hair located on the outer edge of the forearm where grazing angles were captured).

4.4 Effects on Skin Detection

The important conclusion to make in this research is how the BRDF skin measurements affect skin detection efforts. This section presents an application-based interpretation of the results presented in the previous section. In skin detection applications, there are typically three objects essential to the efforts: the sun (light source), exposed human face (target), and camera (multispectral detection system). The effects of the BRDF measurements on the NDSI and NDGRI features (discussed in Section 2.4.2 and Section 2.5.2) are presented followed by example imaging scenarios.

4.4.1 Effect on Skin Detection Features.

After seeing the trends in BRDF skin measurements, it is important to see its effects on the post-processing skin detection algorithms. More specifically, the effects on the Normalized Difference Skin Index (NDSI) and the Normalized Difference Green Red Index (NDGRI). Using Equation (8) and Equation (9) from Section 2.5.2, plots are generated for each of the subjects with the data from their respective bands. Figures 56-58 show the NDSI and NDGRI calculations for Subject 4, Subject 5, and Subject 6 (for plots of remaining subjects, see Figures 130-132 in Appendix A):

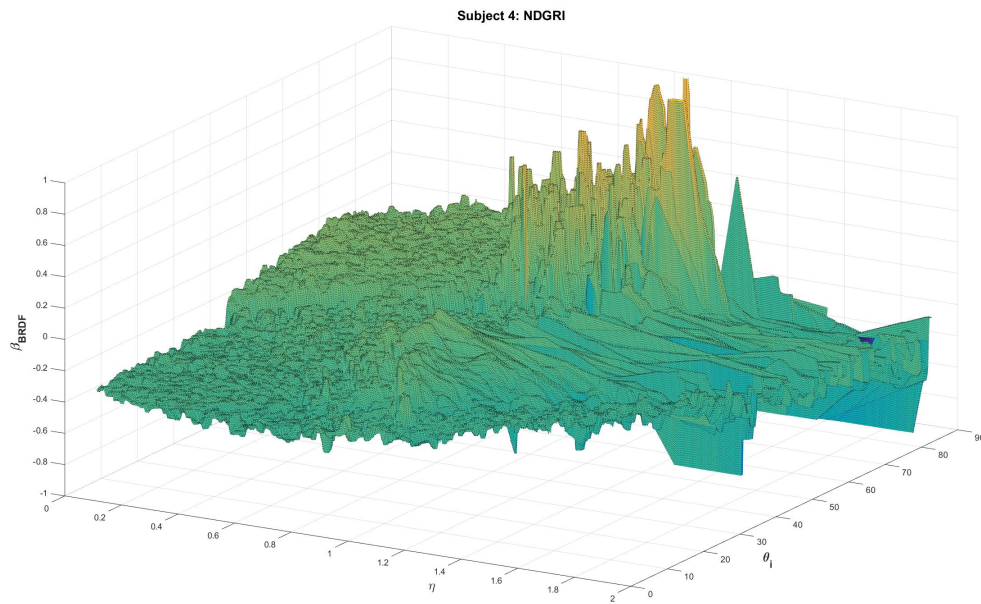
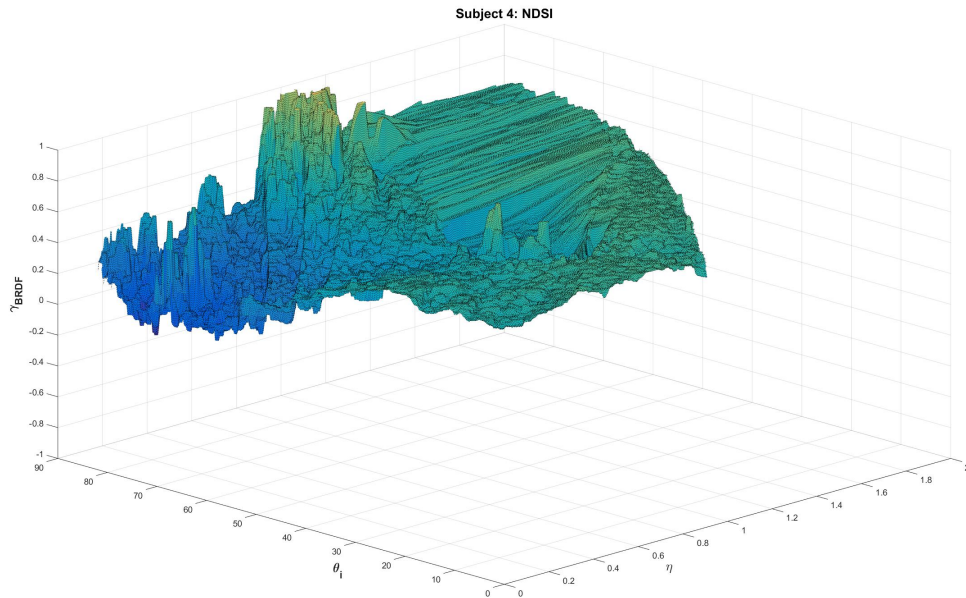


Figure 56. NDSI and NDGRI calculations from Subject 4 data.

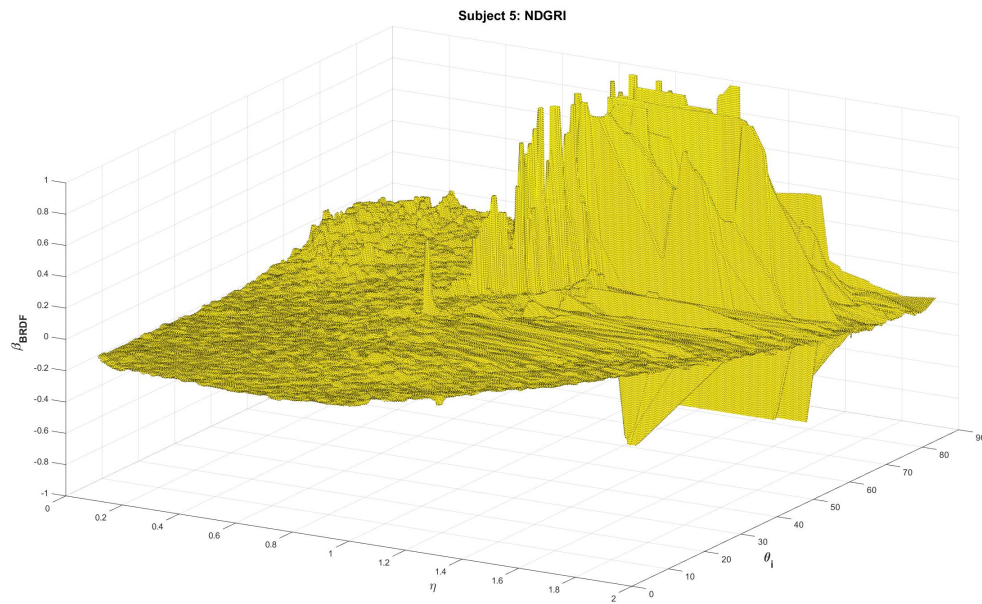
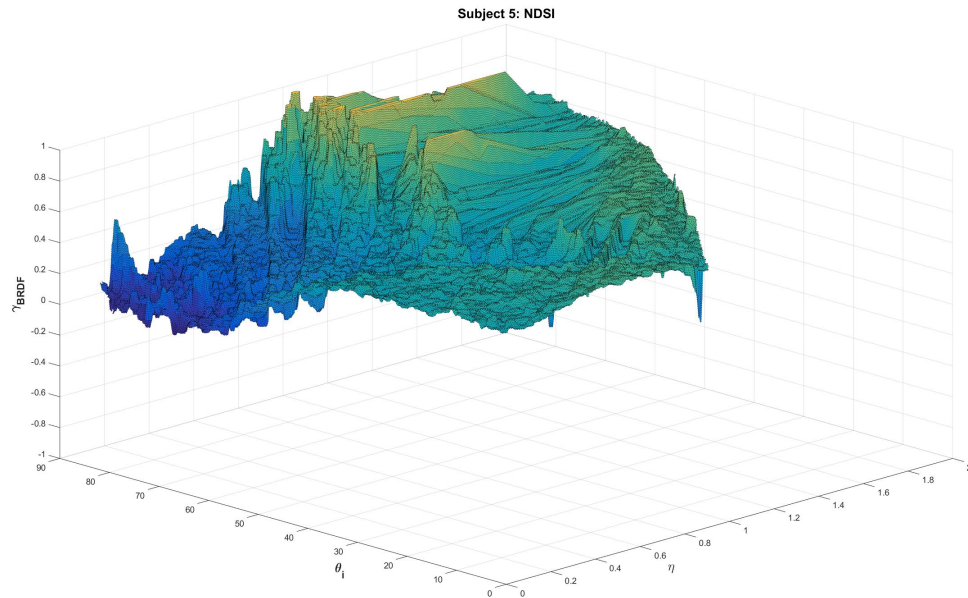


Figure 57. NDSI and NDGRI calculations from Subject 5 data.

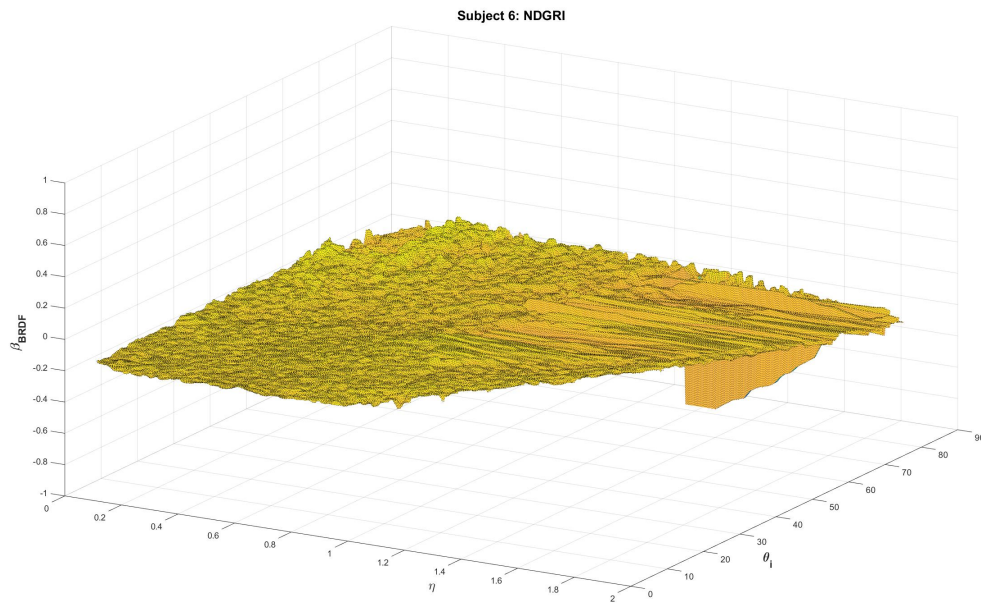
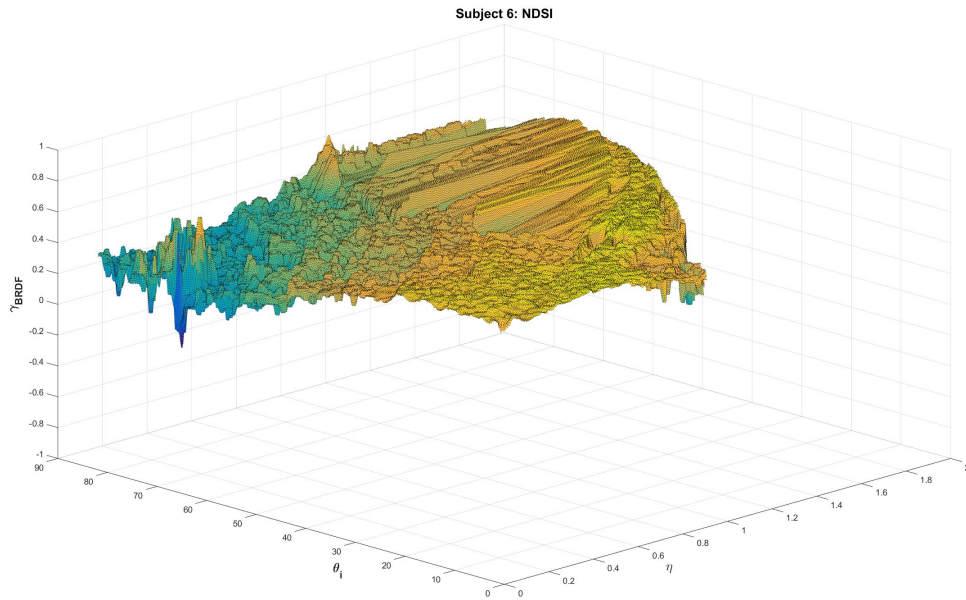


Figure 58. NDSI and NDGRI calculations from Subject 6 data.

NDSI and NDGRI results show some interesting and noteworthy trends that can be related back to previous examples of (NDSI, NDGRI) feature spaces. First, NDSI BRDF values (γ_{BRDF}) tend to match closely to what is typically seen in a 2D feature space such as that shown in Figure 10 in Section 2.5.1. That being said, these NDSI results show where the spread in values is coming from. Focusing on the specular component, NDSI values near the surface intersection of the γ_{BRDF}, θ_i -plane, the range of NDSI values is primarily between 0 and 0.7. The specular effects on Subject 4, 5, and 6 features are better seen in Figures 59-61, where NDSI and NDGRI values are computed with BRDF values for all $\theta_i = \theta_r$ forward-scattering combinations (for plots of remaining subjects, see Figures 133-135 in Appendix A). These specular feature plots were generated with the mean of the first 50 samples slices from the η -plots where η values are between 0 and 0.2.

Subject 4: Specular Component Plots (Mean of first 50 sample slices at η values near 0)

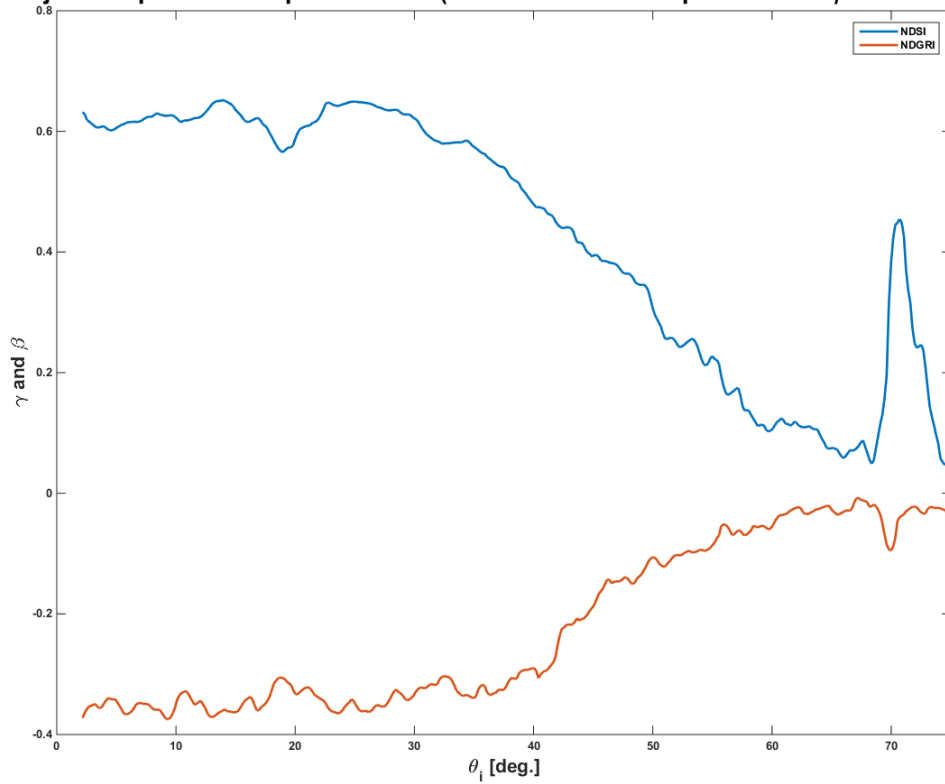


Figure 59. Subject 4 - NDSI and NDGRI values for all $\theta_i = \theta_r$ forward-scattering combinations.

Subject 5: Specular Component Plots (Mean of first 50 sample slices at η values near 0)

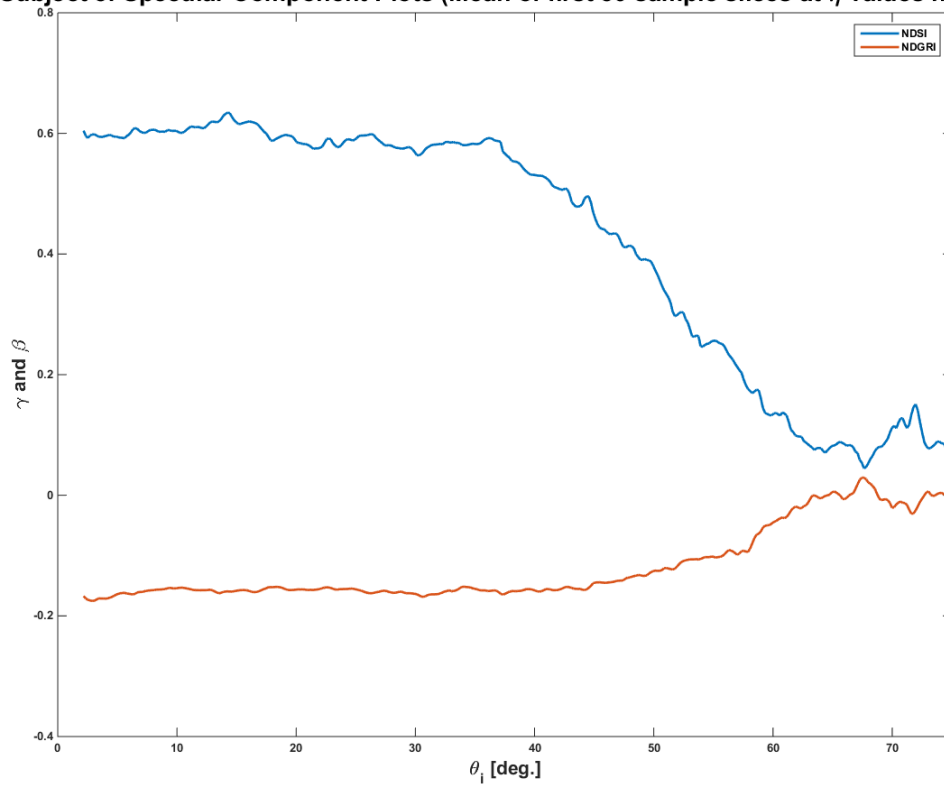


Figure 60. Subject 5 - NDSI and NDGRI values for all $\theta_i = \theta_r$ forward-scattering combinations.

Subject 6: Specular Component Plots (Mean of first 50 sample slices at η values near 0)

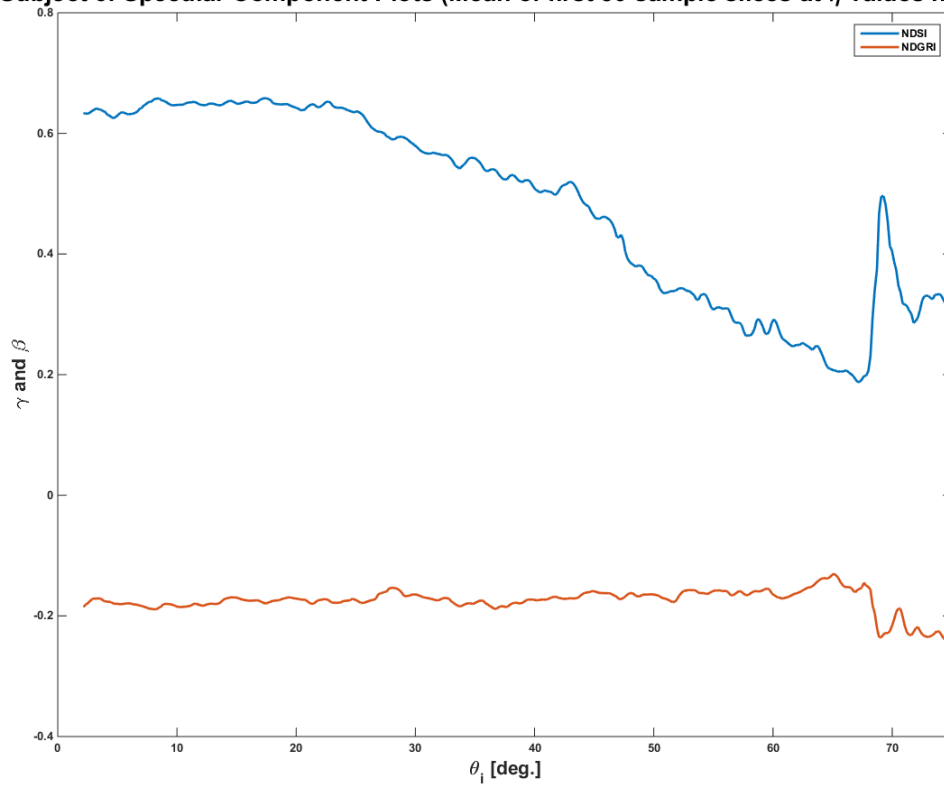


Figure 61. Subject 6 - NDSI and NDGRI values for all $\theta_i = \theta_r$ forward-scattering combinations.

At η values greater than zero (diffuse component), the majority of the surface values are near γ_{BRDF} values between 0.5 and 0.6, which explains the dense clustering at $NDSI(\gamma) = 0.5 - 0.6$ in Figure 10 and Figure 11 from Section 2.5.1 and Section 2.5.2, respectively. Lower values between 0 and 0.2 occur near grazing angles, where θ_i and θ_r approach 90 degrees at $\phi_r = 180$. Some anomalies are also apparent from negative BRDF values calculated from ELM and errors in the forearm edge detection due to hair or background materials. Figures 62-64 show both the diffuse and specular NDSI results, where three ranges for θ_i values are evaluated at ϕ_r close to 180 degrees and plotted in NDSI vs θ_r space (for plots of remaining subjects, see Figures 136-138 in Appendix A). For normal incidence, values stay high at all reflected angles. For 35-40 degree incidence, better results occur at normal observation than at specular, and results worsen at grazing observation. For grazing incidence, NDSI values go to zero at specular and results get better as observation moves to normal.

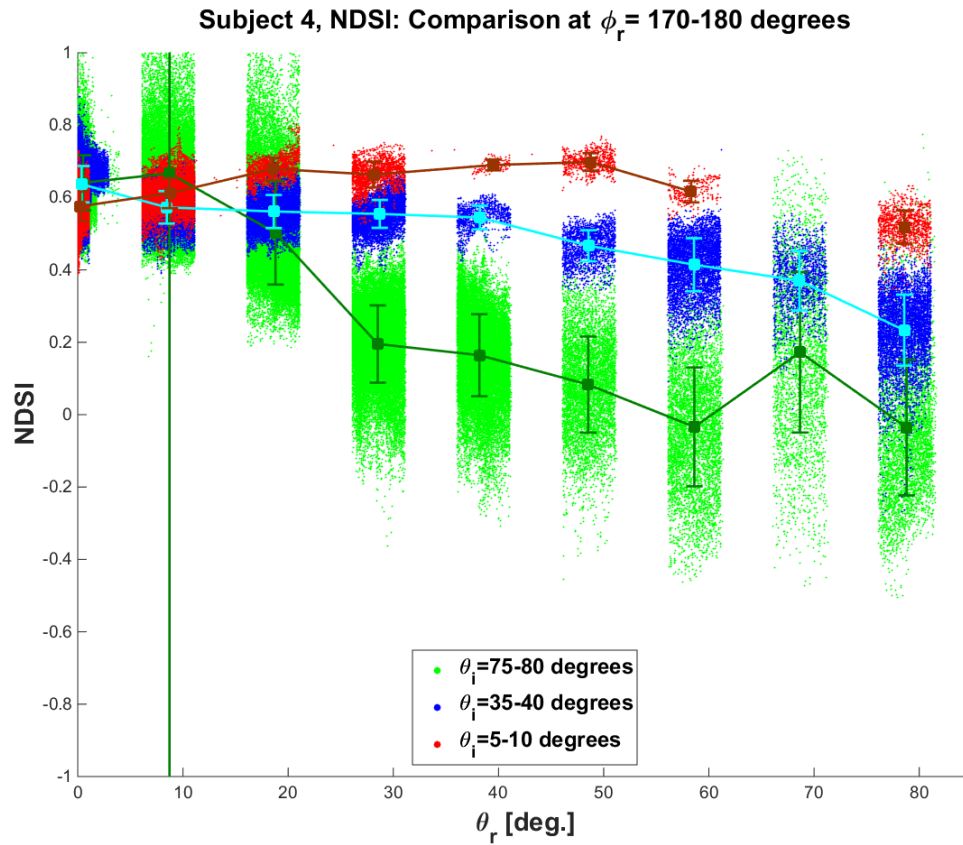


Figure 62. Three ranges for θ_i values are evaluated at ϕ_r close to 180 degrees and plotted in NDSI vs θ_r space for Subject 4.

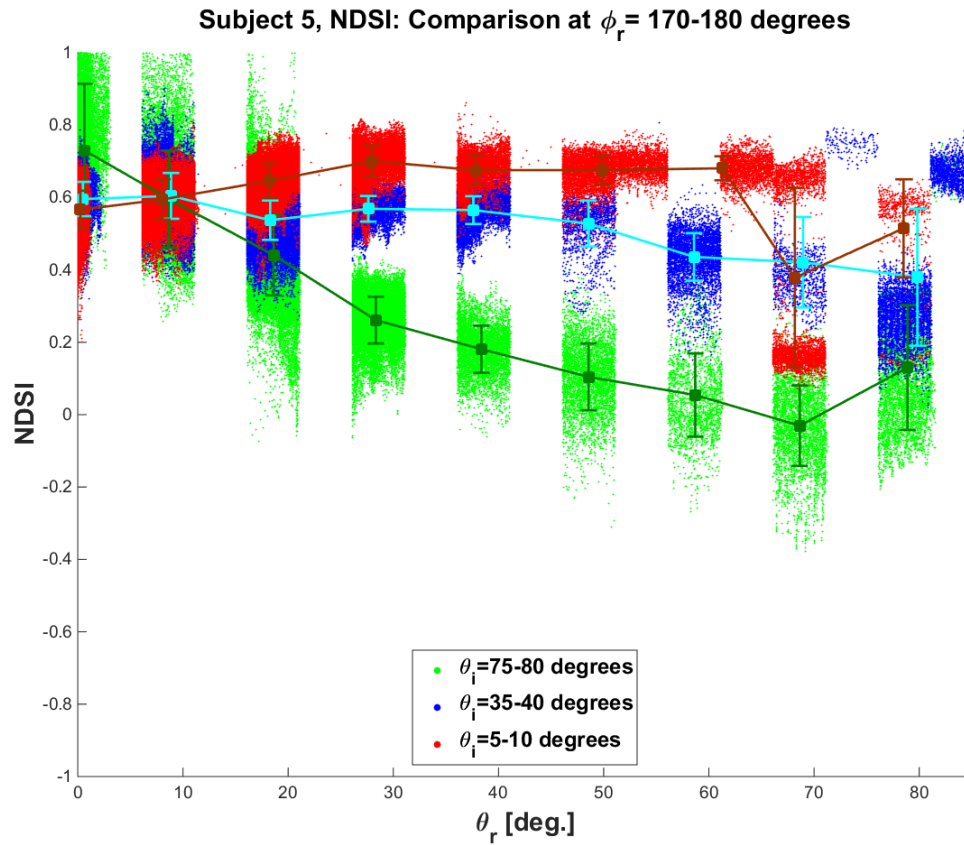


Figure 63. Three ranges for θ_i values are evaluated at ϕ_r close to 180 degrees and plotted in NDSI vs θ_r space for Subject 5.

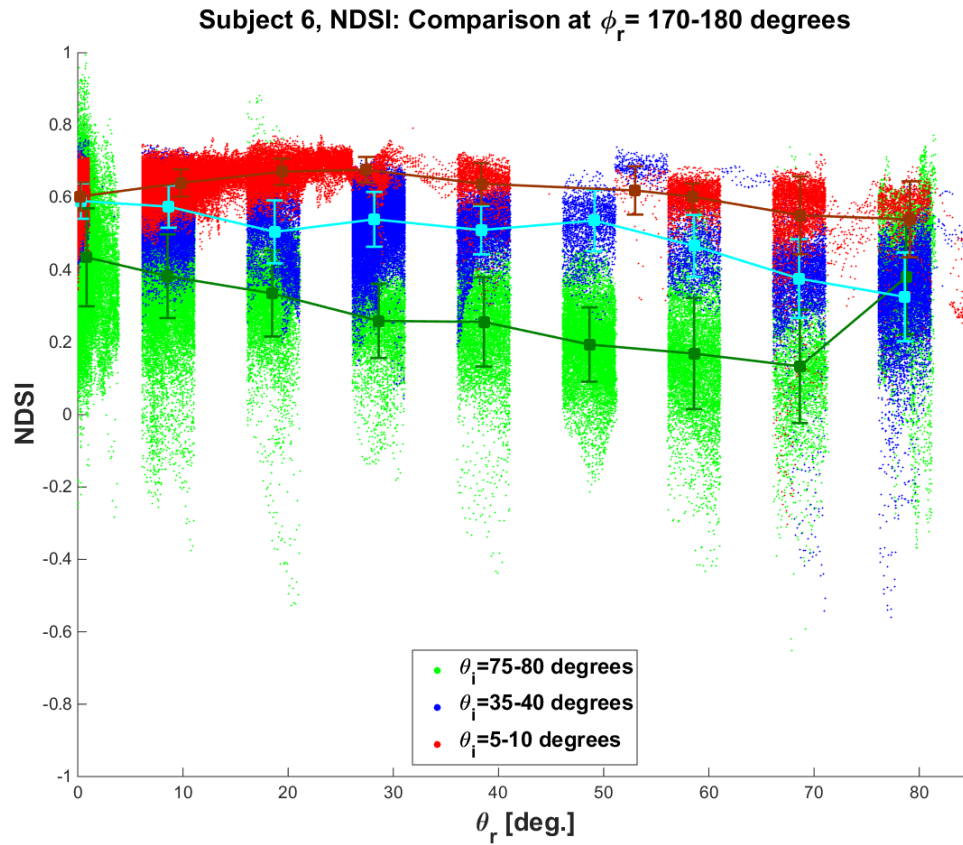


Figure 64. Three ranges for θ_i values are evaluated at ϕ_r close to 180 degrees and plotted in NDSI vs θ_r space for Subject 6.

NDGRI values exist between -0.4 and 0, with NDGRI values closer to -0.4 for higher melanin content subjects such as Subject 4. This is consistent with results obtained in Figures 10 and 11, which contain human subjects with Fitzpatrick Skin Types as dark as V/VI. The highest NDGRI values approaching zero occur near grazing angles, where θ_i and θ_r approach 90 degrees at $\phi_r = 180$. The dense cluster seen in Figures 10 and 11 corresponds to the diffuse measurements seen in the plots at η values greater than zero. The NDGRI samples that are -0.2 or lower are results from direct backscatter scenarios where $\theta_i = \theta_r = 0$, as well as, darker skinned individuals in a variety of other angular scenarios seen in Subject 4's results. Anomalies are also present, occurring from negative BRDF values calculated from ELM and errors in the forearm edge detection due to hair or background materials. These anomalies are most commonly located at the edge of low sampled areas beyond $\eta = 0.8$ and $\theta_i = 50$ degrees. Figures 65-67 show both the diffuse and specular NDGRI results, where three ranges for θ_i values are evaluated at ϕ_r close to 180 degrees and plotted in NDGRI vs θ_r space (for plots of remaining subjects, see Figures 139-141 in Appendix A). The majority of NDGRI results would lead to good detection, with the exception of scenarios where the angle of incidence is far off normal and observation near grazing.

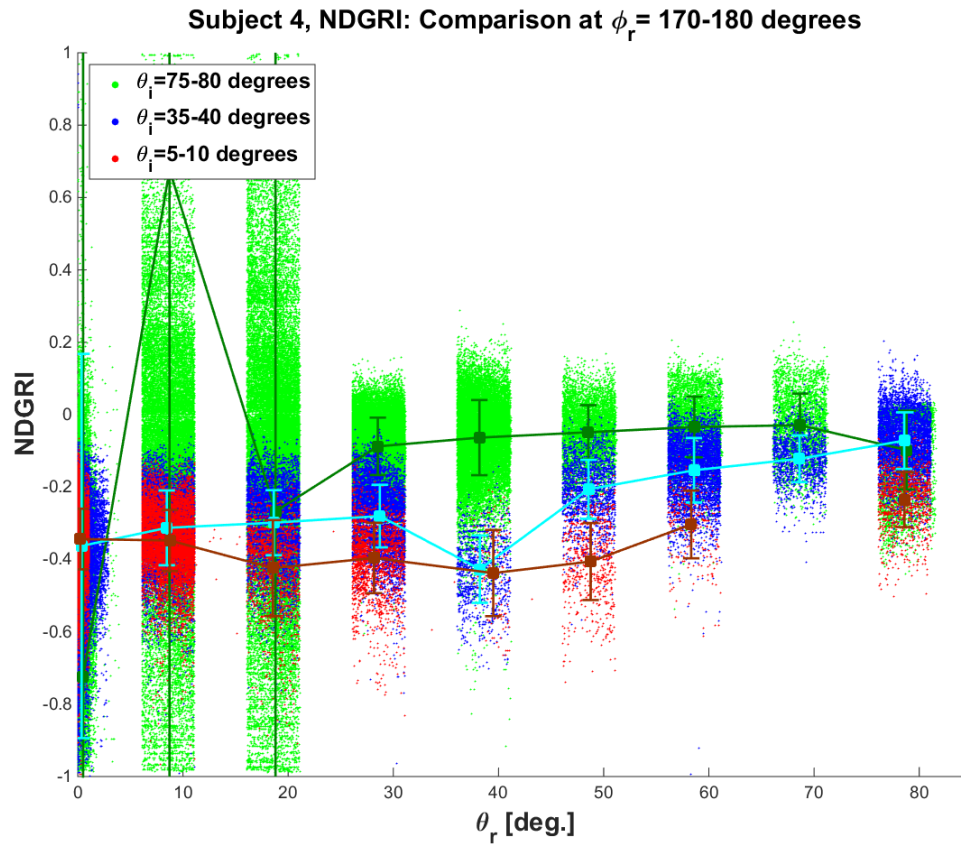


Figure 65. Three ranges for θ_i values are evaluated at ϕ_r close to 180 degrees and plotted in NDGRI vs θ_r space for Subject 4.

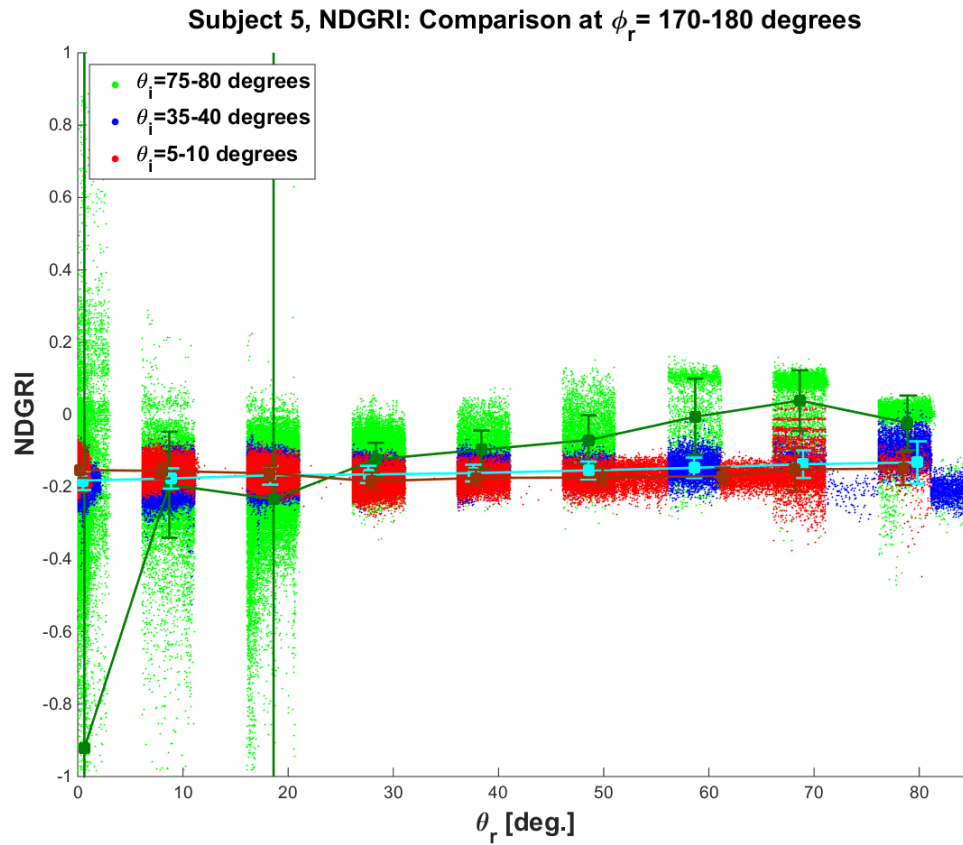


Figure 66. Three ranges for θ_i values are evaluated at ϕ_r close to 180 degrees and plotted in NDGRI vs θ_r space for Subject 5.

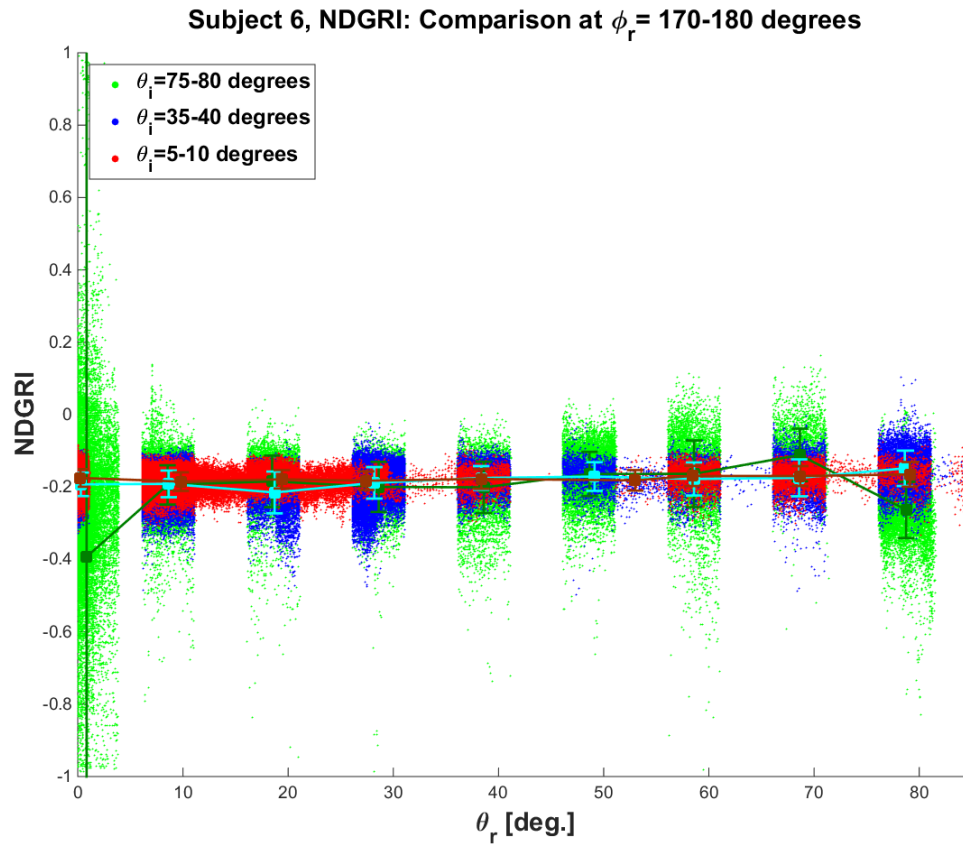


Figure 67. Three ranges for θ_i values are evaluated at ϕ_r close to 180 degrees and plotted in NDGRI vs θ_r space for Subject 6.

Next, the NDSI and NDGRI values are plotted in (NDSI, NDGRI) space to see the direct comparison between the results and previous measurements such as those from Figures 10 and 11. As a sanity check, a comparison between the image-based BRDF measurements and spectrometer data is completed. In order to compare the image-based BRDF measurements with spectrometer data, results are extracted from the identical imaging scenario, where $\theta_i \approx 12$ degrees, $\theta_r \approx 35$ degrees, and $\phi_r \approx 0$ degrees (the inner geometry of the ASD FieldSpec[®] 3 hand-held contact probe). Figure 68 shows overlaying measurements from [28] (a collection from Figure 11) with data obtained under the same geometry in this study. Results show comparable clustering reassuring the validity of the data obtained in this study.

Lastly, Figures 69-74 show both the diffuse and specular (NDSI, NDGRI) feature space results, where three ranges for θ_i values are evaluated at ϕ_r close to 180 degrees for nine groupings of θ_r . These (NDSI, NDGRI) feature space results match the spread typically seen in previous 2D feature space plots like Figure 10.

(NDSI, NDGRI) Spectrometer vs Image-Based Data Comparison at $\theta_i=10-15^\circ$, $\phi_r=0-5^\circ$, $\theta_r=32-37^\circ$

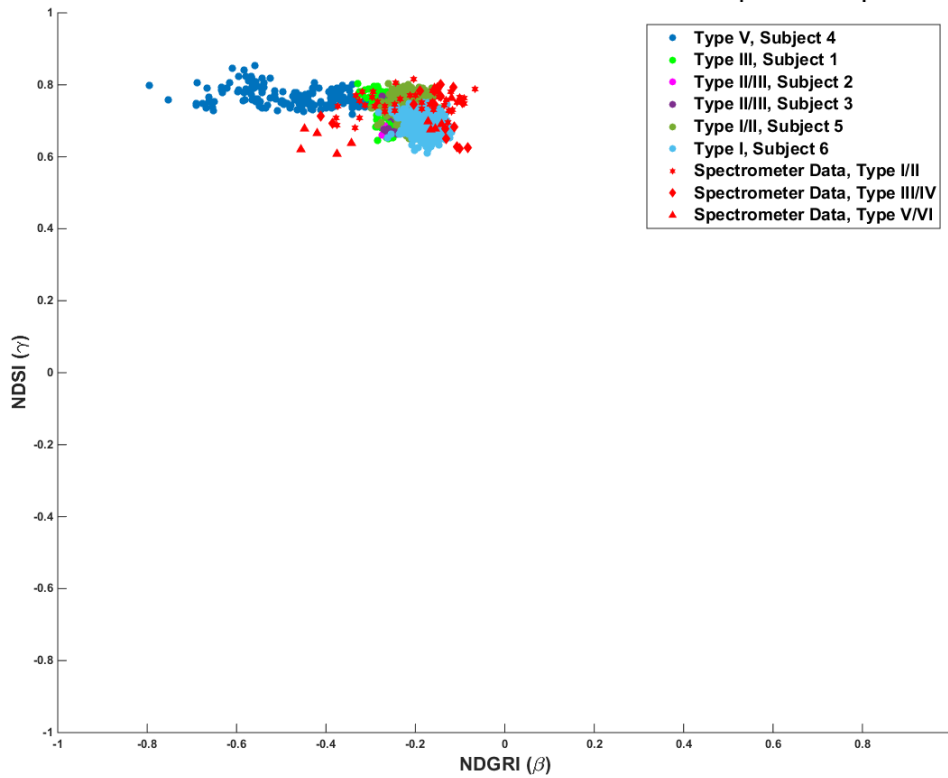


Figure 68. Spectrometer measurements from [28] (red) overlaid on data obtained in this study. Both sets of data are from the identical imaging scenario, where $\theta_i \approx 12$ degrees, $\theta_r \approx 35$ degrees, and $\phi_r \approx 0$ degrees.

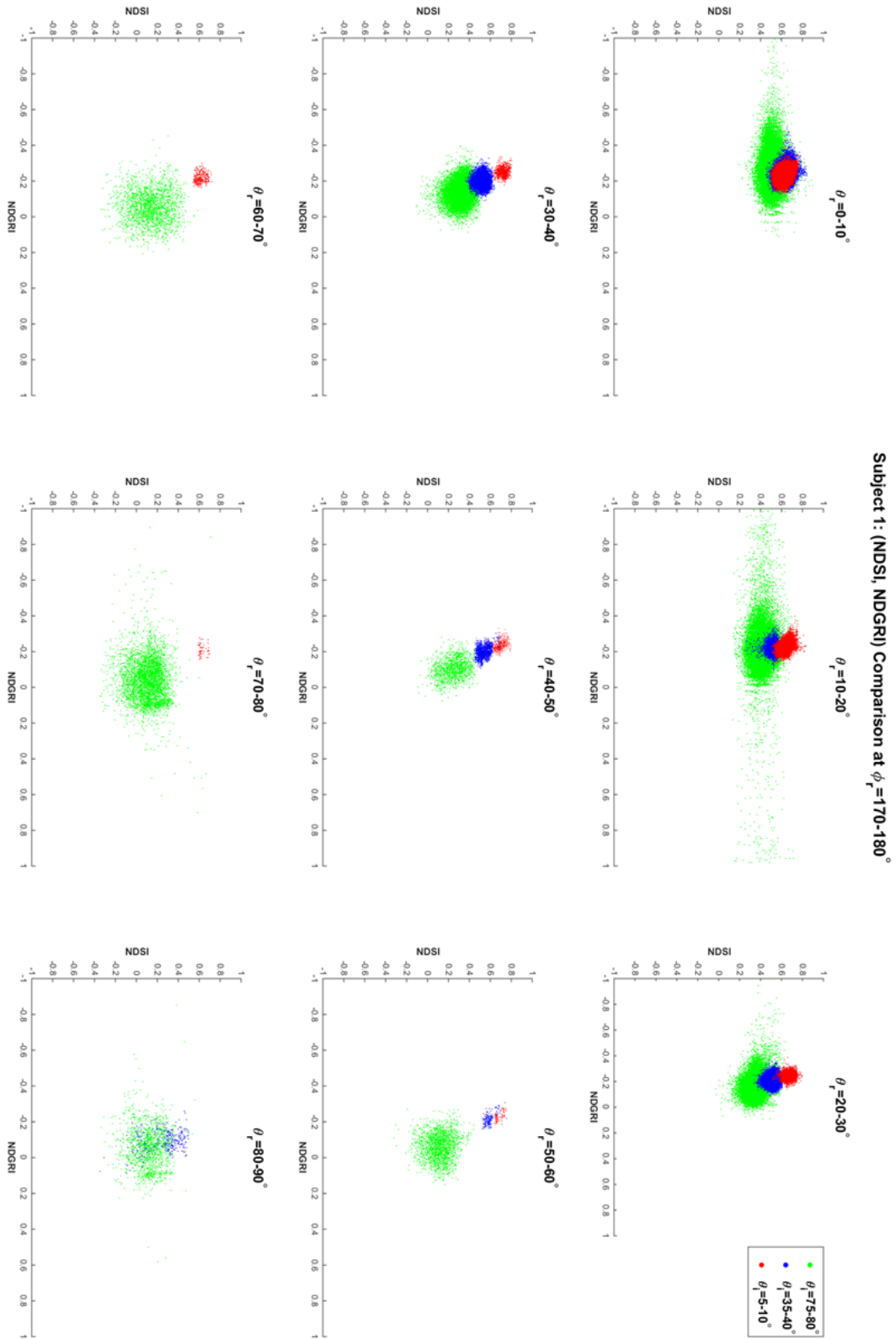


Figure 69. Subject 1 - (NDSI, NDGRI) feature space plots where three ranges for θ_i values are evaluated at ϕ_r close to 180 degrees for nine groupings of θ_r .

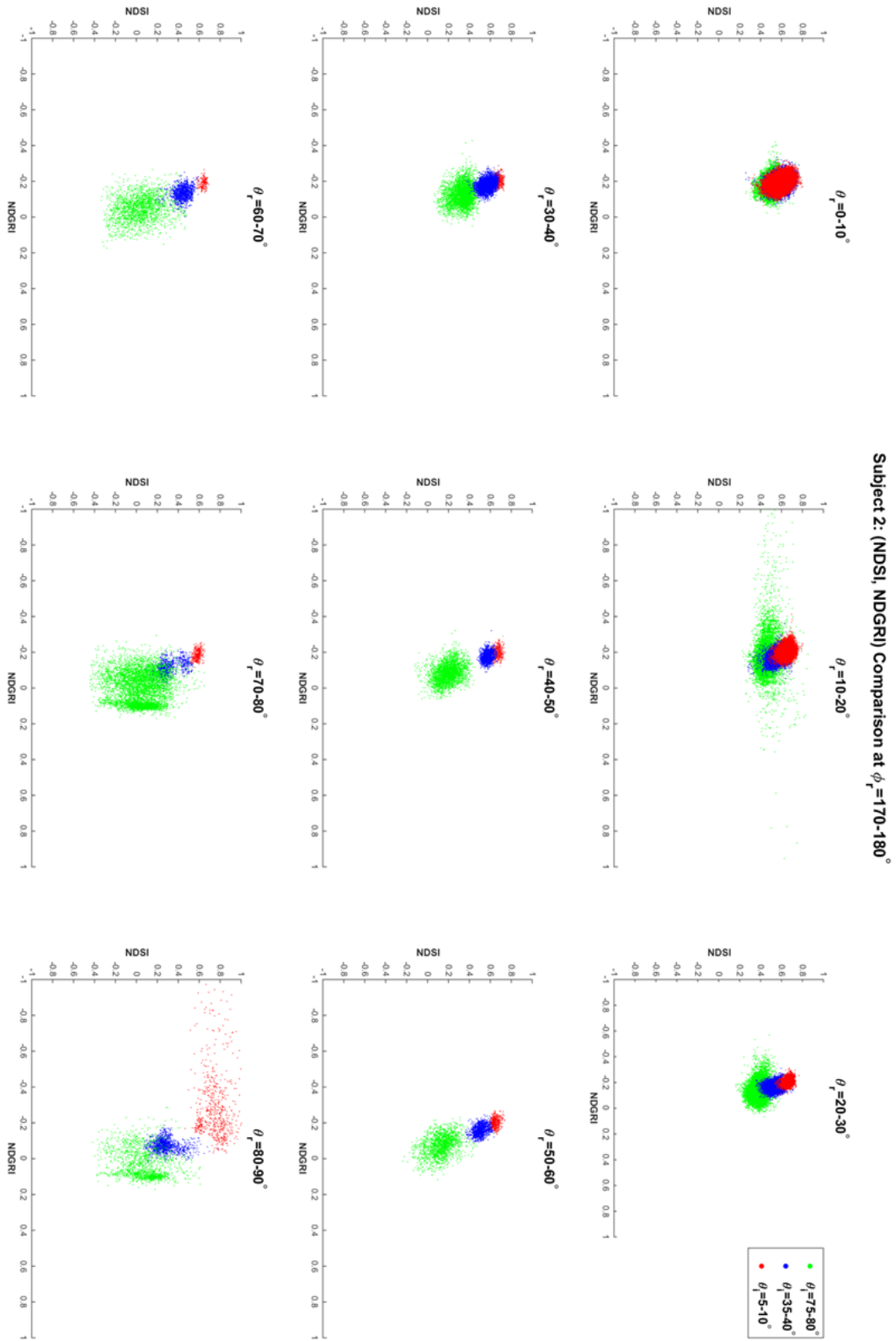


Figure 70. Subject 2 - (NDSI, NDGRI) feature space plots where three ranges for θ_i values are evaluated at ϕ_r close to 180 degrees for nine groupings of θ_r .

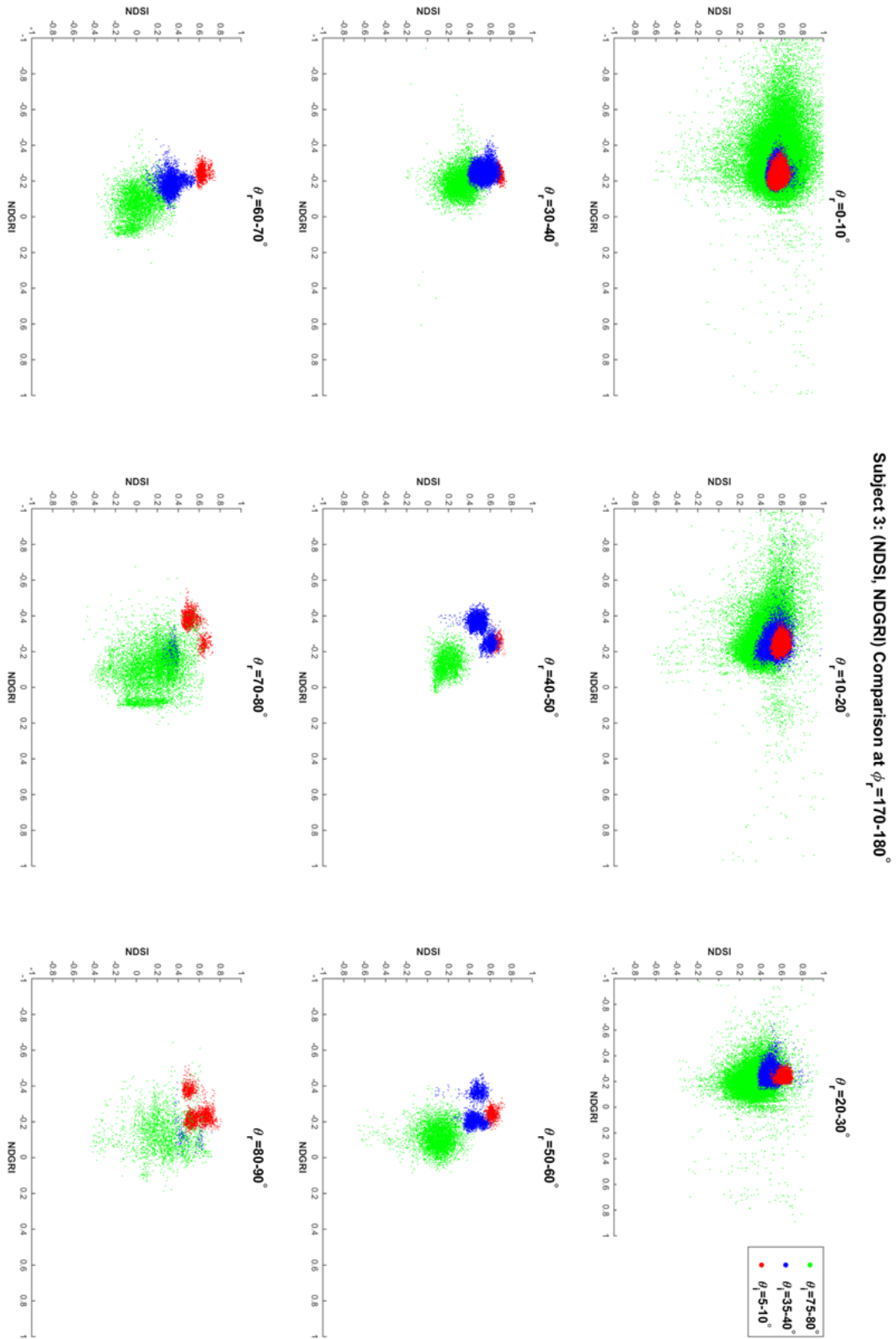


Figure 71. Subject 3 - (NDSI, NDGRI) feature space plots where three ranges for θ_i values are evaluated at ϕ_r close to 180 degrees for nine groupings of θ_r .

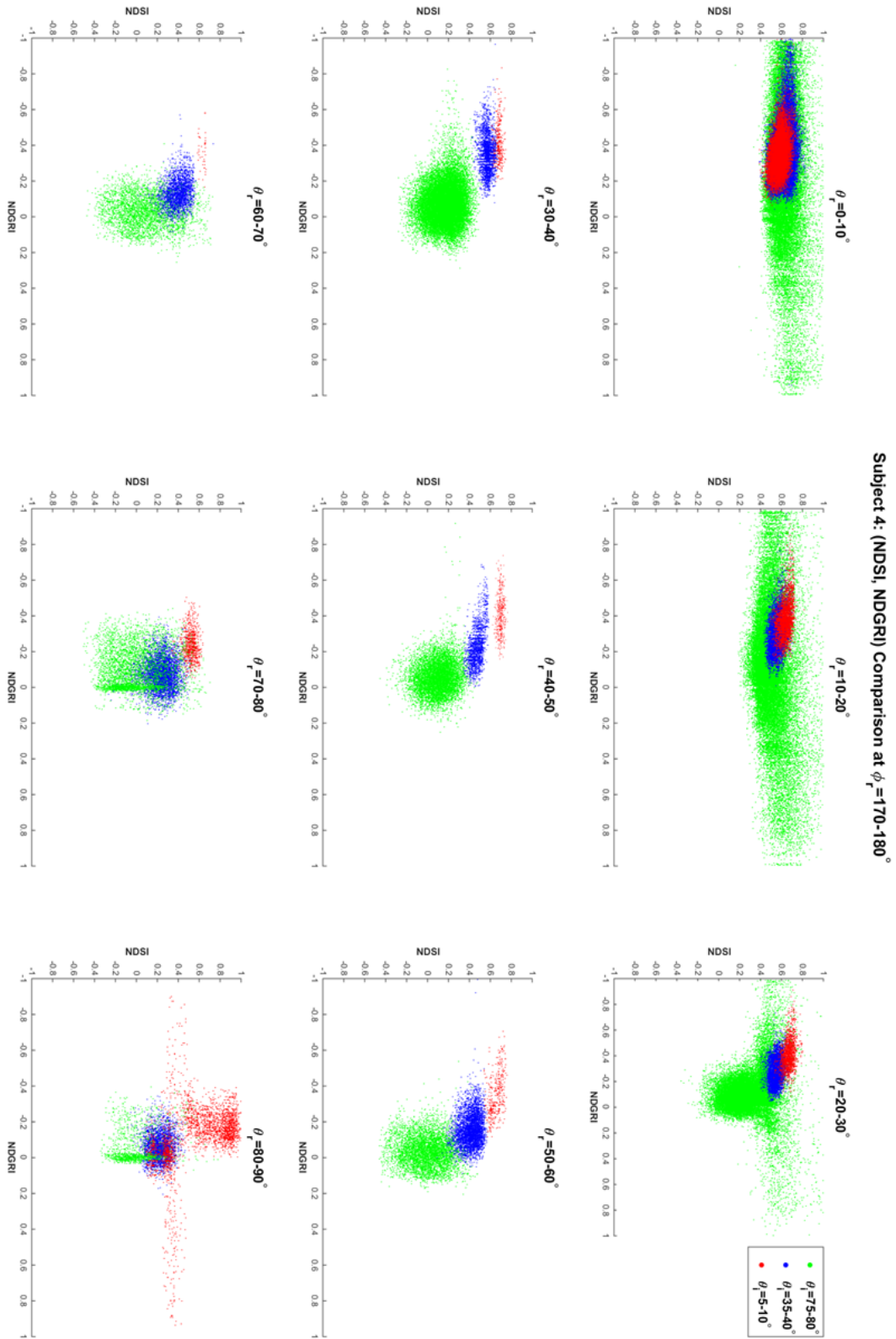


Figure 72. Subject 4 - (NDSI, NDGRI) feature space plots where three ranges for θ_i values are evaluated at ϕ_r close to 180 degrees for nine groupings of θ_r .

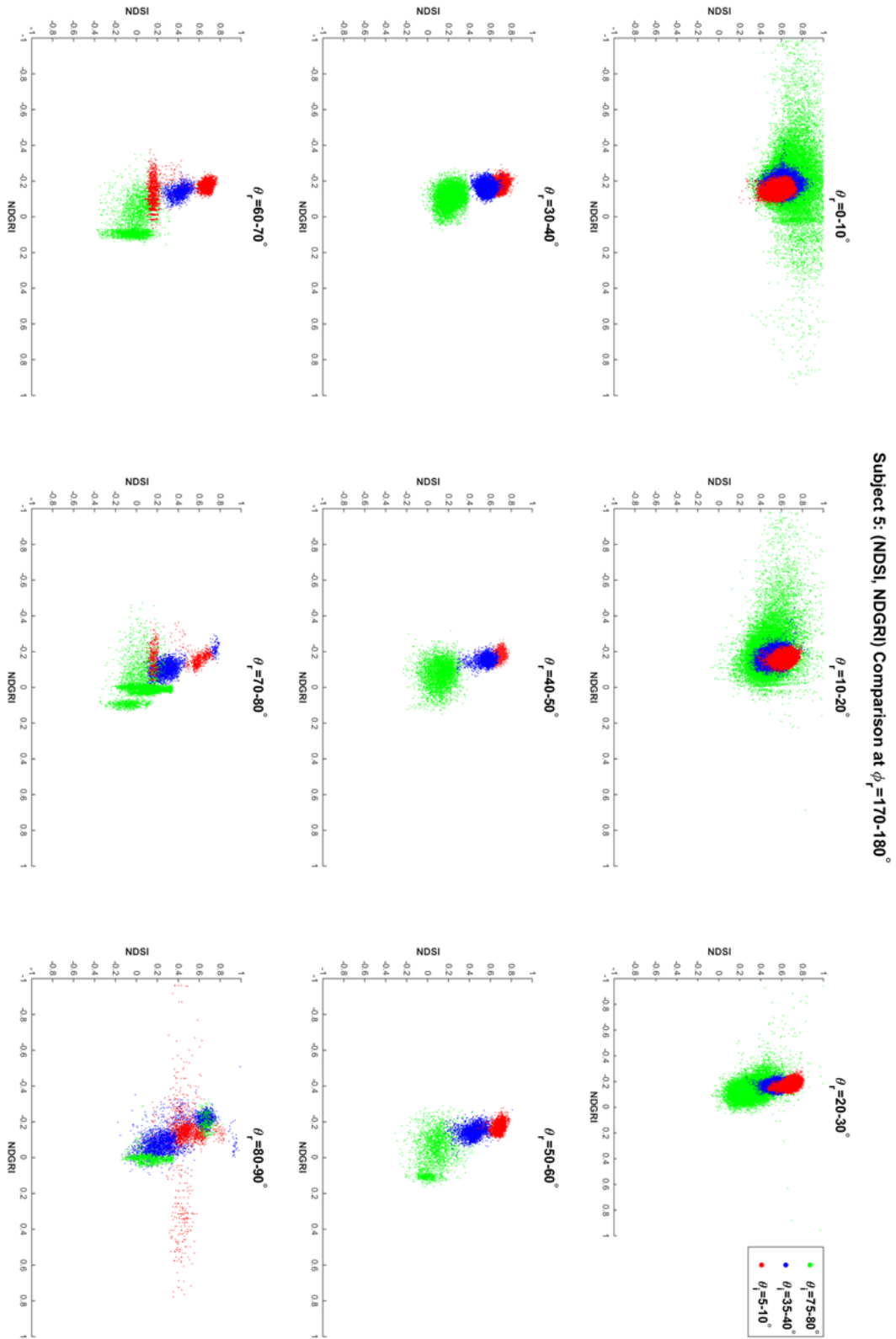


Figure 73. Subject 5 - (NDSI, NDGRI) feature space plots where three ranges for θ_i values are evaluated at ϕ_r close to 180 degrees for nine groupings of θ_r .

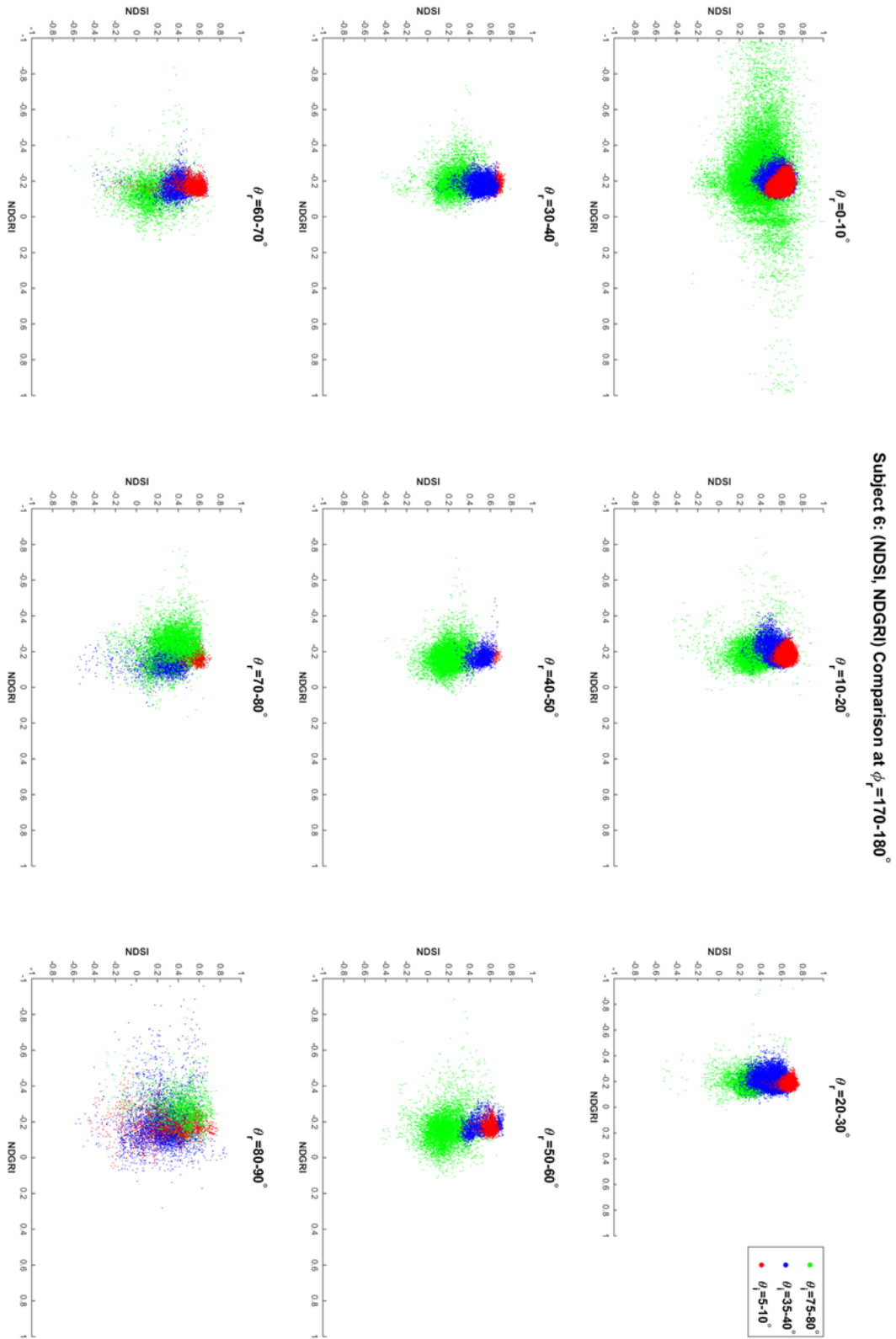


Figure 74. Subject 6 - (NDSI, NDGRI) feature space plots where three ranges for θ_i values are evaluated at ϕ_r close to 180 degrees for nine groupings of θ_r .

4.4.2 Evaluating BRDF effects in Typical Imaging Scenarios.

The first scenario is an overhead imaging effort with the sun location directly above a standing human target. From interpreting the BRDF skin measurements, this is a unique imaging scenario worth studying based on the magnitude of reflectance values that would be obtained. A standing human target's exposed facial features would have a large distribution of surface normals directed the way the individual is facing. This configuration can be seen in Figure 75, Illustration A. In this scenario, most of the incident light is approximately 90 degrees off zenith relative to the majority of surface normals ($\theta_i=90$). The BRDF measurements concluded that near these grazing angles most of the BRDF distribution is concentrated in the specular lobe, which in this scenario is scattered into the ground at reflected angles of 90 degrees off zenith relative to the forward facing surface normals and 180 degrees out of phase from the incident light ($\theta_r=90$ degrees, $\phi_r=180$ degrees). That being said, the imager would be collecting values corresponding to the significantly deflated diffuse reflectance component.

The second scenario is similar to the first. Instead of overhead imaging, this is a ground imaging scenario where the sun is located directly above a standing human target seen in Figure 75, Illustration B. Similar to the first scenario, the imager would be collecting values corresponding to a deflated diffuse reflectance component. With the majority of the light reflecting into the ground, the remaining distribution is relatively low. This includes angles shown in this configuration where the camera is directly in front of the human target ($\theta_r=0$, $\phi_r=180$). This effect can be seen in Figures 46-50 for θ_i range 75-80 degrees near θ_r values of zero. For Subject 5 (Type-I/II skin), the imager would collect skin values of approximately 0.1 sr^{-1} or below based on the BRDF values on the plots. Based on Figures 69-74, the pixel cluster for this scenario in (NDSI, NDGRI) space would be very close to the diffuse

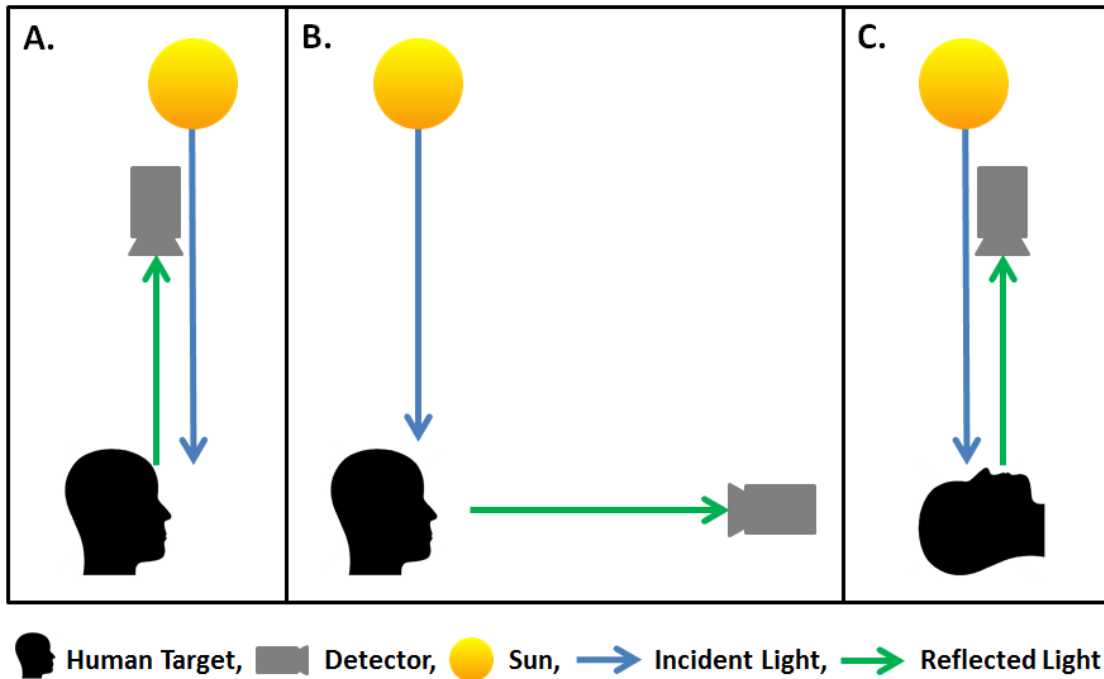


Figure 75. Three possible imaging scenarios: A) Overhead imaging configuration of a standing human target with the sun directly above target, B) Ground imaging configuration of a standing human target with the sun directly above target, C) Overhead imaging configuration of a lying human target with the sun directly above target.

measurements obtained from a spectrometer.

The third imaging scenario results in larger reflectance values received by the detection system. The third scenario is an overhead imaging effort where the sun is located directly above a human target laying on their back, shown in Figure 75, Illustration C. In this scenario, the imager is collecting reflectance values from a direct backscatter where the incident sunlight and reflected sunlight is approximately 0 degrees off zenith relative to the majority of upward facing surface normals ($\theta_i=\theta_r=0$ degrees, $\phi_r=0/180$). Based on the BRDF skin measurements, these reflectance values would be relatively high (BRDF values in Figures 40-45 at θ_i values near zero). This phenomena can also be seen in Figures 46-50 for θ_i range 5-10 degrees near θ_r values of zero. For Subject 5 (Type-I/II skin) at 540nm, the imager would be collecting BRDF values as large as 0.5 sr^{-1} . Based on Figures 69-74, the pixel cluster for this scenario in (NDSI, NDGRI) space would be very close to the diffuse measurements obtained from a spectrometer. This brings into question which imaging scenarios affect detection results the most.

These imaging scenarios are three specific configurations out of a countless number of possible combinations. The sun isn't often directly above the target of interest. Many times the sun is rising or setting and out of phase, azimuthally, from the imager. For example, the closer the sun is to the horizon, the closer you get to a configuration such as that in Figure 75, Illustration C rotated 90 degrees, where a ground imager is imaging a standing human target with a setting/rising sun. Based on Figures 69-74, the imaging scenarios that would result in misdetections are in forward scattering configurations where incident light and reflected light are far off-normal (θ_r and θ_i greater than 35 degrees). Figure 76 shows incident and reflected light in a range of example imaging scenarios that may lead to misdetections. In the figure, as the ray combinations get darker, the farther away the resulting pixel cluster in (NDSI,

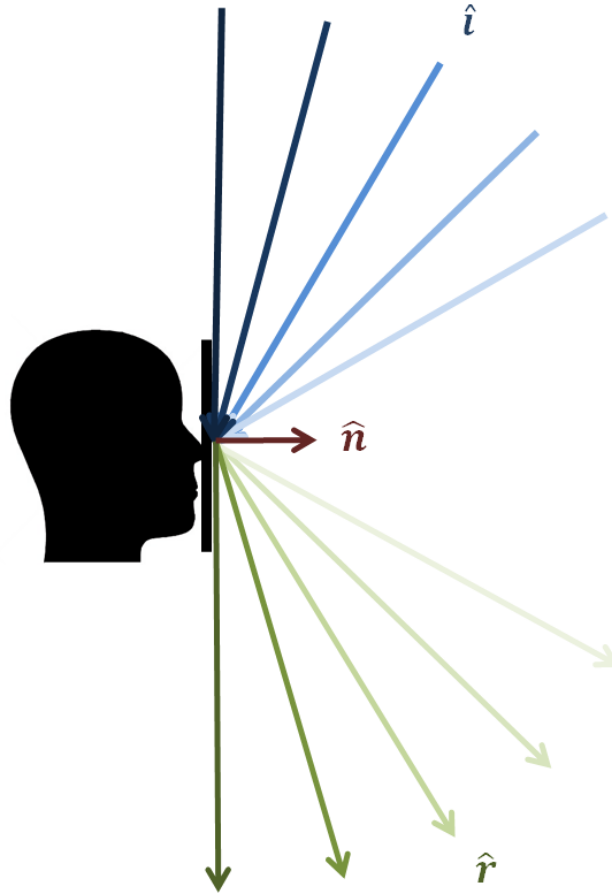


Figure 76. Incident light (blue) and reflected light (green) scenarios that may lead to misdetections. As the ray combinations get darker, the farther away the resulting pixel cluster in (NDSI, NDGRI) space will deviate from other data, e.g., the diffuse data obtained with a spectrometer.

NDGRI) space will deviate from other data, e.g., the diffuse data obtained with a spectrometer. Ideally, calculated NDSI and NDGRI values would remain between $[0.6, 0.8]$ and $[-0.4, 0]$, respectively. As the reflectance characteristics converge in different scenarios between 540 nm and 660 nm and/or 1080 nm and 1580 nm, the normalized differences will decrease towards zero, mixing in with background pixels and causing misdetections and false-alarms.

4.5 Summary

Chapter IV presented the experimental setup, the image-based BRDF skin measurements, and how the results influence skin detection. The experimental setup was presented to give the reader an understanding of the extent and environment of the data collection process. Next, modified Beckmann-Kirchhoff theory was briefly discussed in order to proceed forward with formulation used in the presentation of the BRDF skin measurements. The BRDF skin measurements were presented and the results were interpreted with respect to their dependence on angular configuration, skin's melanin content/hair coverage, and wavelength bands. Finally, the chapter concluded with a relation between the acquired BRDF skin measurements, (NDGRI, NDSI) feature space, and typical imaging scenarios. Results in Chapter IV confirmed the assumption and motivation of these efforts; the current skin detection algorithms are heavily influenced by melanin content (and hair coverage) and the angular location of the detector, light source, and target. At incident and reflected angles far off-normal, the reflectance characteristics converge between 540 nm and 660 nm and 1080 nm and 1580 nm. As this happens, the normalized differences will decrease towards zero, mixing in with background pixels and causing misdetections and false-alarms.

V. Conclusion

The objective of this research was to address the wide distribution of skin pixels in the (NDSI, NDGRI) feature space. Addressing this issue meant better characterizing the angular dependence of skin reflectance in changing scenarios for 540nm, 660nm, 850nm, 1080nm, and 1580nm from a variety of skin types. In order to do so, an image-based BRDF measurement system is constructed, allowing collection of skin reflectance values from a large domain of source, target, and detector locations. With the existing monocular multispectral camera system pivoting between sixteen detector locations, capturing a range of surface geometry, measurements are collected that span all wavelength and angular dependent components of human skin reflectance. That being said, in Chapter V, a summary and conclusion discusses the work accomplished addressing the objective of this thesis. Lastly, recommendations are given for future work related to the integration of the BRDF measurements and the potential for upgrades in the image-based measurement system.

5.1 Concluding Remarks

The goal of this research was to address the distributions of skin pixels in the (NDSI, NDGRI) feature space that lead to an increase in misdetection and false-alarm rates. Current detection methods base the skin pixel selection criteria on a diffuse skin reflectance assumption. However, it can be observed that human skin exhibits a combination of specular and diffuse reflectance. Since the specularity can depend on wavelength, angular, and melanin, NDSI and NDGRI values can be greatly affected in different imaging scenarios. By collecting image-based BRDF skin measurements in the VNIR bands of interest for a range of skin types and angular scenarios, an understanding of the skin pixel distributions can be experimentally derived.

In order to accomplish this goal, an image-based BRDF measurement system was constructed allowing the collection of data from a human forearm over 16 detector locations. A single light source illuminated the target and the forearm geometry was extracted through the use of a grid projection laser. The BRDF coordinates were calculated for each pixel at every detector location and paired with the corresponding estimated reflectance from each band of interest. Results were presented using a variety of plotting configurations.

Lastly, through the presentation and interpretation of data, an understanding of the data with respect to the dependence on angular configuration, skin's melanin content/hair coverage, and wavelength bands was gathered. Results of this work confirmed the wavelength and melanin dependent specularly assumptions and the motivation of this research. The current skin detection algorithms are heavily influenced by the effects from melanin, hair coverage, wavelength, and the angular location of the detector, light source, and target. Ideally, calculated NDSI and NDGRI values would be tightly clustered, between 0.6 to 0.8 and -0.4 to 0, respectively. However, as the reflectance characteristics converge in different scenarios between 540 nm and 660 nm and/or 1080 nm and 1580 nm, the normalized differences will decrease towards zero, mixing in with background pixels and causing misdetections and false-alarms. Based on the results, the imaging scenarios that typically result in misdetections are in forward scattering configurations where incident light and reflected light are far off-normal due to all wavelengths approaching a common peak near grazing.

5.2 Future Work

5.2.1 Model Incorporation.

The goal of future work is to improve the flexibility and versatility of the current skin detection system. To better detect skin, the detection algorithms must adapt and

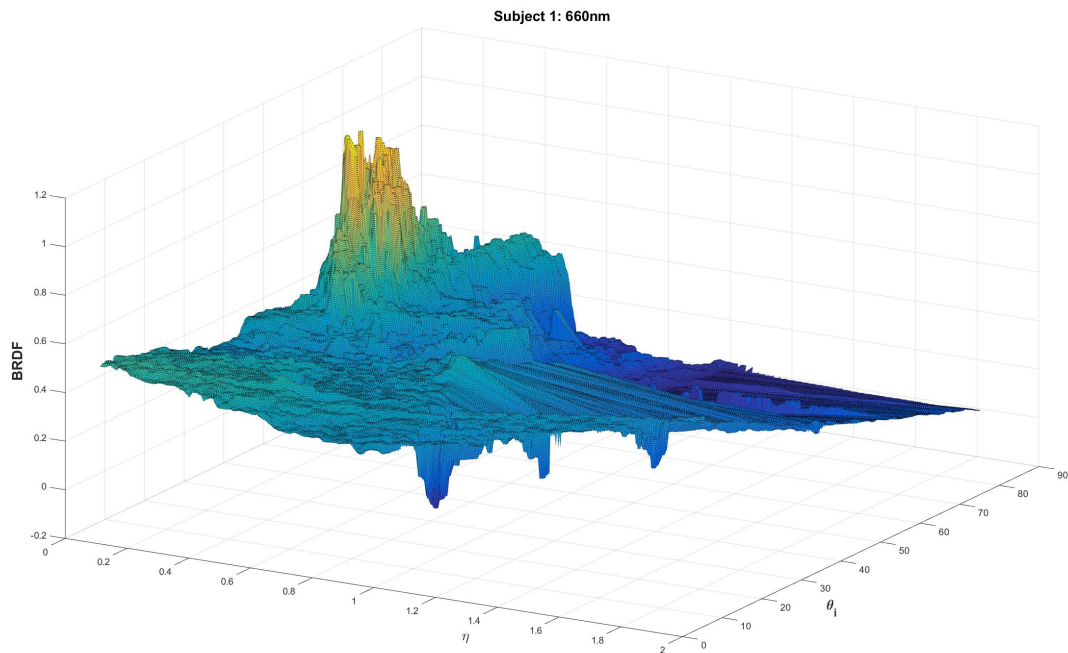
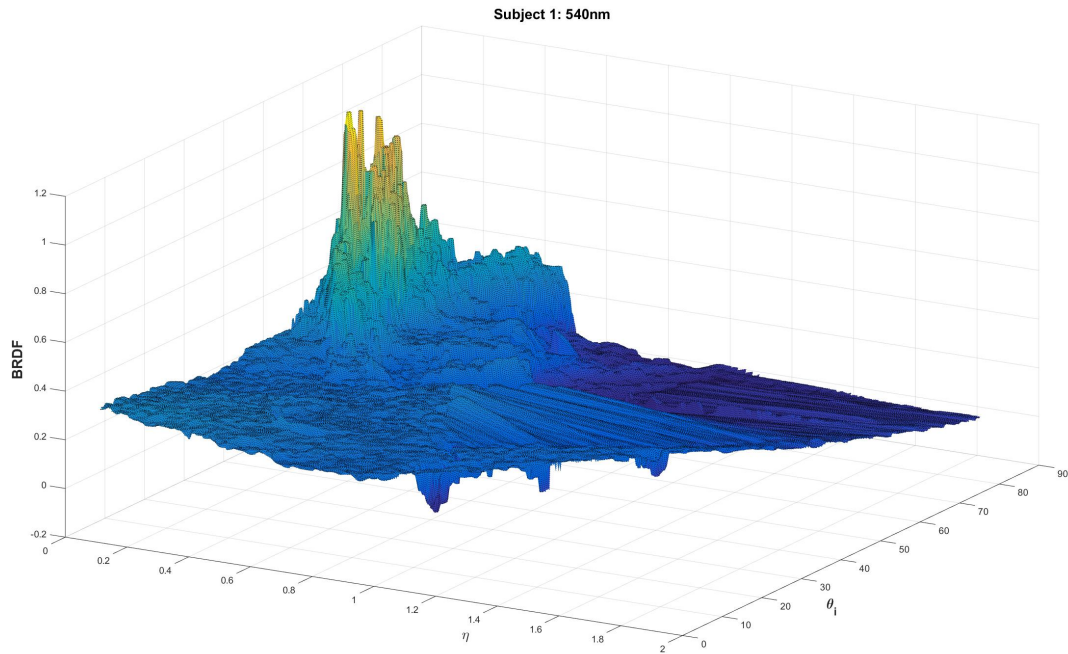
account for the causes leading to misdetections and false-alarms. In this thesis, full image-based BRDF measurements were acquired and a qualitative analysis addressing the effects of these measurements on detection results was discussed. The next step in the process is to incorporate these findings in the current skin detection algorithms. First, a BRDF model must be fit to the image-based BRDF measurements for each subject, wavelength band, and angular scenario. The Sanford-Robertson BRDF model may be an appropriate fit for these measurements. From there, the model must be categorized based on the Fitzpatrick Skin Types. Lastly, the imaging scenario and target skin type need to be an input in the detection algorithms, that is, the detector, sun, and human target orientation along with skin type will be inputted by the operator or automatically based on time of day and geographical location. These inputs will allow the system to adapt to various situations and, in turn, improve skin detection.

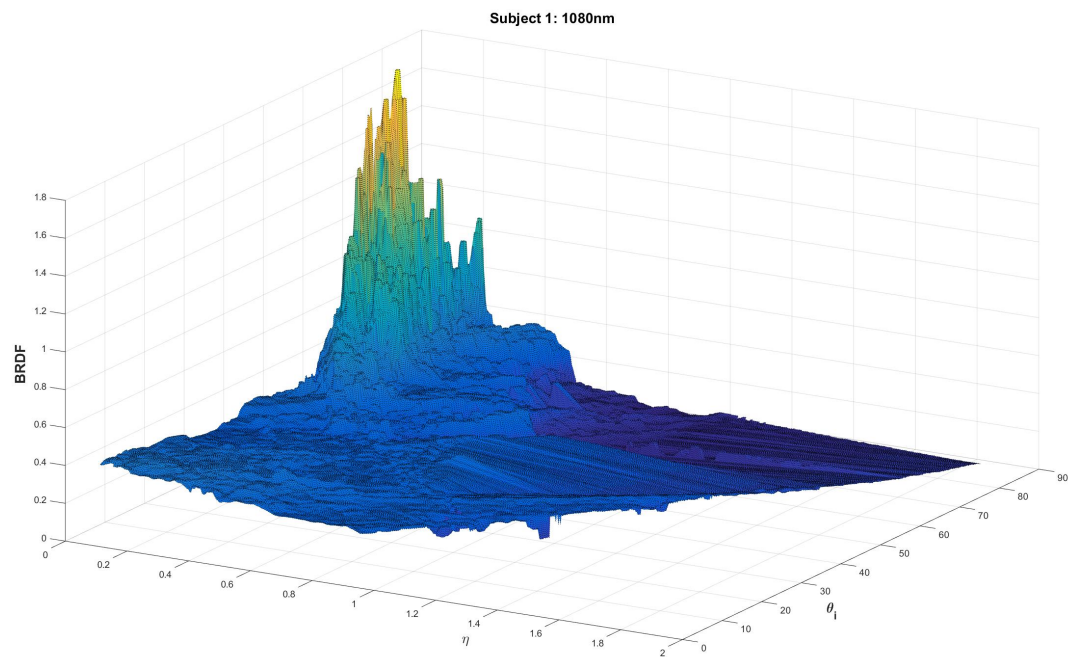
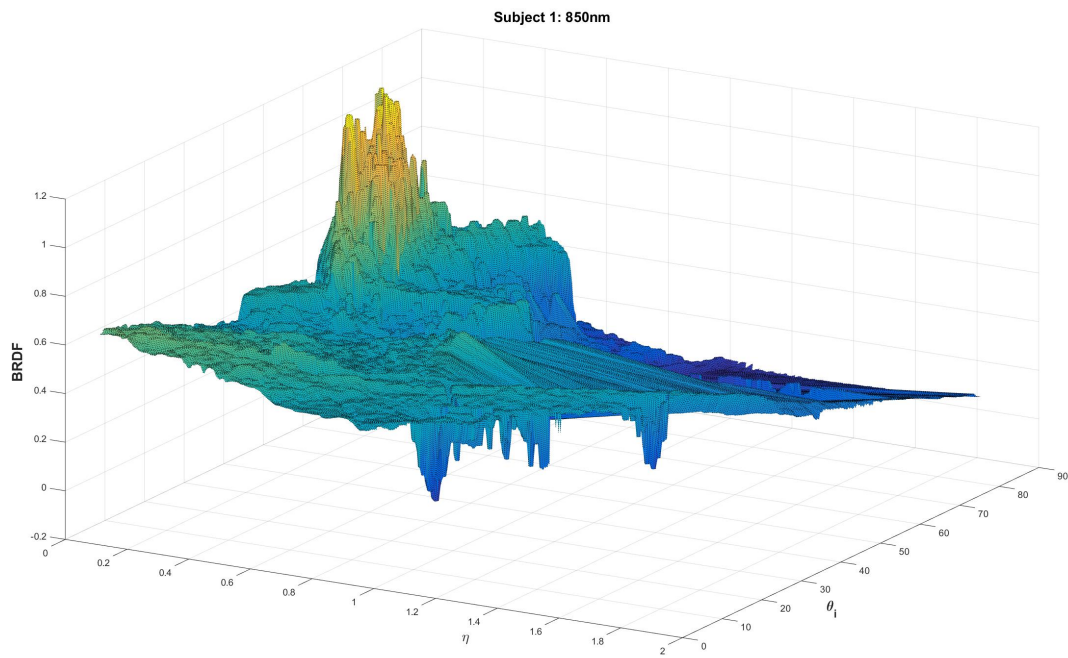
5.2.2 Image-Based BRDF Measurement System.

There are a number of improvements that can be made to the monocular multispectral camera system and image-based BRDF measurement system. The monocular multispectral camera system is a first-generation bread-board prototype, which exhibits unstable sensor and optics alignment. The next step for this camera system is to contract a professional to have the system built in a more compact and field-deployable unit. As for the image-based BRDF measurement system, there is value in attempting image-based measurements on this bench-top set up with a hyperspectral imager. Now that methodology and general software exist, the integration of a hyperspectral imager could be achieved without great effort and provide full-spectrum BRDF measurements. Lastly, the ability to collect BRDF measurements from a variety of targets is currently limited due to the constraints on the surface geometry

extraction techniques. In order to distinguish more complex geometry and orientations, the grid projection laser should be replaced by a more versatile commercial 3D scanner that can relay back precise surface geometry for the BRDF coordinate calculations.

Appendix A. Measurement Results





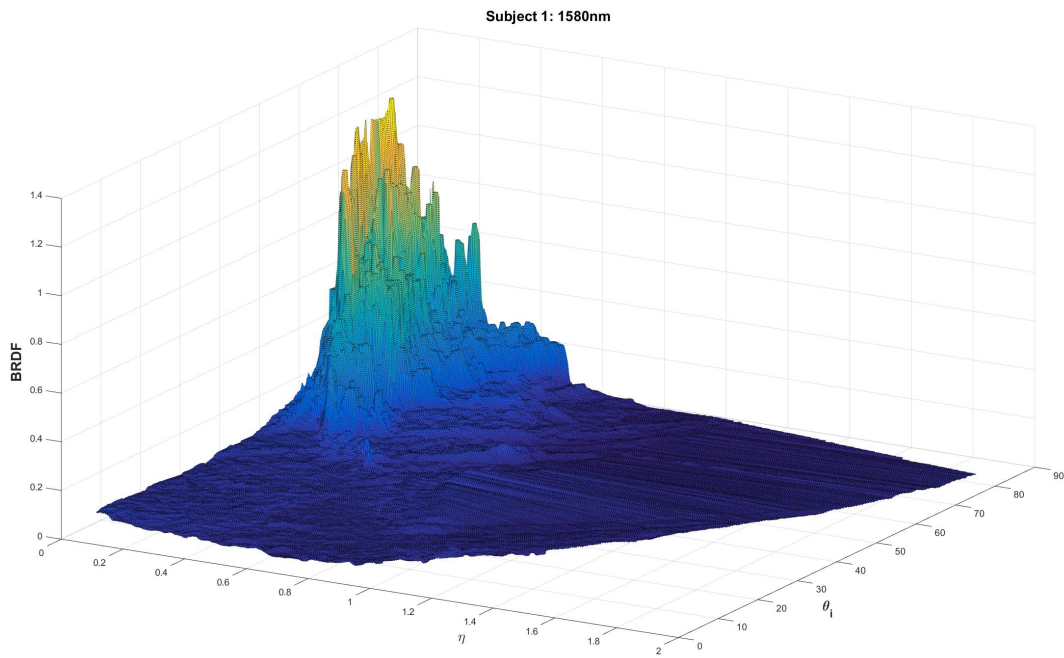
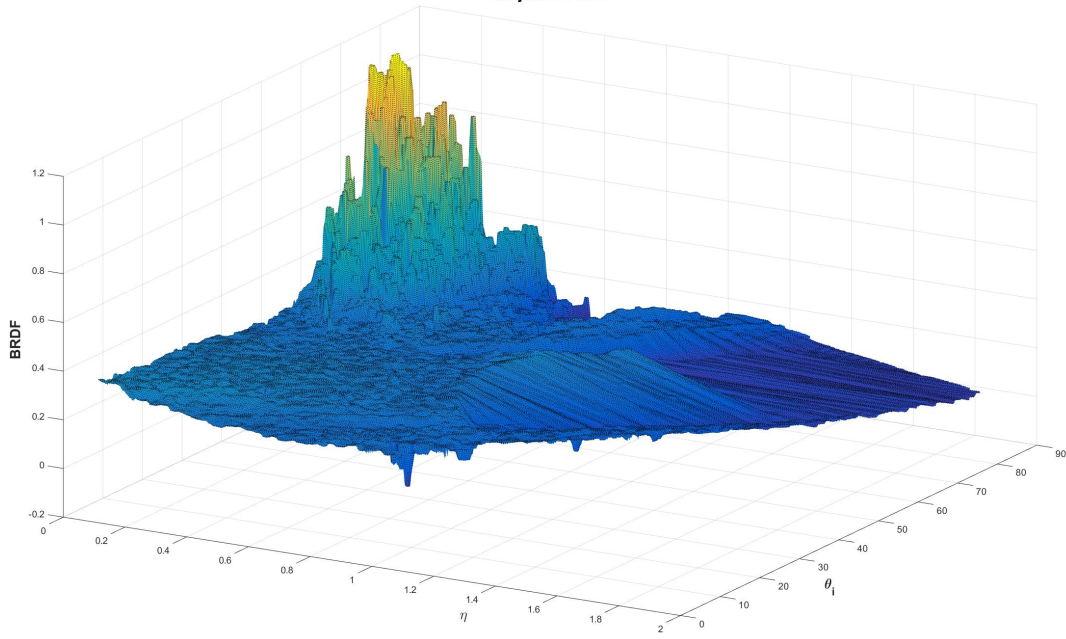
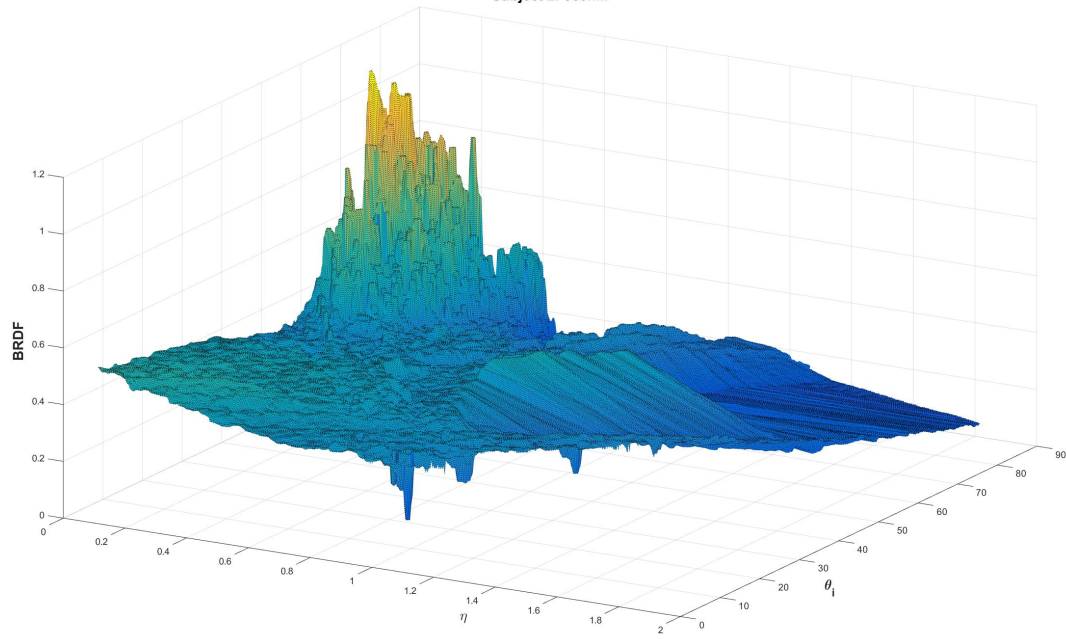


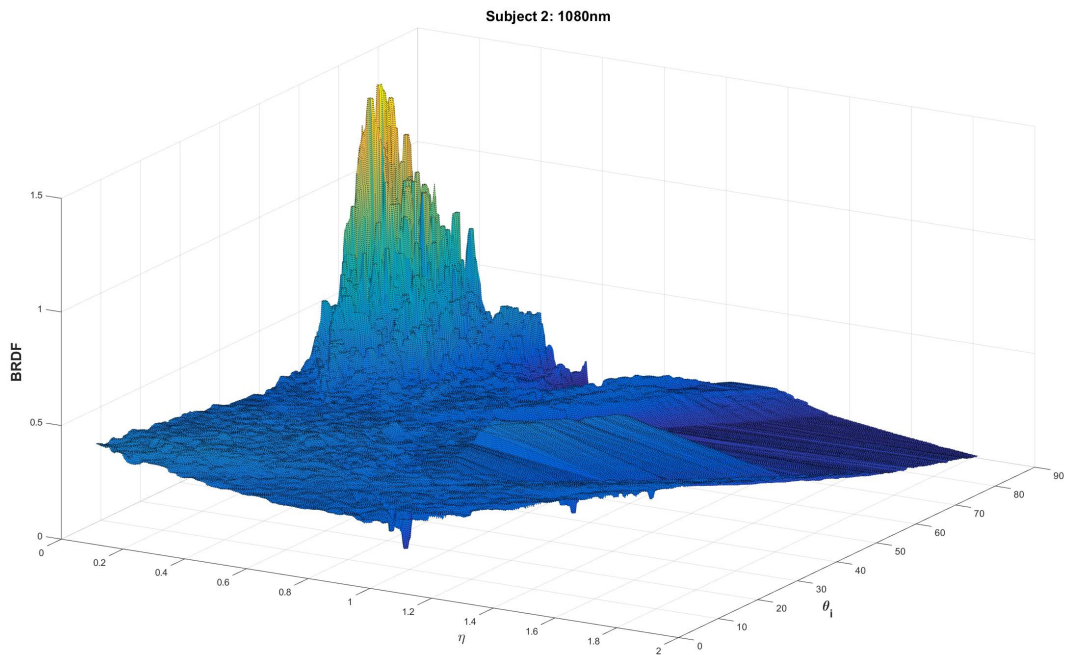
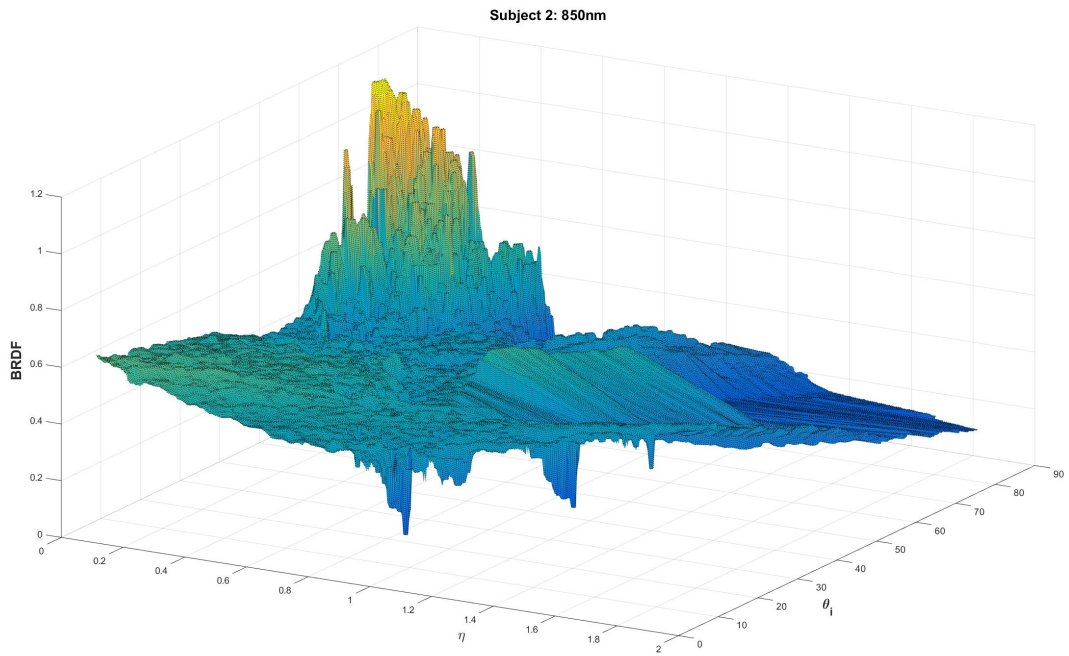
Figure 77. BRDF skin measurements obtained from Subject 1 in the 540nm, 660nm, 850nm, 1080nm, and 1580nm bands. Estimated Fitzpatrick Skin Type: III, Hair Coverage: Low.

Subject 2: 540nm



Subject 2: 660nm





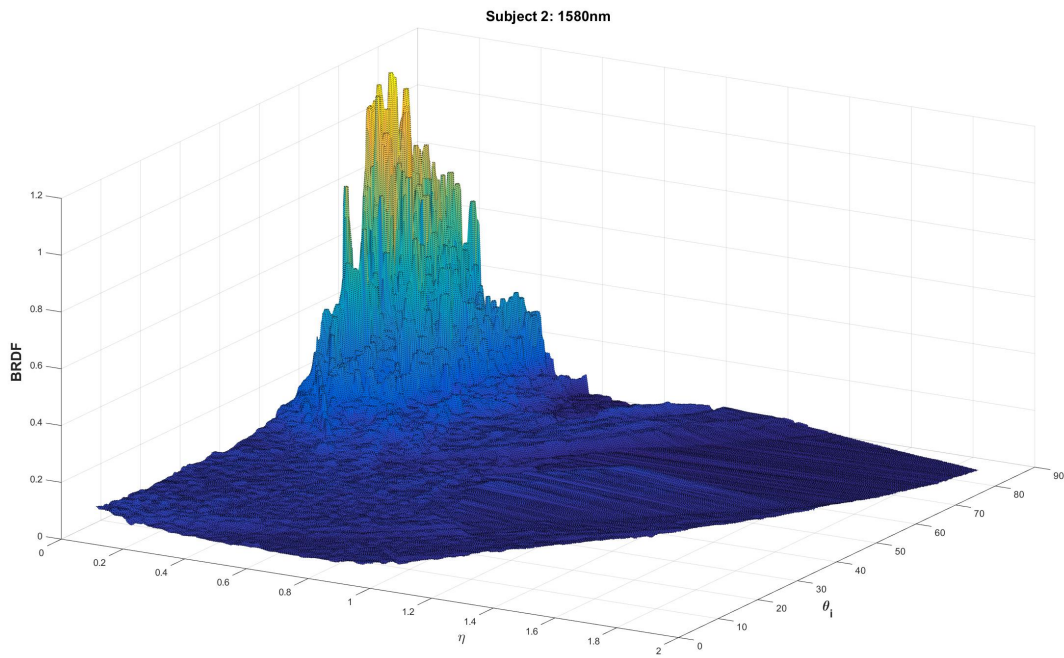
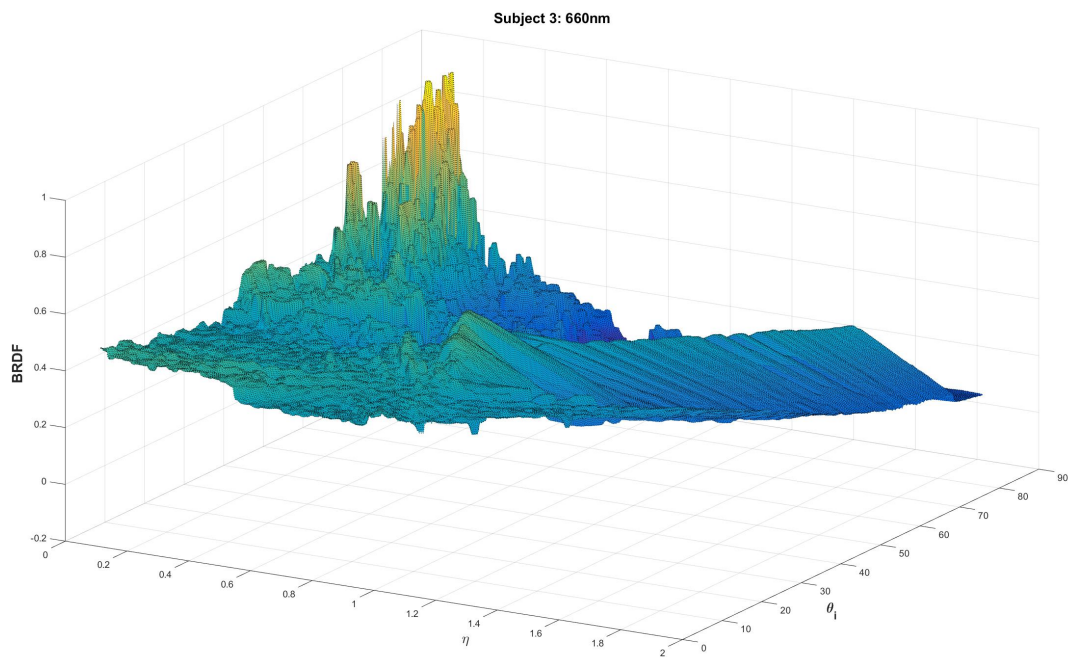
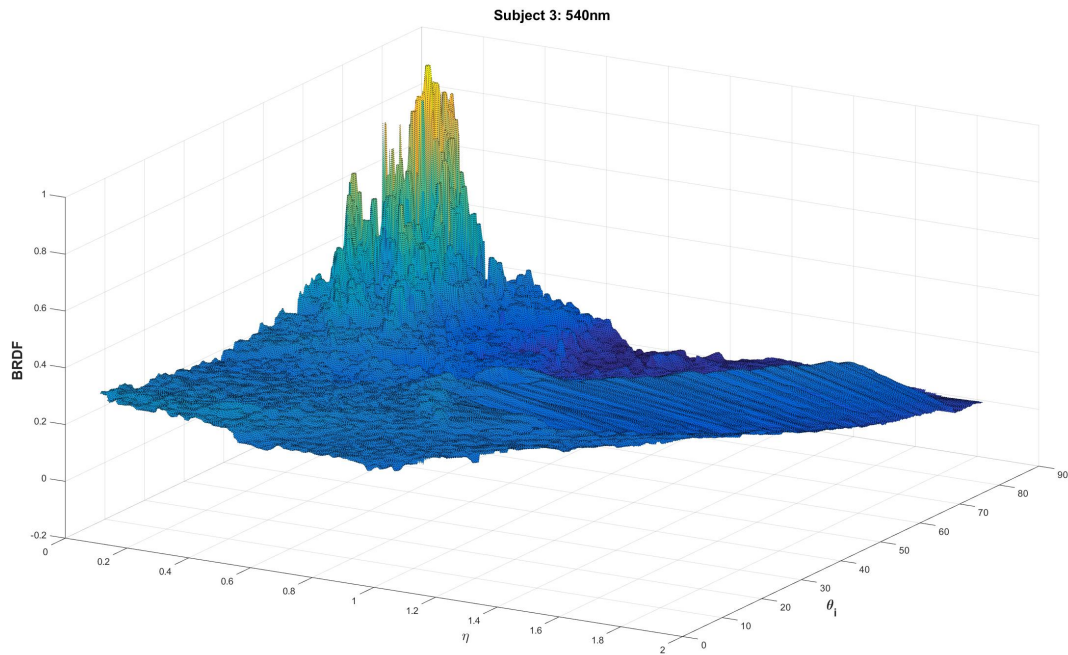
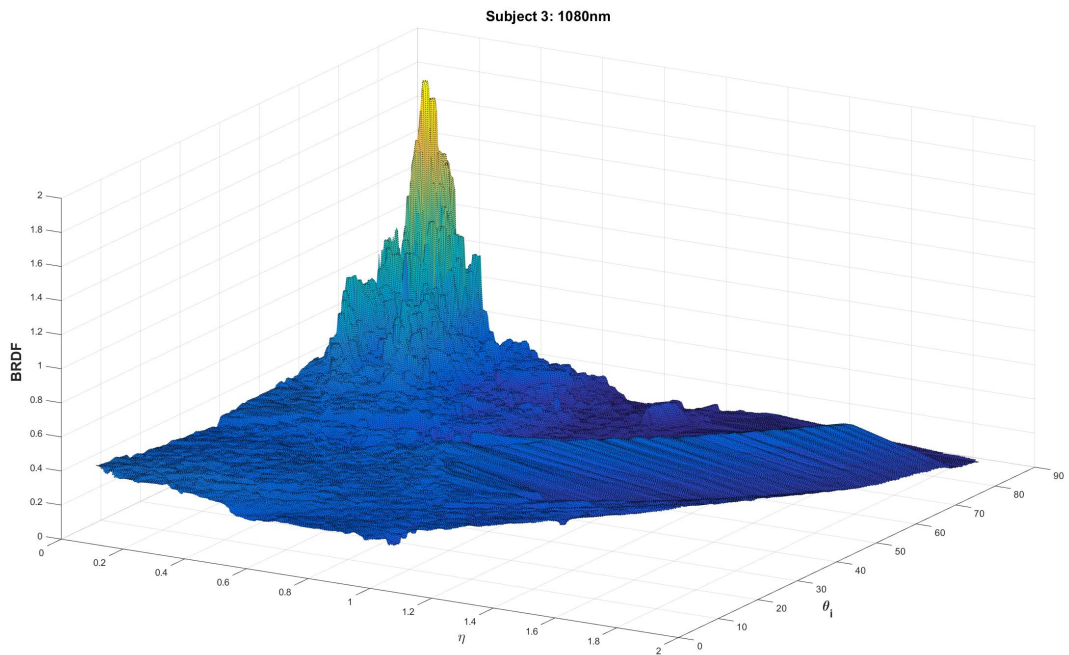
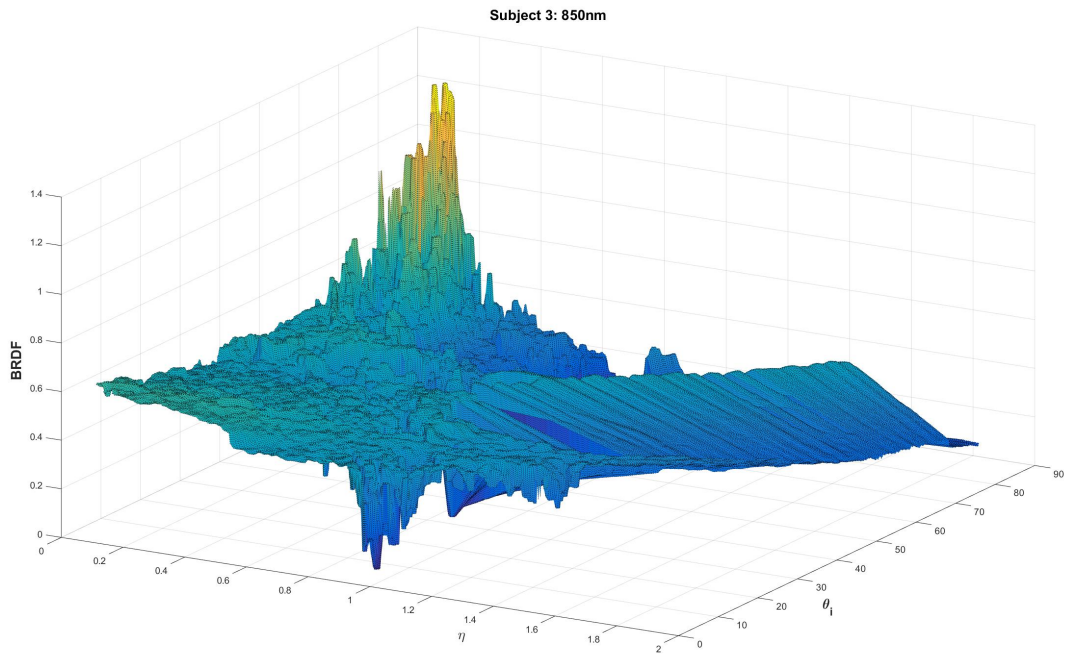


Figure 78. BRDF skin measurements obtained from Subject 2 in the 540nm, 660nm, 850nm, 1080nm, and 1580nm bands. Estimated Fitzpatrick Skin Type: II/III, Hair Coverage: Low.





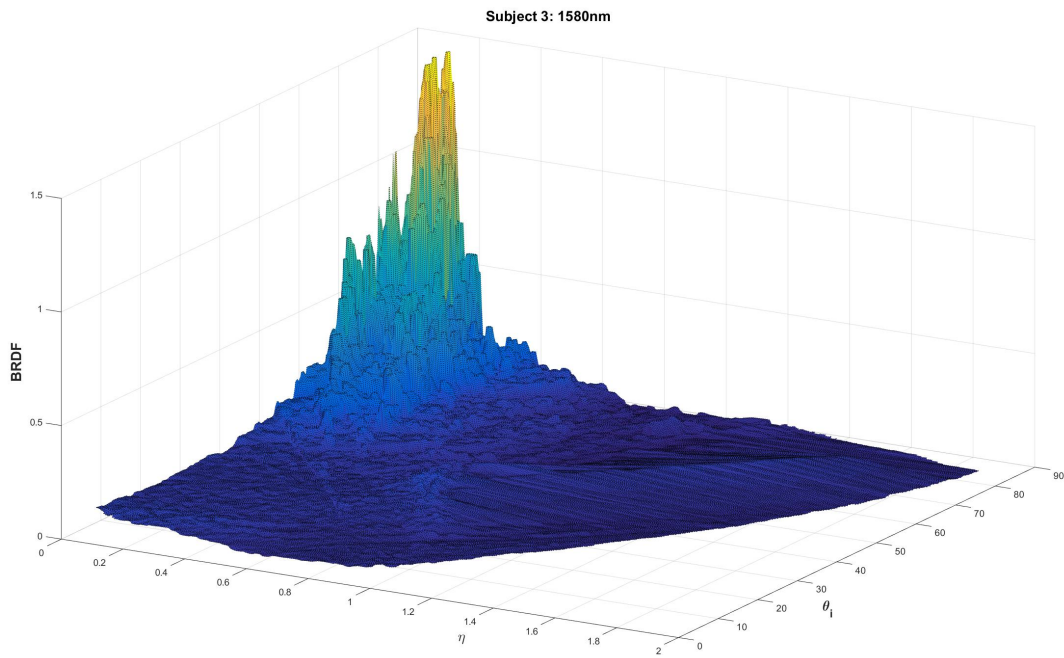


Figure 79. BRDF skin measurements obtained from Subject 3 in the 540nm, 660nm, 850nm, 1080nm, and 1580nm bands. Estimated Fitzpatrick Skin Type: II/III, Hair Coverage: Medium.

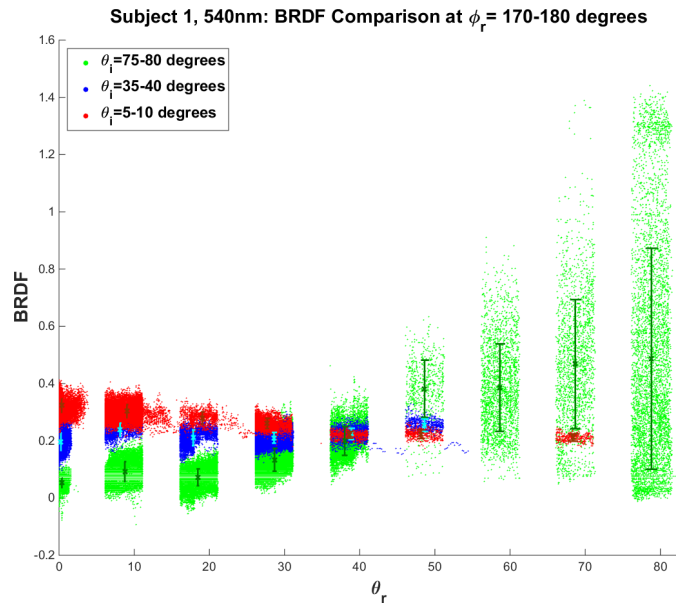


Figure 80. Three ranges for θ_i values are evaluated at ϕ_r close to 180 degrees and plotted in BRDF vs θ_r space for Subject 1 (Type III, Low hair coverage) with data from the 540nm band.

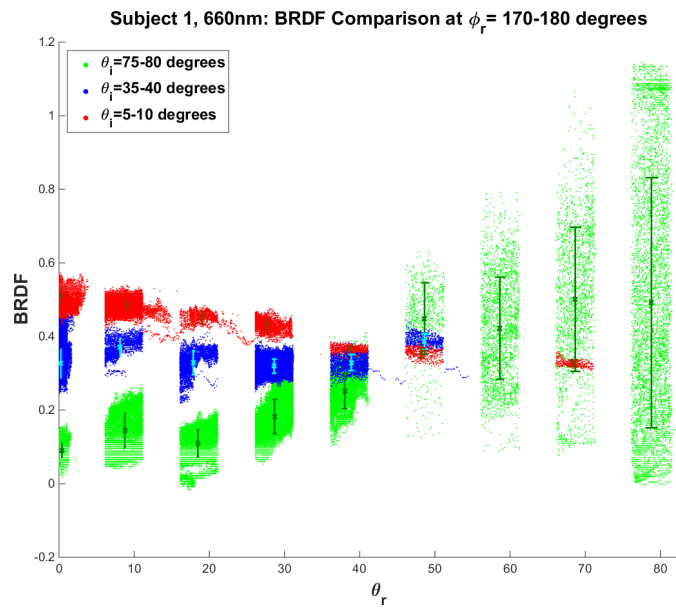


Figure 81. Three ranges for θ_i values are evaluated at ϕ_r close to 180 degrees and plotted in BRDF vs θ_r space for Subject 1 (Type III, Low hair coverage) with data from the 660nm band.

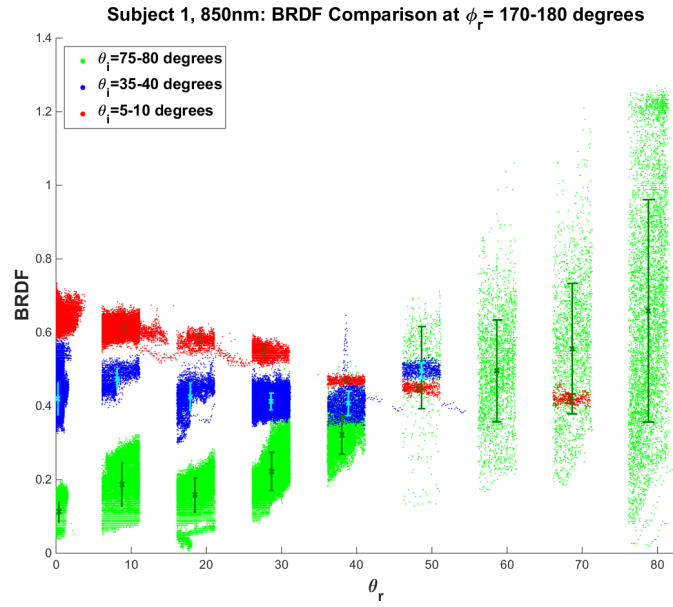


Figure 82. Three ranges for θ_i values are evaluated at ϕ_r close to 180 degrees and plotted in BRDF vs θ_r space for Subject 1 (Type III, Low hair coverage) with data from the 850nm band.

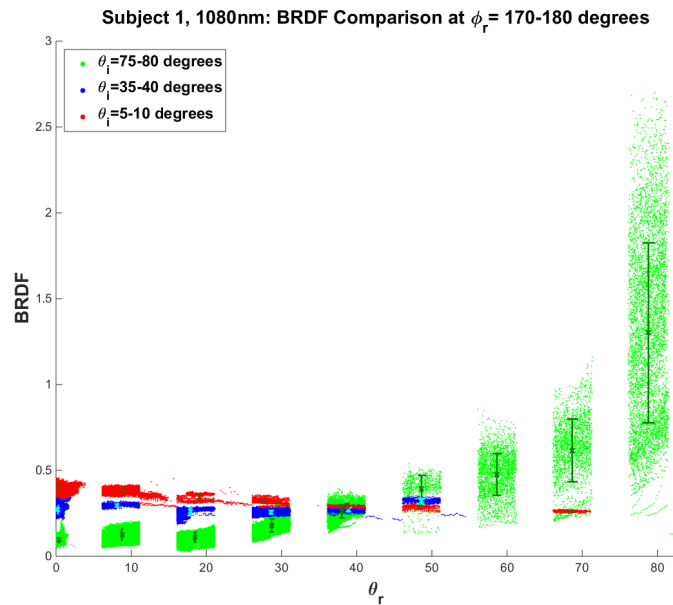


Figure 83. Three ranges for θ_i values are evaluated at ϕ_r close to 180 degrees and plotted in BRDF vs θ_r space for Subject 1 (Type III, Low hair coverage) with data from the 1080nm band.

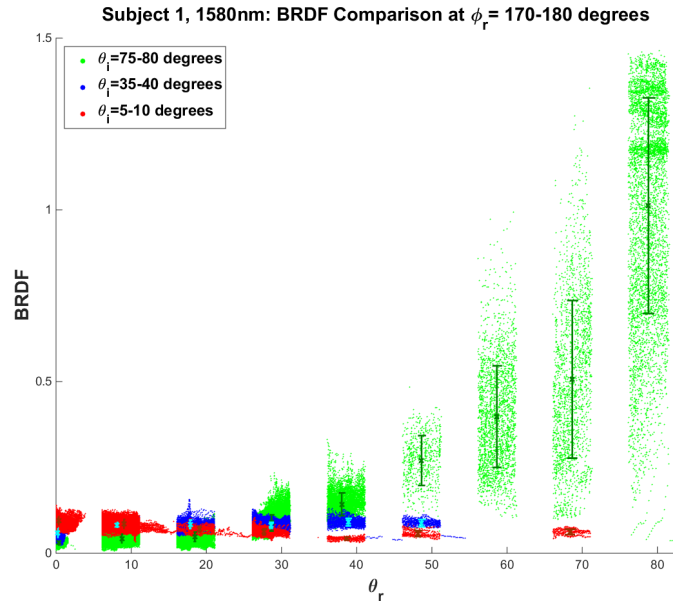


Figure 84. Three ranges for θ_i values are evaluated at ϕ_r close to 180 degrees and plotted in BRDF vs θ_r space for Subject 1 (Type III, Low hair coverage) with data from the 1580nm band.

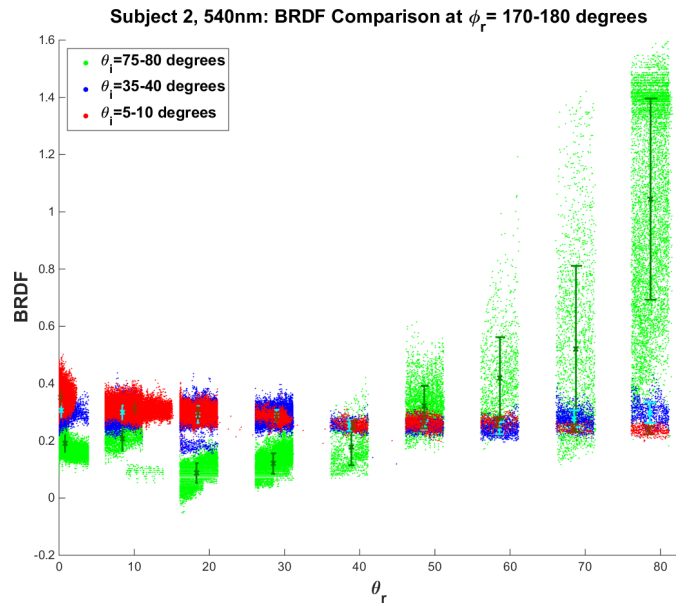


Figure 85. Three ranges for θ_i values are evaluated at ϕ_r close to 180 degrees and plotted in BRDF vs θ_r space for Subject 2 (Type II/III, Low hair coverage) with data from the 540nm band.

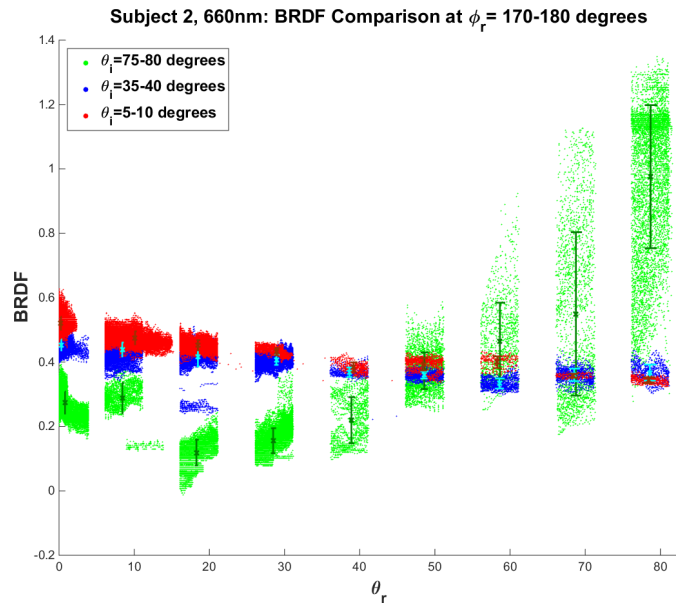


Figure 86. Three ranges for θ_i values are evaluated at ϕ_r close to 180 degrees and plotted in BRDF vs θ_r space for Subject 2 (Type II/III, Low hair coverage) with data from the 660nm band.

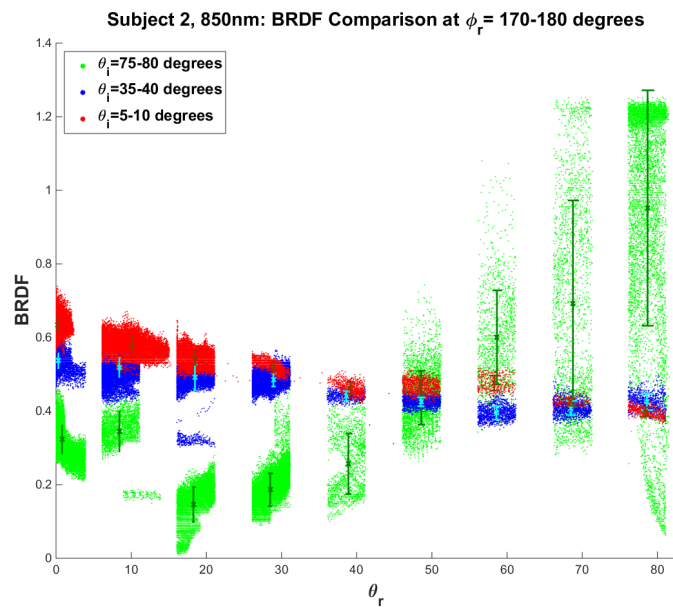


Figure 87. Three ranges for θ_i values are evaluated at ϕ_r close to 180 degrees and plotted in BRDF vs θ_r space for Subject 2 (Type II/III, Low hair coverage) with data from the 850nm band.

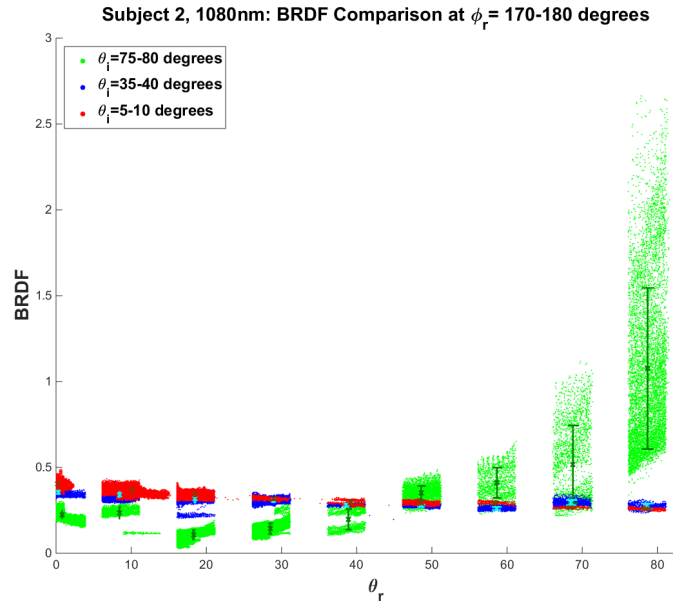


Figure 88. Three ranges for θ_i values are evaluated at ϕ_r close to 180 degrees and plotted in BRDF vs θ_r space for Subject 2 (Type II/III, Low hair coverage) with data from the 1080nm band.

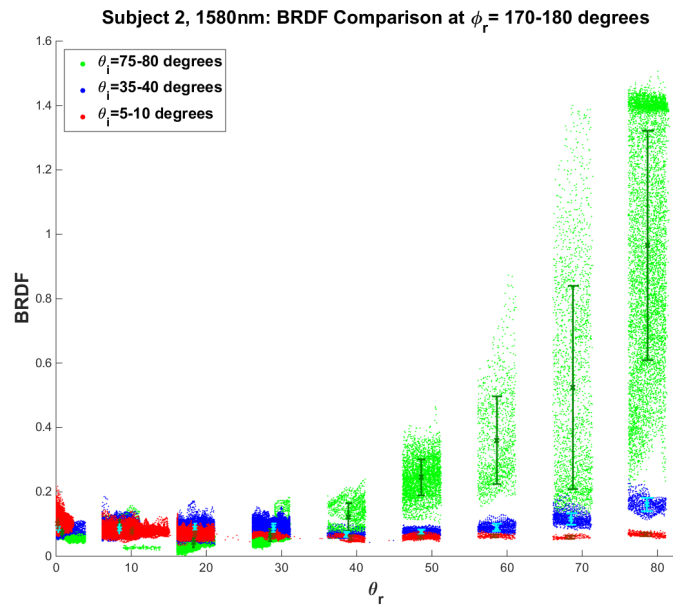


Figure 89. Three ranges for θ_i values are evaluated at ϕ_r close to 180 degrees and plotted in BRDF vs θ_r space for Subject 2 (Type III, Low hair coverage) with data from the 1580nm band.

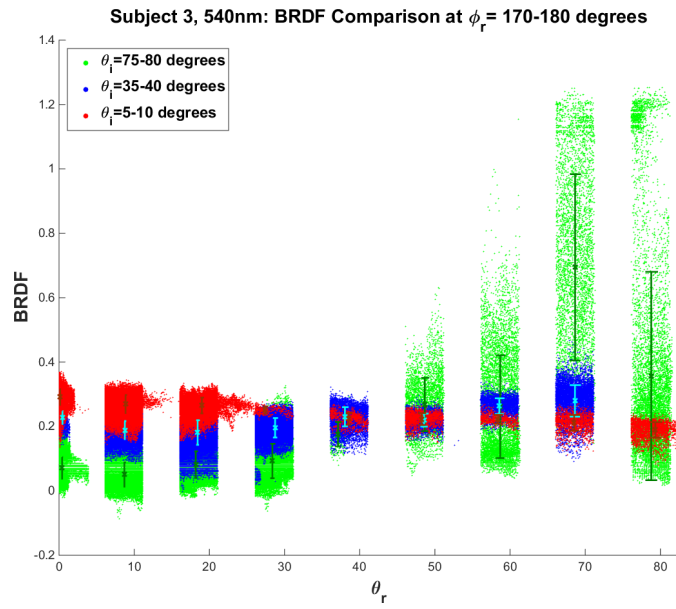


Figure 90. Three ranges for θ_i values are evaluated at ϕ_r close to 180 degrees and plotted in BRDF vs θ_r space for Subject 3 (Type II/III, Medium hair coverage) with data from the 540nm band.

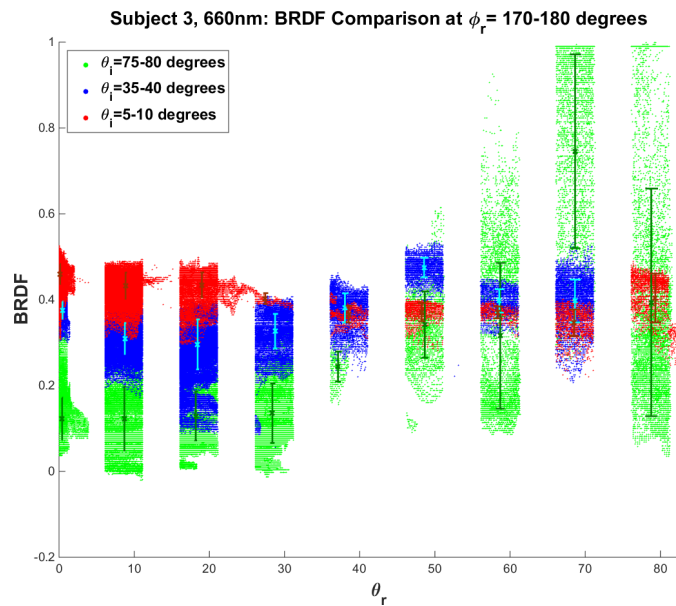


Figure 91. Three ranges for θ_i values are evaluated at ϕ_r close to 180 degrees and plotted in BRDF vs θ_r space for Subject 3 (Type II/III, Medium hair coverage) with data from the 660nm band.

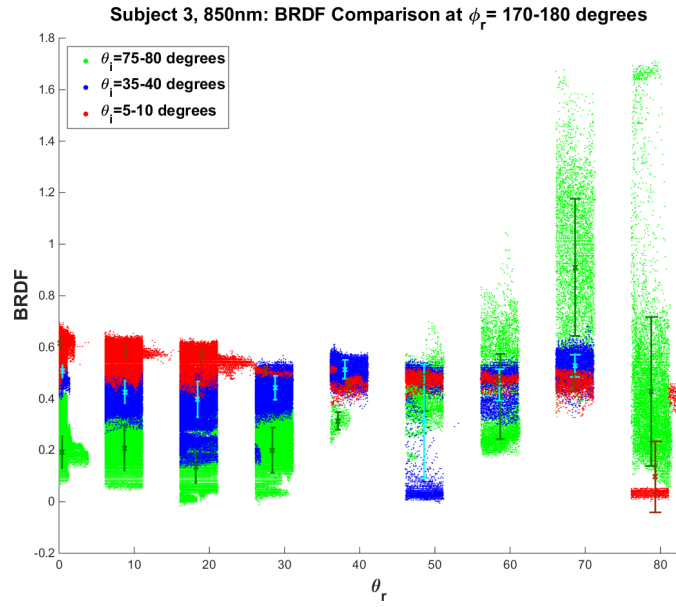


Figure 92. Three ranges for θ_i values are evaluated at ϕ_r close to 180 degrees and plotted in BRDF vs θ_r space for Subject 3 (Type II/III, Medium hair coverage) with data from the 850nm band.

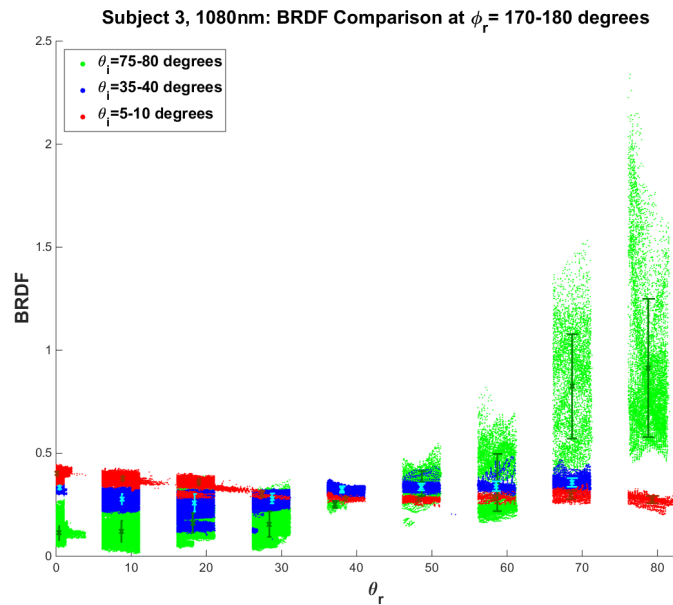


Figure 93. Three ranges for θ_i values are evaluated at ϕ_r close to 180 degrees and plotted in BRDF vs θ_r space for Subject 3 (Type II/III, Medium hair coverage) with data from the 1080nm band.

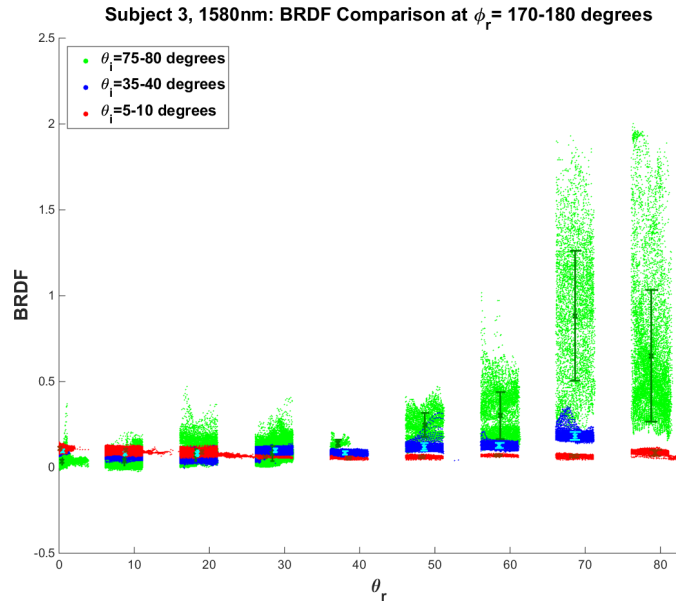


Figure 94. Three ranges for θ_i values are evaluated at ϕ_r close to 180 degrees and plotted in BRDF vs θ_r space for Subject 3 (Type II/III, Medium hair coverage) with data from the 1580nm band.

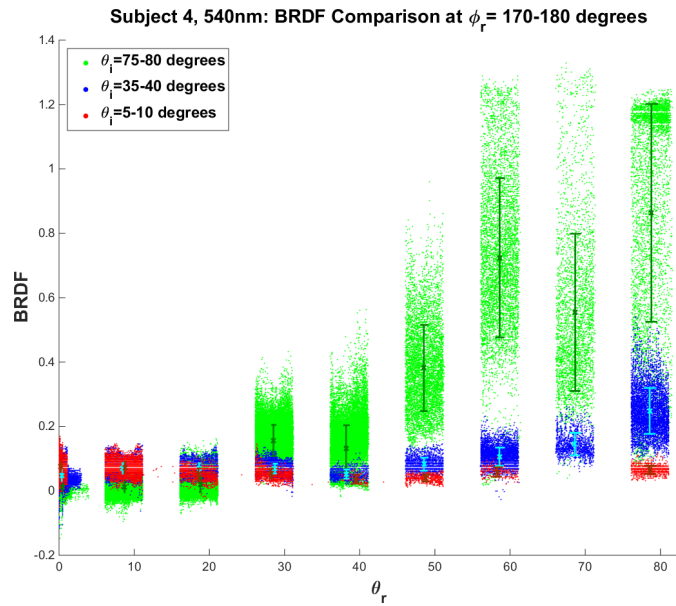


Figure 95. Three ranges for θ_i values are evaluated at ϕ_r close to 180 degrees and plotted in BRDF vs θ_r space for Subject 4 (Type V, Low hair coverage) with data from the 540nm band.

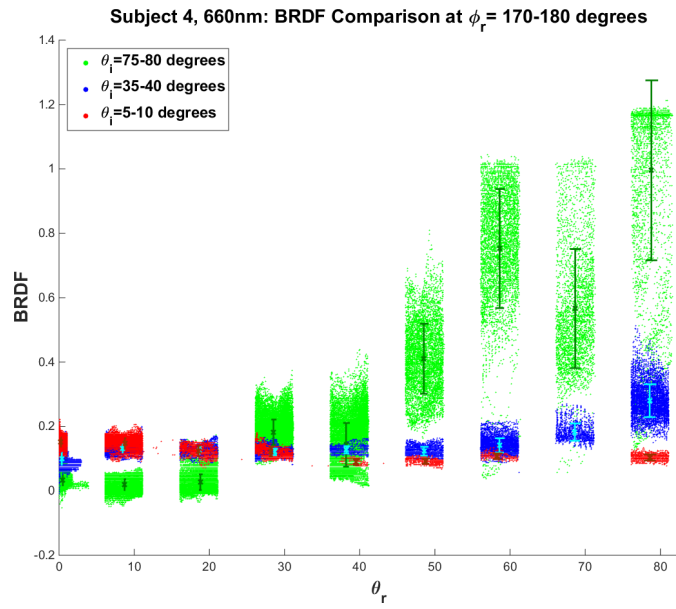


Figure 96. Three ranges for θ_i values are evaluated at ϕ_r close to 180 degrees and plotted in BRDF vs θ_r space for Subject 4 (Type V, Low hair coverage) with data from the 660nm band.

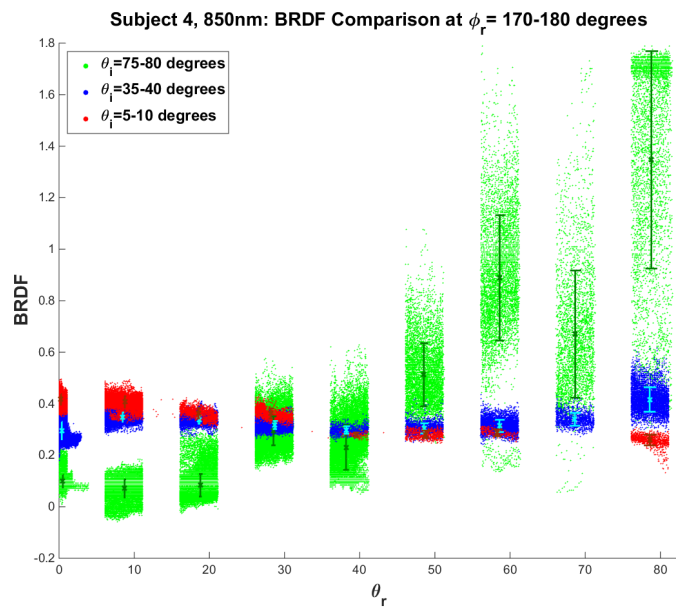


Figure 97. Three ranges for θ_i values are evaluated at ϕ_r close to 180 degrees and plotted in BRDF vs θ_r space for Subject 4 (Type V, Low hair coverage) with data from the 850nm band.

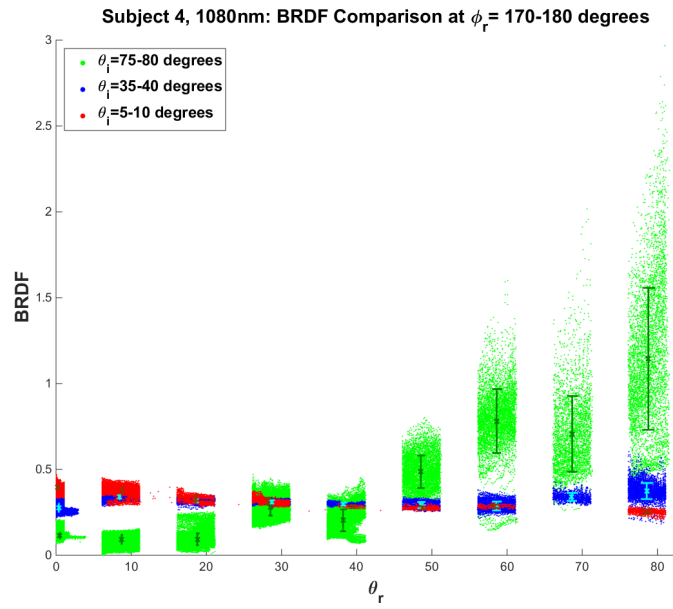


Figure 98. Three ranges for θ_i values are evaluated at ϕ_r close to 180 degrees and plotted in BRDF vs θ_r space for Subject 4 (Type V, Low hair coverage) with data from the 1080nm band.

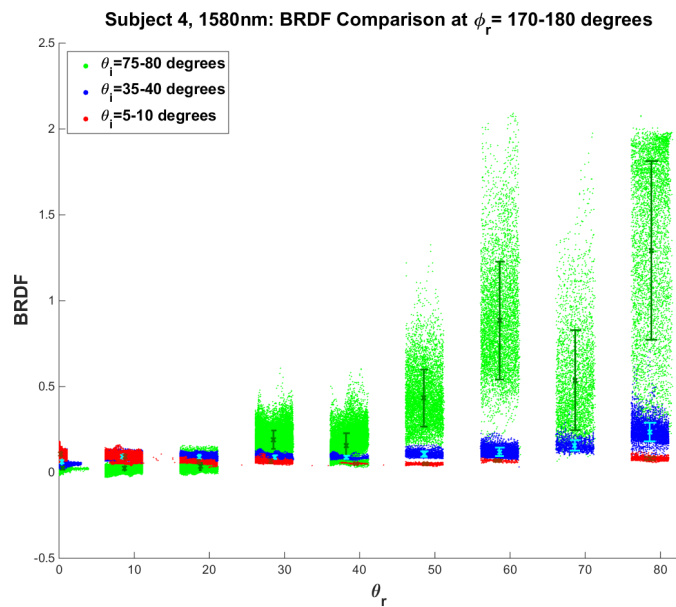


Figure 99. Three ranges for θ_i values are evaluated at ϕ_r close to 180 degrees and plotted in BRDF vs θ_r space for Subject 4 (Type V, Low hair coverage) with data from the 1580nm band.

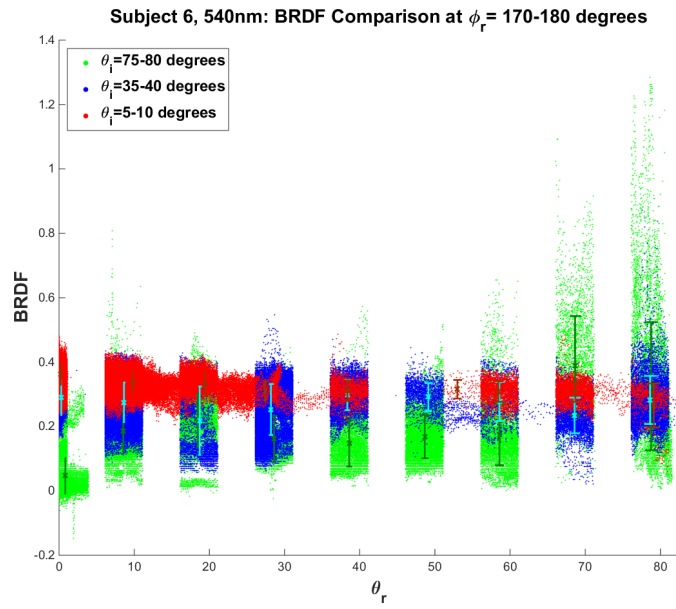


Figure 100. Three ranges for θ_i values are evaluated at ϕ_r close to 180 degrees and plotted in BRDF vs θ_r space for Subject 6 (Type I, High hair coverage) with data from the 540nm band.

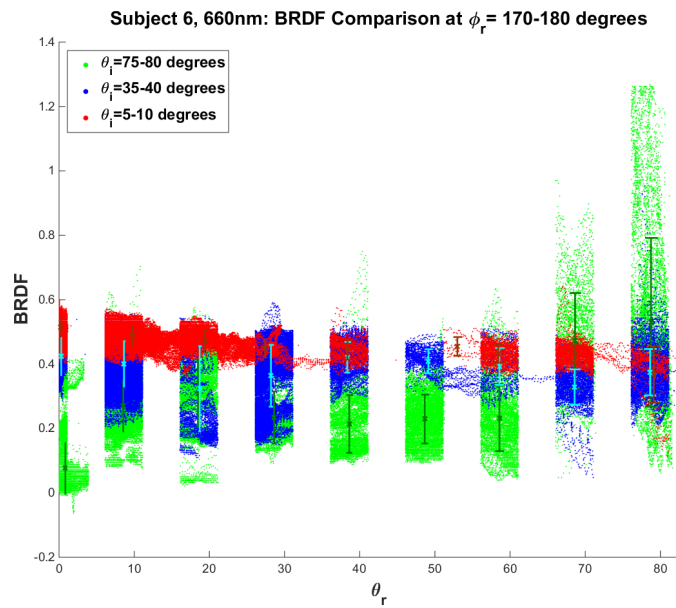


Figure 101. Three ranges for θ_i values are evaluated at ϕ_r close to 180 degrees and plotted in BRDF vs θ_r space for Subject 6 (Type I, High hair coverage) with data from the 660nm band.

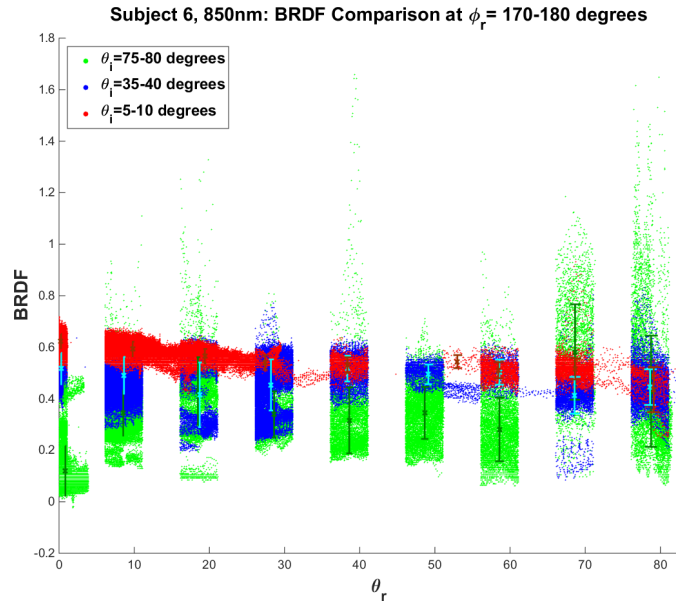


Figure 102. Three ranges for θ_i values are evaluated at ϕ_r close to 180 degrees and plotted in BRDF vs θ_r space for Subject 6 (Type I, High hair coverage) with data from the 850nm band.

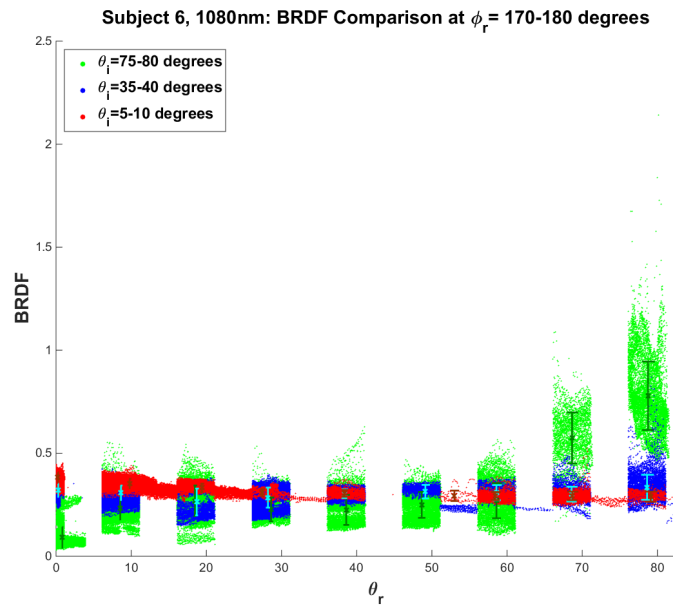


Figure 103. Three ranges for θ_i values are evaluated at ϕ_r close to 180 degrees and plotted in BRDF vs θ_r space for Subject 6 (Type I, High hair coverage) with data from the 1080nm band.

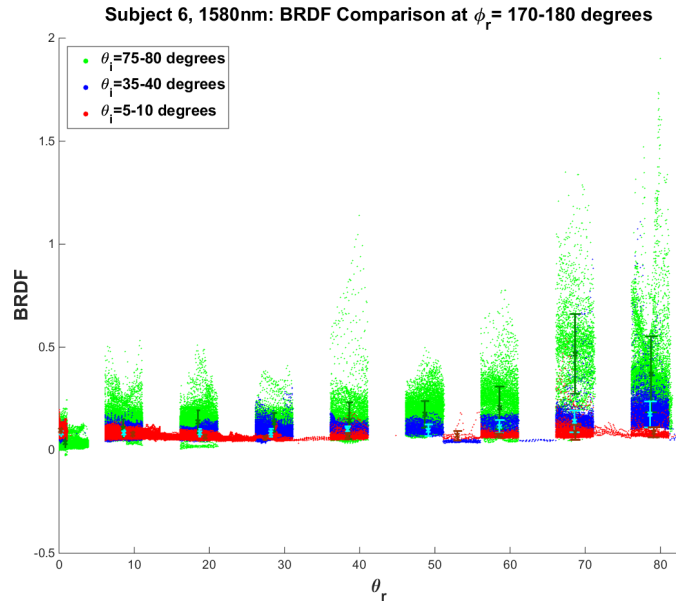


Figure 104. Three ranges for θ_i values are evaluated at ϕ_r close to 180 degrees and plotted in BRDF vs θ_r space for Subject 6 (Type I, High hair coverage) with data from the 1580nm band.

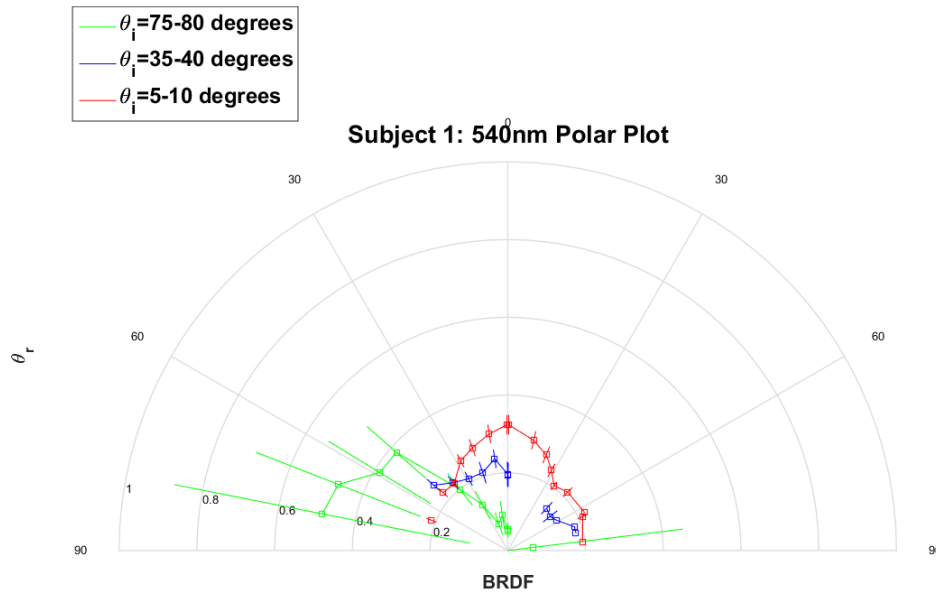


Figure 105. Three ranges for θ_i values are evaluated at ϕ_r close to 180 degrees and plotted in BRDF vs θ_r space for Subject 1 (Type III, Low hair coverage) with data from the 540nm band.

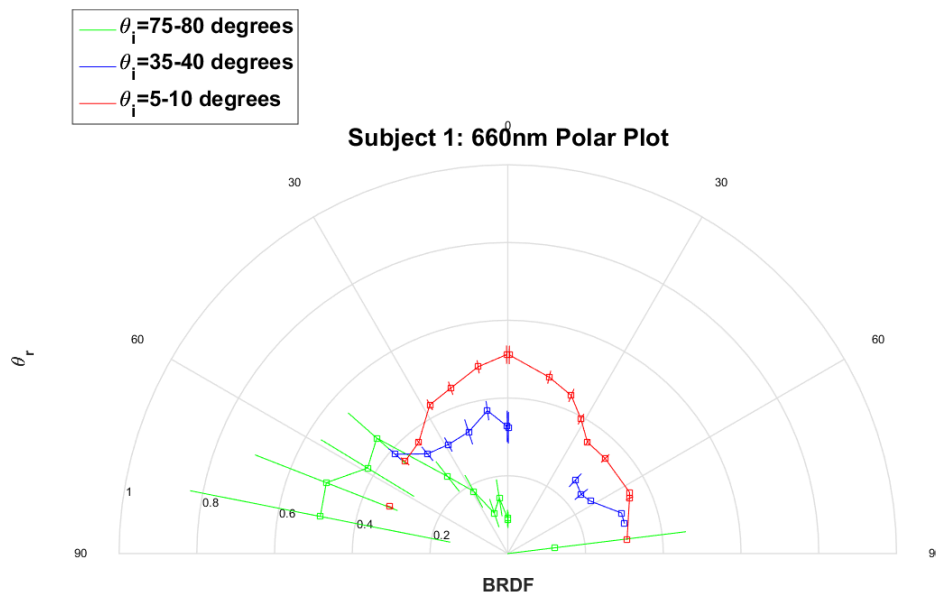


Figure 106. Three ranges for θ_i values are evaluated at ϕ_r close to 180 degrees and plotted in BRDF vs θ_r space for Subject 1 (Type III, Low hair coverage) with data from the 660nm band.

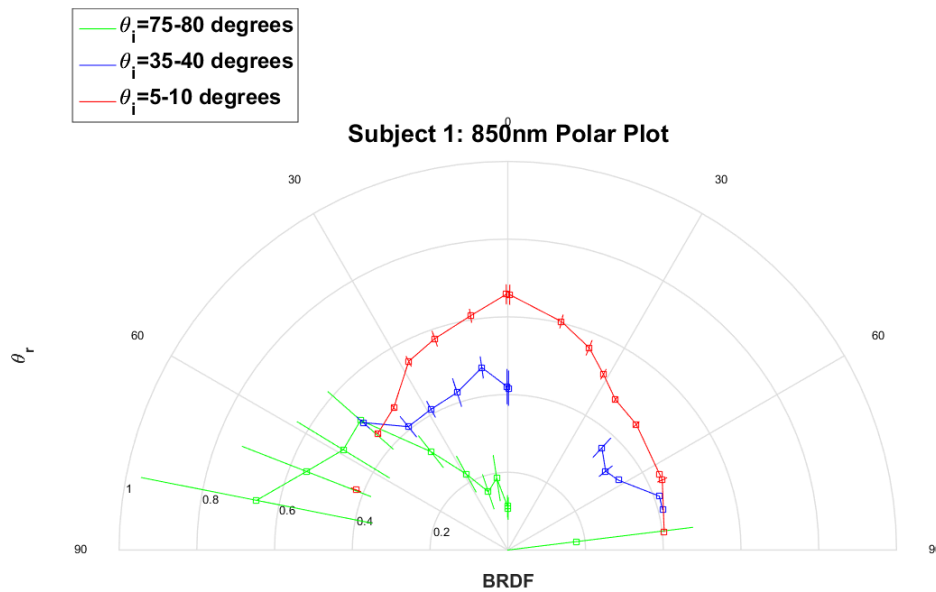


Figure 107. Three ranges for θ_i values are evaluated at ϕ_r close to 180 degrees and plotted in BRDF vs θ_r space for Subject 1 (Type III, Low hair coverage) with data from the 850nm band.

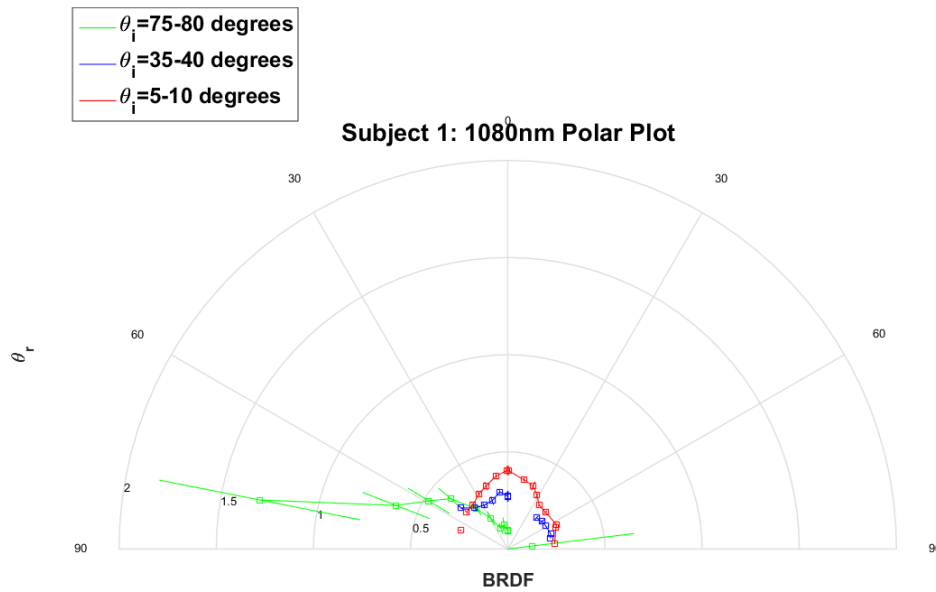


Figure 108. Three ranges for θ_i values are evaluated at ϕ_r close to 180 degrees and plotted in BRDF vs θ_r space for Subject 1 (Type III, Low hair coverage) with data from the 1080nm band.

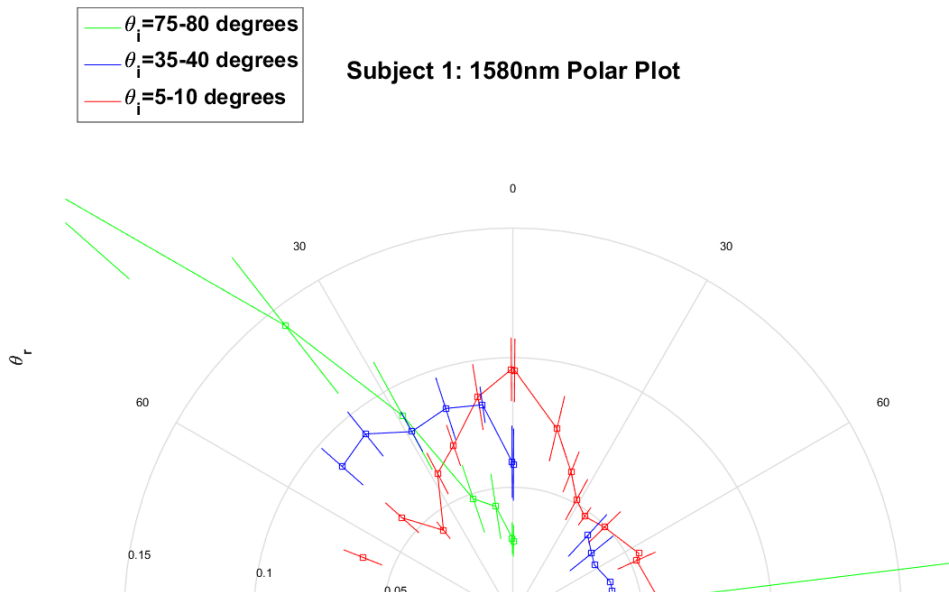


Figure 109. Three ranges for θ_i values are evaluated at ϕ_r close to 180 degrees and plotted in BRDF vs θ_r space for Subject 1 (Type III, Low hair coverage) with data from the 1580nm band. Specular data is cropped for $\theta_i = 75-80$ degrees for a better display of the other two ranges of θ_i .

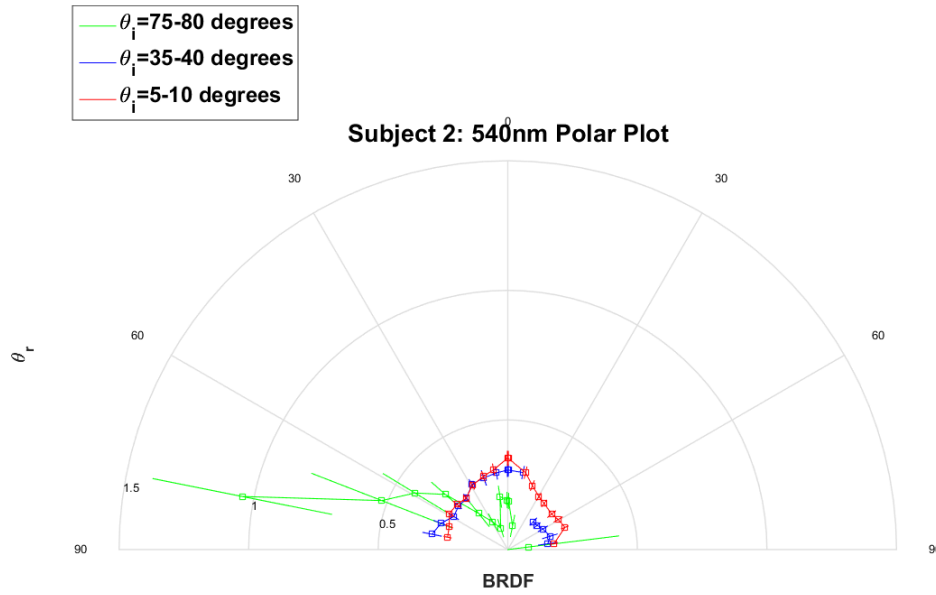


Figure 110. Three ranges for θ_i values are evaluated at ϕ_r close to 180 degrees and plotted in BRDF vs θ_r space for Subject 2 (Type II/III, Low hair coverage) with data from the 540nm band.

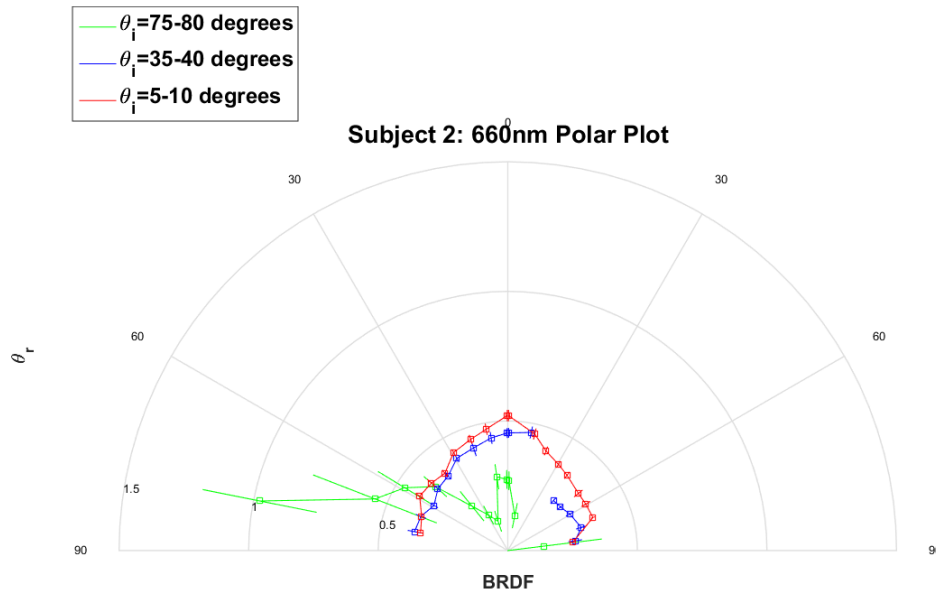


Figure 111. Three ranges for θ_i values are evaluated at ϕ_r close to 180 degrees and plotted in BRDF vs θ_r space for Subject 2 (Type II/III, Low hair coverage) with data from the 660nm band.

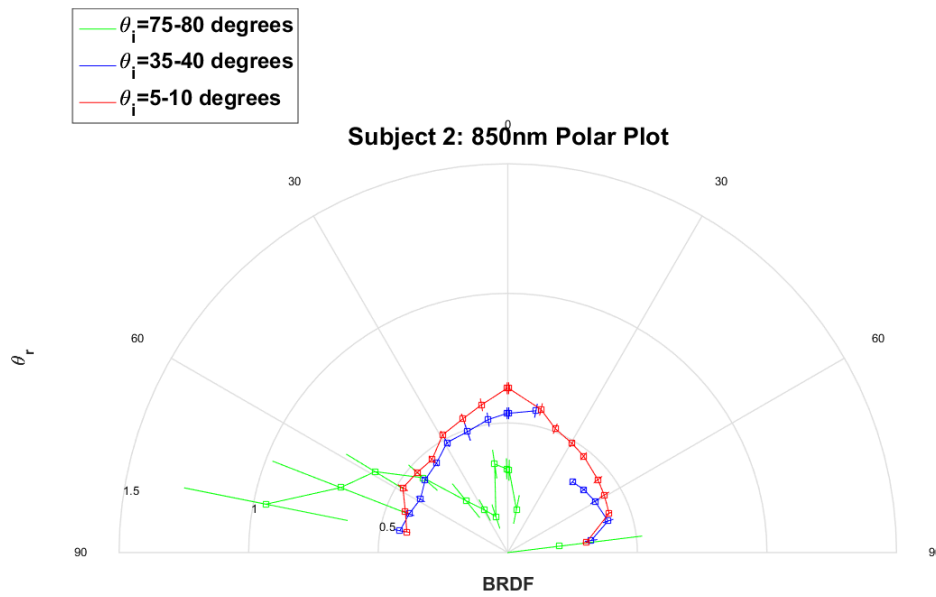


Figure 112. Three ranges for θ_i values are evaluated at ϕ_r close to 180 degrees and plotted in BRDF vs θ_r space for Subject 2 (Type II/III, Low hair coverage) with data from the 850nm band.

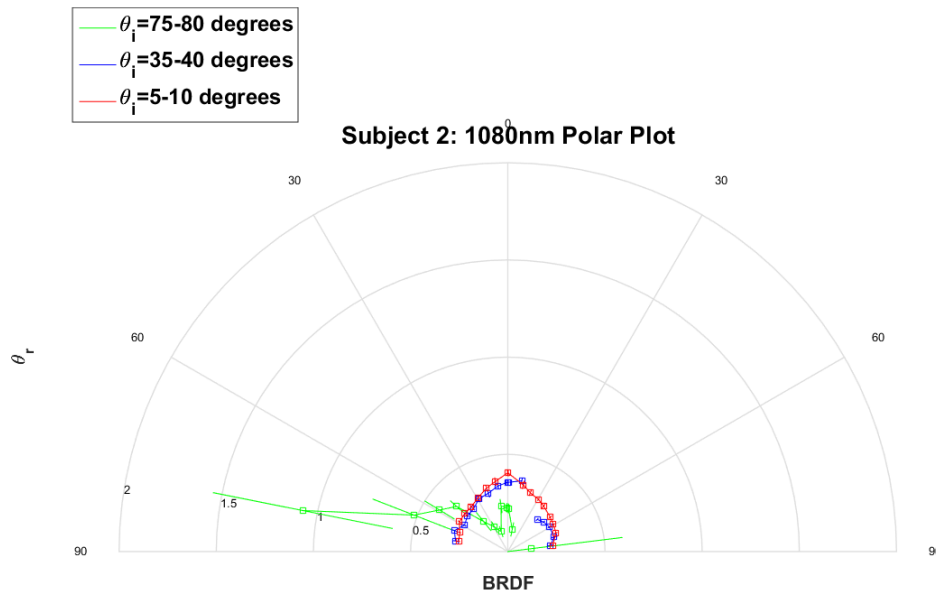
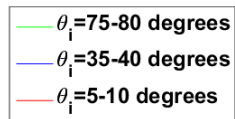


Figure 113. Three ranges for θ_i values are evaluated at ϕ_r close to 180 degrees and plotted in BRDF vs θ_r space for Subject 2 (Type II/III, Low hair coverage) with data from the 1080nm band.



Subject 2: 1580nm Polar Plot

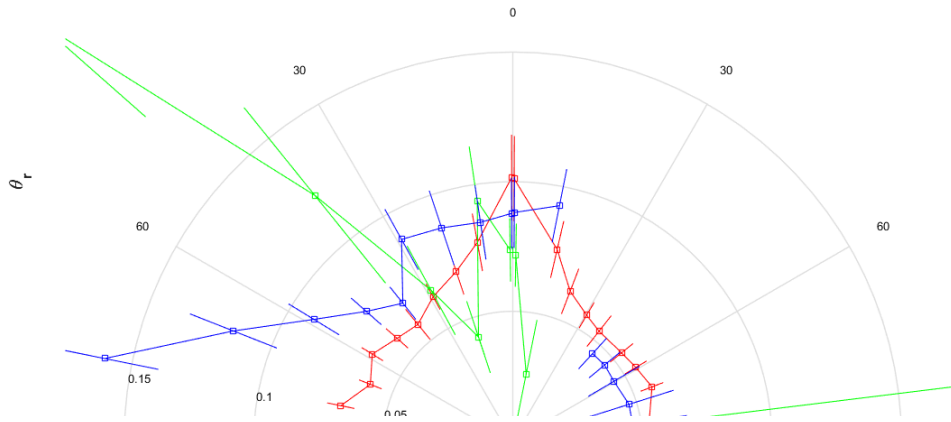


Figure 114. Three ranges for θ_i values are evaluated at ϕ_r close to 180 degrees and plotted in BRDF vs θ_r space for Subject 2 (Type III, Low hair coverage) with data from the 1580nm band. Specular data is cropped for $\theta_i=75-80$ degrees for a better display of the other two ranges of θ_i .

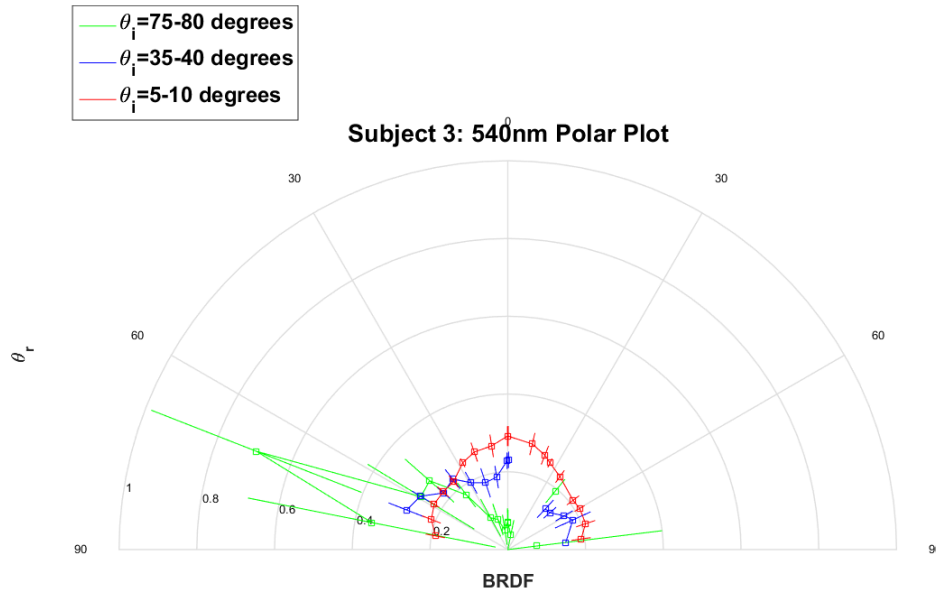


Figure 115. Three ranges for θ_i values are evaluated at ϕ_r close to 180 degrees and plotted in BRDF vs θ_r space for Subject 3 (Type II/III, Medium hair coverage) with data from the 540nm band.

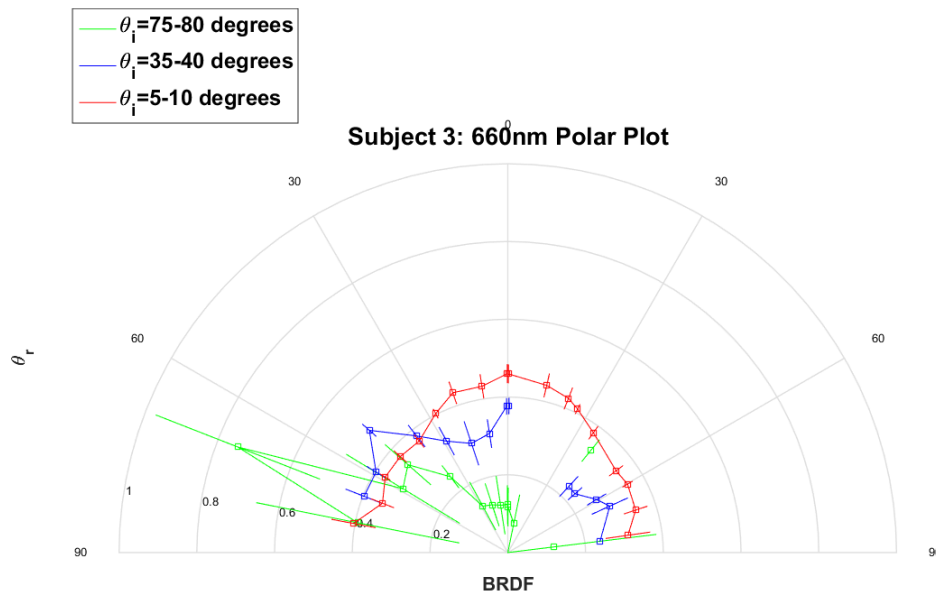


Figure 116. Three ranges for θ_i values are evaluated at ϕ_r close to 180 degrees and plotted in BRDF vs θ_r space for Subject 3 (Type II/III, Medium hair coverage) with data from the 660nm band.

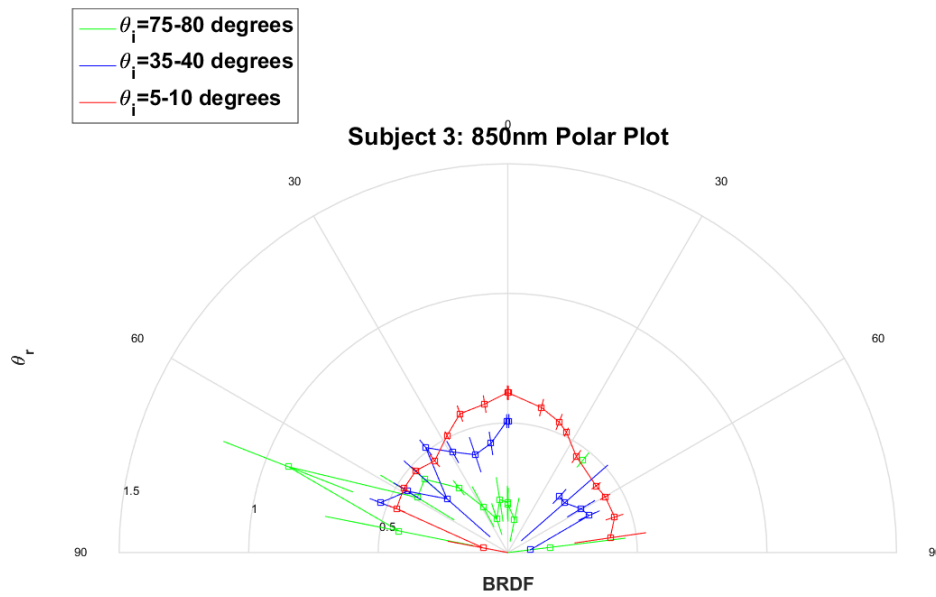


Figure 117. Three ranges for θ_i values are evaluated at ϕ_r close to 180 degrees and plotted in BRDF vs θ_r space for Subject 3 (Type II/III, Medium hair coverage) with data from the 850nm band.

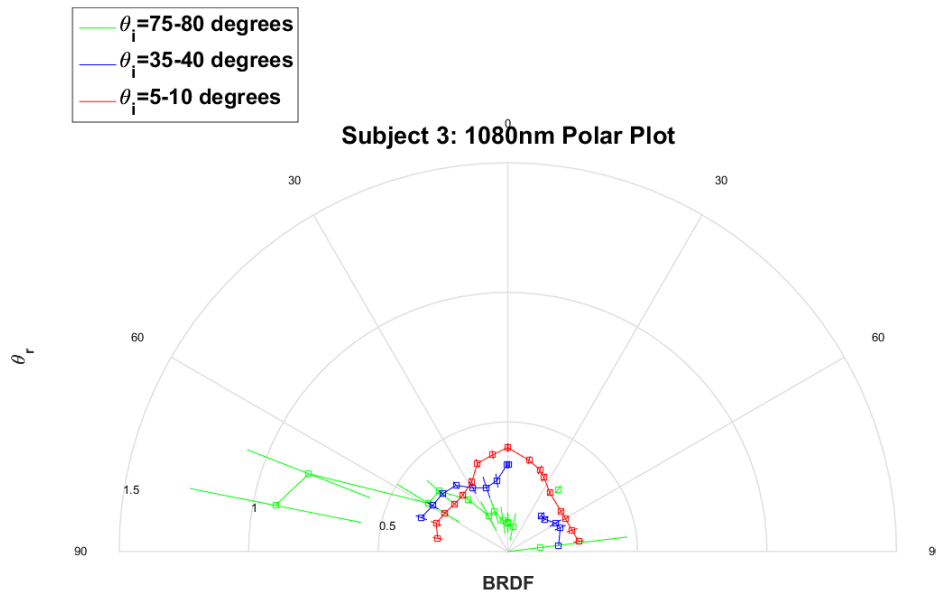
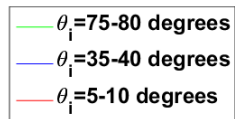


Figure 118. Three ranges for θ_i values are evaluated at ϕ_r close to 180 degrees and plotted in BRDF vs θ_r space for Subject 3 (Type II/III, Medium hair coverage) with data from the 1080nm band.



Subject 3: 1580nm Polar Plot

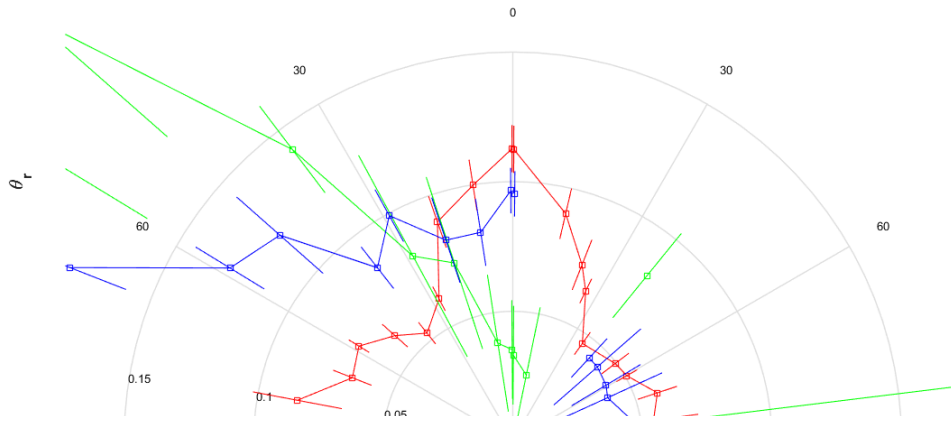


Figure 119. Three ranges for θ_i values are evaluated at ϕ_r close to 180 degrees and plotted in BRDF vs θ_r space for Subject 3 (Type II/III, Medium hair coverage) with data from the 1580nm band. Specular data is cropped for $\theta_i=75-80$ degrees for a better display of the other two ranges of θ_i .

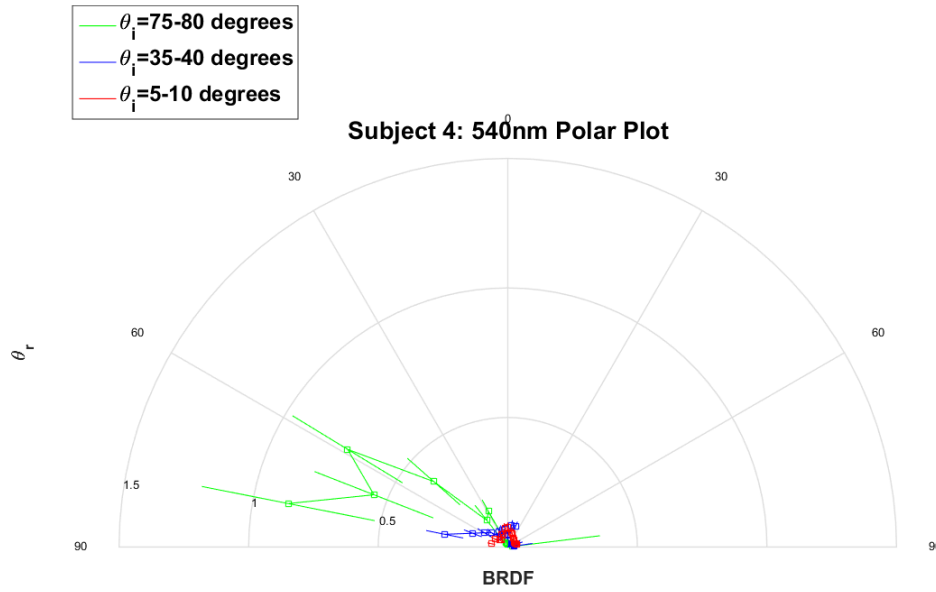


Figure 120. Three ranges for θ_i values are evaluated at ϕ_r close to 180 degrees and plotted in BRDF vs θ_r space for Subject 4 (Type V, Low hair coverage) with data from the 540nm band.

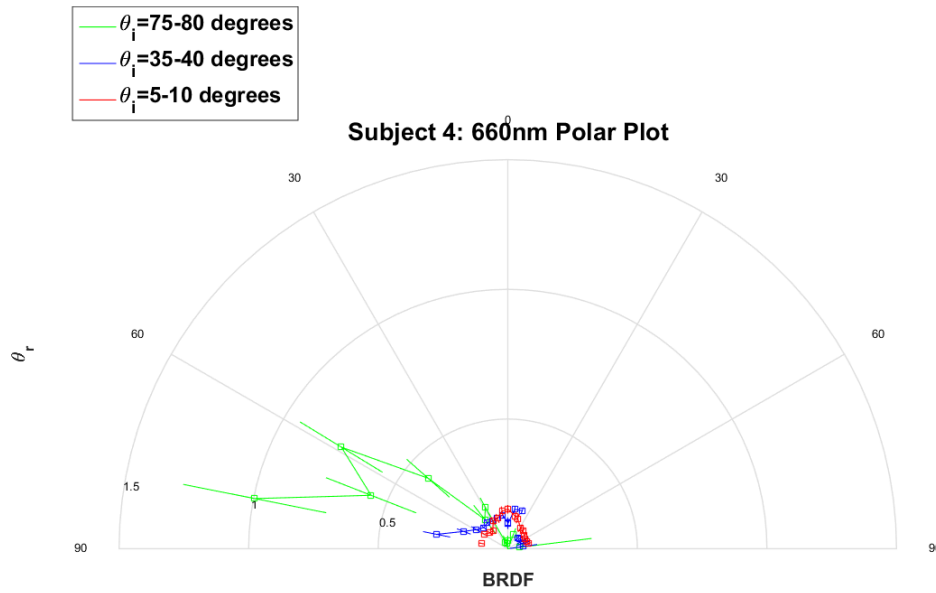


Figure 121. Three ranges for θ_i values are evaluated at ϕ_r close to 180 degrees and plotted in BRDF vs θ_r space for Subject 4 (Type V, Low hair coverage) with data from the 660nm band.

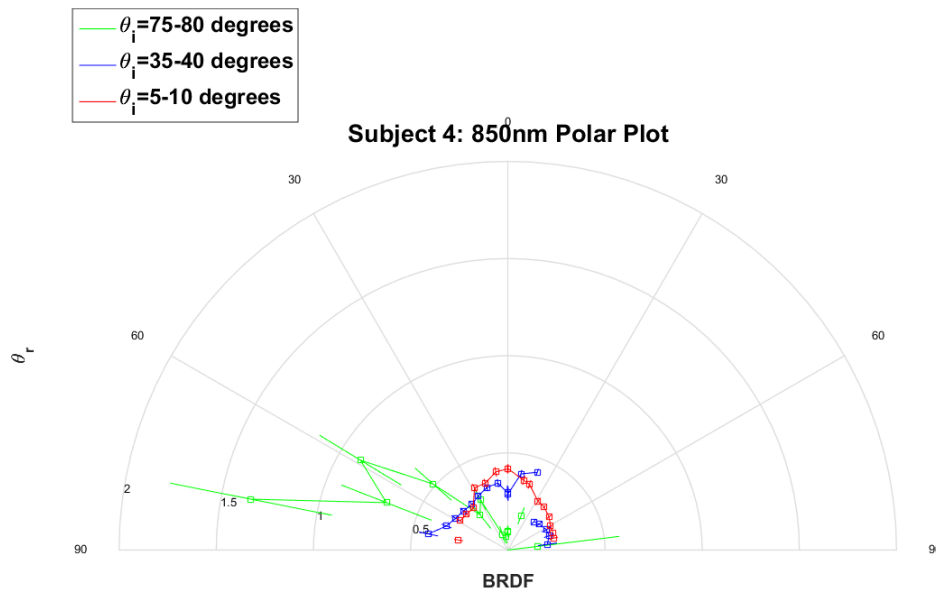


Figure 122. Three ranges for θ_i values are evaluated at ϕ_r close to 180 degrees and plotted in BRDF vs θ_r space for Subject 4 (Type V, Low hair coverage) with data from the 850nm band.

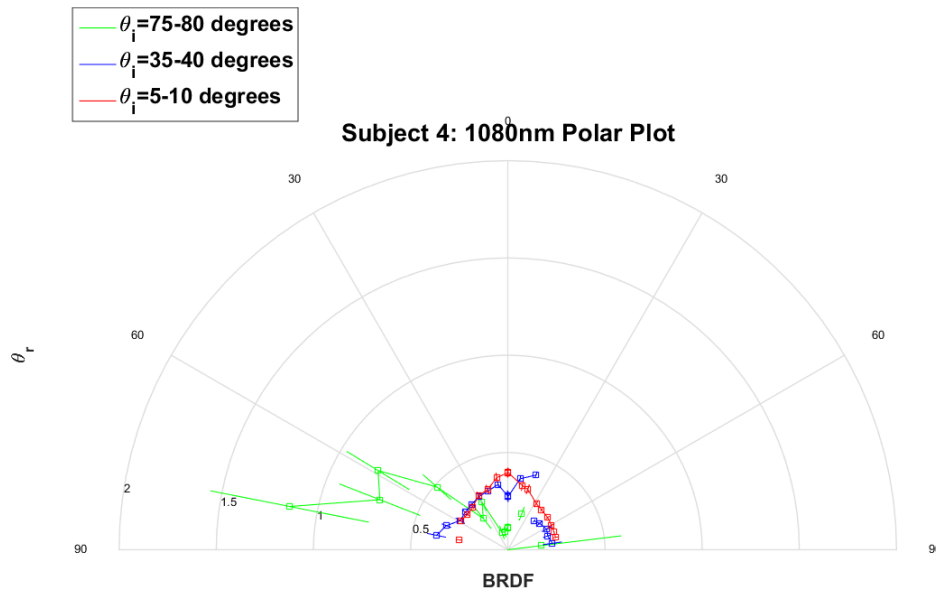


Figure 123. Three ranges for θ_i values are evaluated at ϕ_r close to 180 degrees and plotted in BRDF vs θ_r space for Subject 4 (Type V, Low hair coverage) with data from the 1080nm band.

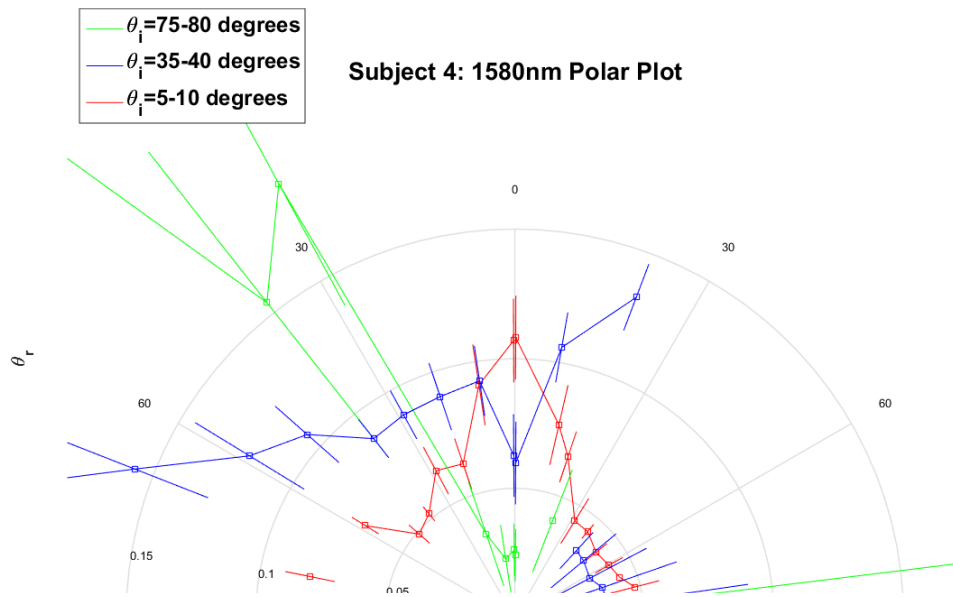


Figure 124. Three ranges for θ_i values are evaluated at ϕ_r close to 180 degrees and plotted in BRDF vs θ_r space for Subject 4 (Type V, Low hair coverage) with data from the 1580nm band. Specular data is cropped for $\theta_i=75-80$ degrees for a better display of the other two ranges of θ_i .

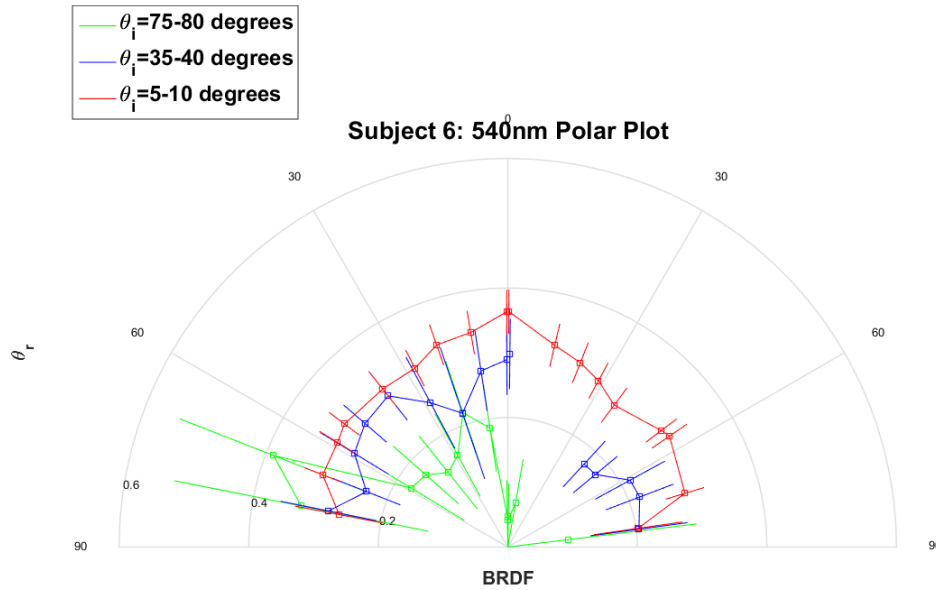


Figure 125. Three ranges for θ_i values are evaluated at ϕ_r close to 180 degrees and plotted in BRDF vs θ_r space for Subject 6 (Type I, High hair coverage) with data from the 540nm band.

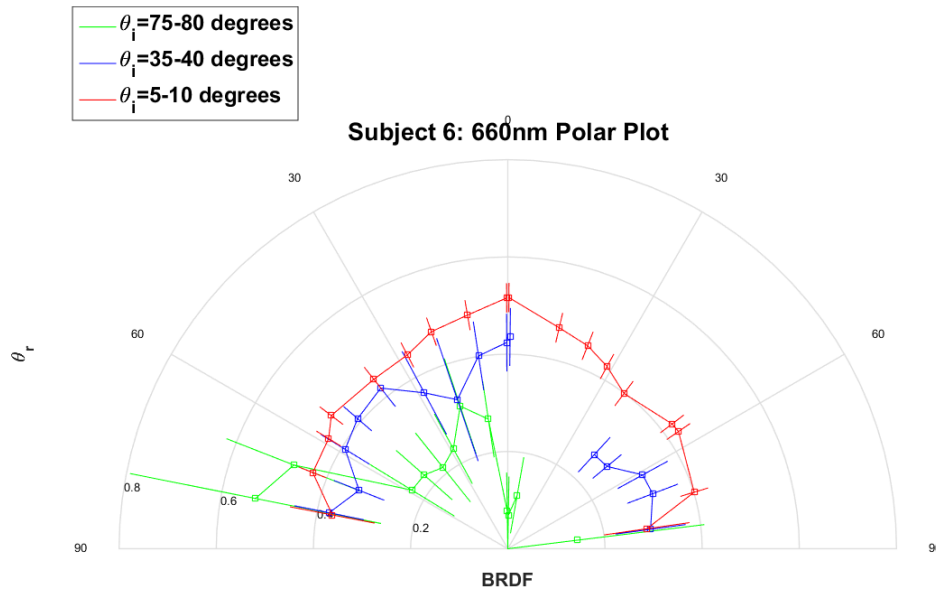


Figure 126. Three ranges for θ_i values are evaluated at ϕ_r close to 180 degrees and plotted in BRDF vs θ_r space for Subject 6 (Type I, High hair coverage) with data from the 660nm band.

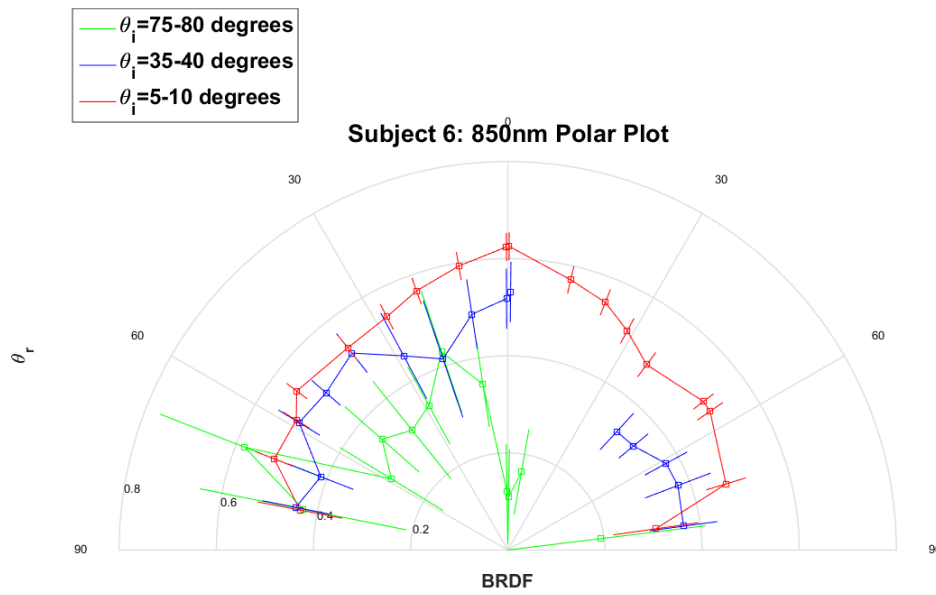


Figure 127. Three ranges for θ_i values are evaluated at ϕ_r close to 180 degrees and plotted in BRDF vs θ_r space for Subject 6 (Type I, High hair coverage) with data from the 850nm band.

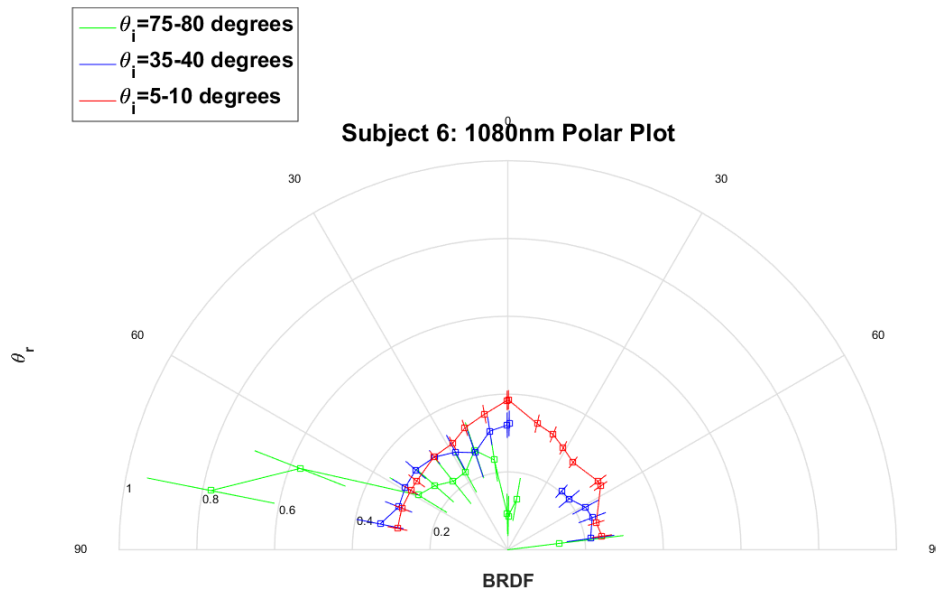


Figure 128. Three ranges for θ_i values are evaluated at ϕ_r close to 180 degrees and plotted in BRDF vs θ_r space for Subject 6 (Type I, High hair coverage) with data from the 1080nm band.

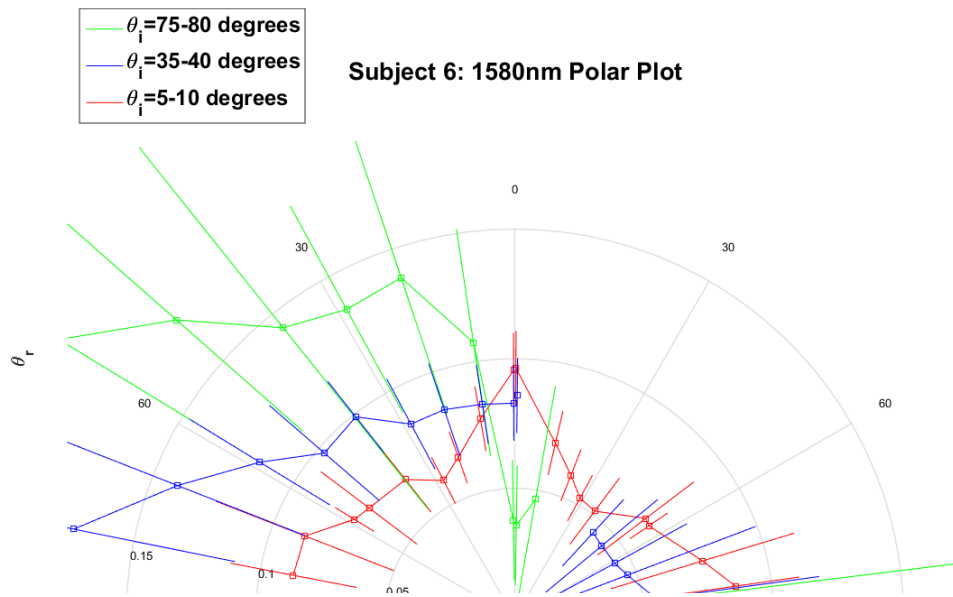


Figure 129. Three ranges for θ_i values are evaluated at ϕ_r close to 180 degrees and plotted in BRDF vs θ_r space for Subject 6 (Type I, High hair coverage) with data from the 1580nm band. Specular data is cropped for $\theta_i=75-80$ degrees for a better display of the other two ranges of θ_i .

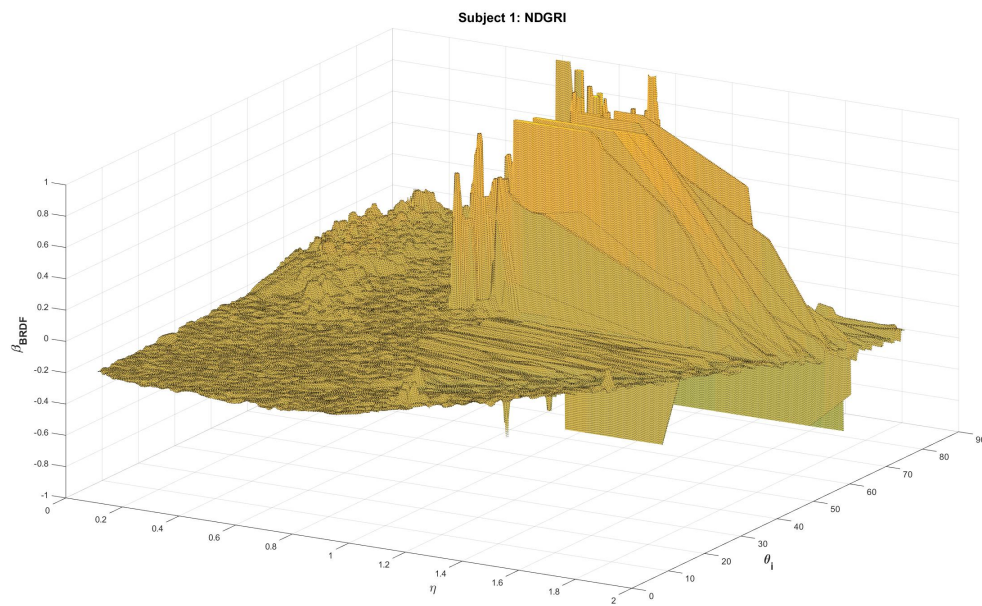
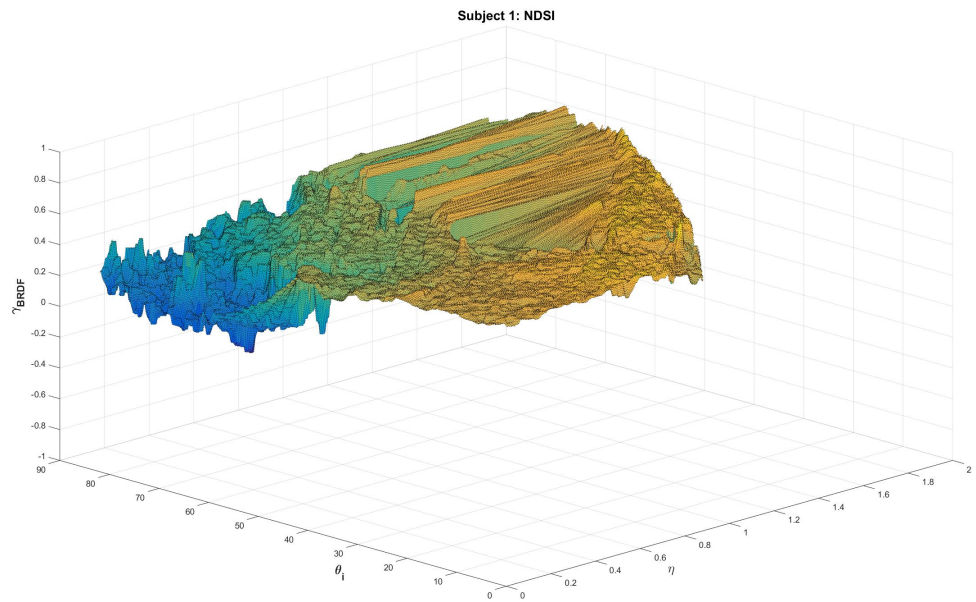


Figure 130. NDSI and NDGRI calculations from Subject 1 data.

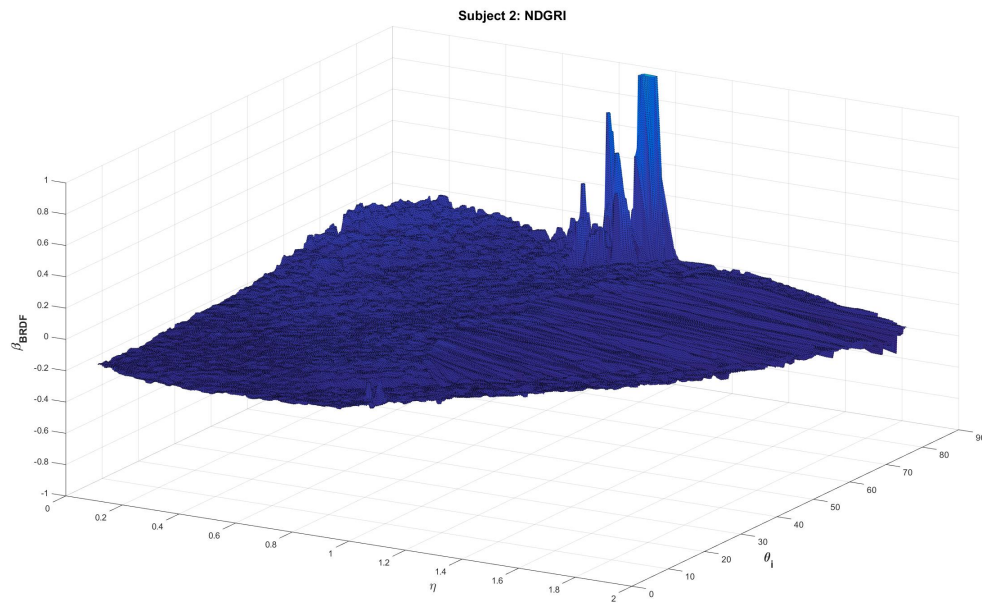
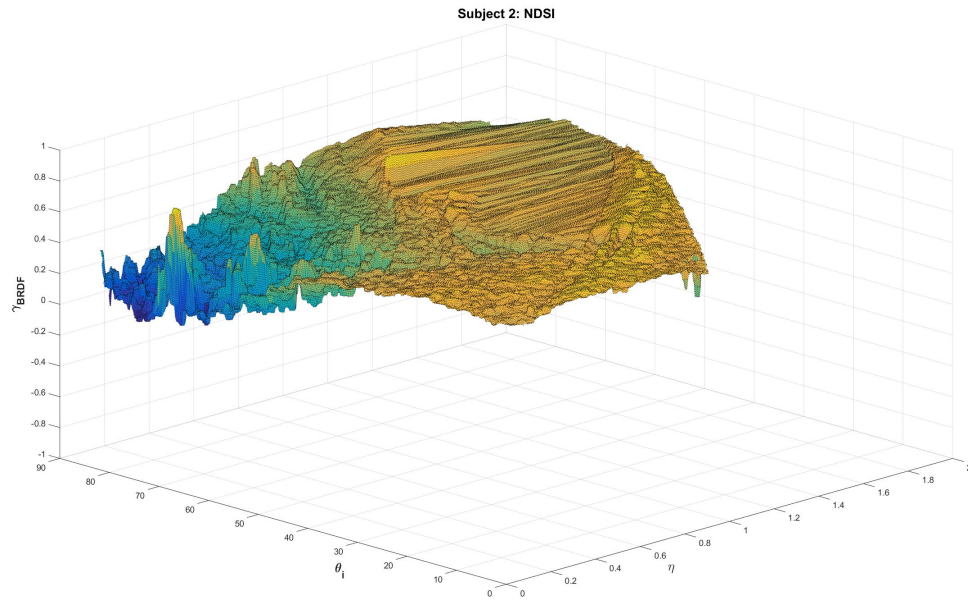


Figure 131. NDSI and NDGRI calculations from Subject 2 data.

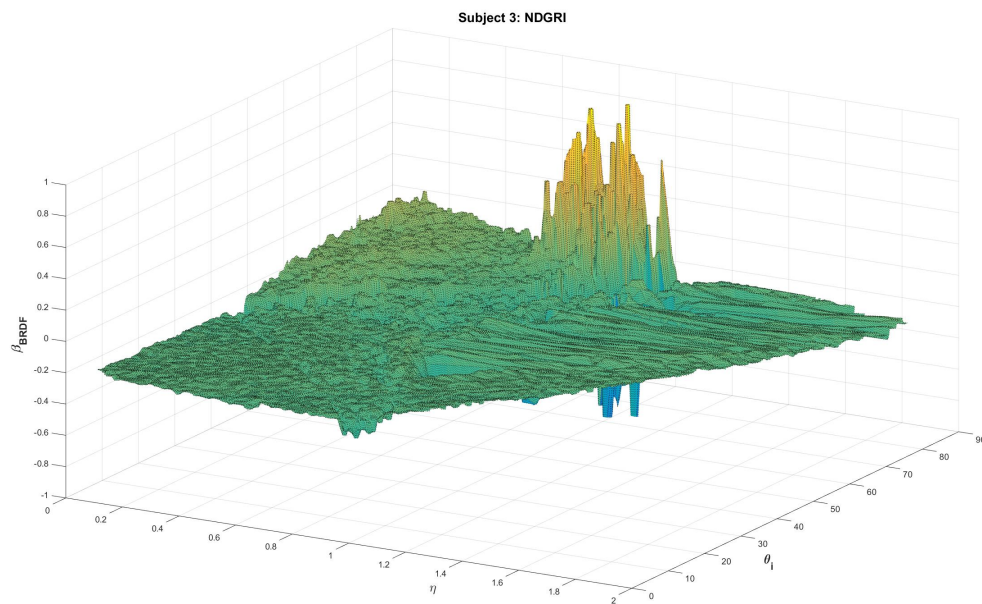
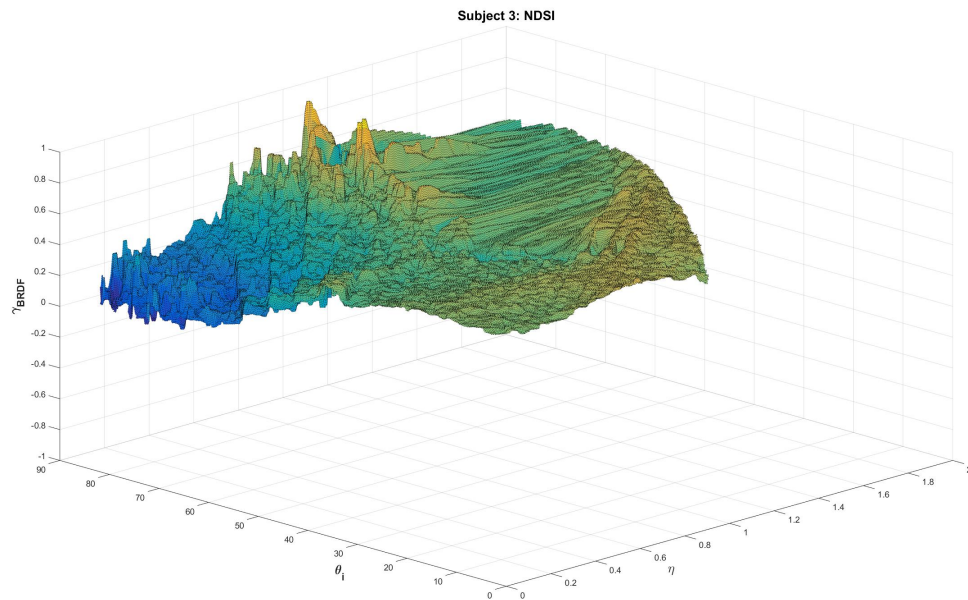


Figure 132. NDSI and NDGRI calculations from Subject 3 data.

Subject 1: Specular Component Plots (Mean of first 50 sample slices at η values near 0)

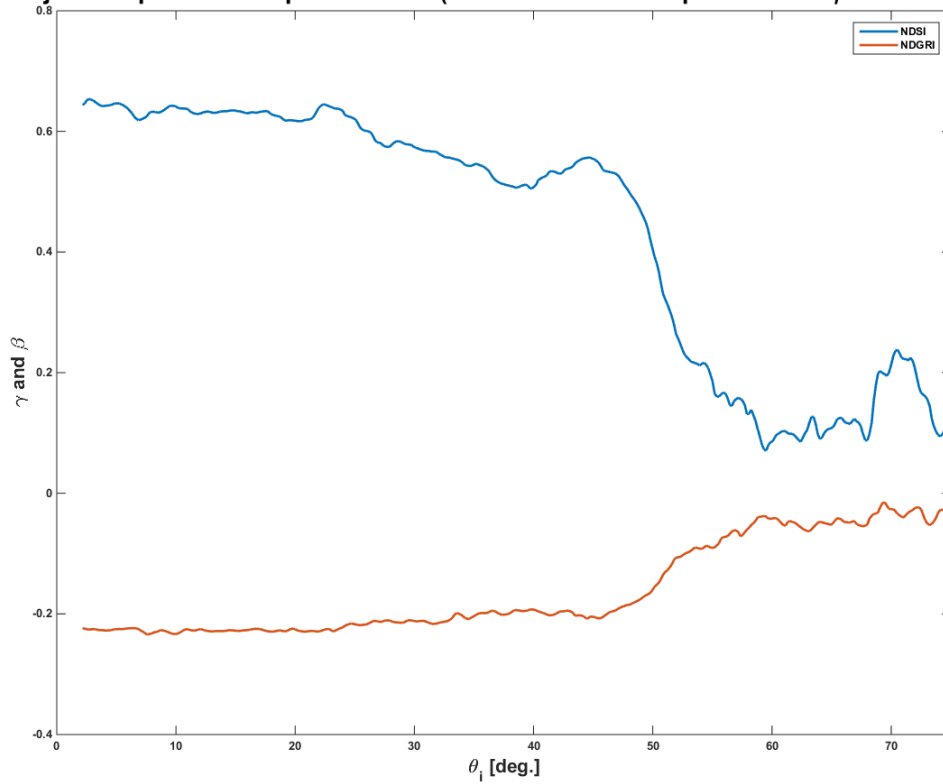


Figure 133. Subject 1 - NDSI and NDGRI values for all $\theta_i = \theta_r$ forward-scattering combinations.

Subject 2: Specular Component Plots (Mean of first 50 sample slices at η values near 0)

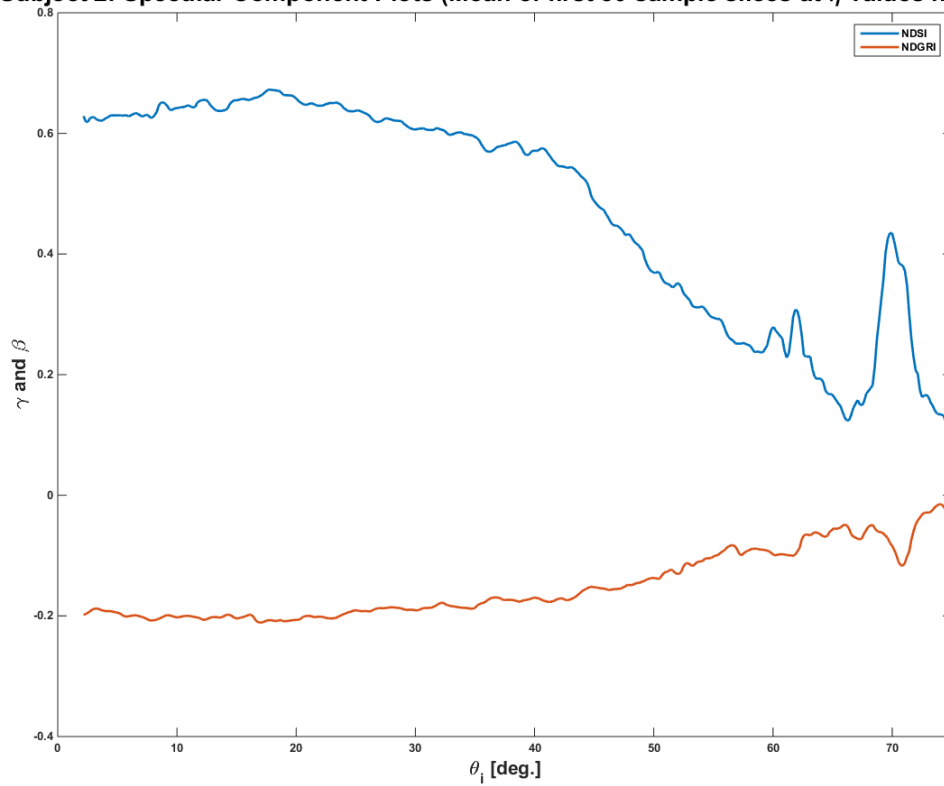


Figure 134. Subject 2 - NDSI and NDGRI values for all $\theta_i = \theta_r$ forward-scattering combinations.

Subject 3: Specular Component Plots (Mean of first 50 sample slices at η values near 0)

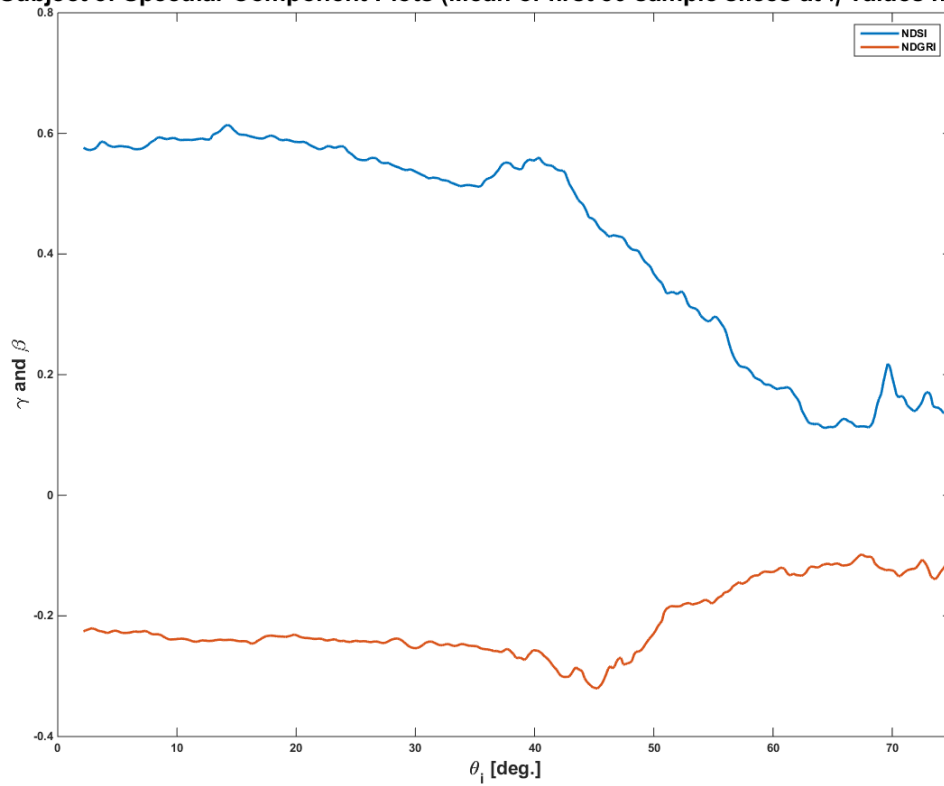


Figure 135. Subject 3 - NDSI and NDGRI values for all $\theta_i = \theta_r$ forward-scattering combinations.

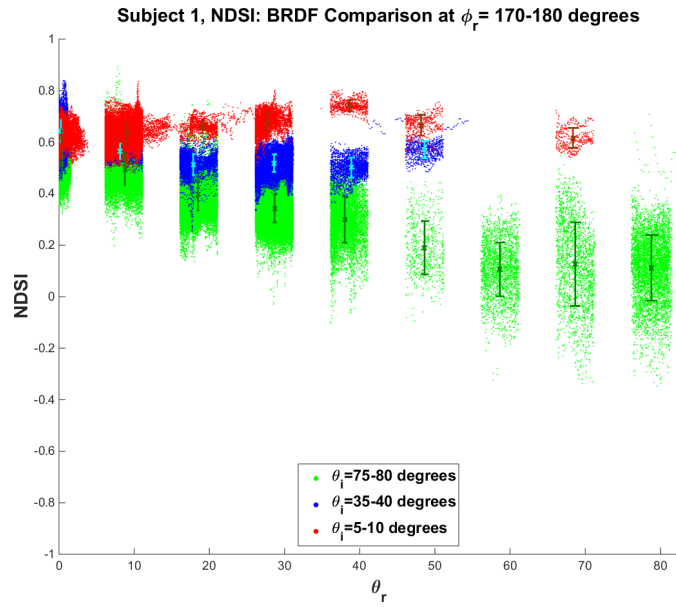


Figure 136. Three ranges for θ_i values are evaluated at ϕ_r close to 180 degrees and plotted in NDSI vs θ_r space for Subject 1.

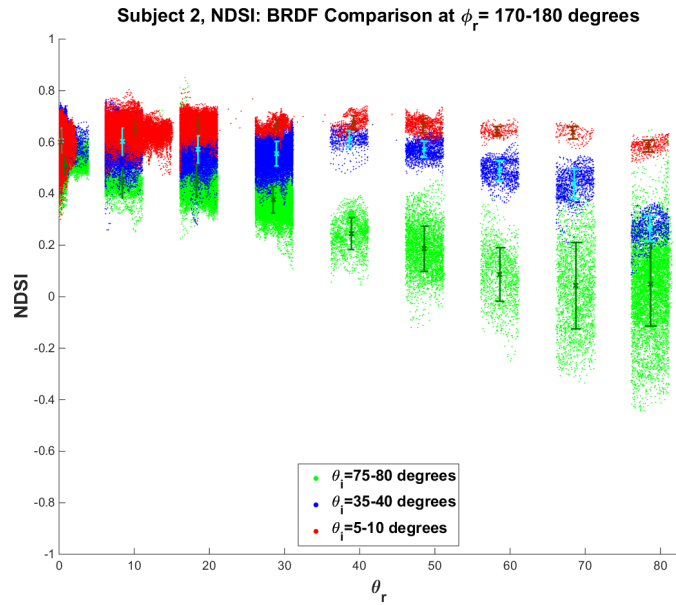


Figure 137. Three ranges for θ_i values are evaluated at ϕ_r close to 180 degrees and plotted in NDSI vs θ_r space for Subject 2.

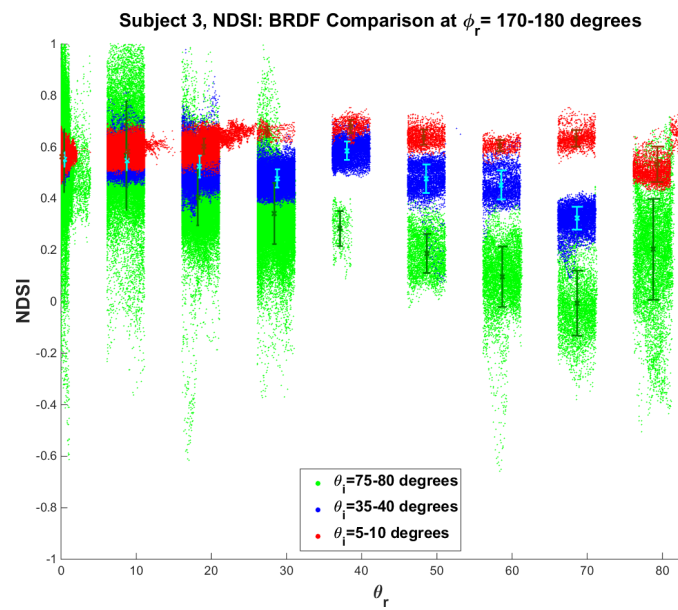


Figure 138. Three ranges for θ_i values are evaluated at ϕ_r close to 180 degrees and plotted in NDSI vs θ_r space for Subject 3.

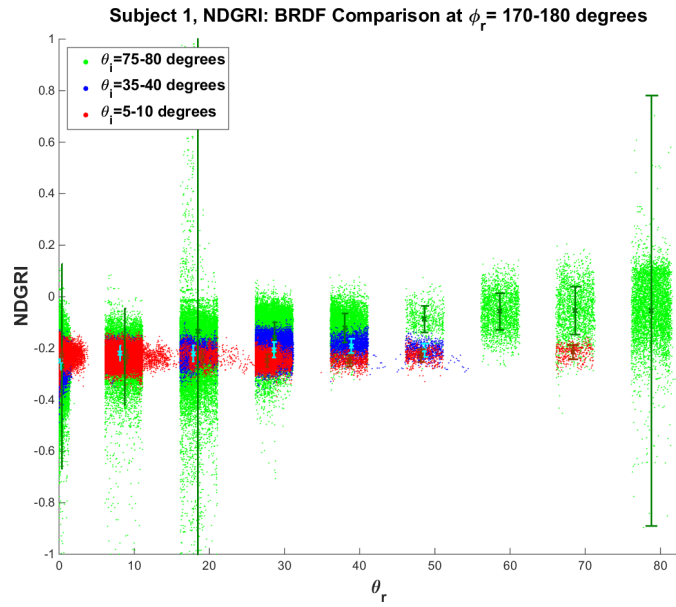


Figure 139. Three ranges for θ_i values are evaluated at ϕ_r close to 180 degrees and plotted in NDGRI vs θ_r space for Subject 1.

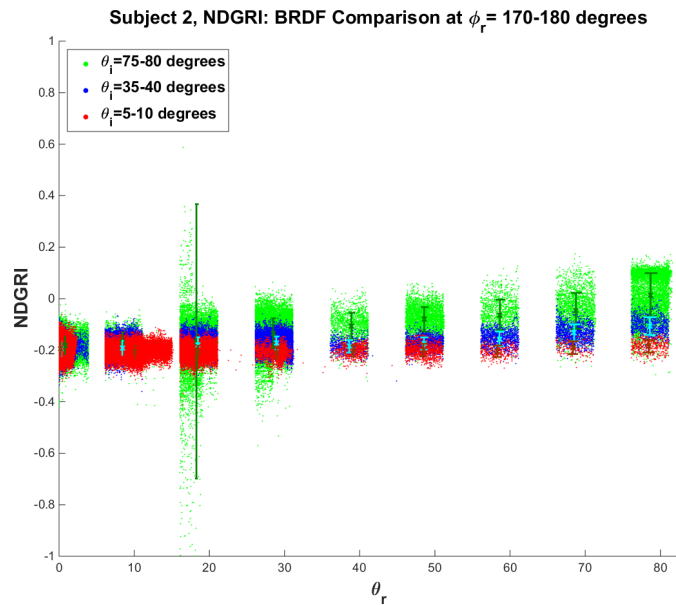


Figure 140. Three ranges for θ_i values are evaluated at ϕ_r close to 180 degrees and plotted in NDGRI vs θ_r space for Subject 2.

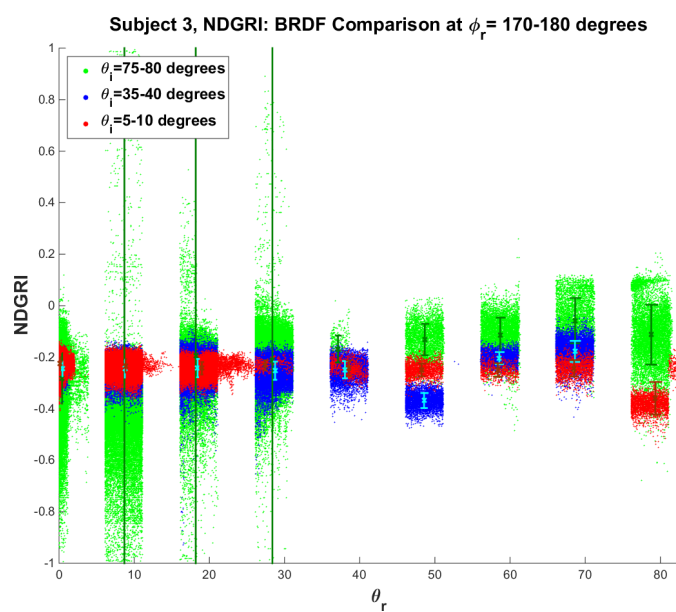


Figure 141. Three ranges for θ_i values are evaluated at ϕ_r close to 180 degrees and plotted in NDGRI vs θ_r space for Subject 3.

Appendix B. IRB Approval



DEPARTMENT OF THE AIR FORCE
AIR FORCE RESEARCH LABORATORY
WRIGHT-PATTERSON AIR FORCE BASE OHIO 45433

MEMORANDUM FOR AFIT/ENG (MICHAEL MENDENHALL)

FROM: 711 HPW/IR

SUBJECT: IRB Approval for the Use of Human Volunteers in Research

1. Protocol title: Human Skin Bi-Directional Reflectance Distribution Function
2. Protocol number: FWR20150135H
3. Protocol version: 1.00
4. Risk: Minimal
5. Approval date: 01 October 2015
6. Expiration date: 30 September 2016
7. Scheduled renewal date: 30 August 2016
8. Type of review: Initial - Expedited
9. Assurance Number and Expiration Date:
 - AFRL DoD Assurance F50002: 06 March 2017
 - TASC Inc FWA00015543: 11 March 2018
 - AFIT DoD Assurance F50301: 05 October 2017
10. CITI Training: Completed
11. The above protocol has been reviewed and approved by the AFRL IRB via expedited review procedures. All requirements, as set by the IRB and its legal counsel, have been fully complied with. The researcher is looking to compute the Bi-Directional Reflectance Distribution Function (BRDF) components (the diffuse and specular reflectance) for human skin at five wavelengths used for skin detection, false alarm suppression, and melanin estimation (approximately 540nm, 620nm, 850nm, 1080nm, 1250nm, and 1580nm) to improve the performance of these methods over a wide variety of operating conditions and scenarios. The study is minimal risk. This protocol therefore meets the criteria for expedited review in accordance with 32 CFR 219.110 (b)(1), U.S. Department of Health and Human Services category (4) Collection of data through noninvasive procedures (not involving general anesthesia or sedation) routinely employed in clinical practice, excluding procedures involving x-rays or microwaves. Where medical devices are employed, they must be cleared/approved for marketing. (Studies intended to evaluate the safety and effectiveness of the medical device are not generally eligible for expedited review, including studies of cleared medical devices for new indications.), and U.S. Department of

Health and Human Services category (6) Collection of data from voice, video, digital, or image recordings made for research purposes.

13. FDA regulations: No investigative drugs or devices are used in this study.

14. This approval applies only to the requirements of 32 CFR 219, DoDI 3216.02_AFI 40-402, and related human research subject regulations. If this project is a survey, attitude or opinion poll, questionnaire or interview, consult AFI 38-501, AF Survey Program, for further guidance. Headquarters AFPC/DPSAS is the final approval authority for conducting attitude and opinion surveys within the Air Force. If the survey, attitude or opinion poll, questionnaire or interview is hosted on a .com server, consult AFI 33-129, Web Management and Effective Use of Internet-based Capabilities, for further guidance. If the study is being conducted under an Investigational New Drug (IND) or Device Exemption (IDE), a copy of the FDA IDE or IND approval letter must be submitted by the Principal Investigator to the IRB.

15. With this approval comes the expectation that the Principle Investigator has the funding to fully execute the protocol. Partial protocol funding, particularly with Greater than Minimal Risk studies, should prompt a re-examination of the protocol by both the Principle Investigator and the IRB with specific emphasis on the risk-benefit evaluation.

16. Any serious adverse event or issues resulting from this study should be reported immediately to the IRB. Amendments to protocols and/or revisions to informed consent documents must have IRB approval prior to implementation. Please retain both hard copy and electronic copy of the final approved protocol and informed consent document.

17. All inquiries and correspondence concerning this protocol should include the protocol number and name of the primary investigator. Please ensure the timely submission of all required progress and final reports and use the templates provided on the AFRL IRB web site <http://www.wpafb.af.mil/library/factsheets/factsheet.asp?id=7496> .

18. For questions or concerns, please contact the IRB administrator, 2d Lt Alexander Trigo at alex.trigo.2@us.af.mil, 937-656-5437, or DSN 986-5437. All inquiries and correspondence concerning this protocol should include the protocol number and name of the primary investigator. For protocol submissions, please send documents to the IRB organizational inbox at AFRL.IR.ProtocolManagement@us.af.mil.



KIM E. LONDON, JD, MPH, CIP
Chair, AFRL IRB

1st Indorsement to AFIT/ENG (MICHAEL MENDENHALL) 01 October 2015, Approval for Use of Humans in Research, Initial Review - Expedited, FWR20150135H

MEMORANDUM FOR 711 HPW/IR (KIM LONDON)

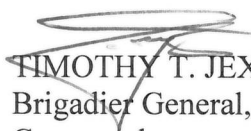
I have reviewed all protocol records and found them to be complete and accurate.



ALEXANDER M. TRIGO, 2d Lt, USAF
Lead Administrator, AFRL IRB

2nd Indorsement to AFIT/ENG (MICHAEL MENDENHALL) 01 October 2015, Approval for Use of Humans in Research, Initial Review - Expedited, FWR20150135H

This protocol has been reviewed and approved by the AFRL IRB. I concur with the recommendation of the IRB and approve this research.



TIMOTHY T. JEX
Brigadier General, USAF, MC, CFS
Commander
711th Human Performance Wing

02 OCT 2015

Bibliography

1. A. L. Brooks. Improved multispectral skin detection and its application to search space reduction for histograms of oriented gradients-based dismount detection. Master's thesis, Graduate School of Engineering, Air Force Institute of Technology (AETC), Wright-Patterson AFB OH, 2010.
2. S. D. Butler, S. E. Nauyoks, and M. A. Marciniak. Comparison of microfacet BRDF model to modified Beckmann-Kirchhoff BRDF model for rough and smooth surfaces. *Optics Express*, 23:29100–29112, October 2015.
3. K. J. Dana, B. van Ginneken, S. K. Nayar, and J. J. Koenderink. Reflectance and texture of real-world surfaces. *ACM Transactions on Graphics*, 18(1):1–34, January 1999.
4. K. J. Dana and J. Wang. Device for convenient measurement of spatially varying bidirectional reflectance. *Optical Society of America*, 21(1):1–12, 2004.
5. E. L. Dereniak and G. G. Boreman. *Infrared Detectors and Systems*. A Wiley-Interscience Publication, New York, NY, 1996.
6. M. T. Eismann. *Hyperspectral Remote Sensing*. SPIE Press Book, Bellingham, WA, 2012. With AFIT classnotes.
7. M. Goesele. Image-based BRDF measurement. University Lecture, IMPA Mini-course 2005.
8. J. E. Harvey, A. Krywonos, and C. L. Vernold. Modified Beckmann-Kirchhoff scattering model for rough surfaces with large incident and scattering angles. *Optical Engineering*, 46(7):078002, July 2007.
9. T. Hastie, R. Tibshirani, and J. Friedman. *The Elements of Statistical Learning*. Springer, Upper Saddle River, NJ, 2001.
10. G. Heinz, Louis J. Peterson, R. W. Johnson, and C. J. Kerk. Exploring relationships in body dimensions. *Journal of Statistics Education*, 11(2), 2003.
11. G. R. Hunt and J. W. Salisbury. *Visible and Near-Infrared Spectra of Minerals and Rocks: I Silicate Materials*. Hanscom Field, Bedford, MA, 1970.
12. S. L. Jacques. Skin optics. *Oregon Medical Center News*, January 1998.
13. C. M. Jengo and J. D. LaVeigne. Sensor performance comparison of hyperspectral instruments 1 and 2. *Proceedings IEEE Aerospace Conference*, 3:1799–1805, March 2004.

14. D. B. Kim, K. Y. Kim, K. S. Park, M. K. Seo, and K. H. Lee. A fast and accurate image-based measuring system for isotropic reflection materials. *Proceedings of SPIE*, 7065, 2008.
15. B. M. Koch. A multispectral bidirectional reflectance distribution function study of human skin for improved dismount detection. Master's thesis, Graduate School of Engineering, Air Force Institute of Technology (AETC), Wright-Patterson AFB OH, 2011.
16. A. Krywonos. *Predicting surface scatter using a linear systems formulation of non-paraxial scalar diffraction*. PhD thesis, University of Central Florida, 2006.
17. A. Krywonos, J. E. Harvey, and N. Choi. Linear systems formulation of scattering theory for rough surfaces with arbitrary incident and scattering angles. *J. Opt. Soc. Am. A*, 28(6):1121–1138, June 2011.
18. C. Leonard. Performance of an EO/IR sensor system in marine search and rescue. *Proc. SPIE*, 5787:122–133, 2005.
19. S. Marschner. *Inverse Rendering for Computer Graphics*. PhD thesis, Cornell University, Ithaca, New York, 1998.
20. S. R. Marschner, E. P. F. Lafortune, K. E. Torrance, S. H. Westin, and D. P. Greenberg. Image-based BRDF measurement including human skin. *Eurographics Workshop on Rendering*, 1999.
21. S. R. Marschner, S. H. Westin, E. P. F. Lafortune, and K. E. Torrance. Image-based BRDF measurement. *Applied Optics*, 39(16), 2000.
22. P. Matts, P. Dykes, and R. Marks. The distribution of melanin in skin determined in vivo. *British Journal of Dermatology*, 156(4):620–628, April 2007.
23. W. Matusik, H. Pfister, M. Brand, and L. McMillan. A data-driven reflectance model. *ACM Transactions on Graphics*, 22(3):759–769, 2003.
24. G. Meister. *Bidirectional Reflectance of Urban Surfaces*. PhD thesis, University of Hamburg, Hamburg, Germany, 2000.
25. M. J. Mendenhall, A. S. Nunez, and R. K. Martin. Human skin detection in the visible and near infrared. *Applied Optics*, 54(35):10559–10570, December 2015.
26. T. Moon. The expectation-maximization algorithm. *IEEE Signal Processing Magazine*, 1(6):47–60, 1996.
27. F. E. Nicodemus, J. C. Richmond, J. J. Hsia, I. W. Ginsberg, and T. Limperis. Geometrical considerations and nomenclature for reflectance. National Bureau of Standards Monograph 160, Department of Commerce, 1977.

28. A. S. Nunez. *A Physical Model of Human Skin and Its Application for Search and Rescue*. PhD thesis, Graduate School of Engineering, Air Force Institute of Technology (AETC), Wright-Patterson AFB OH, 2009.
29. A. S. Nunez and M. J. Mendenhall. Detection of human skin in near infrared hyperspectral imagery. *IGARSS*, 5787(2):621–624, 2008.
30. K. R. Peskosky. Design of a monocular multi-spectral skin detection, melanin estimation, and false-alarm suppression system. Master’s thesis, Graduate School of Engineering, Air Force Institute of Technology (AETC), Wright-Patterson AFB OH, 2010.
31. J. Rouse, J. A. Schell R. H. Haas, and D. W. Deering. Monitoring vegetation systems in the great plains with erts. *Third Earth Resources Technology Satellit-1 Symposium*, pages 309–317, December 1973.
32. G. Shaw and D. Manolakis. Signal processing for hyperspectral image exploitation. *IEEE Signal Processing Magazine*, pages 1053–5888, January 2002.
33. J. R. Shell. Bidirection reflectance: An overview with remote sensing applications and measurement recommendations. *Technical Report*, 2004.
34. J. R. Simard, P. Mathieu, G. Fournier, and V. Larochelle. A range-gated intensified spectrographic imager: An instrument for active hyperspectral imaging. *Proceedings of Laser Radar Technology and Applications V*, 4035:180–191, 2000.
35. C. Simi, A. Hill, and H. Kling. Airborne remote spectrometry support to rescue personnel at ground zero after the world trade center attack on september 11, 2001. *Proceedings of Imaging Spectrometry VIII*, 4816.
36. B. Stevenson, R. O’Connor, W. Kendall, A. Stocker, W. Schaff, R. Holasek, D. Alexa D. Even, J. Salvador, M. Eismann, R. Mack, P. Kee, S. Harris, B. Karch, and J. Kershenstein. The civil air patrol archer hyperspectral sensor system. *Airborne Intelligence, Surveillance, Reconnaissance (ISR) Systems and Applications II*, 5787:17–28, 2005.
37. S. Subramanian and N. Gat. Subpixel object detection using hyperspectral imaging for search and rescue. *Automatic Target Recognition VIII*, 3371:216–225, 1998.
38. M. Topping, J. Pfeiffer, A. Sparks, K. Jim, and D. Yoon. Advanced airborne hyperspectral imaging system (aahis). *Proceedings of Imaging Spectrometry VIII*, 4816:1–11, 2002.
39. G. J. Ward. Measuring and modeling anisotropic reflection. *SIG-GRAPH Computer Graphics*, 26(2):265–272, 1992.

40. T. Weyrich, W. Matusik, H. Pfister, J. Lee, A. Ngan, H. Wann, and J. M. Gross. A measurement-based skin reflectance model for face rendering and editing. Technical Report, July 2005.
41. T. Weyrich, W. Matusik, H. Pfister, J. Lee, A. Ngan, H. Wann, J. M. Gross, C. Tu, and J. Mcandless. Analysis of human faces using a measurement-based skin reflectance model. *ACM Transactions on Graphics*, 25:1013–1024, 2006.

REPORT DOCUMENTATION PAGE

Form Approved
OMB No. 0704-0188

The public reporting burden for this collection of information is estimated to average 1 hour per response, including the time for reviewing instructions, searching existing data sources, gathering and maintaining the data needed, and completing and reviewing the collection of information. Send comments regarding this burden estimate or any other aspect of this collection of information, including suggestions for reducing this burden to Department of Defense, Washington Headquarters Services, Directorate for Information Operations and Reports (0704-0188), 1215 Jefferson Davis Highway, Suite 1204, Arlington, VA 22202-4302. Respondents should be aware that notwithstanding any other provision of law, no person shall be subject to any penalty for failing to comply with a collection of information if it does not display a currently valid OMB control number. **PLEASE DO NOT RETURN YOUR FORM TO THE ABOVE ADDRESS.**

1. REPORT DATE (DD-MM-YYYY) 24-03-2016		2. REPORT TYPE Master's Thesis		3. DATES COVERED (From — To) September 2014 — March 2016	
4. TITLE AND SUBTITLE Image-Based Bidirectional Reflectance Distribution Function of Human Skin in the Visible and Near Infrared				5a. CONTRACT NUMBER	
				5b. GRANT NUMBER	
				5c. PROGRAM ELEMENT NUMBER	
6. AUTHOR(S) Bintz, Jeffrey R., Second Lieutenant, USAF				5d. PROJECT NUMBER 16G201	
				5e. TASK NUMBER	
				5f. WORK UNIT NUMBER	
7. PERFORMING ORGANIZATION NAME(S) AND ADDRESS(ES) Air Force Institute of Technology Graduate School of Engineering and Management (AFIT/EN) 2950 Hobson Way WPAFB OH 45433-7765				8. PERFORMING ORGANIZATION REPORT NUMBER AFIT-ENG-MS-16-M-004	
9. SPONSORING / MONITORING AGENCY NAME(S) AND ADDRESS(ES) Dr. Timothy Webb 711 Human Performance Wing, Human-MASINT Section 2800 Q Street, B824, WPAFB OH 45433-7765 Phone: 937-255-6542 Email: timothy.webb.8@us.af.mil				10. SPONSOR/MONITOR'S ACRONYM(S) 711 HPW/RHXBA	
				11. SPONSOR/MONITOR'S REPORT NUMBER(S)	
12. DISTRIBUTION / AVAILABILITY STATEMENT Distribution Statement A: Approved for Public Release; Distribution Unlimited.					
13. SUPPLEMENTARY NOTES This material is declared a work of the U.S. Government and is not subject to copyright protection in the United States.					
14. ABSTRACT Human detection is an important first step in locating and tracking people in many missions including SAR and ISR operations. Recent detection systems utilize hyperspectral and multispectral technology to increase the acquired spectral content in imagery and subsequently better identify targets. This research demonstrates human detection through a multispectral skin detection system to exploit the unique optical properties of human skin. At wavelengths in the VIS and NIR regions of the electromagnetic spectrum, an individual can be identified by their unique skin parameters. Current detection methods base the skin pixel selection criteria on a diffuse skin reflectance model; however, it can be observed that human skin exhibits a combination of specular and diffuse reflectance. The objective of this effort is to better characterize human skin reflectance by collecting image-based BRDF skin measurements for future model incorporation in the existing multispectral skin detection system. Integrating multispectral BRDF data should reduce misdetections and better describe skin reflectance as a function of illumination source, target, and detector orientation.					
15. SUBJECT TERMS Human Skin Detection, Bidirectional Reflectance Distribution Function, Image-Based BRDF Measurement, Surface Normal Extraction, Search and Rescue					
16. SECURITY CLASSIFICATION OF:			17. LIMITATION OF ABSTRACT	18. NUMBER OF PAGES	19a. NAME OF RESPONSIBLE PERSON
a. REPORT	b. ABSTRACT	c. THIS PAGE			Dr. Michael J. Mendenhall, AFIT/ENG
U	U	U	UU	201	19b. TELEPHONE NUMBER (include area code) (937)255-3636 x4382 ; michael.mendenhall.1@us.af.mil